UCF Senior Design 1 Final Report

I.R.I.S.

Infrared Reliability Inspection System

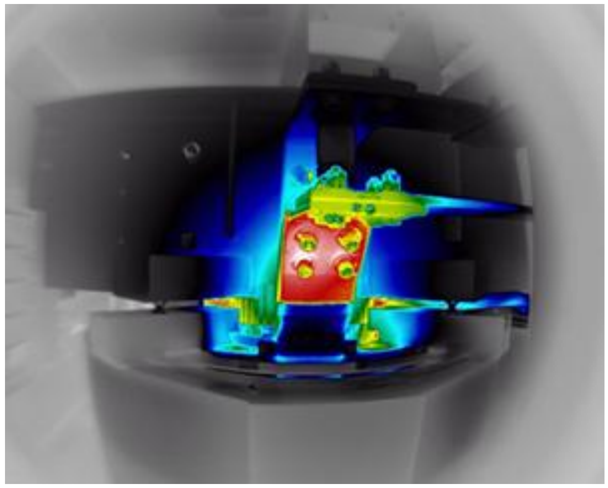

Final Report Document
Department of Electrical Engineering and Computer Science
University of Central Florida

Group 3

Sean Willie - Electrical Engineering

Andrew VanAuken - Electrical Engineering

Jason Ha - Photonic Science & Engineering

Shea Meyer - Computer Engineering

Reviewers / Advisors / Contributors

Faculty Advisor: Dr. Chung Yong Chan

Faculty Advisor: Dr. Lei Wei

Optics Advisor: Dr. Leisher (CREOL)

Reviewer 1: Dr. Qichen Yang

Reviewer 2: Dr. Piotr Kulik

Reviewer 3: Dr. Robert Grimming (CREOL)

Table of Contents

List of Figures

List of Tables

Chapter 1 – Executive Summary

IRIS (Infrared Reliability Inspection System) is a senior design project developed at the University of Central Florida by a team of undergraduate students in electrical, computer, and photonics engineering. The purpose of this project is to identify and monitor abnormal temperature conditions in electrical equipment through the use of infrared sensing and embedded electronics. As industrial and power systems continue to demand higher reliability, there is a growing need for safer inspection methods that do not require direct access to energized components. IRIS addresses this need by enabling continuous thermal monitoring within environments such as switchgears, transformers, and distribution panels.

The system is built around an infrared thermopile sensor combined with a simplified optical assembly and a motorized scanning mechanism. Rather than using a full thermal imaging array, IRIS implements a raster-scanning approach in which a two-axis mirror detects the sensor's field of view across the target area. Temperature measurements are collected sequentially and later reconstructed into a thermal representation of the scene through software processing. This design significantly reduces system cost and complexity while still providing the ability to detect hotspots and monitor temperature trends over time.

To maintain accurate spatial alignment between measurements and their corresponding locations, the scanning mechanism incorporates magnetic rotary encoders on each axis. These encoders provide real-time angular feedback, allowing the system to track mirror orientation and improve repeatability. This feedback is especially important for minimizing errors caused by mechanical tolerances or missed motor steps, ensuring that reconstructed thermal data remains consistent and reliable.

System control and data handling are managed by an embedded microcontroller platform with integrated wireless communication capabilities. The controller coordinates sensor data acquisition, motor actuation, and encoder feedback while handling communication with external interfaces. Collected data is transmitted to a locally hosted web-based dashboard, where users can monitor system status, view thermal information, and receive notifications when predefined temperature thresholds are exceeded. Additional environmental sensing is included to provide context for measurements and improve overall system reliability.

The IRIS system is designed for permanent installation within electrical enclosures, particularly those equipped with infrared inspection windows. By operating behind these windows, the system allows inspections to be performed without opening panels, reducing the risk associated with energized equipment and supporting established electrical safety practices. The modular architecture of the system allows it to be adapted to different installations and expanded to multiple monitoring points.

This report presents the complete development process of the IRIS system, including theoretical background, component evaluation, and design decisions. It also details the system architecture, hardware implementation, and software functionality. Relevant standards and design constraints are discussed, followed by documentation of prototyping, testing, and project management considerations. The report concludes with an assessment of system performance and potential directions for improvement.

Chapter 2 – Project Description

2.1 Project Background and Motivation

Electrical power equipment such as switchgear, transformers, and distribution panels are critical assets in industrial and utility environments. Failures in these systems often originate from localized overheating at electrical connections, bus joints, or internal conductors due to loose connections, corrosion, overloading, or insulation degradation. If left undetected, these thermal anomalies can progress into equipment damage, unplanned downtime, and hazardous events such as arc flash.

Infrared, IR, thermography is widely used as a condition-based maintenance technique for identifying abnormal heating while equipment remains energized. Preventive maintenance guidance such as detailed by the National Fire Protection Association (NFPA)'s **NFPA 70B** emphasizes thermographic inspections as a key tool for monitoring energized electrical equipment and recommends routine monitoring of switchgear, transformers, and distribution equipment — often at least annually and in some cases more frequently — under representative loading conditions [1]. However, traditional industry practice typically relies on **manual, periodic inspections** using handheld thermal cameras. These inspections are labor-intensive, require trained personnel, and may be performed infrequently, allowing faults to develop between inspection cycles.

A major barrier to frequent open-panel inspections is safety. Industry safety standards and regulations, including **OSHA 1910** from the U.S. Occupational Safety and Health Administration (OSHA), **NFPA 70E**, and harmonized standards such as CSA Z462 from the Canadian Standards Association, emphasize minimizing personnel exposure to energized conductors and circuit parts, and encourage keeping equipment doors and panels closed when energized [1]. Arc flash events are especially severe because they can be triggered by common human interactions such as removing panels, dropping tools, or accidental contact with energized parts; the resulting arc blast can produce extreme thermal and pressure effects that personal protective equipment (PPE) does not fully protect against [1]. As a result, facilities increasingly adopt engineering controls that reduce the need for invasive, open-door inspection practices.

To enable safer inspection workflows, many facilities install **IR inspection windows** (also called IR viewports). An IR window is an inspection point installed on an enclosure that allows IR to transmit to the outside environment while maintaining enclosure integrity and environmental sealing (e.g., maintaining an enclosure's IP/NEMA rating when properly selected and installed) [1]. Importantly, sealed IR inspection windows help preserve the "enclosed" and "guarded" condition of the equipment, enabling thermographic data collection without exposing personnel to energized components or creating a change-of-state risk, which can substantially reduce hazard exposure and PPE requirements relative to open-panel inspection [1].

Despite these improvements, most IR-window-enabled thermography remains **manual and non-continuous**, producing only snapshot measurements at discrete times. This approach may miss transient or load-dependent heating and provides limited visibility into gradual degradation trends. Measurement quality and "trendability" depend on consistency in parameters such as measurement point, collection angle, and distance; IR windows improve repeatability by enforcing consistent geometry across inspection cycles [1]. Building on these principles, this project proposes a **permanently installed thermal monitoring system mounted behind an existing IR viewport** to automate data collection, generate continuous thermal trends, and provide timely alerts — improving safety, reliability, and maintenance efficiency by reducing reliance on infrequent manual surveys while preserving the benefits of closed-door inspection [1].

2.2 Current Commercial Technologies and Existing Projects

2.2.1 Insight IR Camera

IR-based preventative maintenance has already been implemented in commercial settings. One such application of this concept is the LayerZero Power Systems INSIGHT IR® [2]. The INSIGHT IR® is a proprietary device to provide fixed, continuous IR monitoring of critical electrical connections within power distribution equipment. INSIGHT IR® utilizes permanently installed IR cameras embedded directly into LayerZero's equipment to monitor lug connections, bus interfaces, and other high-risk thermal points. By continuously collecting temperature data, the system builds a thermal baseline over time and detects slow-developing thermal anomalies that may be missed by periodic handheld IR inspections.

INSIGHT IR® is designed for mission-critical environments such as data centers, industrial facilities, and semiconductor manufacturing plants where uptime and safety are paramount. The system emphasizes safety by eliminating the need to open energized cabinets during routine inspections and reduces reliance on external IR inspection services. Instead of capturing isolated snapshots during annual or semi-annual maintenance windows, the system provides continuous visibility into thermal behavior across varying load conditions. However, INSIGHT IR® is tightly integrated into proprietary power distribution equipment and is not intended as a retrofit solution for existing switchgear or as a flexible research platform.

The proposed senior design project shares the same core motivation for improving electrical safety and reliability through continuous thermal monitoring but differs significantly in scope and implementation. Rather than embedding sensors into new, proprietary equipment, this project focuses on a modular, vendor-agnostic system designed to operate behind existing IR viewports already installed on many electrical enclosures. This approach enables compatibility with a wide range of existing infrastructure while maintaining the safety benefits of closed-door inspection. Additionally, the proposed system emphasizes transparency, extensibility, and engineering analysis, allowing experimentation with sensor calibration, optical considerations, data processing, and dashboard-based visualization.

Overall, the existence of commercial systems such as INSIGHT IR® validates the importance and industry relevance of continuous thermal monitoring in power systems. This project builds upon those established principles while exploring a lower-cost, retrofit-compatible, and research-oriented implementation suitable for academic development and broader applicability across existing power equipment installations.

2.2.2 FLIR AX8 9 Hz Thermal Monitoring Camera

The FLIR AX8 9 Hz is a compact, permanently installed thermal monitoring camera designed for continuous condition monitoring where temperature and temperature trends indicate developing faults. The AX8 is positioned as an "affordable and accurate temperature measurement solution" with built-in analysis, alarm functionality, and autonomous communication over standard industrial Ethernet networks. It supports distributed deployments ranging from a single camera to multi-camera installations using standard Ethernet hardware.

The AX8 uses an uncooled microbolometer focal plane array (FPA) operating in the 7.5–13 µm spectral band. The infrared image resolution is 80 × 60 pixels, with 11.1 mrad IFOV, and a fixed-focus lens with 48° × 37° field of view and 1.54 mm focal length. The camera operates at 9 Hz, which aligns with export-friendly thermal imaging configurations while remaining sufficient for slow thermal processes common in electrical equipment monitoring. Thermal sensitivity is specified as < 0.10°C NETD at +30°C (100 mK), supporting detection of small temperature differences useful for trending and early anomaly recognition.

For measurement, the AX8 specifies an object temperature range of –10 to +150°C, with accuracy of ±2°C or ±2% of reading over +10 to +100°C object temperature when ambient is +10 to +35°C. The device includes embedded measurement tools such as six spotmeters, and six analysis boxes with min/max/average reporting, plus automatic hot/cold detection that reports the extreme value and its position within a defined region. To improve measurement correctness and repeatability across installations, the AX8 includes multiple correction capabilities including emissivity adjustment (0.01 to 1.0), reflected apparent temperature correction, atmospheric transmission correction (based on distance, ambient temperature, and humidity inputs), and external optics/window transmission correction (based on user-input window transmission and window temperature). These corrections are particularly relevant for closed-door workflows where measurements may occur through an IR window or other transmissive optics.

A key differentiator of the AX8 is its "smart" monitoring stack: the camera can generate automatic alarms from any selected measurement function, with up to five alarms configured simultaneously. Alarm actions include digital output, image storage, network notification, and automated file sending (FTP) or email (SMTP) of analysis results or images. The AX8 includes a built-in web server for configuration and control, and supports multiple streaming formats including MJPEG, MPEG-4, and H.264 with streaming resolution listed as 640 × 480 (matching the included 640 × 480 visual camera). For industrial integration, the AX8 supports both EtherNet/IP and Modbus TCP, enabling connection to PLCs and industrial monitoring systems using standard field bus protocols.

The AX8 supports Power over Ethernet (PoE) IEEE 802.3af Class 2 and can also run from 12/24 VDC. Its continuous power is specified as 2 W (with 4.7 W absolute max) over an allowed voltage range of 10.8–30 VDC. Mechanically, the camera is compact (54 × 25 × 79 mm without connectors; 54 × 25 × 95 mm with connectors) and lightweight (0.125 kg). It is rated IP67 and specified for industrial environments including –10°C to +50°C operating temperature and high humidity qualification (up to 95% RH over IEC cycling conditions). Ethernet is specified as 100 Mbps with an M12 8-pin X-coded connector (adapter required to standard X-coded), and power/digital I/O use an M12 8-pin A-coded connector. The digital I/O includes one opto-isolated input and one opto-isolated output, both rated 10–25 VDC, with output current up to 0.6 A, enabling direct interface to external alarm devices or PLC input modules.

The FLIR AX8 demonstrates a mature commercial approach to continuous thermal monitoring: small-form fixed thermal imaging, embedded measurement analytics, and industrial Ethernet integration for alarms and data flow. Its support for external optics/windows correction is particularly relevant to closed-door thermography workflows where imaging is performed through IR inspection windows. However, the AX8's design assumes a fixed camera viewing geometry and relies on an imaging array to capture the scene at once. In contrast, the proposed senior design system explores a retrofit-friendly architecture behind existing IR viewports using a mechanically scanned field of view with a lower-cost sensing approach and a research-focused emphasis on extensibility, calibration experimentation, and custom data pipelines.

2.2.3 Optris Xi 410 Thermal Monitoring Camera

One more example of a professional industrial thermal imaging system is the Optris Xi 410 compact infrared camera. This device represents a class of fixed-install thermal monitoring systems used for industrial condition monitoring, process control, and safety applications. Studying such systems helps establish realistic performance benchmarks and design considerations for the IRIS project.

The Optris Xi 410 is a compact industrial infrared camera designed for continuous non-contact temperature monitoring in harsh environments. The camera uses an uncooled focal plane array (FPA) detector with a resolution of 384 × 240 pixels and a spectral range of 8–14 µm, which corresponds to the long-wave infrared region commonly used for industrial thermal imaging. The system can measure temperatures across multiple configurable ranges, with the primary operating range extending from approximately –20 °C to 900 °C, and optional configurations supporting temperatures up to 1500 °C.
The camera captures thermal images at 25 frames per second when connected via Ethernet, allowing real-time monitoring of thermal conditions in industrial processes.

When operating via USB, the frame rate is reduced to approximately 4 Hz, while fully autonomous operation can provide thermal monitoring at approximately 1.5 Hz. The camera includes a motorized focus control, allowing the optical focus to be adjusted remotely. This feature is particularly valuable in industrial installations where the camera may be mounted near hazardous or difficult-to-access equipment.

The Xi 410 is designed for industrial automation environments and includes multiple communication and integration options. The system supports Fast Ethernet, USB 2.0, and RS485 interfaces, enabling communication with industrial monitoring software or control systems. The camera can also operate in autonomous mode, where onboard processing performs temperature analysis and directly outputs alarms or analog signals without requiring a connected computer. This capability allows the camera to function as a stand-alone thermal monitoring device.

To support industrial process integration, the Xi 410 provides direct analog outputs and alarm signals, including 0–10 V or 4–20 mA outputs, which are standard interfaces used in industrial instrumentation. Optional Process Interface Modules (PIF) can be stacked to expand the number of analog outputs, alarm relays, and digital inputs, enabling integration with programmable logic controllers (PLCs) or supervisory control systems. This architecture allows the camera to trigger alarms or automated responses when temperature thresholds are exceeded.

The optical system of the Xi 410 can be configured with several field-of-view options, including 18°, 29°, 53°, and 80° lenses, allowing the camera to monitor either small, detailed areas or larger regions depending on the application. With a distance-to-spot ratio of approximately 390:1, the camera can accurately measure temperatures of relatively small targets even from a significant distance. The system also offers a thermal sensitivity of approximately 60 mK, enabling the detection of very small temperature differences.

Physically, the Xi 410 is designed to withstand demanding industrial environments. The device is housed in a compact cylindrical enclosure measuring approximately 36 mm in diameter and 100 mm in length, with an IP67 protection rating, making it resistant to dust and moisture. The camera weighs approximately 220 grams, allowing flexible mounting configurations. The system also complies with several industrial vibration and shock standards, ensuring reliable operation in manufacturing environments with mechanical disturbances.

Industrial thermal cameras such as the Xi 410 provide several advantages compared to traditional temperature sensors. First, they allow non-contact temperature measurement, making it possible to monitor moving objects or extremely hot surfaces without physical contact. Second, thermal cameras provide two-dimensional temperature distribution data, enabling detection of hot spots or abnormal thermal patterns that may indicate equipment faults or safety hazards. Third, integration with industrial communication protocols allows these systems to function as part of automated monitoring or control systems, triggering alarms or protective actions when necessary.

Despite these advantages, industrial thermal cameras also have limitations. High-performance thermal imaging systems such as the Xi 410 typically cost several thousand dollars, which can make them impractical for low-cost or portable monitoring systems. Additionally, these systems often require network infrastructure, specialized analysis software, and integration with industrial control systems, increasing system complexity. The cameras are also designed primarily for fixed industrial installations, making them less suitable for portable inspection tools.

The IRIS (Infrared Reliability Inspection System) project aims to develop a cost-effective thermal monitoring device for detecting abnormal heating in electrical equipment. While industrial cameras such as the Optris Xi 410 demonstrate the capabilities of professional thermographic monitoring systems, their performance level and cost exceed the requirements of the IRIS design. Instead of using a full thermal imaging array, the IRIS system employs a single infrared temperature sensor combined with a motorized scanning mechanism to approximate thermal imaging functionality. This approach significantly reduces system cost while still allowing detection of temperature anomalies across monitored equipment.

Analyzing advanced thermal imaging systems such as the Xi 410 provides valuable insight into industrial thermography architecture, system integration techniques, and performance expectations. These insights help guide the design of the IRIS system while ensuring the project remains focused on achieving a simpler, more affordable thermal monitoring solution suitable for electrical inspection applications.

2.2.4 Summary

The commercial systems discussed above demonstrate the effectiveness of continuous infrared monitoring in industrial environments. However, these systems typically rely on full thermal imaging arrays and are designed as fixed installations with significant hardware cost and infrastructure requirements. The IRIS system instead explores a lower-cost architecture using a mechanically scanned infrared sensor combined with embedded data processing. This approach aims to provide many of the safety and diagnostic benefits of thermal imaging while maintaining compatibility with existing infrared inspection windows and significantly reducing system cost.

2.3 Goals and Objectives

2.3.1 Goals

Goals represent our qualitative motivations behind the project, ensuring that as they are met that the product we are developing is providing the solution intended. This project mainly focuses on creating an affordable IR monitoring solution that is designed for industrial and manufacturing environments. The goals are designed to describe functionality that encourages the adoption of frequent automatic inspection over the more labor-intensive practice of routine manual inspection. The objectives and goals for this project are provided below and are organized as basic, advanced, and stretch.

Basic Goals:

- Improve electrical equipment safety and operational uptime through continuous thermal imaging.
- Provide a permanently mountable integrated solution compatible with existing IR viewports.
- Detect, classify, and record thermal hotspots and other events over time.
- Provide remote access to imaging, event records, and system status through a web-based dashboard.

Advanced Goals:

- Increase image quality and reliability through pre and post processing techniques.
- Continuously monitor enclosure and outside environmental conditions for preventative maintenance.
- Provide alerts to the end user after threshold conditions are reached.
- Provide operational data using the onboard display.

Stretch Goals:

- Enhance the diagnostic capability through load-based monitoring to reduce false alarms.
- Improve the adaptability of the system for different enclosure types and installation scenarios.
- Provide co-imaging with visible light imaging system to aid hotspot location.
- Implement non-interfering active cooling systems to improve durability and reliability in harsh industrial environments.

2.3.2 Objectives

Our objectives describe the tasks or systems that must be completed for our team to consider project goals met.

Basic Objectives:

- Design and implement an mechanical scanning single detector imaging system.
- Create reliable timing and image reconstruction software to interpret measurements.
- Implement physical interfaces to manage system.
- Wirelessly connect to the network via the onboard Wi-Fi module.
- Design and implement battery management system and power delivery.
- Design, implement, and calibrate motor driver integrated circuits for control.
- Design and implement custom PCB that incorporates the MCU, optoelectronics, and any other required subsystems.
- Implement data logging using external storage for thermal frames and event history.

- Design and implement a browser-based dashboard for visualization of thermal images, hotspot locations, and system status.
- Implement wireless data transmission between the IRIS system and a host device using the onboard Wi-Fi module.
- Store thermal frames and event logs to enable analysis and trending of system behavior.
- Implement real-time alert notifications within the dashboard when temperature thresholds are exceeded.
- Validate dashboard performance to ensure compliance with system specifications, including latency and data update rate.

Advanced Objectives:

- Calibrate optics according to reference subjects to achieve reliable imaging.
- Implement signal averaging and frame integration techniques to preprocess measurements.
- Implement low pass filter circuit to block high frequency noise from measurements.
- Enhance contrast and reduce noise using post processing techniques.
- Utilize camera and enclosure temperature sensors for environmental temperature monitoring.
- Utilize enclosure accelerometers to monitor and recognize collisions or earthquakes.
- Design browser-based dashboard UI for thermal visualization.
- Implement wireless data upload between IRIS and host server.
- Implement alert notification system.

Stretch Objectives:

- Implement and calibrate hall effect sensor to continuously monitor system or bus load.
- Design adjustable mounting option to broaden compatibility.
- Integrate wide FOV visible light camera for co-imaging.
- Design and implement active cooling system based on enclosure and camera temperature.

2.4 Hardware Specifications and Standards

2.4.1 Specification Tables

Table 2.1 – System Specifications

Parameter	**Specification**	**Description**
Imaging Temperature	≤40 – 120≤°C	Resolvable temperature range to support intended use.
Temperature Measurement Accuracy	≤±10°C	Maximum allowable deviation between the camera's reported temperature and the true surface

		temperature, whichever is greater, across the imaging temperature range.
FOV	≥[15° × 15°] (H × V)	Angular visual coverage at operating distance.
Frame Rate	≥0.033 fps	Thermal image update rate to ensure detection of developing hotspots and maintain trends for monitoring.
Spatial Resolution	≤20 mm	Spatial resolution corresponding with spatial spot imaged at working distance.
Stimulus to Alert Response Time	≤ 30 seconds	Maximum time between detection of a thermal anomaly and generation of a user alert.
Hotspot Detection Accuracy	≥90%	Minimum accuracy for correctly identifying thermal hotspots relative to known reference conditions during system validation.
False Alarm Rate	≤5%	Maximum allowable percentage of alerts triggered by non-fault conditions such as normal load variation or environmental temperature changes.
Data Update Rate	≥1 frame/minute	Minimum rate at which processed thermal data is transmitted to the monitoring dashboard for visualization and logging.
Dashboard Latency	≤5 seconds	Maximum delay between data transmission from the device and visualization of the user dashboard interface.
Average Power Consumption (1 hour)	≤35 W	Maximum average power draw during operation over 1 hour.
Battery Life	≥4 Hours	Continuous operating time on a single battery charge.
System Cost	$500 – 1000	Target cost range for the project.
SNR	≥10 dB	Defines the acceptable signal quality threshold for sensor and system measurement.
Weight	≤10lbs	Total weight of all system components.

These specifications represent the minimum verifiable system performance required for project success and are derived from the objectives outlined in Section 2.3.2

Table 2.2 – MCU Specifications

Parameter	**Specification**	**Description**
MCU Specifications		
MCU Flash Capacity	3 – 4 MB	Non-volatile memory for firmware and configuration data.
MCU SRAM Capacity	400 – 512 KB SRAM	Volatile memory for runtime operations.
MCU Wi-Fi Bit Rate	10 – 50 Mbps	Maximum supported wireless throughput.

Table 2.3 – Thermal Sensor Specifications

Parameter	**Specification**	**Description**
Thermal Sensor Specifications		
Sensor Type	Thermopile	Infrared detector that converts thermal radiation into electrical signals for temperature measurement.
Spectral Range	8 µm – 14 µm	Long-wave infrared range suitable for thermal emission detection from electrical components.
Active Area	2 mm × 2 mm	Sensitive detection region that captures incident infrared radiation.
Temperature Range	40°C – 120°C	Operational measurement range aligned with expected hotspot conditions.
Response Time	$<$100 ms	Time required for the sensor output to stabilize after a change in temperature.
Sensitivity	$\leq$0.5°C	Minimum detectable temperature difference, defining measurement resolution.

Table 2.4 – Lens Specifications

Parameter	**Specification**	**Description**
Lens Specifications		
Lens Type	LWIR Thermal Imaging Lens	Designed for long-wave infrared applications and compatible with thermopile sensing.
Material	Chalcogenide Glass	Infrared-transparent material optimized for LWIR transmission.
Focal Length	6.3 mm	Detectable FOV and spatial coverage of the scanning system.

Diameter	12.7 mm (1 inch)	Physical aperture size affecting light collection efficiency.
Spectral Range	8 µm – 14 µm	Matches the thermopile sensor response for efficient energy transfer.

Table 2.5 – Mirror Specifications

Parameter	**Specification**	**Description**
Mirror Specifications		
Mirror Type	Flat Reflective Mirror	Used to redirect infrared radiation during raster scanning.
Coating	Gold-Coated (Mid-IR Enhanced)	Provides high reflectivity in the long-wave infrared spectrum.
Diameter	25.4 mm (1 inch)	Ensures sufficient reflective area for the scanning optical path.
Spectral Range	8 µm – 14 µm	Optimized reflectivity for thermal infrared wavelengths.

Table 2.6 – Stepper Motor Specifications

Parameter	**Specification**	**Description**
Stepper Motor Specifications		
Motor Type	Stepper Motor	Provides precise, discrete angular motion for controlled scanning.
Step Angle	5.625° / 64 (~0.088°)	Fine angular resolution achieved through internal gear reduction
Operating Voltage	5 V	Supply voltage required for motor operation.
Current	~200 mA	Typical current draw during operation.
Gear Reduction	64:1	Improves positioning accuracy and torque.
Control	Digital Pulse Input	Controlled via step signals generated by the microcontroller.

Table 2.7 – Motor Driver Specifications

Parameter	**Specification**	**Description**
Motor Driver Specifications		
Driver Type	Darlington Array	Amplifies low-current control signals to drive the stepper motor.
Input Voltage	3.3 V – 5 V	Compatible with microcontroller.
Output Voltage	Up to 50 V	Supports higher voltage loads if required.
Current per Channel	500 mA max	Maximum current drive capability per output channel.
Channels	7	Multiple outputs allow for control of motor phases.

Interface	Digital GPIO	Receives control signals directly from the microcontroller.

Table 2.8 – Battery Specifications

Parameter	**Specification**	**Description**
Battery Specifications		
Battery Type	Lithium-Ion 18650	Rechargeable battery commonly used for portable embedded systems.
Nominal Voltage	3.6 V – 3.7 V per cell	Provides sufficient voltage for regulation and motor operation.
Maximum Charge Voltage	4.2 V per cell	Safe upper limit for charging to prevent battery damage.
Capacity	~3500 mAh per cell	Determines runtime during portable operation.
Configuration	2S	Increases voltage while maintaining capacity.
Rechargeable	Yes	Supports repeated charge/discharge cycles.
Charging Method	CC/CV (Constant Current / Constant Voltage)	Standard Li-ion charging method.
Interface	Battery Management System (BMS)	Provides protection against overcharge, over-discharge, and short circuits.
Estimated Runtime	≥4 hours	Meets system-level requirements for portable operation.

Table 2.9 – Storage Specifications

Parameter	**Specification**	**Description**
Storage Specifications		
Storage Type	Onboard Flash (ESP32)	Integrated memory used for firmware and temporary data storage.
Capacity	4 MB	Sufficient for firmware, configuration, and logging.
Interface	SPI Flash	High-speed interface between MCU and memory.
Function	Data Logging / Firmware Storage	Stores system data and program instructions.

Table 2.10 – Display Specifications

Parameter	**Specification**	**Description**
Display Specifications		
Display Type	LCD 16 × 2	Alphanumeric display for basic system feedback.

Interface	I^2C	Reduces wiring complexity and GPIO usage.
Operating Voltage	5 V	Supply voltage for display operation.
Characters	16 × 2	Displays text-based system status.
Backlight	LED	Improves visibility in low-light environments.
Function	Status Display	Provides user feedback such as system state and alerts.

Table 2.11 – Temperature Sensor Specifications

Parameter	**Specification**	**Description**
Temperature Sensor Specifications		
Sensor Type	Digital Temperature Sensor	High-accuracy sensor for ambient and system temperature monitoring.
Interface	I^2C	Enables communication with the microcontroller using minimal wiring.
Accuracy	±0.25°C	Provides precise environmental measurements for compensation.
Operating Voltage	2.7 V – 5.5 V	Wide supply range compatible with system design.
Response Time	Fast (<250 ms)	Quick response time to temperature change.
Function	Environmental Monitoring	Used to measure ambient conditions for calibration and system reliability

These component-level specifications are derived from the selected parts listed in the BOM and define the measurable performance characteristics of each subsystem within the IRIS system.

2.4.2 Communication Protocol Standards

Table 2.12 – Communication Protocols

Standard	**Description**
USB	Supported external interfaces
IEEE 802.11	Wi-Fi Communications Standard for website UI interface and data transfer
UART	Temperature and Accelerometer Sensors
I^2C	LCD display and accelerometer communication protocol

2.5 House of Quality

Correlation	
+	Positive
-	Negative
O	None

Relationship	
^^	Strongly Positive
^	Positive
O	No Relation
V	Negative
VV	Strongly Negative

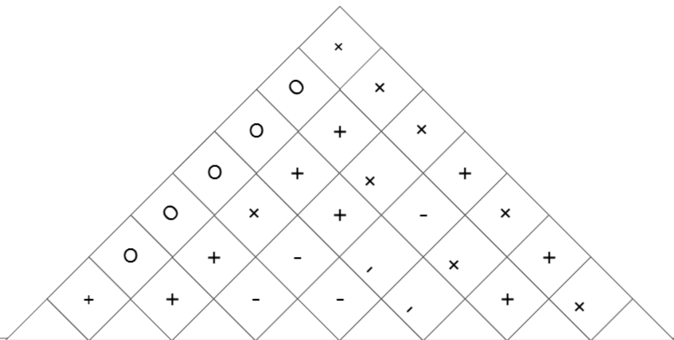

Customer Requirements	Engineering Requirements / Direction of Improvement	Weight	Power Consumption	FOV	Frame Rate	SNR	Stimulus to Alert Response Time	Hotspot Detection Accuracy	Cost
		↓	↓	↑	↑	↑	↓	↑	↓
Ease of Installation	↑	^^	^	O	O	O	O	O	O
Ease of Use	↑	^^	^^	^	^	^	^^	^^	^
Reliability	↑	^	^^	^	^^	^	^^	^^	^
Battery Life	↑	O	^^	V	VV	V	V	V	^^
Customization	↑	^	O	^	O	O	O	O	^^
Maintainability	↑	^^	^^	O	VV	O	O	O	^^
Time Savings	↑	^	^^	^^	^^	^	^^	^^	O
Engineering Target Requirements		8-10 lbs	30-35W	10x10-15x15	0.03-0.05 FPS	7-10 dB	25-30s	80-90%	$600-$1000

Figure 2.1 – House of Quality

2.6 System Design

2.6.1 Hardware Block Diagram

IRIS's hardware design is centered around its imaging system along with supporting peripherals to collect environmental information used to discriminate hotspots. The sensing capabilities utilizes a thermopile detector paired with matching collection and mechanical beam steering optics to capture infrared radiation from the scene and convert it into an electrical signal proportional to the incident thermal energy. This signal is processed and managed by the on board ESP32 microcontroller, which serves as the control unit for data acquisition, timing, and coordination. Power demands are met utilizing a battery and regulated through the system's power management ICs to ensure stable and low noise operation. Additional peripheral sensing ICs such as an accelerometer or ambient temperature sensor provide additional context for sensing while aiding in calibration. After a determination is made, wireless data can be shared using the onboard wireless communication module, alerting the end user without requiring active management.

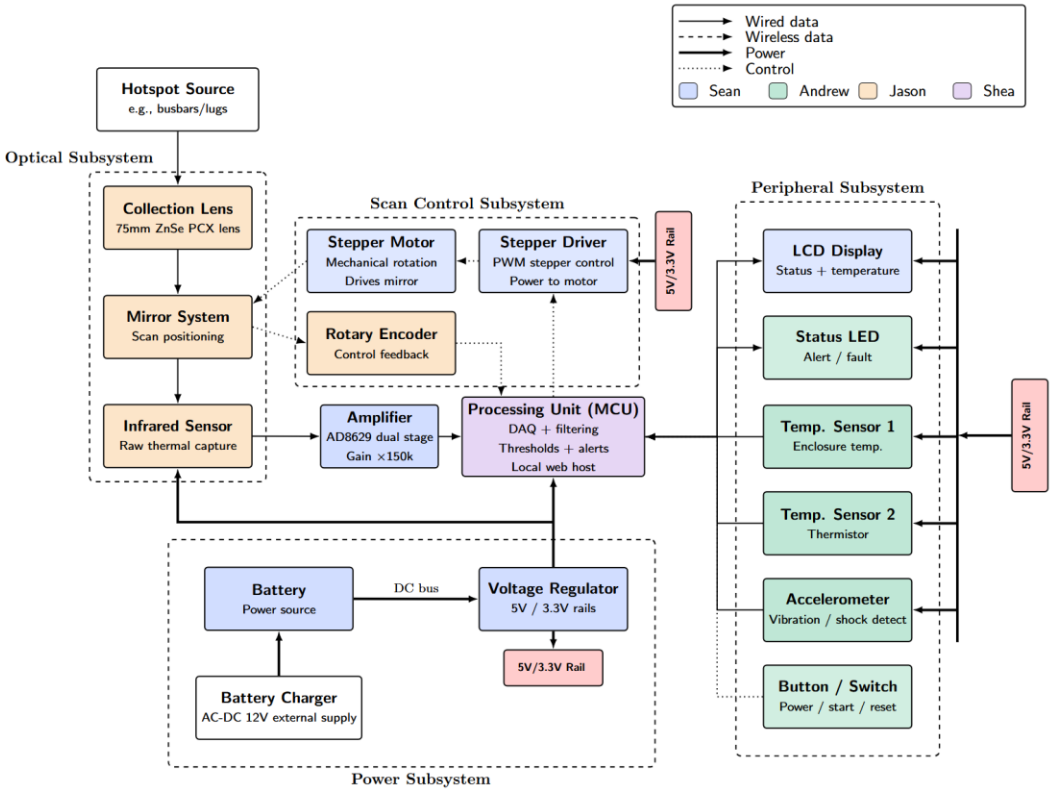

Figure 2.2 – Hardware Block Diagram

2.6.1.1 IR Sensor & Optics Subsystem

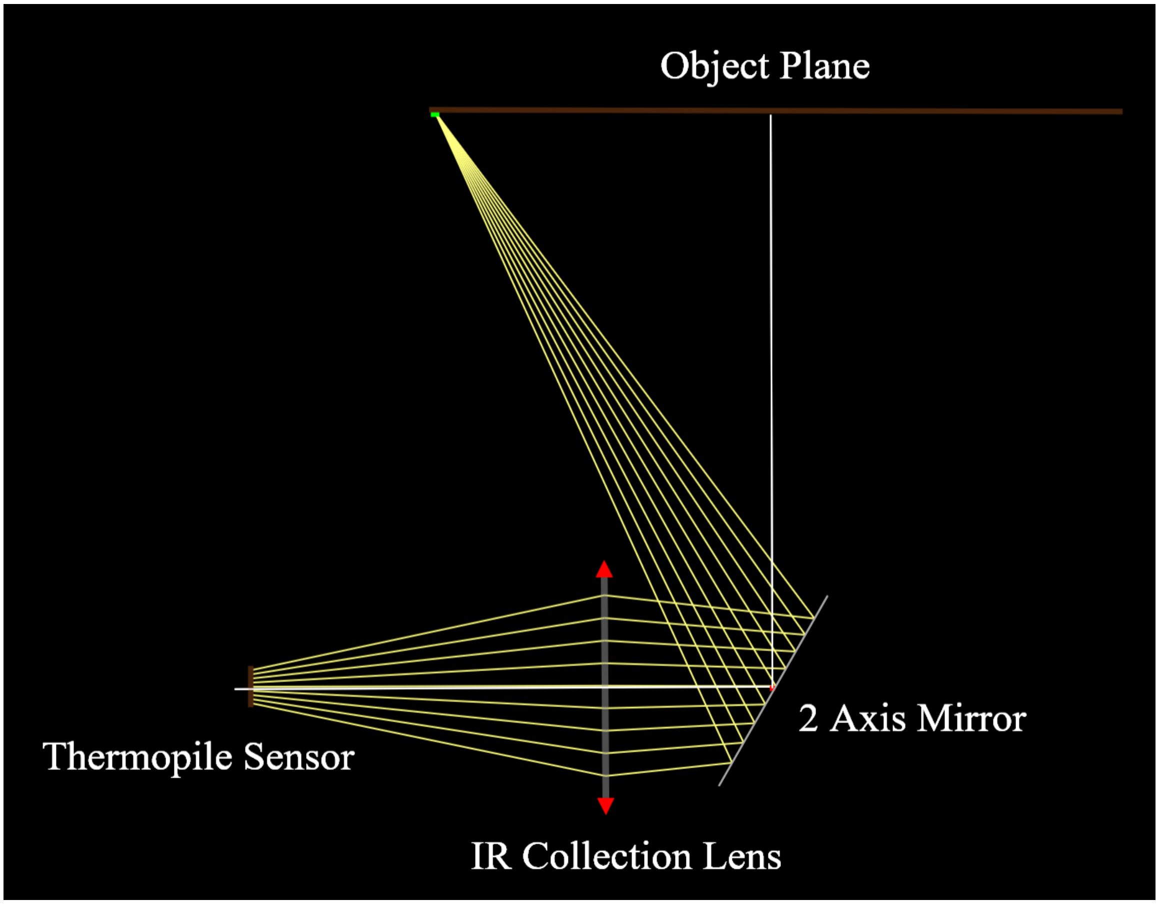

Figure 2.3 – Schematic of Optical Setup

The operating principle behind thermal imaging lies with how objects emit electromagnetic radiation as a function of their temperature. The bulk of this emission is much longer than visible light, with most thermal imaging done in the mid-far infrared spectrum around 8-14 µm. IR wavelengths require specialized lens materials such as germanium or zinc selenide, which are niche and more expensive to manufacture. [5] Typical IR cameras rely on complex multi-element lens assemblies to image a scene onto a large sensor array. As the quality and complexity of these imaging systems rises, so do their material and manufacturing costs significantly. This problem motivated the research and development of a lower complexity, cost-effective monitoring system.

In this project, these challenges are addressed by implementing an afocal single-detector raster-scanning technique that uses one collection lens rather than a full imaging lens stack. The input optical power is guided through the scanning mirror subsystem, which controls which part of the scene is actively imaged, onto the thermopile sensor. Using a known reference value for the emissivity of the subject along with optical power measurements, we can determine the temperature of the subject. By sacrificing imaging speed and sampling the scene with servo-controlled mirrors and a single detector, we can reconstruct an image of the scene with fewer elements. This approach was chosen because it meets the needs of its application, continuous monitoring of systems, with as few elements as possible, and without unnecessary specifications such as higher frame rates or higher image quality.

2.6.1.2 Power Subsystem

The primary function of the power subsystem is to provide stable, reliable, and continuous power to all system components, including the IR sensing module, mirror/servo system, processing electronics, communication systems, and the user display. The power system is designed to support both stationary operation and temporary battery-backed operation to ensure uninterrupted monitoring during power disturbances or for our demonstration. This subsystem consists of regulated power supplies, a rechargeable battery, and a battery management system (BMS) to ensure safe charging, discharging, and protection against over-voltage, under-voltage, and over-current situations.

A key design goal of the power subsystem is to deliver clean, low noise power suitable for our IR single pixel detector. The quality of the output is highly dependent on the quality of the input power, so adequate filtering is crucial. Electrical noise introduced by poorly regulated supplies can degrade thermal measurement accuracy and introduce false readings. Therefore, appropriate regulation, filtering, and isolation strategies are required to maintain signal integrity across the system. Our battery capacity must also be sufficient to support extended operation without external power, allowing the system to remain functional for demonstration and short-term monitoring use cases.

Since the system is intended for deployment within industrial electrical enclosures, the power electronics must tolerate elevated ambient temperatures and electromagnetic interference. Power efficiency is therefore emphasized to minimize internal heat generation and reduce the need for active cooling.

2.6.1.3 Communication and Interface Subsystem

The communication and interface subsystem enable data exchange between the MCU and external devices, as well as basic user interaction during setup or diagnostics. This subsystem includes USB and UART interfaces for debugging, terminal output, firmware development, along with a simple LCD display to provide local user feedback.
USB connectivity is intended to support initial programming, system configuration, and direct monitoring during development and testing. UART interfaces provide a lightweight and reliable communication method for debugging low-level system monitoring. These interfaces allow engineers to verify sensor data, power status, and system health without requiring full network connectivity. Simple physical interfaces such as buttons and LEDs may be incorporated to support reset functionality, mode selection, or visual indication of system state, such as power-on, fault, or alarm conditions.

Design constraints for this subsystem include minimizing connector count and cable complexity to maintain a compact and reliable installation within electrical enclosures. All interfaces must be electrically isolated or adequately protected to prevent ground loops and reduce susceptibility to electromagnetic interference commonly present in power equipment environments. We could also consider more industry standards for communications, such as RS485 Serial or Modbus, for easier integration in industry.

2.6.1.4 Temperature Sensing Subsystem

The temperature sensing subsystem is responsible for monitoring both localized component temperatures and overall enclosure conditions to support accurate thermal interpretation and system health assessment.

Local temperature measurements are used to compensate for environmental effects on IR sensor performance, such as sensor drift due to self-heating or ambient temperature changes. Enclosure temperature data also provides valuable context when analyzing thermal trends, allowing the system to distinguish between true electrical faults and global temperature increases caused by external operating conditions.

These sensors must be placed strategically to ensure representative measurements without being overly influenced by localized heat sources such as power regulators. Accuracy, response time, and long-term stability are key considerations, as erroneous temperature readings could lead to incorrect alarms or missed fault conditions.

2.6.1.5 Load-Based Monitoring Subsystem

The load-based monitoring subsystem enhances the system's diagnostic capability by measuring electrical current in the monitored equipment using a Hall effect sensor. This sensor detects the magnetic field generated by current-carrying conductors, allowing the system to estimate load without any direct electrical contact, preserving safety and isolation. By combining load data with thermal measurements, the system can distinguish normal temperature increases due to higher operating loads from abnormal heating that may indicate faults such as loose connections or insulation degradation.

Incorporating load measurements also enables more advanced alarm logic, reducing false positives when temperature thresholds are exceeded under expected operating conditions. The Hall effect sensor can be positioned to accommodate different enclosure layouts while avoiding interference with normal equipment operation. Overall, this subsystem provides an additional layer of context that improves fault classification, enhances predictive maintenance capabilities, and increases overall system reliability.

2.6.1.6 Display and User Feedback Subsystem

The display and user feedback subsystem provides local visualization of system status and key thermal information. This may include a small display or indicator panel used during installation, commissioning, or maintenance activities. The display allows users to quickly verify system operation, sensor functionality, and alarm status without requiring external devices.

The design emphasizes clarity and simplicity, ensuring that critical information such as temperature readings, fault indicators, or communication status can be interpreted easily by maintenance personnel. The display must operate reliably under industrial environmental conditions and consume minimal power to avoid unnecessary load on the power subsystem.

2.6.1.7 Thermal Management and Filtering

Thermal management and signal filtering are critical to ensuring accurate and stable system operation. The electronics must be adequately cooled to prevent self-heating from influencing temperature measurements or degrading component reliability. Passive cooling techniques such as heat sinks and enclosure ventilation are preferred to minimize system complexity and power consumption. Signal filtering is applied to both thermal sensor outputs and auxiliary measurements to reduce noise and improve signal-to-noise ratio. Filtering techniques may include analog filtering at the sensor interface and digital filtering within the processing unit. These measures are necessary to suppress electrical noise, environmental interference, and transient artifacts that could otherwise lead to inaccurate readings or false alarms.

2.6.2 Software

IRIS's software implementation is designed to effectively monitor and integrate the various hardware components to gather data and draw conclusions. The MCU has several auxiliary tasks to support other components, such as adjusting the mirror servos via a predetermined script or in real time as feedback informs it of its position. Additionally, it communicates over Wi-Fi to support its primary function to store and process data for identifying hotspots, measuring temperatures, and inferring electronic load on the observed circuit.

In our proposed system, the image will be reconstructed using data gathered from a raster-scanning approach with a single IR detector. A two-axis scanning mirror sequentially steers the detector's field of view across the scene in horizontal scan lines, sampling at the minimum angular step the motor can provide. At each position, the IR emission from the scene will be collected by the lens and focused onto the thermopile, producing an electrical signal which will be recorded, digitized, and stored on the MCU. Using the known scan timing and mirror scan angles, the image can be reconstructed and uploaded for viewing. [6]

With this reconstruction, the entire image data can be processed for faulty sensor readings and can be used to perform various calculations. For example, certain temperature thresholds can be used to measure where components exceed specifications in absolute temperature. The measurements can also be averaged over a certain area of the raster to identify hotspots exceeding maximum junction temperature. Additionally, this temperature data can also be utilized to compare relative temperatures between components as well. This information is certainly useful, but the utility of this information can be greatly enhanced with further auxiliary sensor readings that serve to provide context to the observed hardware.

One of the key improvements that IRIS seeks to provide is automation. This means that the MCU needs a way to perform these diagnostics and effectively communicate the results to a maintenance team. This is achieved by utilizing the ESP 32's built-in Wi-Fi standard capabilities to interface with a PC-hosted website that will then receive and contain the UI necessary to examine the full results of IRIS. This eliminates the need for manual inspections while also providing scalability as multiple IRIS can communicate with the same site.

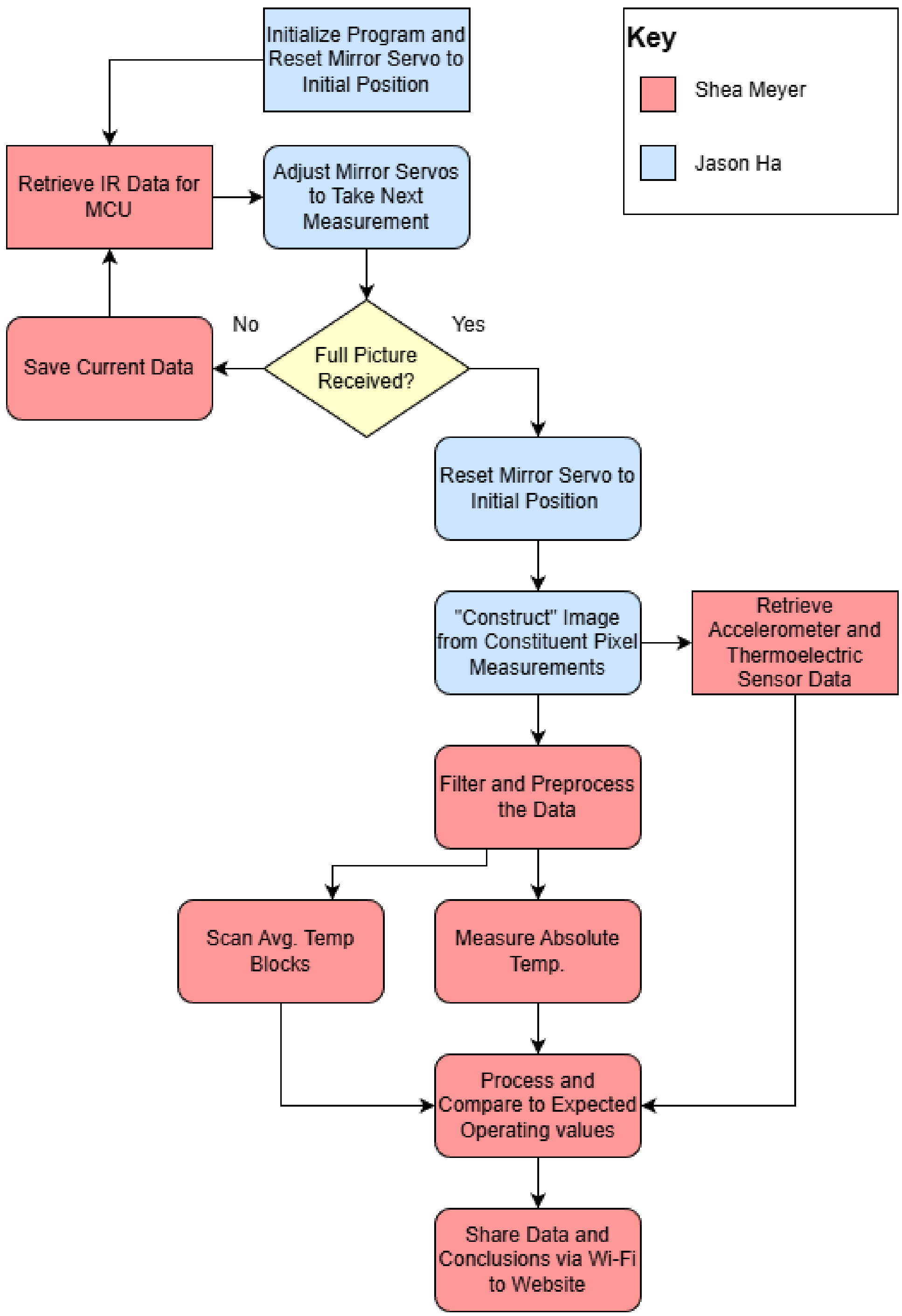

Figure 2.4 – Core Software Block Diagram

2.7 Early Prototype Rendering

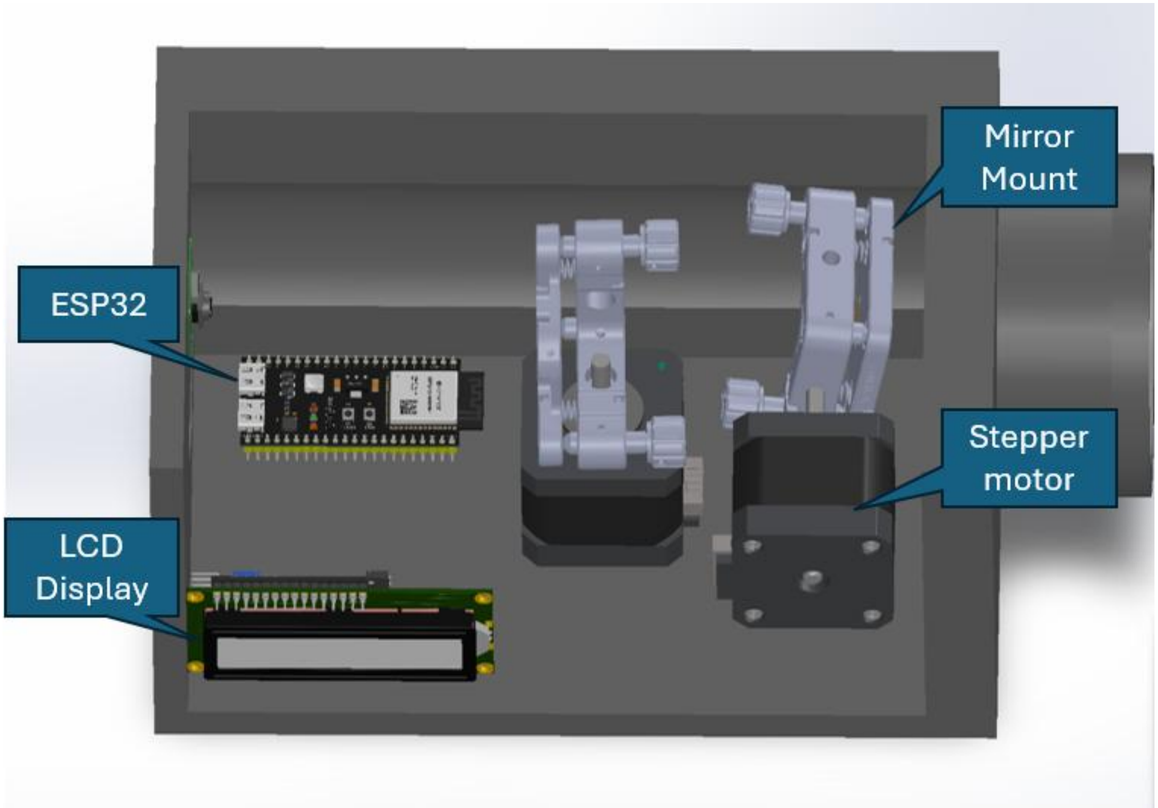

Figure 2.5 – Imaging system with MCU

This figure shows an early concept for the imaging system assembly integrated with the processing electronics. This rendering shows the placement of the mirror mount, stepper motor, ESP32 microcontroller, and LCD display.

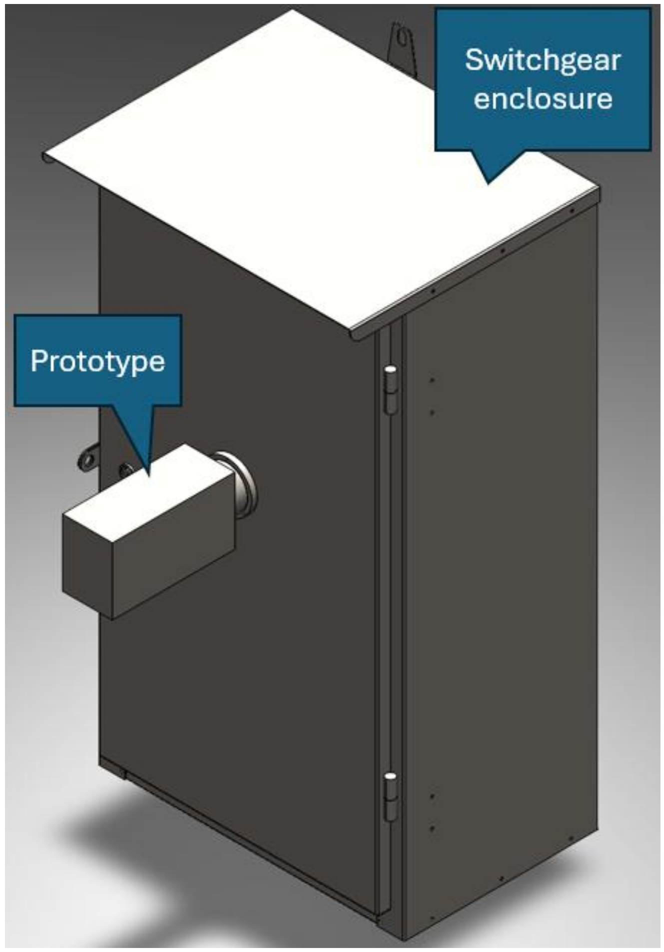

Figure 2.6 – Example installation of system on enclosure

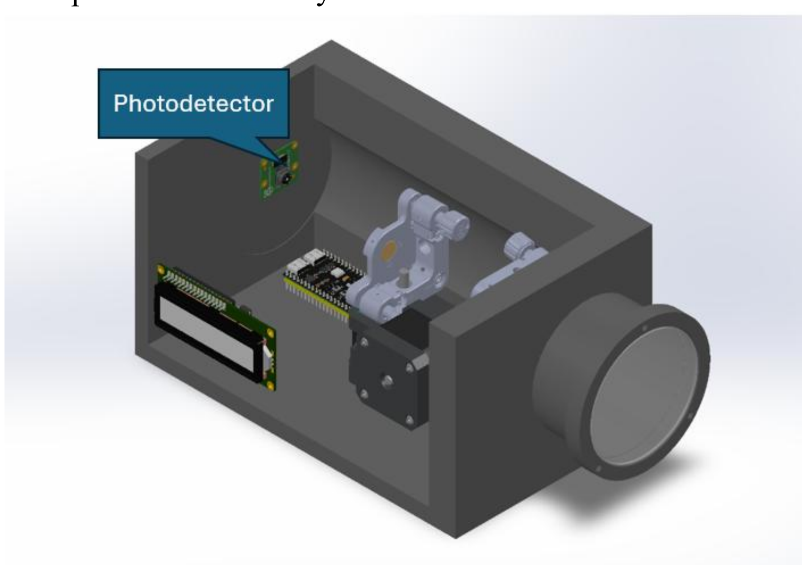

Figure 2.7 – Early Full System Render

Chapter 3 – Research

3.1 Imaging Architecture Selection

3.1.1 Line Scanning

Single detector imaging systems can be created using several different imaging and image reconstruction architectures. Each has their own tradeoffs, making it important to compare suitable options to gain confidence that our approach uses the technology that's most appropriate for our goals. If we're interested in imaging electrical systems like switchgears, it follows that we're imaging a fairly wide scene from a relatively close distance, and it becomes important that our design is able to image a static scene well while maintaining some space efficiency. Line scanning appears as an obvious candidate for this type of imaging, as it may use either a single detector or an array of detectors arranged in a line to reconstruct an image by moving either the subject or the camera along a transfer direction. [7]

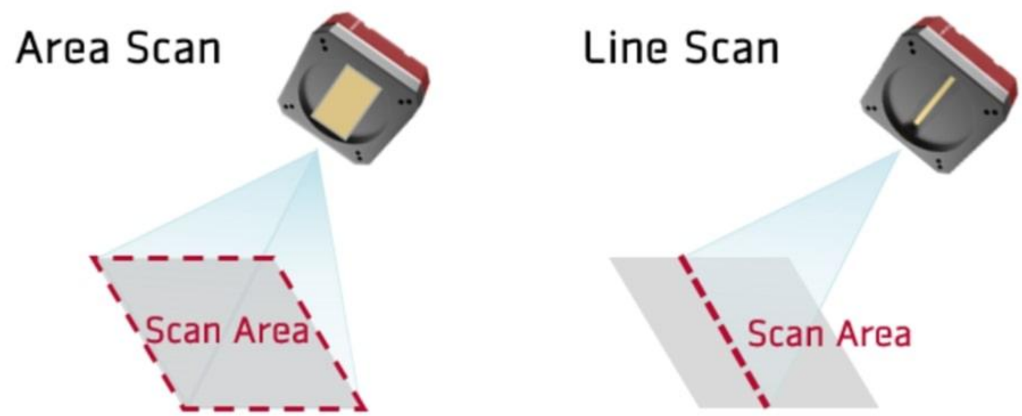

Figure 3.1 – Line Scanning Illustration

The benefits of this system towards our needs are that it can greatly simplify the mechanical design, but it requires controlled linear motion along 2 axes to capture the full scene, making the assembly quite large. [7]

3.1.2 Polygon Mirror Scanning

Another imaging approach is the polygon mirror scanner, which uses a multi-faceted mirror to achieve high speed angular scanning along one axis. By implementing a mechanical method to move the assembly along another perpendicular axis, we saw the possibility that this technology could be a good basis for our scanning system, as it's used in practice in systems such as laser printers and LiDAR [9]. The system does appear as a relatively simple and precise high speed method, but in practice we were unable to source an accessible or affordable component that was reflective in the IR wavelength band. This is counter to our intention to make the system cost efficient, although the potential for affordable static imaging remains.

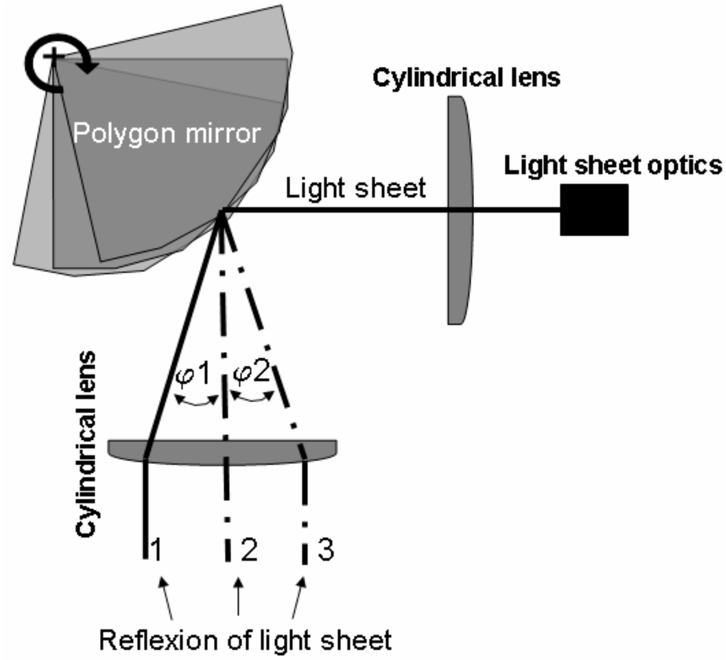

Figure 3.2 – Polygon Scanning Illustration

3.1.3 Raster Scanning

One of the oldest image reconstruction architectures, raster scanned imaging [10], appeared well rounded in its benefits and limitations in our research. This technique utilizes scanning according to a predetermined pattern called the raster pattern, collecting a set of measurements that can be used to reconstruct the image.

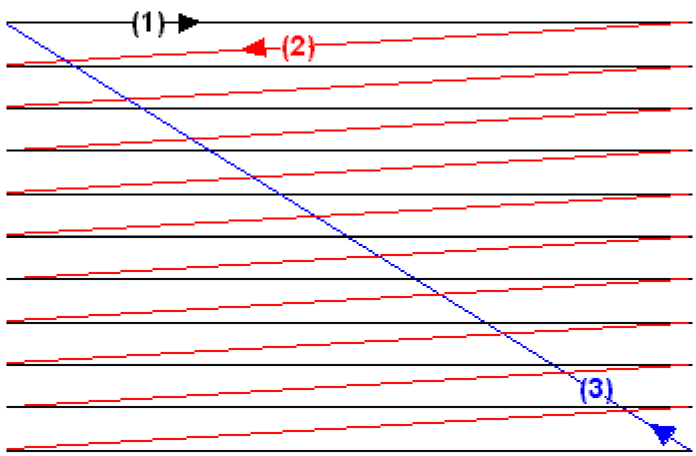

Figure 3.3 – Raster Scanning Illustration

Mirror raster scanning imaging requires movement in two axes as well as precise timing to allow for sufficient and repeatable measurement while being relatively slow. There's also the presence of backlash and alignment sensitivity among the mechanical components, an issue not present when a fully integrated mechanical solution is purchased. Despite this, the architecture is well known and offers high controllability and cost effectiveness, as one mirror can be used if implemented in a gimbal style setup.

3.1.4 Chosen Architecture and Geometric Validation

For our project's application, the raster scanned imaging architecture remains the most practical for meeting the cost efficient and space conscious constraints set. It doesn't require any motion in the target to enable its scanning, and enables low complexity in the optical component stack. We proceed with this method with the intention that it's paired with a precise scanning mirror assembly with a high angular resolution, allowing frequent samples throughout the scene.

In our dual axis mirror scanning approach, we intend to keep the sensor's position fixed. To achieve scanning with part of our optical path fixed, we position the normal of the sensor and the normal of the object scene perpendicular with respect to one another. The mirror is placed where those axes intersect, with the law of reflection governing the relationship between the direction of the incoming wavefront and the outgoing wavefront. As the path lengths are far above the wavelength, the ray optics model is sufficient in predicting its behavior.

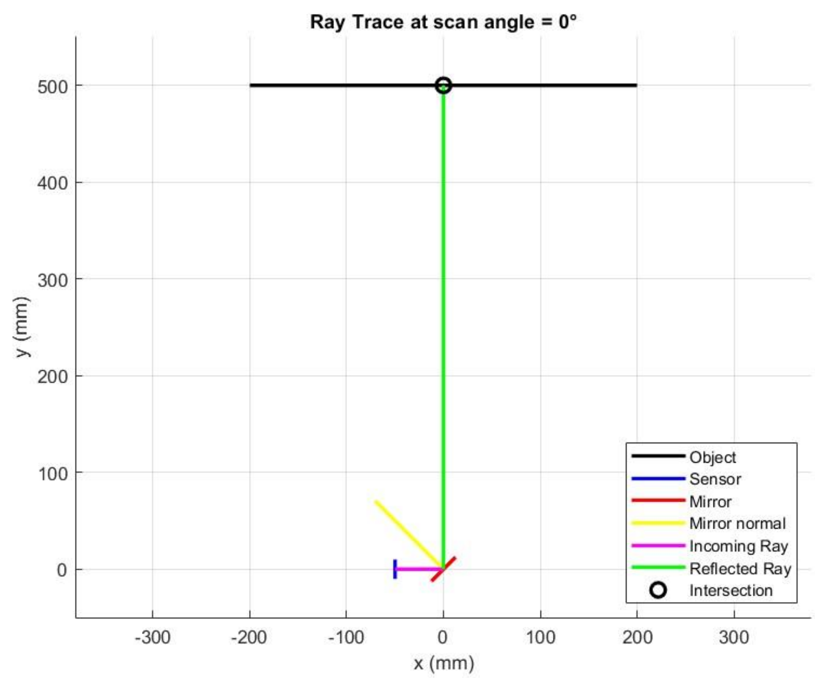

Figure 3.4 – Simulated Ray Trace at object center

In this simulation, we model a laser placed at the sensor's position and the ray traveling backwards through the system. The simulation assumes an object distance of 500mm with respect to the mirror, and a sensor distance of 50mm with respect to the mirror. The law of reflection states that the incoming and outgoing ray angles are equal with respect to the mirror normal, which is implemented in our code using the following equation.

$$v_{out} = v_{in} - 2(v_{in} * n)n$$

This allows the simulation to perform vector math using the mirror normal and calculating the direction of the incoming and outgoing rays.

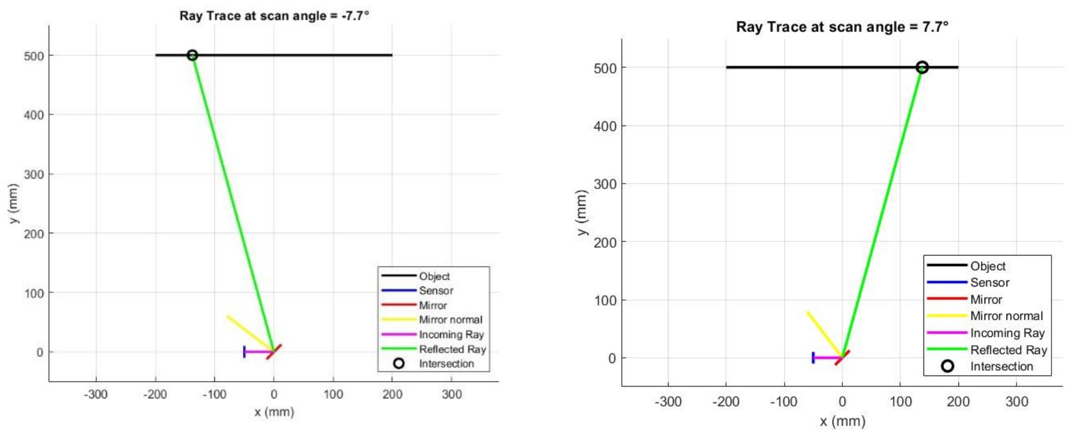

Figure 3.5 – Ray Traces at edges of object scene

Our project promises an FOV of [15x15] degrees, therefore a half FOV of 7.5 degrees. As we show through the MATLAB simulation, by changing the rotation of the mirror, and therefore the direction of the mirror normal, we fix the position of the sensor and image different areas of the scene. As we can demonstrate the incoming and reflected ray paths for both the negative and positive half FOV, it follows that for every point in between those maximums there exists a valid ray path. With this analysis, we can continue towards implementation.

3.1.5 Mechanical Scanning Architecture Selection

Several mechanical scanning architectures were considered for our project, each with their own tradeoffs between scanning fidelity and feasibility. The most common architecture in comparable projects is likely the galvanometer-based scanner. Galvo systems offer higher speed and precision but require dedicated closed-loop driver electronics and precision optomechanical mounts that far exceed the budget as well as development time and scope of our project. Polygon mirror scanners are mechanically constrained to a single axis and therefore need an additional mechanism to be viable for our 2-dimensional scanning needs, not to mention polygon mirrors themselves are not as commercially available as standard circular mirrors. Instead, our team took inspiration from existing mechanical designs that utilize a pan-tilt gimbal architecture.

This pan-tilt architecture was selected as the most practical approach to 2 axis raster scanning with our constraints. Not only is it highly manufacturable, which the process of prototype being able to be completely handled with 3D printing, but as mechanical complexity is added to improve scanning fidelity hardly any mass is added as well.

Additionally, this basic architecture has seen wide adoption across a variety of available designs. This allowed our team to research existing designs and adapt them to meet the needs of our project, saving precious development time. Finally, as the design is highly customizable, we are able to use existing external hardware, such as optical mounts and off the shelf optical components to achieve a quick production and iteration time.

The primary tradeoff of the pan-tilt approach is geometric image distortion at wider scan angles, arising from the nonlinear mapping between mirror rotation angle and projected pixel position on the target plane. This distortion is well-characterized and fully correctable through coordinate remapping in software, making it an acceptable and manageable limitation rather than a fundamental hardware constraint. Compared to all alternatives evaluated, the pan-tilt gimbal offered the most favorable balance of mechanical simplicity, component availability, fabrication accessibility, and integration with the existing IRIS electronics architecture.

3.2 Optical Element Selection

3.2.1 Lens Stack Complexity

With our project's goals in mind, we needed to conduct a preliminary assessment of the complexity of the lens stack. Typically, lens stacks with many components are used in order to achieve high image quality, a driving factor in cost for cameras that use sensor arrays. In a single-detector raster-scanning system, the optical requirements are significantly simpler than in conventional imaging systems that form a full 2D image on a focal plane array. Because the scene is sampled one angular direction at a time by the scanning mirrors, the lens does not need to correct for wide-field aberrations across a large image plane. Instead, its primary role is to collect infrared radiation from a given direction and focus it onto a single detector element.

As a result, the imaging stack can be simplified to a single lens element that sets the effective focal length (EFFL), determines the system’s F-number (F/#), and provides sufficient optical power to focus incoming radiation onto the detector. Since the detector size defines the instantaneous field of view (IFOV), the focal length becomes the main knob for setting the angular resolution. Knowing this, the lens must be chosen to balance optical power with angular resolution. Additional corrections for distortion or field curvature are less critical, as only one point in the scene is imaged at a time and geometric distortions can be handled in software. Finally, as the FOV is relatively narrow, aberrations such as coma and astigmatism are less impactful than in traditional systems. The main concern is that the focused spot size remains on the detector and does not significantly bleed over the detector’s surface.

3.2.2 Lens Material and Lens Selection

As the optics represent the bulk of the cost in our system, careful selection will be vital to having a successful project. The most important characteristics of our lens will be the effective focal length, EFFL, and f/# as they influence both the angular resolution and ability of the imaging stack to collect light. Our imaging system’s primary concern is being able to receive a reliable signal, differentiable from optical and electronic noise. In that regard instantaneous field of view, or IFOV, is one of the most important constraints.

The IFOV determines the detector’s footprint onto the object scene. Depending on the IFOV, the target area on the scene may be partially or fully resolved. In a fully resolved object, all the power collected by the lens from the scene is radiation from the target area, in our case representing a hotspot.
We approach constraining our EFFL through the following process. Assuming a detector size of 1mm, a typical active detector area for thermopiles, we’re able to calculate using the following equation the approximate IFOV corresponding to different focal lengths.

$$IFOV = \frac{d}{f}$$

Table 3.1 – EFFL to IFOV

EFFL (mm)	IFOV
25	0.040 rad or 2.29 deg
50	0.020 rad or 1.15 deg
75	0.0133 rad or 0.76 deg

Considering the target area’s angular extent in the scene is approximately 2.291 degrees, At around 1.2 degrees, 50 mm represents a practical middle ground for focal length while preserving angular resolution. After determining our necessary focal length, we approach determining an f/# in a similar manner.

Through our research, we consider an f-number in the range of ~f/1 to f/2.5 is ideal for our system because a lower f/# allows more infrared radiation to reach the thermopile detector, improving signal strength and sensitivity to temperature differences. This is especially important since thermopile detectors are relatively low sensitivity compared to focal plane arrays, so maximizing power directly improves measurement quality. However, extremely fast f/# can introduce optical aberrations and alignment sensitivity, so a moderate range like f/1.5–f/3 provides a good balance between signal collection and image quality. In our research on potential lenses to acquire, we also consider slower f/# since we may be able to compensate for the smaller aperture with a longer integration time.

From here, we may further narrow down our choices for lenses by material. Material selection is important as it sets the wavelengths through which we are transmissive. Since we promised a resolvable temperature range of 50-130 deg C, wavelengths in the long wave infrared band are most important, around 8-14 µm. Readily available lenses are typically available from Edmund Optics in the form of Calcium Fluoride, Germanium, or Zinc Selenide lenses. However, the CaF_2 lenses are not transmissive in a significant portion of our lower temperature range. Other materials such as fused silica or barium fluoride may not be transmissive in the longer wavelengths where a significant amount of energy lies, since black body radiation peaks are broad.

With these criteria, we selected a few different lenses to compare and created the following table.

Table 3.2 – Lens Comparison Table

Parameter	**Edmund Ge PCX, Uncoated, ISP Optics**	**Edmund Ge PCX, Uncoated**	**Edmund ISP Optics ZnSe PCX, Uncoated**
Source	Edmund Optics	Edmund Optics	Edmund Optics
Material	Germanium (Ge)	Germanium (Ge)	Zinc Selenide (ZnSe)
Diameter	12.7 mm	25.0 mm	38.1 mm
Effective Focal Length (EFFL)	50.8 mm	35 mm	75mm
F/# (approx.)	f/4	f/1.4	f/2
Surface Type	Plano-Convex	Plano-Convex	Plano-Convex
Coating	Uncoated	Uncoated	Uncoated
Spectral Range	2–14 µm	2–14 µm	0.6-18 µm
Price (USD)	$270	$655	$312
Availability	Low	High	High
Optical Quality	High	High	High

The Edmund Optics Zinc Selenide Lens was selected because it provides full transmission in the 8–14 µm LWIR range while meeting the required focal length and aperture constraints for the system. Although the lens is uncoated and introduces additional reflection losses, it still delivers sufficient infrared signal for hotspot detection given the project's demonstration-focused goals. Additionally, its low availability yet relatively low cost compared to uncoated alternatives make it a practical and reliable choice within our project's budget and timeline constraints.

With this information, we were able to do a preliminary evaluation using Zemax to determine optimal back focal distance and stop placements to minimize the root mean square of the optical spot size.

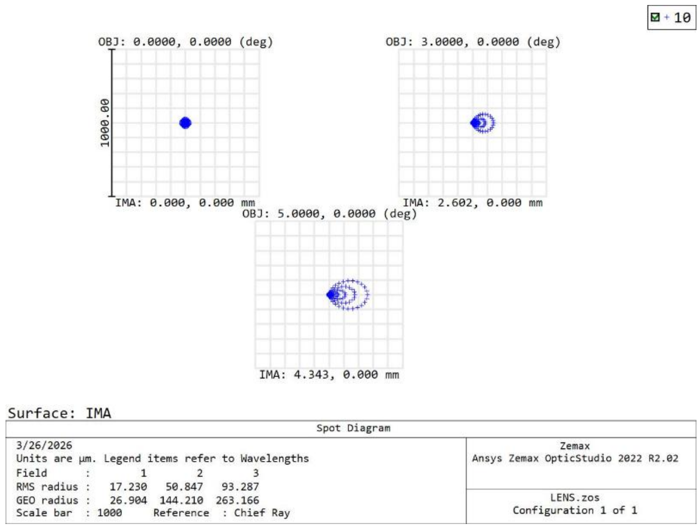

Figure 3.6 – Optical Spot Size Before Optimization

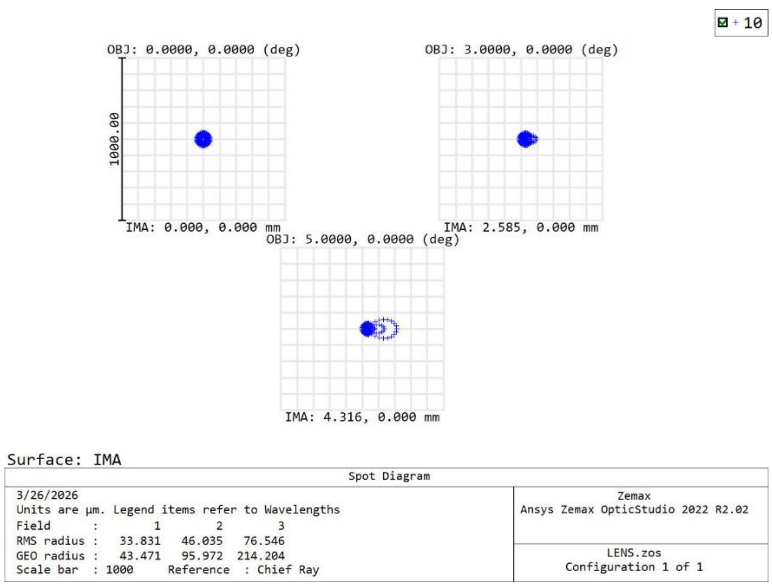

Figure 3.7 – Optical Spot Size After Optimization

The Zemax optimization may have doubled the RMS radius in the end, however one notable observation is that spot seems much tighter, the aberration from coma seems reduced, and ~60 µm spot diameter is not unreasonable compared to a 2 mm detector size.

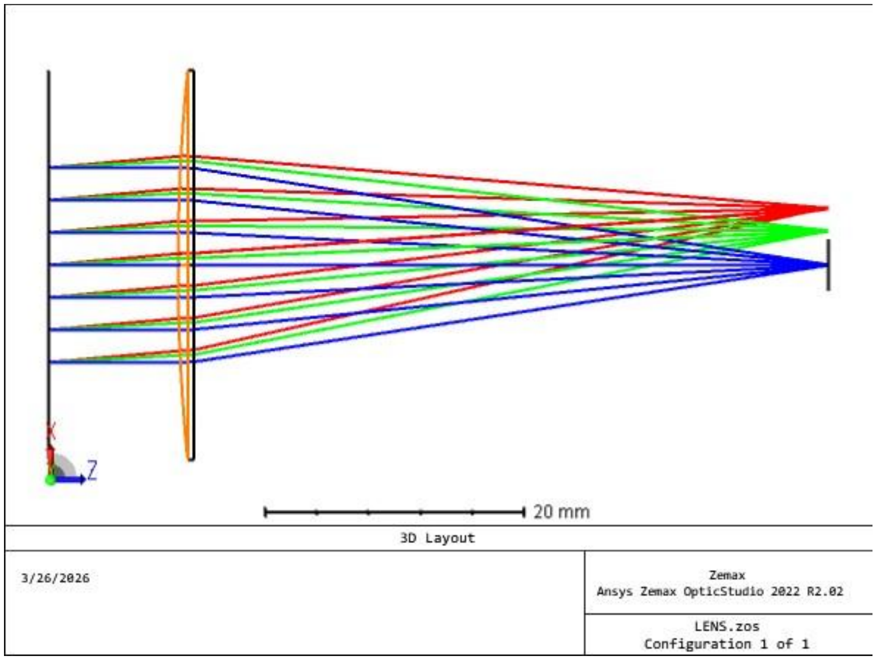

Figure 3.8 – ZEMAX 3D Layout taken in the XZ plane

We have noticed that even small field angle difference such as 3 degrees may shift the spot off of the detector, which we expect as that represents rays coming outside of our instantaneous FOV.

3.2.3 Mirror Selection

The mirror selection was driven primarily by two needs, matching the entendue of the selected lens and the need to maximize infrared reflectivity within the long-wave infrared (LWIR) band. In this wavelength range (8–14 µm), material choice is critical, as many common reflective coatings used in visible optics perform poorly. Gold was selected due to its exceptionally high reflectivity in the infrared, typically exceeding 95% across the LWIR band, ensuring that minimal signal is lost during reflection. This is especially important for our thermopile-based system, where detector sensitivity is limited and preserving optical power is a key priority.

We made the decision to purchase a 1-inch mirror for its balance between optical performance and mechanical constraints. A larger mirror increases the effective aperture of the system and reduces the likelihood of vignetting at higher scan angles, which can be helpful for achieving the desired ±7.5° field of view. At the same time, the mirror must remain lightweight enough to be driven by our stepper motor system without introducing excessive inertia or reducing scan speed. The mirror size matches well considering the lenses considered for this project are far below its 1 inch or 25mm diameter.

Finally, the use of a commercially available gold-coated mirror from Thorlabs was motivated by considering reliability, availability, and ease of integration. Thorlabs mirrors are well-characterized, robust, and compatible with standard optical mounts, allowing for straightforward alignment and integration. Although lower-cost alternatives may exist, the performance and reliability of the mirror makes it our choice for the project's practical needs.

Table 3.2.1 – Mirror Comparison Table

Parameter	**Thorlabs PF10-03-M02**	**Thorlabs PF10-03-M01**	**Thorlabs ME1-G01**
Material	Mid-IR Enhanced Gold	Standard Protected Gold	Protected Aluminum
Diameter	25.4 mm (1 inch)	25.4 mm (1 inch)	25.4 mm (1 inch)
Spectral range	8–14 µm	0.8 – 20 µm	2 – 20 µm
Approx. reflectivity	~95% in LWIR	~96% in LWIR	~95% in LWIR
Price	$76.01	$70	$36.67

3.3 Thermal Sensor Selection

When designing an infrared scanning imaging system, we focused on selecting a single-detector sensor technology that balances sensitivity with system simplicity. We considered common options such as pyroelectric detectors, bolometers, and thermopiles. Pyroelectric sensors require a modulated or chopped input signal and cannot measure steady-state radiation, which makes them less suitable for continuous thermal observation. Bolometers offer high sensitivity but typically require more complex readout circuitry and, in some cases, cooling or more elaborate biasing schemes, which increases system complexity and power requirements. In contrast, we chose a thermopile-based approach using the HMS J21 thermopile with an integrated F8–14 µm infrared filter from Heimann Sensors. This type of sensor directly converts incident infrared radiation into a voltage without requiring cooling or signal modulation, which makes it well suited for a compact, uncooled scanning system. Since our application operates in the long-wave infrared band where most thermal emission occurs, the built-in 8–14 µm filter helps ensure that the sensor primarily responds to relevant thermal radiation while rejecting out-of-band noise.

Within the thermopile-based design, we used the J21 sensor because it provides a practical balance between responsivity, stability, and ease of integration at an undergraduate design level. Unlike digital-output temperature sensors, the J21 provides an analog voltage proportional to incident radiant power, which we can process using standard amplification and data acquisition circuitry. This gives us more flexibility in tuning gain and filtering based on system noise performance. We also benefit from the integrated optical filtering of the F8–14 µm bandpass window, which reduces the need for additional external optical filtering components. While thermopiles generally have lower sensitivity compared to more complex detector types, the J21's response is sufficient for detecting relatively strong thermal sources in our target environment, especially when combined with appropriate signal conditioning and low-noise amplification.

To ensure that the measured signal primarily corresponds to the target rather than background radiation, we carefully considered the optical design of the system, particularly the field of view and mechanical housing geometry. The effective IFOV is determined by the detector active area and the optics used to collect and direct infrared radiation onto the thermopile. We designed the tube length and aperture so that the sensor only accepts radiation from the intended scene area defined by the optical geometry, reducing the influence of stray thermal sources outside the target region. By matching the optical field of view to the detector's acceptance angle, we improve measurement consistency and reduce background-induced noise. This alignment allows us to more directly relate the measured thermopile voltage to the target's radiance within the 8–14 μm band, which simplifies calibration and improves the reliability of the infrared scanning system in real-world environments.
We can directly justify its suitability for our infrared scanning system based on its datasheet characteristics. The built-in bandpass filter restricts sensitivity to the long-wave infrared atmospheric window (8–14 μm), which aligns well with peak thermal emission from room-temperature objects and helps suppress out-of-band radiation that would otherwise contribute to noise. The datasheet reports a responsivity on the order of tens of V/W along with a thermal time constant of roughly ~10 ms, which is fast enough to support scanning operation without significant motion-induced smearing while still providing a usable voltage signal for moderate-gain amplification. This combination of spectral selectivity, response speed, and analog output makes the sensor well-suited for converting scene radiance into a measurable electrical signal in a straightforward imaging architecture.

From a system design perspective, the datasheet also highlights that the J21 is an uncooled, room-temperature-operating device with stable thermopile behavior and relatively high detectivity (on the order of 10^8 cm·Hz$^{1/2}$/W), allowing it to resolve small changes in incident infrared power without requiring complex thermal management or biasing circuitry. This simplifies integration significantly at the undergraduate design level, since the sensor can be directly interfaced with a low-noise amplifier and ADC for signal conditioning. The combination of uncooled operation, integrated optical filtering, and sufficient sensitivity ensures that the measured output is both practical and robust for real-world scanning conditions, while keeping the overall system compact, low-power, and easy to implement.

Other detectors in this same performance range were often lacking the additional benefits to this detector design, such as the packaging, integrated semiconductor filter, or low output referred noise. This decision took some time, but we considered it the most appropriate for the project.

Table 3.3 – Thermal Sensor Comparison Table

Parameter	**HMS J21 Thermopile with 8-14 um filter**	**Thorlabs TD2X Unmounted Thermal Power Detector**	**Amphenol Thermometrics ZTP-135SR**
Sensitivity	44 V/W	>0.1 V/W typ	62 V/W
Output referred noise	35 nV/ sqrt(hz)	35 nV/ sqrt(hz)	32 nV/ sqrt(hz)
Active area size	1.2 mm^2	4.0 mm^2	0.49 mm^2
Time constant	10 ms	~ 1.5 s (rise time)	25 ms
Field of view	120 degrees	120 degrees	85 degrees

3.4 Environmental Temperature Selection

Temperature sensing in the IRIS system provides environmental context for interpreting infrared measurements and enables monitoring of enclosure conditions that may affect system performance. Accurate ambient temperature data improves measurement reliability and supports detection of abnormal thermal conditions within electrical switchgear.

The selected temperature sensing solution must provide high measurement accuracy, simple integration with the ESP32 microcontroller, and reliable communication using standard embedded interfaces such as I²C. To determine the most appropriate solution, multiple temperature sensing technologies and devices were evaluated based on accuracy, interface compatibility, implementation complexity, and cost.

3.4.1 Thermistors

Thermistors are temperature-dependent resistive devices whose resistance varies with temperature. According to IEC 60539, NTC thermistors exhibit a negative temperature coefficient, meaning their resistance decreases as temperature increases [57]. In embedded systems, thermistors are commonly used because they are inexpensive, widely available, and highly sensitive to small temperature changes [58]. However, thermistors do not directly provide temperature values. Instead, the microcontroller must measure resistance using an analog-to-digital converter and compute temperature using calibration data or lookup tables [58]. The nonlinear resistance-versus-temperature behavior of thermistors further increases implementation complexity, particularly when accurate measurement is required over a wide operating range [58].

For the IRIS system, this requirement introduces additional hardware and software overhead. Although thermistors are attractive from a cost perspective, their need for signal conditioning and resistance-to-temperature conversion makes them less suitable for a system that prioritizes simplicity and direct integration with the ESP32.

3.4.2 Analog Temperature Sensors

Analog temperature sensors provide an output voltage that varies in proportion to temperature. This allows the microcontroller to determine temperature using its built-in analog-to-digital converter. Compared with thermistors, analog integrated sensors simplify the sensing circuit because they provide a direct voltage representation of temperature rather than requiring resistance measurement and conversion [58].

However, analog temperature sensors still depend on the accuracy and resolution of the microcontroller's analog-to-digital converter, and their measurements can be affected by electrical noise present in the system. For the IRIS platform, these devices offer a simpler interface than thermistors, but they still require analog signal acquisition and careful PCB design to preserve measurement accuracy.

3.4.3 Digital Temperature Sensors

Digital temperature sensors include internal signal-conditioning and temperature-conversion circuitry, allowing them to provide temperature data directly in digital form. Rather than outputting an analog voltage, these sensors communicate with the microcontroller using standard serial interfaces such as I^2C, SMBus, or SPI [40]. This reduces the burden on the microcontroller because no external analog conversion or resistance-to-temperature computation is required.

Digital temperature sensors offer high measurement accuracy, low operating current, and straightforward integration into embedded systems [40]. Because the ESP32 supports digital communication protocols and the IRIS system must minimize wiring complexity while maintaining reliable environmental monitoring, digital temperature sensors provide the most suitable balance of accuracy, simplicity, and compatibility.

3.4.4 Temperature Sensor Technology Comparison

Table 3.3.1 – Temperature Sensor Comparison Table

Technology	**Example Device**	**Interface**	**Accuracy**	**Cost**	**Advantages**	**Limitations**
Thermistor	NTC Thermistor	Analog	High	Very Low	Very sensitive and inexpensive	Requires calibration and signal

						conditioning
Analog Sensor	LM35	Analog	±0.5°C	Low	Simple voltage output	Susceptible to noise
Digital Sensor	DS18B20	1-Wire	±0.5°C	Low	Direct digital communication	Slightly higher cost

Based on this evaluation, digital temperature sensors provide the most convenient integration and reliable operation for the system because they combine direct temperature-to-digital conversion with standard serial communication, reducing both circuit complexity and sensitivity to analog measurement errors.

3.4.5 Digital Temperature Sensor Product Comparison

After selecting digital temperature sensing technology, several commercially available sensors were evaluated to determine which device best meets the system requirements.

Table 3.4 – Digital Sensor Comparison Table

Sensor	**Interface**	**Temperature Range**	**Accuracy**	**Operating Voltage**	**Cost**
DS18B20	1-Wire	-55°C to 125°C	±0.5°C	3.0 - 5.5 V	$3 - $6
MCP9808	I^2C	-40°C to 125°C	±0.25°C	2.7 - 5.5 V	$4 - $6
TMP102	I^2C	-40°C to 125°C	±0.5°C	1.4 - 3.5 V	$8 - $12

Each device offers reliable temperature measurement capability, but differences in communication interface, measurement accuracy, and system compatibility influenced the final selection.

3.4.6 Temperature Sensor Evaluation

The Adafruit MCP9808 High Accuracy I^2C Temperature Sensor Breakout was selected for the IRIS system due to its high accuracy and simple integration with the microcontroller [40].

The MCP9808 communicates using the I^2C protocol, which allows it to connect directly to the ESP32 while sharing the communication bus with other peripherals such as the LCD display. This reduces wiring complexity and minimizes the number of required GPIO connections.

One of the most important advantages of the MCP9808 sensor is its high measurement accuracy, typically within ±0.25°C, which is significantly better than many low-cost temperature sensors. This level of precision helps ensure reliable monitoring of enclosure conditions and improves the accuracy of thermal interpretation.

The additional advantages of the MCP9808 includes:
- High measurement precision
- Reliable I²C communication interface
- Low power consumption
- Good compatibility with ESP32 development libraries

Because of these characteristics, the MCP9808 provides a reliable and accurate solution for monitoring ambient temperature within the IRIS system enclosure.

3.5 Accelerometer Selection

Electrical switchgear enclosures are known to experience mechanical vibration during normal operation. Research has shown that vibration in high-voltage switchgear is primarily driven by electromagnetic forces acting on internal busbars, which are excited at frequencies of 100 Hz, 200 Hz, and 300 Hz under typical power frequency loading conditions. A study by Long et al. [7] found that when load current exceeds approximately 75–80% of rated capacity, vibration amplitude increases significantly, with measured accelerations on cabinet surfaces reaching values above 1 G at the dominant frequency components. Additional sources of vibration include cooling fans and structural resonance caused by the busbar bridge geometry and support insulator spacing.

Because the IRIS system is designed for deployment inside or adjacent to switchgear enclosures, these vibration characteristics present a practical concern. Mechanical disturbances at the mounting location of the device could affect the alignment of the optical scanning assembly or introduce noise into infrared thermal measurements during data acquisition. To detect and log these disturbances, a piezoelectric vibration sensing subsystem was incorporated into the IRIS design.

The vibration sensor provides two functions within the system. First, it allows the system to flag measurement frames that were captured during periods of elevated vibration, which may reduce the reliability of the thermal data. Second, it provides a secondary monitoring channel that can detect abnormal vibration events in the switchgear environment, which may themselves be indicative of electrical or mechanical faults.

Several types of accelerometer technologies were evaluated during the design phase, including MEMS accelerometers, piezoresistive accelerometers, and piezoelectric accelerometers. Each of these technologies offers different advantages in terms of sensitivity, frequency response, cost, and ease of integration. Since the dominant vibration frequencies in switchgear environments fall in the range of 100–300 Hz, the selected sensor needed to provide reliable sensitivity across this frequency range while remaining compatible with the IRIS embedded electronics.

3.5.1 MEMS Accelerometers

Microelectromechanical systems (MEMS) accelerometers are widely used in consumer electronics and embedded systems. These sensors measure acceleration by detecting changes in capacitance caused by the movement of microscopic mechanical structures within the device.

MEMS accelerometers are commonly used in applications like smartphones, wearable devices, and robotics. They are compact, inexpensive, and easy to integrate with microcontrollers using digital communication protocols such as I^2C or SPI.

Advantages of MEMS accelerometers include small physical size, low power consumption, a simple digital interface, and low cost. However, MEMS accelerometers typically have limited sensitivity compared to other sensing technologies when detecting small, high-frequency vibration signals. For applications requiring detection of periodic mechanical disturbances in the 100–300 Hz range, higher sensitivity sensors are preferred.

3.5.2 Piezoresistive Accelerometers

Piezoresistive accelerometers measure acceleration using strain-sensitive resistive elements that change resistance when mechanical stress is applied. When the sensor experiences acceleration, the internal structure deforms slightly, causing a measurable change in electrical resistance.

These sensors are commonly used in applications requiring measurement of both static and dynamic acceleration, including automotive crash detection systems, structural monitoring, and industrial measurement systems. Their advantages include the ability to measure both static and dynamic acceleration, high shock tolerance, and reliable performance in harsh environments.

However, piezoresistive accelerometers typically require additional signal conditioning circuitry and may have higher power consumption than simpler sensing technologies. For an application focused primarily on detecting periodic vibration signatures rather than static orientation or low-frequency motion, the added complexity is not warranted.

3.5.3 Piezoelectric Sensors

Piezoelectric sensors measure dynamic mechanical events using materials that generate an electrical charge when subjected to mechanical stress [37]. When the sensor experiences vibration or impact, the piezoelectric element produces a voltage proportional to the applied force. This operating principle makes piezoelectric sensors inherently well suited to detecting periodic vibration and shock events, which are the primary disturbance types of concern in the IRIS application.

Piezoelectric sensing elements are available in a range of form factors, from precision industrial accelerometers to compact ceramic module assemblies designed for embedded electronics integration. While high-end industrial piezoelectric accelerometers offer calibrated outputs and extended frequency ranges, simpler ceramic piezoelectric modules provide sufficient sensitivity for detecting the dominant vibration signatures present in switchgear environments at significantly lower cost and with straightforward analog interfacing.

Advantages of piezoelectric sensors for this application include high sensitivity to dynamic vibration, a wide frequency response covering the 100–300 Hz range of interest, no requirement for static measurement capability, and compatibility with analog input systems already present in the IRIS hardware design.

3.5.4 Accelerometer Technology Comparison

Table 3.5 – Accelerometer Technology Comparison

Accelerometer Type	Example Device	Sensitivity	Interface	Advantages	Disadvantages
MEMS	MPU-6050	Moderate	I²C / SPI	Small size, low cost	Lower vibration sensitivity
Piezoresistive	ADXL375	Moderate	Analog	High shock tolerance	Requires signal conditioning
Piezoelectric	FTVOGUE Ceramic Module	High	Analog / Digital	High vibration sensitivity, low cost	No static measurement

Based on this comparison, and considering that the dominant vibration signatures in switchgear environments occur as periodic signals in the 100–300 Hz range, piezoelectric sensing provides the most suitable technology for detecting these disturbances in the IRIS system.

3.5.5 Accelerometer Part Comparison

After selecting piezoelectric sensing technology, several options were evaluated ranging from precision industrial accelerometers to compact embedded modules. These were compared based on sensitivity, output interface, size, cost, and suitability for integration with the IRIS electronics.

Table 3.6 – Accelerometer Part Comparison

Sensor	Manufacturer	Sensitivity	Interface	Advantages	Disadvantages
ADXL1001	Analog Devices	High	Analog	High precision vibration measurement	High cost
830M1	PCB Piezotronics	Very High	Analog	Industrial grade, calibrated output	Large size, high cost
Ceramic Piezo Module	FTVOGUE	High	Analog + Digital	Low cost, module form factor,	Not industrially calibrated

				adjustable sensitivity	

3.5.6 Selected Accelerometer

The vibration sensor selected for the IRIS system is the FTVOGUE ceramic piezoelectric vibration sensor module [59]. This sensor uses a ceramic piezoelectric element to generate an analog voltage output proportional to detected vibration, with an additional digital threshold output configurable via an onboard potentiometer. The adjustable sensitivity allows the detection threshold to be tuned to the vibration levels characteristic of switchgear operation, reducing false triggers from ambient noise while remaining responsive to the 100–300 Hz electromagnetic excitation frequencies of interest.
The module's compact form factor and direct analog output make it straightforward to integrate with the ESP32 microcontroller via its analog-to-digital converter, without requiring additional signal conditioning circuitry. Vibration data is logged alongside thermal measurements, allowing the system to correlate periods of elevated mechanical disturbance with infrared scan quality.

While the FTVOGUE module does not carry industrial calibration ratings, the IRIS application does not require quantitative acceleration measurement — only detection and flagging of elevated vibration events. For this purpose, the sensitivity and frequency response of the ceramic piezoelectric element are well matched to the disturbance signatures present in switchgear enclosures, and the low component cost supports the broader design goal of producing an accessible and deployable monitoring system.

The advantages of the selected sensor for this application include high sensitivity to dynamic vibration in the frequency range relevant to switchgear operation, adjustable detection threshold via onboard potentiometer, a compact module design suitable for embedded mounting, analog and digital output compatibility with the ESP32, and low component cost.

3.6 Instrumentation Amplifier Research

The IRIS system relies on a Heimann HMS-J21-F8.14 thermopile sensor to detect infrared radiation emitted from objects within the scanning field of view. Thermopile sensors generate extremely small differential voltage signals on the order of microvolts to low millivolts, which must be amplified before they can be digitized by the ESP32's analog-to-digital converter. Because these signals are small and may be accompanied by significant common-mode noise from the surrounding electrical environment, an instrumentation amplifier is required rather than a standard operational amplifier.

According to the HMS-J21-F8.14 datasheet, the thermopile produces a typical signal voltage of approximately 140 µV under standardized test conditions, with an RMS noise voltage of 37 nV/√Hz and a source resistance of approximately 84 kΩ at room temperature [63]. To produce a signal that can be reliably resolved by the ESP32 ADC, the thermopile output must be amplified by a factor on the order of several hundred to several thousand, while preserving the integrity of the signal in the presence of common-mode interference.

When selecting an instrumentation amplifier for this project, several design requirements were considered. The amplifier must provide high common-mode rejection to suppress noise that appears equally on both inputs, low input bias current to avoid loading the high-impedance thermopile output, and low input voltage noise to preserve the small signal generated by the sensor. The amplifier must also operate within the project's available supply voltages, support gains in the range required to bring the thermopile signal to a usable level, and remain cost-effective while integrating cleanly with the existing system hardware. To determine the most suitable amplifier, several common instrumentation amplifier architectures and specific commercially available models were researched and evaluated before selecting a final candidate.

3.6.1 Three Op-Amp Instrumentation Amplifier Architecture

The classic instrumentation amplifier topology uses three operational amplifiers arranged in two stages. The first stage consists of two op-amps configured as buffered differential preamplifiers, and the second stage consists of a single op-amp configured as a unity-gain difference amplifier that removes the common-mode signal from the buffered differential output. The overall gain of the amplifier is typically programmed by a single external resistor placed between the two preamplifier stages.

This architecture provides high input impedance on both inputs, which is critical when amplifying signals from high-impedance sensors such as thermopiles. It also allows for very high common-mode rejection ratios when the internal resistor matching is precisely trimmed during manufacturing. Discrete implementations of this architecture using individual op-amps are possible but suffer from accumulated resistor mismatch errors, lower CMRR, increased component count, and significantly higher supply current.

Monolithic instrumentation amplifiers integrate the three op-amps and laser-trimmed resistor network onto a single die, providing far better matching, lower offset voltage, lower drift, and significantly reduced power consumption compared to discrete designs. For this reason, the design effort focused on monolithic instrumentation amplifier ICs rather than discrete op-amp implementations.

3.6.2 Indirect Current Feedback Architecture

A more modern alternative to the three op-amp topology is the indirect current feedback (ICF) architecture, used in devices such as the AD8420 and AD8421. In this approach, two matched transconductance amplifiers convert the input differential voltage and the feedback differential voltage into currents, and an integrator drives the output until the two currents are equal. The gain is set by an external resistor pair connected between the output, feedback pin, and reference pin.

The primary advantage of the ICF architecture is that the input common-mode range is decoupled from the output swing, which allows the amplifier to handle common-mode voltages that extend close to or beyond the supply rails without limiting the available output range. This is particularly useful in low-voltage single-supply systems. ICF amplifiers are also typically lower in supply current than three op-amp designs, with parts such as the AD8420 drawing only 90 µA maximum.

However, ICF amplifiers require two external resistors to set the gain rather than one, and the gain accuracy and drift depend directly on the matching and temperature coefficients of these external resistors. They are also generally limited to lower bandwidths than three op-amp designs at equivalent gains.

3.6.3 Zero-Drift (Chopper-Stabilized) Architecture

Zero-drift instrumentation amplifiers, such as those built around devices like the LTC2066 family, use internal switching circuitry to continuously self-calibrate the amplifier's input offset voltage and low-frequency noise. By heterodyning DC and 1/f flicker noise to higher frequencies where they can be filtered out, these devices achieve extremely low input offset voltages in the single-microvolt range and offset drifts as low as 0.02 µV/°C [LTC Datasheet].

Zero-drift amplifiers are exceptionally well suited for very low-frequency, very low-amplitude DC measurements, such as bridge sensors and electrochemical sensors. However, the internal switching introduces transient currents at the input pins, which can interact with high source impedances to produce clock feedthrough artifacts. Zero-drift amplifiers also typically have lower bandwidths than standard precision instrumentation amplifiers, often limited to tens of kilohertz, and require additional design care when interfacing with sensors that have significant source impedance.

3.6.4 Architecture Comparison

Table 3.7 – Instrumentation Amplifier Architecture Comparison Table

Architecture	**Gain Setting**	**Key Strength**	**Key Limitation**	**Typical Applications**
Three Op-Amp (Monolithic)	Single external resistor	High CMRR, wide bandwidth, simple gain programming	Input common-mode range limited by output swing	Bridge sensors, ECG, transducers, data acquisition
Indirect Current Feedback	Two external resistors	Wide common-mode range, low supply current	Gain accuracy depends on resistor matching	Single-supply battery-powered instrumentation
Zero-Drift / Chopper	Two external resistors	Very low offset and 1/f noise	Lower bandwidth, clock feedthrough at high impedance	DC bridge measurements, electrochemical sensors

For the IRIS system, the three op-amp monolithic architecture provides the best overall match. The thermopile signal of interest is low-frequency but not pure DC, the source impedance is moderately high at approximately 84 kΩ, and the gain required is in a range that benefits from the high CMRR and predictable bandwidth of a classic three op-amp design. The clock feedthrough concerns associated with zero-drift amplifiers and the resistor-pair gain dependency of ICF amplifiers were judged to be unnecessary complications for this application.

3.6.5 Instrumentation Amplifier Model Evaluation

Following the selection of the three op-amp monolithic architecture, several commercially available instrumentation amplifier ICs were evaluated to identify the most suitable option for the IRIS system. The primary evaluation criteria were supply voltage compatibility, common-mode rejection ratio, input voltage noise, input bias current, gain programming simplicity, package availability, and overall cost. Because the IRIS system uses a dual-supply architecture suitable for ±5 V to ±15 V operation and the thermopile produces a high-impedance, microvolt-level differential signal, the selected amplifier needed to provide low input bias current, low input voltage noise, and reliable performance at gains of approximately 100 to 1000.

AD620 (Analog Devices)

The AD620 is a low-cost, low-power monolithic instrumentation amplifier based on the classic three op-amp topology with laser-trimmed internal resistors and Superβeta input transistors. It operates over a wide power supply range from ±2.3 V to ±18 V and supports gains from 1 to 10,000 programmed by a single external resistor according to the relation $G = 1 + (49.4\ k\Omega/R_G)$ [AD620 datasheet]. The amplifier draws a maximum of 1.3 mA of supply current, has a maximum input offset voltage of 50 µV (B grade) with offset drift of 0.6 µV/°C maximum, a maximum input bias current of 1.0 nA, and provides a minimum CMRR of 100 dB at G = 10.

The AD620's input voltage noise of 9 nV/√Hz at 1 kHz and 0.28 µV peak-to-peak in the 0.1 Hz to 10 Hz band is well matched to the thermopile signal range, and its 1.0 nA maximum input bias current does not significantly load the 84 kΩ source impedance of the HMS-J21-F4.26 sensor. At a gain of approximately 100, the AD620 provides 120 kHz of bandwidth and a 15 µs settling time to 0.01%, both of which substantially exceed the bandwidth requirements of the slow thermal raster scan performed by the IRIS system. The single-resistor gain programming is particularly attractive because it eliminates the resistor-pair matching requirement of indirect current feedback amplifiers, which directly translates to better gain accuracy and lower gain drift without requiring matched precision resistor networks.

The AD620 is available in 8-lead PDIP and SOIC packages, both of which are well suited to prototyping and single-board production. It is widely stocked through major distributors and is supported by extensive application documentation, including reference designs for ECG front ends, bridge sensor amplification, and transducer interfaces, good for applications that share many of the same signal-conditioning characteristics as a thermopile front end. Unit cost is approximately $8 to $12 depending on grade and package.

AD8420 (Analog Devices)

The AD8420 is a wide-supply-range, micropower instrumentation amplifier based on the indirect current feedback architecture. It operates from a single supply of 2.7 V to 36 V or a dual supply of ±2.7 V to ±18 V, and draws a maximum quiescent current of only 90 μA on a 5 V supply [AD8420 datasheet]. This makes it well suited to battery-powered and ultra-low-power applications. The AD8420 features rail-to-rail output, a maximum input offset voltage of 125 μV, and a minimum CMRR of 100 dB at DC.

While the AD8420's micropower current consumption is attractive, several characteristics make it less suitable for the IRIS thermopile application. Its input voltage noise of 55 nV/√Hz is approximately six times higher than that of the AD620, which would significantly degrade the signal-to-noise ratio when amplifying the small thermopile output. The bandwidth at G = 100 is only 2.5 kHz, compared to 120 kHz for the AD620, which while still adequate for the slow raster scan represents a substantial reduction in margin. Additionally, the ICF architecture requires two external resistors to set the gain, and the gain accuracy at higher gains depends directly on the matching of these resistors. For the IRIS system, where minimizing component count and achieving predictable gain across the scan are priorities, the AD620's single-resistor gain programming and lower noise floor are decisive advantages.

AD8421 (Analog Devices)

The AD8421 is a high-performance, low-noise instrumentation amplifier also based on the three op-amp topology, designed as a higher-bandwidth, lower-noise successor to the AD620. It provides an input voltage noise of only 3.2 nV/√Hz maximum at 1 kHz, a bandwidth of 10 MHz at G = 1 and 2 MHz at G = 100, and a maximum supply current of 2.3 mA [AD8421 datasheet]. The AD8421 supports the same single-resistor gain programming as the AD620, with the gain set by $G = 1 + (9.9\ k\Omega/R\_G)$.

The AD8421 represents the highest performance option in this comparison. Its 3 nV/√Hz noise floor is approximately three times lower than the AD620, which would improve the signal-to-noise ratio of the thermopile signal chain. However, this performance advantage is most significant in applications with very low source impedance, where amplifier voltage noise dominates the total system noise. With the HMS-J21-F4.26 thermopile's source resistance of approximately 84 kΩ, the Johnson noise of the source itself is approximately 37 nV/√Hz at room temperature, which dominates the overall system noise regardless of whether the AD620 (9 nV/√Hz) or AD8421 (3 nV/√Hz) is used. The AD8421's noise advantage therefore does not translate into a meaningful improvement in this specific application. Additionally, the AD8421 is approximately three to four times more expensive than the AD620, and its higher bandwidth introduces additional layout sensitivity that is unnecessary for the slow thermal scan rate of the IRIS system.

Instrumentation Amplifier Model Comparison

Table 3.8 – Instrumentation Amplifier Model Comparison Table

Specification	AD620 (Analog Devices)	AD8420 (Analog Devices)	AD8421 (Analog Devices)
Architecture	Three op-amp	Indirect current feedback	Three op-amp
Supply Voltage Range	±2.3 V to ±18 V	2.7 V to 36 V (single)	±2.5 V to ±18 V
Quiescent Current (max)	1.3 mA	90 µA	2.3 mA
Gain Programming	Single resistor	Two resistors	Single resistor
Gain Equation	1 + (49.4 kΩ/R_G)	1 + (R2/R1)	1 + (9.9 kΩ/R_G)
Input Voltage Noise (1 kHz)	9 nV/√Hz	55 nV/√Hz	3.2 nV/√Hz max
Max Input Offset Voltage	50 µV (B grade)	125 µV	25 µV (B grade)
Max Input Bias Current	1.0 nA	27 nA	0.5 nA (B grade)
Min CMRR (G = 10)	100 dB	100 dB	114 dB (B grade)
Bandwidth (G = 100)	120 kHz	2.5 kHz	2 MHz
Package	8-PDIP / 8-SOIC	8-MSOP	8-SOIC / 8-MSOP / 8-LFCSP
Approx. Cost	\$8–\$12	\$4–\$7	\$10–\$15

Based on this evaluation, the AD620 provides the most suitable balance of noise performance, input characteristics, gain programming simplicity, and cost for the IRIS thermopile signal chain. The AD8420's micropower operation is not required for this design, and its higher input voltage noise would degrade the thermopile signal quality. The AD8421 offers superior noise performance but at a cost premium that is not justified by the application, since the thermopile's own source resistance dominates the system noise floor regardless of which amplifier is selected. The AD620's 9 nV/√Hz input voltage noise is well below the thermopile's intrinsic source noise, its 1.0 nA maximum input bias current does not meaningfully load the 84 kΩ sensor output, its 100 dB minimum CMRR provides robust rejection of common-mode interference, and its single-resistor gain programming allows the required gain to be set precisely with one component. Additionally, the AD620's extensive use in ECG and bridge sensor front ends for applications that share the high-impedance, microvolt-level signal characteristics of the thermopile. This provides a well-documented design precedent for the IRIS signal conditioning stage.

3.6.6 Selecting the AD8629 in implementation

During the implementation phase in Senior Design II, as our electronic designs were being reviewed for approval in the PCB stage, our advisor urged us to look further into the amplifier design. Through this, we were able to converge on the AD8629 as the final appropriate amplifier both in terms of noise performance as well as limited voltage offset and voltage drift with respect to temperature.

The signal produced by the thermopile detector was on the order of tens of microvolts, making amplifier selection a critical aspect of the system design. The revisit was warranted, as candidate amplifiers needed to be re-evaluated based on characteristics that directly affect low-level DC measurements, including input-referred noise, input offset voltage, input bias current, thermal drift, and overall stability. While instrumentation amplifiers such as the AD620 offer good common-mode rejection and are widely used for sensor signal conditioning, they are optimized for general-purpose instrumentation rather than precision amplification of extremely small, near-DC signals. Because the thermopile output changes slowly with temperature and contains little high-frequency content, minimizing low-frequency noise and offset errors was more important than maximizing bandwidth.

The AD8629 precision operational amplifier was ultimately selected because its specifications more closely matched the requirements of the thermopile readout circuit. Compared with the AD620, the AD8629 provides significantly lower low-frequency noise, substantially lower input offset voltage, and input offset drift that is orders of magnitude smaller over temperature. These characteristics reduce measurement errors caused by amplifier offset and environmental temperature changes, improving the ability to resolve small changes in detector output over extended operating periods. Although additional design measures such as shielding and careful PCB layout were still required to preserve signal integrity, the AD8629 provided a more suitable foundation for amplifying the microvolt-level thermopile signal and contributed to the system's ability to achieve the required temperature measurement accuracy.

3.7 Analog-to-Digital Converter Research

The IRIS system requires an analog-to-digital converter (ADC) to digitize the amplified output of the AD620 instrumentation amplifier so that thermopile measurements can be processed by the ESP32 microcontroller. While the ESP32 includes integrated ADC peripherals, the resolution, linearity, and noise performance of these built-in converters were judged insufficient for the precision required to resolve small temperature differences across the 16×16 thermal image. An external, dedicated ADC was therefore selected to provide the measurement accuracy needed to translate the conditioned thermopile signal into reliable digital temperature data.

When selecting an ADC for this project, several design requirements were considered. The ADC must provide sufficient resolution to resolve small variations in the amplified thermopile signal, low noise and offset to preserve the precision established by the AD620 signal conditioning stage, and a programmable input range that can be matched to the expected output voltage of the amplifier. The ADC must also operate from the IRIS system's 3.3 V supply rail, communicate with the ESP32 through a standard digital interface, and remain cost-effective while integrating cleanly with the existing system hardware. Because the IRIS system performs a slow raster scan that produces 256 measurements per frame, sample rates beyond a few hundred samples per second are not required. To determine the most suitable ADC, several common ADC architectures and specific commercially available models were researched and evaluated before selecting a final candidate.

3.7.1 Successive Approximation Register (SAR) ADCs

Successive approximation register (SAR) ADCs determine the digital value of an input signal through a binary search algorithm. An internal sample-and-hold capacitor captures the input voltage, and the ADC compares this voltage against successive approximations generated by an internal digital-to-analog converter, resolving one bit per clock cycle from most significant to least significant. SAR ADCs are widely used in embedded data acquisition because they offer a good balance of resolution, speed, and power consumption, and because their conversion time is predictable and proportional to the resolution.

SAR ADCs are well suited to applications that require moderate resolution at sample rates ranging from tens of kilosamples per second up to several megasamples per second. They are commonly available in resolutions from 8 to 18 bits and are typically interfaced to microcontrollers using SPI. However, the resolution of a SAR ADC is fundamentally limited by the matching of its internal capacitor array, and achieving 16-bit precision requires careful internal trimming or external reference and filtering circuitry. SAR ADCs are also generally more sensitive to broadband input noise than oversampling architectures, which can degrade effective resolution when amplifying low-level sensor signals.

3.7.2 Delta-Sigma (ΔΣ) ADCs

Delta-sigma ADCs use a fundamentally different approach, sampling the input signal at a frequency much higher than the desired output data rate and using digital filtering and decimation to produce a high-resolution result. The internal modulator typically operates at hundreds of kilohertz to several megahertz, while the output data rate is reduced through oversampling to produce conversion results at rates from a few samples per second to several thousand samples per second. By averaging many samples of the modulator, delta-sigma ADCs achieve very low input-referred noise and high effective resolution.

Delta-sigma ADCs are particularly well suited to applications involving slow-changing, low-amplitude signals from sensors such as thermocouples, thermistors, strain gauges, and thermopiles. The architecture's intrinsic averaging behavior provides strong rejection of high-frequency noise and, with appropriate output data rate selection, can also reject power-line interference at 50 Hz and 60 Hz. The trade-off is that delta-sigma ADCs are slower than SAR converters at equivalent resolutions, with maximum sample rates typically limited to a few thousand samples per second for 16-bit devices. They also have a fixed relationship between data rate and effective resolution, with lower data rates producing better noise performance.

3.7.3 Flash and Pipeline ADCs

Flash ADCs convert analog signals to digital by comparing the input voltage simultaneously against a network of reference voltages using a bank of comparators, producing a result in a single clock cycle. Pipeline ADCs use a multi-stage approach in which each stage produces a few bits of the final result and passes a residue to the next stage, allowing high sample rates with moderate-to-high resolution. Both architectures are designed for applications requiring sample rates of tens of megasamples per second or higher, such as video processing, high-speed instrumentation, and software-defined radio.

These architectures are not well suited to the IRIS system. Their high sample rates are unnecessary for a slow thermal raster scan, their power consumption is significantly higher than SAR or delta-sigma alternatives, and their cost and integration complexity exceed what is appropriate for an embedded sensor measurement application.

3.7.4 ADC Architecture Comparison

Table 3.9 – ADC Architecture Comparison Table

Architecture	Operating Principle	Typical Resolution	Typical Sample Rate	Best Suited For
Successive Approximation (SAR)	Binary search via internal DAC and comparator	8–18 bits	10 kSPS – 10 MSPS	General-purpose data acquisition, moderate-speed sensor reading
Delta-Sigma (ΔΣ)	Oversampling with digital filtering and decimation	16–32 bits	1 SPS – 10 kSPS	Precision low-frequency sensor measurement (thermocouples, thermopiles, bridges)
Flash / Pipeline	Parallel comparison or multi-stage residue conversion	6–14 bits	10 MSPS – 1 GSPS	Video, communications, high-speed instrumentation

For the IRIS system, the delta-sigma architecture provides the best overall match. The thermopile signal of interest is a slowly varying DC-coupled voltage in the millivolt range after amplification by the AD620, the system performs only 256 measurements per scan frame, and noise rejection is more important than conversion speed. The intrinsic averaging behavior of a delta-sigma ADC complements the precision DC characteristics of the AD620, preserving the low-noise, low-drift performance of the signal conditioning stage through digitization.

3.7.5 ADC Model Evaluation

Following the selection of the delta-sigma architecture, several commercially available delta-sigma ADC modules were evaluated to identify the most suitable option for the IRIS system. The primary evaluation criteria were resolution, supply voltage compatibility, input range and programmability, communication interface, package availability, ease of integration with the ESP32, and overall cost. Because the IRIS system uses a 3.3 V logic rail and an I²C bus is already available on the ESP32 for communication with other peripherals, the selected ADC needed to operate from a 3.3 V supply and support I²C communication to keep the system architecture consistent and minimize the number of distinct interfaces in firmware.

ADS1115 (Texas Instruments)

The ADS1115 is a 16-bit delta-sigma ADC with an integrated low-drift voltage reference, internal oscillator, programmable gain amplifier (PGA), and four-channel input multiplexer that allows either four single-ended measurements or two differential pairs. It operates from a single supply of 2.0 V to 5.5 V, draws only 150 µA in continuous-conversion mode, and communicates over I²C with four pin-selectable addresses, allowing up to four ADS1115 devices to share a single bus [ADS1115 datasheet]. The integrated PGA provides selectable full-scale input ranges from ±0.256 V to ±6.144 V, and the programmable data rate can be set from 8 SPS to 860 SPS.

The ADS1115's 16-bit resolution is well matched to the precision provided by the AD620 signal conditioning stage. With a full-scale range of ±2.048 V, the LSB size is 62.5 µV, which is fine enough to resolve small variations in the amplified thermopile output without losing precision in quantization. The integrated PGA eliminates the need for additional external gain or scaling circuitry between the AD620 output and the ADC input, simplifying the analog signal path. The internal voltage reference and oscillator further reduce the external component count, requiring only a single 0.1 µF supply decoupling capacitor and two I²C pull-up resistors for basic operation.

The ADS1115's 3.3 V compatibility aligns directly with the ESP32's logic level and supply rail, and the I²C interface integrates cleanly with the bus already used by the AS5600 magnetic encoders. This shared bus architecture reduces the number of GPIO pins required by the ADC and keeps the firmware peripheral configuration consistent. The ADS1115 is widely available on breakout modules from multiple suppliers at unit costs of approximately $2 to $5 for the module form, or approximately $3 to $7 for the bare IC, making it among the most cost-effective 16-bit delta-sigma ADCs available. Extensive Arduino and ESP32 library support, including the well-maintained Adafruit ADS1X15 library, further reduces firmware development time.

ADS1015 (Texas Instruments)

The ADS1015 is the 12-bit counterpart to the ADS1115, sharing the same package, pinout, supply range, PGA, multiplexer, and I²C interface, but operating at higher sample rates of 128 SPS to 3300 SPS [ADS1015 datasheet]. Because the two devices are pin-compatible, the ADS1015 represents a direct alternative whenever resolution can be traded for speed.

For the IRIS system, however, the trade-off favors the ADS1115. The thermal raster scan produces only 256 measurements per frame and the scan rate is limited primarily by the mechanical settling time of the stepper-driven mirror assembly rather than by ADC throughput, so the ADS1015's higher sample rate provides no practical benefit. At a full-scale range of ±2.048 V, the ADS1015's LSB size is 1 mV, which is sixteen times coarser than the ADS1115's 62.5 µV, which would unnecessarily quantize the precision provided by the AD620 signal chain and reduce the dynamic range available for resolving small temperature differences. Because the two devices are sold at nearly identical price points and use the same firmware drivers, there is no cost or integration advantage to selecting the lower-resolution part.

MCP3008 (Microchip)

The MCP3008 is an 8-channel, 10-bit SAR ADC with an SPI interface, designed for general-purpose embedded data acquisition. It operates from a 2.7 V to 5.5 V supply, draws approximately 425 µA active current at 5 V, and supports sample rates up to 200 kSPS at 5 V or 75 kSPS at 2.7 V [MCP9808 datasheet]. The MCP3008 provides eight single-ended or four pseudo-differential channels and is widely available in PDIP, SOIC, and TSSOP packages at unit costs of approximately $3 to $4.

The MCP3008 is a well-established and reliable ADC and is commonly used in microcontroller-based data acquisition projects, particularly with the Raspberry Pi platform. However, its 10-bit resolution is insufficient for the IRIS application. With a full-scale reference of 3.3 V, the MCP3008 provides an LSB size of approximately 3.2 mV, which is roughly fifty times coarser than the ADS1115 and represents a substantial loss of the precision provided by the AD620 signal conditioning stage. The MCP3008 also lacks an integrated PGA, an internal voltage reference, and a programmable input range, requiring additional external components, including a precision voltage reference, helping to achieve stable, repeatable measurements. Furthermore, its SPI interface would require dedicated GPIO pins on the ESP32 rather than sharing the existing I²C bus used by the AS5600 encoders, increasing both the pin count and the firmware complexity. While the MCP3008 is suitable for many embedded applications, its resolution and architecture are mismatched with the precision sensing requirements of the IRIS system.

ADC Model Comparison

Table 3.10 – ADC Model Comparison Table

Specification	ADS1115 (TI)	ADS1015 (TI)	MCP3008 (Microchip)

Architecture	Delta-sigma (ΔΣ)	Delta-sigma (ΔΣ)	Successive approximation (SAR)
Resolution	16 bits	12 bits	10 bits
LSB Size (FSR ±2.048 V)	62.5 µV	1 mV	3.2 mV (at 3.3 V Vref)
Channels	4 SE / 2 differential	4 SE / 2 differential	8 SE / 4 pseudo-differential
Supply Voltage	2.0 V – 5.5 V	2.0 V – 5.5 V	2.7 V – 5.5 V
Operating Current	150 µA	150 µA	~425 µA
Programmable Gain Amplifier	Yes (±0.256 V to ±6.144 V)	Yes (±0.256 V to ±6.144 V)	No
Internal Reference	Yes	Yes	No (external required)
Sample Rate	8 – 860 SPS	128 – 3300 SPS	Up to 200 kSPS
Communication Interface	I^{2}C	I^{2}C	SPI
I^{2}C Addresses Available	4	4	N/A
Approx. Cost (module)	\$2–\$5	\$2–\$5	\$3–\$5

Based on this evaluation, the ADS1115 provides the most suitable balance of resolution, integration, supply compatibility, and cost for the IRIS thermal measurement signal chain. The MCP3008's 10-bit resolution and lack of integrated reference and PGA make it unsuitable for preserving the precision established by the AD620 signal conditioning stage, and its SPI interface would add complexity without providing any benefit over the I^{2}C bus already used in the system. The ADS1015 shares the ADS1115's integration advantages but provides only 12-bit resolution, which would unnecessarily quantize the conditioned thermopile signal at no cost or speed advantage given the slow raster scan rate of the IRIS system.

The ADS1115's 16-bit resolution, combined with its programmable ±2.048 V full-scale range, allows the AD620's amplified output to be digitized with a 62.5 µV LSB, well below the noise floor of the upstream signal chain and fine enough to resolve small temperature differences across the thermal image. Its integrated low-drift voltage reference and internal oscillator eliminate the need for external precision components, its 150 µA quiescent current is a small contribution to the overall system power budget, and its I^{2}C interface integrates cleanly with the bus already used by the AS5600 magnetic encoders, reducing both pin count and firmware complexity. The widespread availability of breakout modules and well-tested Arduino and ESP32 libraries further simplifies prototyping and integration, making the ADS1115 the most practical and cost-effective choice for the IRIS system.

3.8 Processing Unit Selection

The microcontroller serves as the central control unit of the IRIS system, coordinating sensor data acquisition, stepper motor actuation for raster scanning, and wireless communication with the external monitoring interface. As a result, the selected microcontroller must provide sufficient processing capability for real-time control, support multiple peripheral interfaces, and enable reliable wireless data transmission while maintaining low power consumption and system simplicity. To ensure these requirements are met, a comparison of several candidate microcontroller platforms was performed to determine the most suitable solution for the IRIS system.

3.8.1 MSP430 Microcontroller

The MSP430 is a low-power microcontroller developed by Texas Instruments, designed specifically for energy-efficient embedded applications. It features an ultra-low-power architecture, with current consumption as low as 0.1 µA in standby modes and approximately 250 µA per MIPS during active operation, making it highly suitable for battery-powered systems [1]. The device utilizes a 16-bit RISC CPU architecture capable of up to 16 MIPS, providing efficient processing with a compact instruction set [1].

In addition to its low power consumption, the MSP430 integrates a wide range of peripherals, including analog-to-digital converters (ADC), timers, and communication interfaces such as UART, I²C, and SPI, allowing it to support mixed-signal sensing applications with minimal external components [1].

While the MSP430 excels in low-power and simple sensing applications, it lacks integrated wireless communication capabilities and has limited processing performance compared to more advanced microcontrollers. Because the IRIS system requires real-time motor control, sensor data processing, and wireless communication, the MSP430 would require additional external modules, increasing system complexity and design overhead. Therefore, the MSP430 is considered less suitable for this application.

3.8.2 ESP32 Microcontroller

The ESP32 is a high-performance microcontroller developed by Espressif Systems that integrates Wi-Fi and Bluetooth communication directly into the module. It features a dual-core processor operating between 80 MHz and 240 MHz, providing sufficient computational capability for real-time embedded applications [2].

The ESP32 also includes a wide range of integrated peripherals, including I²C, SPI, UART, PWM, ADC, and DAC interfaces, enabling direct communication with sensors, motor drivers, and other system components without requiring additional hardware [2]. This high level of integration significantly reduces system complexity and component count.

In addition, the ESP32 supports multiple power-saving modes, including deep-sleep operation with microamp-level current consumption, making it suitable for energy-efficient embedded systems [2]. The inclusion of FreeRTOS support further enables deterministic task scheduling and real-time system control.

Because the ESP32 integrates wireless communication, processing capability, and peripheral interfaces into a single platform, it eliminates the need for external communication modules while maintaining sufficient performance for real-time control. Therefore, the ESP32 provides a highly suitable solution for the IRIS system.

3.8.3 Raspberry Pi

The Raspberry Pi is a small, ARM-based single-board computer capable of performing many of the functions of a traditional desktop system, including running a full Linux operating system and supporting multimedia applications [3]. It features a 700 MHz processor, dedicated graphics hardware, and multiple high-level interfaces such as HDMI, USB, and Ethernet [3].

Additionally, the Raspberry Pi provides access to general-purpose input/output (GPIO) pins and communication interfaces such as I^2C, SPI, and UART, allowing it to interface with external hardware [3]. However, these interfaces are managed within a full operating system environment rather than through direct low-level hardware control.

While the Raspberry Pi offers significantly greater computational capability than typical microcontrollers, it introduces increased power consumption, system complexity, and dependence on an operating system. For applications requiring deterministic real-time control, such as coordinated sensor acquisition and motor actuation, this added complexity can reduce system reliability and responsiveness.

Because the IRIS system requires efficient real-time embedded control rather than general-purpose computing, the Raspberry Pi is considered unnecessarily complex and less suitable for this application.

3.8.4 Microcontroller Platform Comparison

A comparison of the evaluated microcontroller platforms is summarized in Table 3.11.

Table 3.11 – Microcontroller Platform Comparison Table

Feature	**MSP430**	**ESP32**	**Raspberry Pi**
Processing Capability	Low	Moderate–High	High
Power Consumption	Very Low	Low	High
Wireless Communication	External Required	Integrated	Integrated
Real-Time Control	Excellent	Excellent	Limited

System Complexity	Low	Moderate	High

The MSP430 provides extremely low power consumption but lacks the processing capability and integrated communication required for the IRIS system. The Raspberry Pi offers high computational performance but introduces unnecessary complexity, higher power consumption, and reliance on an operating system.

The ESP32 provides a balanced solution by combining sufficient processing capability, integrated wireless communication, and direct hardware control within a single platform. Therefore, it offers the most suitable balance of performance, efficiency, and system integration for the IRIS system requirements.

3.8.5 Processing Unit Selection

Based on the comparison of available platforms, the ESP32 was selected as the microcontroller for the IRIS system.

The ESP32 provides the necessary computational performance to handle sensor data acquisition and motor control, while also supporting integrated wireless communication for data transmission. Its wide range of peripheral interfaces allows seamless integration with system components, including temperature sensors, motor drivers, and display modules.

Additionally, the ESP32's support for real-time operating systems enables deterministic scheduling of tasks, ensuring reliable system performance. By combining these features into a single module, the ESP32 minimizes system complexity while meeting all functional requirements.

Therefore, the ESP32 represents the most appropriate microcontroller solution for the IRIS system.

3.8.6 ESP32 Module Comparison

After selecting the ESP32 platform, several ESP32-based modules were evaluated to determine the most suitable implementation for the IRIS system. The modules considered include the ESP32 DevKit V1, ESP32-WROOM-32, and ESP32-S3-WROOM-1.
The ESP32 DevKit V1 is a development board that integrates the ESP32 microcontroller with onboard USB-to-UART circuitry, voltage regulation, and pin headers for rapid prototyping. While it simplifies development and testing, its larger size and inclusion of unnecessary support components make it less suitable for integration into a custom PCB design.

The ESP32-WROOM-32 is a compact, widely used module that integrates the ESP32 microcontroller, flash memory, and antenna into a single package. It provides a balance between performance and integration, with support for Wi-Fi, Bluetooth, and a wide range of peripherals [2].

The ESP32-S3-WROOM-1 is a newer module in the ESP32 family that includes enhanced processing capability, increased memory options, and improved support for advanced applications such as vector instructions and AI acceleration. It also maintains full compatibility with common embedded interfaces and wireless communication features.
A comparison of the evaluated modules is shown in Table 3.12.

Table 3.12 – ESP32 Module Comparison Table

Feature	**ESP32 DevKit V1**	**ESP32-WROOM-32**	**ESP32-S3-WROOM-1**
Type	Development Board	Embedded Module	Embedded Module
CPU	Dual-core 240 MHz	Dual-core 240 MHz	Dual-core up to 240 MHz
RAM	~520 KB SRAM	~520 KB SRAM	Up to 512 KB SRAM + PSRAM support
Flash Memory	4 MB (typical)	4 MB	4–16 MB (configurable)
Wireless	Wi-Fi + Bluetooth	Wi-Fi + Bluetooth	Wi-Fi + Bluetooth LE
GPIO Pins	~30	~34	~45
Power Consumption	Higher (board overhead)	Moderate	Low–Moderate
Size	Large (dev board)	Compact	Compact
USB Support	External UART	External UART	Native USB support
PCB Integration	Poor	Excellent	Excellent
Cost	Low–Moderate	Low	Moderate

3.8.7 Microcontroller Module Selection

Based on the comparison of available ESP32 modules, the ESP32-S3-WROOM-1 was selected for the IRIS system.

While the ESP32 DevKit V1 is useful for prototyping, it is not suitable for final system integration due to its size and inclusion of unnecessary support circuitry. The ESP32-WROOM-32 provides a compact and well-supported solution; however, it offers fewer GPIO pins and less flexibility in memory configuration compared to newer modules. The ESP32-S3-WROOM-1 provides the most suitable balance of performance, integration, and expandability. Its increased GPIO availability supports the multiple peripherals required by the IRIS system, including sensors, motor drivers, and communication interfaces. Additionally, its support for expanded memory and native USB functionality improves system flexibility for future development and debugging.

Because the ESP32-S3-WROOM-1 meets all system requirements while providing improved scalability and integration capability, it was selected as the microcontroller module for the IRIS system.

3.9 Motor Technology Overview

The motor system provides the mechanical actuation required for the device to perform controlled motion. Because the system requires precise and repeatable movement of mechanical components, selecting appropriate motor technology was an important step during the design phase.

Several types of electric motors are commonly used in embedded systems and robotics applications, including brushed DC motors, servo motors, and stepper motors. Each of these motor types offers different advantages in terms of speed control, positional accuracy, torque characteristics, and ease of integration with microcontroller-based systems.

When selecting a motor for this project, several design requirements were considered. The motor must provide controlled motion that can be managed through software commands generated by the ESP32 microcontroller. The motor must also operate within the project's voltage and current limitations while remaining cost-effective and simple to integrate with the system hardware.

Because the device requires repeatable positioning of mechanical components rather than continuous high-speed rotation, the design prioritizes position control, predictable motion, and reliable low-speed operation over high rotational speed. To determine the most suitable motor type, several common motor technologies were researched and evaluated before selecting specific models for further comparison.

3.9.1 Brushed DC Motors

Brushed DC motors are one of the simplest types of electric motors and are widely used in consumer electronics and small mechanical systems. These motors typically use two electrical connections for power and ground, and they rotate continuously when voltage is applied.

The rotational speed of a DC motor is generally proportional to the applied voltage. Speed control is commonly achieved using pulse width modulation (PWM), which rapidly switches power on and off to regulate the average voltage supplied to the motor. By adjusting the duty cycle of the PWM signal, the motor speed can be controlled.
DC motors are commonly used in applications that require continuous rotation at relatively high speeds, such as cooling fans, pumps, and wheeled robotic vehicles.

Although DC motors are inexpensive and easy to control, they do not provide inherent position control. If precise positioning is required, additional sensors such as rotary encoders must be incorporated into the system. This increases system complexity and adds additional hardware requirements.

Because the system requires controlled positioning rather than continuous rotation, DC motors were considered less suitable for this application.

3.9.2 Servo Motors

Servo motors are designed to provide controlled angular positioning and are widely used in robotics and motion control applications. A typical servo motor contains a DC motor, gear reduction system, internal control circuitry, and a position sensor, which is usually implemented using a potentiometer.

Servo motors typically use three electrical connections: power, ground, and a control signal. The control signal is a PWM waveform whose pulse width corresponds to the desired angular position of the motor shaft.

Unlike standard DC motors, servo motors do not rotate continuously. Instead, they are designed to move within a limited angular range, typically around 0° to 180°. When a new position command is received, the servo motor moves to the specified angle and actively holds that position by adjusting the internal motor drive.

Servo motors are commonly used in applications such as robotic arms, steering mechanisms, and control surfaces where accurate angular positioning is required. Although servo motors provide built-in feedback and relatively simple control, their limited range of motion and internal control circuitry reduce the flexibility available for custom motion control algorithms.

3.9.3 Stepper Motors

Stepper motors are widely used in measurement and control applications where precise, repeatable positioning is required. Unlike DC motors, which rotate continuously, stepper motors move in discrete angular increments known as steps. Because the motor moves in quantified increments, the position of the shaft is known at all times simply by counting the steps performed, without requiring an external feedback sensor [3]. This open-loop positioning capability makes stepper motors particularly well suited for embedded systems where hardware simplicity is a priority.

Stepper motors operate using multiple electromagnets arranged around a central rotor. By energizing these electromagnets in a specific sequence, the motor shaft rotates incrementally from one position to the next. Each incremental movement corresponds to a fixed step angle, allowing precise control of motor position. Additional characteristics that make stepper motors attractive for control applications include their brushless construction, which eliminates the failure-prone commutator and brush assembly found in conventional DC motors, their ability to hold a stationary position when energized, and their excellent response to starting, stopping, and direction reversal [10].

Stepper motors are commonly found in devices such as 3D printers, CNC machines, scanners, and positioning systems, where predictable incremental motion is essential.

3.9.4 Unipolar and Bipolar Configurations

Stepper motors are typically available in two winding configurations: unipolar and bipolar. Understanding the distinction between these configurations is important because it directly influences the driver circuitry required and the torque available to the system.

Unipolar stepper motors use windings with a center tap, which allows current direction to be controlled using a relatively simple drive circuit. Because only one half of each winding is energized at any given time, however, the magnetic field produced is weaker than what would be generated if the full winding were used. Bipolar stepper motors use the entire winding during each energization cycle, which produces approximately 30% more torque than a comparable unipolar motor of the same physical size [10]. This performance advantage comes at the cost of increased driver complexity, as bipolar motors require an H-bridge circuit to reverse current direction through each winding.

For applications where torque demands are moderate and driver simplicity is preferred, unipolar motors offer a practical and cost-effective solution. The 28BYJ-48, the motor selected for the IRIS system, is a unipolar permanent magnet stepper motor with an integrated gearbox, and is driven using the ULN2003 Darlington transistor array, which interfaces directly with the ESP32 microcontroller's GPIO pins without requiring H-bridge circuitry.

Due to their ability to provide controlled incremental motion, open-loop positional accuracy, and reliable low-speed holding torque, stepper motors are well suited for systems that require predictable positioning and repeatable movement [11].

3.9.5 Motor Type Comparison

Table 3.13 – Motor Technology Comparison Table

Motor Type	**Rotation Behavior**	**Control Method**	**Position Control**	**Typical Applications**
DC Motor	Continuous rotation	PWM speed control	Requires encoder	Fans, pumps, vehicle wheels
Servo Motor	Limited angular rotation	PWM position control	Built-in feedback	Robotics, steering systems
Stepper Motor	Incremental step rotation	Step pulse control	Inherent positional control	CNC machines, scanners, 3D printers

From this comparison, stepper motors provide the most suitable characteristics for applications that require precise positioning and predictable motion.

3.9.6 Motor Model Evaluation

Following the selection of stepper motor technology, several commercially available stepper motor models were evaluated to identify the most suitable option for the IRIS system. The primary evaluation criteria were operating voltage compatibility, holding torque, step resolution, driver requirements, physical size, and overall cost. Because the IRIS system includes a dedicated 5 V power rail for peripheral components, the selected motor needed to operate within this voltage range while providing sufficient holding torque to reliably position the scanning assembly at each increment. The motor also needed to be compatible with a driver circuit that could accept logic-level control signals from the ESP32 microcontroller's GPIO pins, minimizing additional power conversion hardware and keeping the overall system architecture straightforward.

28BYJ-48 (Rajguru Electronics)

The 28BYJ-48 is a 4-phase unipolar permanent magnet stepper motor with an integrated 1:64 planetary gearbox. It is rated for 5 V DC operation and draws approximately 160 mA per phase across a coil resistance of 50 Ω. The integrated gearbox reduces the effective step angle from 5.625° to 5.625°/64 at the output shaft, yielding 2048 steps per revolution and providing fine incremental positioning without requiring micro-stepping hardware. As noted in the motor datasheet, positional accuracy is within ±5% of a step and this error is non-cumulative across successive steps, ensuring reliable open-loop positioning over repeated scan cycles [29].

The IRIS system is designed to produce a 16×16 thermal image through raster scanning of an infrared photodiode across a 15° × 15° field of view, requiring 16 discrete, evenly spaced positions per scan axis with an angular spacing of approximately 0.94° per pixel. With 2048 steps per revolution at the output shaft, the 28BYJ-48 provides a native angular resolution of approximately 0.176° per step. Each pixel position therefore corresponds to roughly 5 motor steps, meaning the motor is capable of positioning to approximately five times finer resolution than the scan requires. This margin ensures that each of the 16 scan positions per axis can be reached with consistent, repeatable step counts and without accumulated positioning error across a full scan cycle, satisfying the system's spatial resolution requirement of 2 cm per pixel at the target operating distance.

The motor's 5 V operating voltage is directly compatible with the IRIS system's dedicated 5 V peripheral rail, and it is driven using the ULN2003 Darlington transistor array, which interfaces directly with the ESP32 GPIO pins without requiring additional power conversion hardware. The 28BYJ-48 is widely available, well-documented, and carries a unit cost of approximately \$2–\$5, making it among the most cost-effective stepper solutions for embedded systems. One limitation of the geared design is the introduction of mechanical backlash when reversing direction, as gear trains must take up slack before motion reverses [33]. For the IRIS system, which performs unidirectional scanning sweeps along each raster row, this limitation does not affect positioning accuracy during normal operation.

17HE08-1004S (STEPPERONLINE)

The 17HE08-1004S is a compact 2-phase bipolar NEMA 17 stepper motor with a step angle of 1.8°, yielding 200 steps per revolution. It provides a holding torque of 170 mN·m, a rated current of 1 A per phase, and a phase resistance of 3.5 Ω. At only 23 mm in body length and 180 g, it is among the shortest and lightest NEMA 17 motors available, making it physically suitable for compact embedded designs [30]. The motor is readily available through major distributors including Amazon, which reduces lead time concerns during prototyping.

However, the 17HE08-1004S is a bipolar motor and requires an H-bridge driver such as the A4988 or DRV8825 to reverse current through each phase winding. These drivers are typically rated for supply voltages of 8–35 V, meaning that a separate higher-voltage power rail would need to be added to the IRIS system — a requirement not present in the current power architecture. Additionally, at 200 native steps per revolution and no integrated gearing, each step corresponds to 1.8° of shaft rotation. Covering the required 0.94° per pixel scan increment would require micro-stepping at a minimum division of 2, adding software and driver complexity that the ULN2003 and 28BYJ-48 pairing avoids entirely. While the 17HE08-1004S is a capable and accessible motor, its bipolar drive requirements and voltage constraints make it less suitable for the IRIS system than a 5 V unipolar solution.

SF2421-10B11 (Sanyo Denki)

The SF2421-10B11 is a compact 42 mm square 2-phase bipolar stepper motor from Sanyo Denki's SANMOTION F2 series. It offers a holding torque of 290 mN·m, a step angle of 1.8°, and a positional accuracy tolerance of ±0.054° [32]. With a rated current of 1 A per phase, it is more power-efficient than many larger NEMA-class motors and is physically compact enough to suit embedded integration. The SF2421-10B11 would be well suited to applications requiring higher torque and finer native step resolution than the 28BYJ-48 provides. However, it requires a 24 V DC supply and is specified for use with the Sanyo Denki F2BED200P100 dedicated bipolar driver, which itself operates at 24 V. Incorporating this motor would require an additional power conversion stage to generate 24 V from the system supply — a rail not present in the IRIS power architecture — as well as a specialized industrial driver that significantly increases cost and integration complexity. Like the 17HE08-1004S, its native step angle of 1.8° would require micro-stepping to meet the 0.94° per pixel scan increment required by the 15° × 15° field of view specification. The SF2421-10B11 carries a unit cost of approximately $30–$50, substantially higher than both alternative motors evaluated. While it represents the highest-performance option in this comparison, its voltage, driver, and cost requirements are mismatched with the IRIS system's design constraints.

<u>Motor Model Comparison</u>

Table 3.14 – Motor Model Comparison Table

Specification	**28BYJ-48 (Rajguru)**	**17HE08-1004S (STEPPERONLINE)**	**SF2421-10B11 (Sanyo Denki)**
Operating Voltage	5 V DC	8–35 V DC (driver dependent)	24 V DC
Phase Configuration	4-phase unipolar	2-phase bipolar	2-phase bipolar
Steps/Revolution	2048 (with 1:64 gearing)	200	200
Step Angle	5.625° / 64	1.8°	1.8°
Holding Torque	34.3 mN·m	170 mN·m	290 mN·m
Rated Current	~160 mA	1 A/phase	1 A/phase
Phase Resistance	50 Ω	3.5 Ω	3.5 Ω
Driver Required	ULN2003	A4988 / DRV8825	F2BED200P100
Body Length	19 mm	23 mm	33 mm
Weight	—	180 g	230 g
Approx. Cost	$2–$5	$8–$14	$30–$50+

Based on this evaluation, the 28BYJ-48 provides the most suitable balance of voltage compatibility, positional resolution, torque sufficiency, and integration simplicity for the IRIS system. Both the 17HE08-1004S and the SF2421-10B11 offer higher holding torque but their bipolar drive requirements, higher operating voltages, and coarser native step angles would each require micro-stepping and additional power supply infrastructure that fall outside the IRIS system's current power architecture. The 28BYJ-48's geared output delivers approximately five times the positional resolution required by the 16×16 raster scan across the 15° × 15° field of view, its 5 V compatibility aligns directly with the system power rail, and its ULN2003 interface eliminates the need for additional driver hardware, making it the most practical and cost-effective choice for this application.

3.10 Rotary Encoder Selection

Rotary encoders are used to measure angular position by converting rotational motion into electrical signals [46]. In the IRIS system, precise knowledge of mirror position is critical for accurate raster scanning and image reconstruction. Without position feedback, errors such as missed steps, backlash, or mechanical drift in the stepper motor system can lead to distortion in the reconstructed thermal image.

By incorporating rotary encoders on each scanning axis, the system is able to track the absolute or incremental angular position of the mirror assembly. This enables improved repeatability, accurate mapping between measured temperature data and spatial position, and the ability to implement closed-loop control if necessary.

Several rotary encoder technologies were evaluated, including optical encoders, mechanical encoders, and magnetic encoders. Each technology offers different tradeoffs in terms of accuracy, robustness, cost, and environmental tolerance.

3.10.1 Optical Encoder

Optical encoders determine angular position by detecting interruptions in a light beam caused by a rotating disk with patterned slots [46]. These devices offer very high resolution and accuracy, making them suitable for precision motion control applications.

However, optical encoders are sensitive to environmental conditions such as dust, debris, and vibration. In an industrial electrical enclosure, these factors can degrade performance and reliability. Additionally, optical encoders are generally more expensive and require more careful alignment during installation.

3.10.2 Mechanical Encoder

Mechanical encoders use physical contacts to generate signals corresponding to rotational motion [46]. These devices are simple and low cost and are commonly used for basic user input applications.

Despite their simplicity, mechanical encoders suffer from wear over time due to physical contact between components. They also provide lower resolution and are less suitable for applications requiring precise position feedback, making them less appropriate for the IRIS scanning system.

3.10.3 Magnetic Encoder

Magnetic encoders determine angular position by sensing changes in a magnetic field generated by a rotating magnet [43]. These devices operate without physical contact, providing improved durability and long-term reliability.

Magnetic encoders are well suited for industrial environments due to their resistance to dust, vibration, and electromagnetic interference. While their resolution is typically lower than high-end optical encoders, they provide sufficient accuracy for many embedded motion control applications.

3.10.4 Rotary Encoder Technology Comparison

Table 3.15 – Rotary Encoder Technology Comparison Table

Technology	Principle	Advantages	Disadvantages
Optical Encoder	Uses light interruption through slotted disk	Very high accuracy and resolution	Sensitive to dust, more expensive
Mechanical Encoder	Uses physical contacts	Low cost, simple	Wear over time, lower precision
Magnetic Encoder	Uses magnetic field sensing	Non-contact, robust, compact	Slightly lower resolution than optical

Magnetic encoders were selected as the most suitable option due to their non-contact operation, high durability, and resistance to dust and vibration. These characteristics are especially important for operation within electrical enclosures where environmental conditions may not be ideal.

3.10.5 Magnetic Encoder Module Comparison

Table 3.16 – Magnetic Encoder Module Comparison Table

Parameter	**MT6701**	**AS5600**
Resolution	14-bit	12-bit
Interface	I²C / PWM	I²C / PWM / Analog
Measurement Type	Absolute	Absolute
Contact Type	Non-contact magnetic	Non-contact magnetic
Complexity	Moderate	Low
Cost	Low	Very Low

The MT6701 and AS5600 encoder modules are compared based on manufacturer specifications and module characteristics [43], [47].

3.10.6 Selected Encoder

The AS5600 magnetic rotary encoder was selected for the IRIS system due to its balance of accuracy, simplicity, and ease of integration [43].

While the MT6701 offers higher resolution, the AS5600 provides sufficient angular resolution (12-bit) to meet the spatial accuracy requirements of the raster scanning system. Additionally, the AS5600 supports multiple output interfaces, including I²C, PWM, and analog voltage, allowing flexible integration with the ESP32 microcontroller.

A key advantage of the AS5600 is its straightforward implementation. The device requires minimal external components and has strong library support, reducing software development complexity. Its non-contact magnetic sensing mechanism improves long-term reliability and eliminates mechanical wear, making it well suited for continuous operation.

Overall, the AS5600 provides an effective solution for angular position feedback while minimizing system complexity, making it the most practical choice for the IRIS system.

3.11 Display Screen Selection

During the design phase, several display technologies were evaluated to provide user feedback and system status information. The primary candidates considered were OLED displays, LCD displays, ePaper displays, and multi-segment LED displays. Each of these technologies offers different advantages in terms of readability, power consumption, cost, and ease of integration.

Because the display in this project is primarily intended to show simple system information such as temperature readings, status messages, and network connectivity, the design prioritized simplicity, low cost, and straightforward microcontroller integration over advanced graphical capability. Since the system is based on an ESP32 microcontroller, compatibility with common embedded interfaces such as I²C and SPI was also an important consideration.

To determine the most suitable display technology, several common display types were researched and compared before selecting the final display used in the prototype.

3.11.1 OLED Displays

OLED displays are widely used in embedded systems because they provide high contrast and do not require a backlight [35]. Instead, each pixel emits its own light, allowing the display to remain clearly visible in low-light environments.

OLED modules are often used in small embedded devices because they are compact, lightweight, and capable of displaying both text and simple graphics. They are commonly found in wearable electronics, sensor modules, and portable instruments where visual clarity is important.

Although OLED displays provide excellent visual performance, they are generally more expensive than simple character LCD modules. In addition, their graphical capability introduces additional software complexity that is not required for this project. Because the system only needs to display basic text-based information, OLED displays were considered more capable than necessary for the application.

3.11.2 LCD Displays

Liquid Crystal Displays (LCDs) are widely used in embedded systems because they are inexpensive, reliable, and easy to integrate [34]. Unlike OLED displays, LCDs require a backlight to illuminate the display, but they remain one of the most common choices for low-cost electronic systems.

Character LCD modules are especially common in embedded applications. These displays are designed to show letters, numbers, and symbols in predefined character positions rather than full graphics. A standard 16×2 LCD, for example, can display two rows of sixteen characters and is well suited for presenting system status and sensor values.

LCD modules are commonly used in appliances, instrumentation, educational electronics projects, and microcontroller-based systems where only simple text output is needed. Their low cost, wide availability, and strong software support make them practical for rapid prototyping and final implementation.

Although character LCDs are limited to text output and cannot display complex graphics, this limitation is acceptable for the IRIS system. Because the project only requires basic status messages and sensor readings, LCD displays were considered highly suitable for this application.

3.11.3 ePaper Displays

ePaper displays are designed to resemble printed paper and are known for their extremely low power consumption [36]. Power is mainly required only when the display content is updated, allowing the image to remain visible even when power is removed.

These displays are commonly used in devices such as e-readers, price tags, and battery-powered systems that require infrequent updates and good readability in bright lighting conditions.

Despite their low power usage and strong visibility, ePaper displays have very slow refresh rates compared to other display technologies. This makes them less suitable for systems that need to update sensor readings and status information regularly. Because the IRIS system requires periodic changes to the displayed information, ePaper displays were considered less appropriate for this project.

3.11.4 Multi-Segment LED Displays

Multi-segment LED displays are commonly used to present numerical information in a simple and highly reliable format. These displays use individual illuminated segments arranged to form numbers or, in some cases, limited characters.

They are widely used in digital clocks, calculators, counters, and measuring instruments where only a small amount of numeric information must be shown.

Although multi-segment LED displays are durable and easy to control, they are limited in the amount of information they can present. They are not well suited for displaying multiple lines of text, device status messages, or network information. Because the IRIS system requires more flexible text output, multi-segment LED displays were considered less suitable for this application.

3.10.5 Display Technology Comparison

Table 3.17 – Display Technology Comparison Table

Display Type	Example Module	Interface	Resolution / Format	Power Consumption	Key Advantages	Key Drawbacks
OLED	UCTRONICS 0.96" OLED (SSD1306)	I²C	128 × 64 pixels	Low	High contrast, compact,	Higher cost and software complexity

					supports graphics	
LCD (Character)	SunFounder LCD1602 I²C Module	I²C	16 × 2 characters	Low	Very low cost, simple integration	Text-only output
ePaper	LAFVIN 2.13" ePaper HAT	SPI	250 × 122 pixels	Very low	Persistent image, excellent outdoor visibility	Slow refresh rate
Multi-Segment LED	Typical 7-segment display	GPIO / driver IC	Numeric characters	Very low	Durable and easy to drive	Limited information display

From this comparison, character LCD displays provide the most suitable characteristics for a system that requires simple text output, low cost, and easy integration with the ESP32.

3.11.6 Display Module Evaluation

Following the selection of character LCD technology as the most suitable display type, several commercially available display modules were evaluated to determine the best fit for the IRIS system. The primary evaluation criteria included operating voltage compatibility, interface type, power consumption, physical size, readability, and overall cost.

Because the IRIS system includes both 3.3 V and 5 V power rails and relies on the ESP32 microcontroller, the selected display module needed to support low-pin-count communication (preferably I²C) and operate reliably within the system voltage constraints. Additionally, the display needed to provide sufficient character space to present system status information clearly while maintaining a compact form factor.

LCD1602 (SunFounder I²C Module)

The LCD1602 is a widely used 16×2 character display module based on the HD44780 controller [34]. When paired with an I²C interface backpack, it requires only two communication lines (SDA and SCL), significantly reducing wiring complexity. The module operates at 5 V and is fully compatible with the IRIS system's power architecture.

This display provides sufficient character space to show temperature readings, system status messages, and connectivity indicators. It is inexpensive, typically costing between $6 and $10, and is supported by well-established libraries for the ESP32 platform.

OLED 0.96-inch (UCTRONICS SSD1306)

The 0.96-inch OLED display uses the SSD1306 driver and supports I²C communication [35]. It operates from 3.3 V to 5 V and provides a resolution of 128 × 64 pixels, allowing both text and simple graphics to be displayed.

While this display offers higher visual quality and flexibility than a character LCD, it introduces additional software complexity for rendering text and graphics. It is also more expensive than a standard LCD1602 module, typically ranging from $10 to $15.

ePaper 2.13-inch (LAFVIN Module)

The 2.13-inch ePaper display provides a resolution of 250 × 122 pixels and communicates using an SPI interface [36]. It offers extremely low power consumption and excellent readability in bright environments.

However, the display has a slow refresh rate and requires more complex control compared to LCD and OLED modules. These characteristics make it less suitable for applications requiring frequent updates, such as real-time system monitoring.

Table 3.18 – Display Module Comparison Table

Specification	**LCD1602 (SunFounder)**	**OLED 0.96" (SSD1306)**	**ePaper 2.13"**
Interface	I²C	I²C	SPI
Voltage	5 V	3.3–5 V	3.3 V
Display Type	Character (16×2)	Graphical (128×64)	Graphical (250×122)
Power Consumption	Low	Low	Very low
Refresh Rate	Fast	Fast	Very slow
Cost	$6–$10	$10–$15	$15–$25
Complexity	Low	Moderate	High

From this comparison, the LCD1602 provides the most suitable balance of simplicity, cost-effectiveness, and compatibility with the IRIS system requirements.

3.11.7 Selected Display

The final display selected for the system is the SunFounder LCD1602 module with an I²C interface. This display provides two rows of sixteen characters, which is sufficient for showing key information such as system temperature, device status, connectivity indicators, and error messages.

The LCD1602 was selected because it offers a practical balance of cost, simplicity, and functionality. Its I²C interface reduces the required microcontroller connections to only two communication lines, which simplifies wiring and preserves GPIO pins for other subsystems. In addition, the module is widely available, inexpensive, and supported by common embedded software libraries.

3.12 Physical User Interface (UI) Selection

The physical user interface (UI) provides a direct method for user interaction with the IRIS system, enabling control of system operation without requiring access to external devices such as a computer or mobile interface. Because the system is designed for use in environments involving energized electrical equipment, the physical UI must prioritize simplicity, reliability, and safe operation.

In industrial environments, operators may be required to wear personal protective equipment (PPE), including insulated gloves, which limits the effectiveness of sensitive or high-precision input mechanisms. Additionally, interaction time must be minimized to reduce exposure to hazardous conditions. As a result, the UI must support rapid, discrete inputs that can be executed with minimal effort and high confidence.

The IRIS system requires only a limited set of control functions, including system initialization, scan triggering, and system reset or fault acknowledgment. Therefore, the physical UI must be optimized for simplicity rather than complex user interaction.

To determine the most appropriate solution, several physical UI technologies were evaluated, including pushbuttons, rotary encoders, toggle switches, and capacitive touch interfaces.

3.12.1 Pushbutton Interface

Pushbuttons are one of the most commonly used input devices in embedded systems due to their simplicity and reliability. These devices provide a momentary digital input signal that can be directly interfaced with a microcontroller using a pull-up or pull-down resistor configuration.

Pushbuttons are well suited for discrete control actions such as initiating a scan or resetting the system. Their mechanical design provides tactile feedback, allowing users to confirm actuation even in environments where visual attention is limited.

Additionally, pushbuttons are highly robust in electrically noisy environments and are not affected by external interference or environmental conditions such as moisture or debris. Their compatibility with gloved operation makes them particularly suitable for industrial applications.

However, pushbuttons are limited in functionality, as each button corresponds to a single input action. Multiple buttons may be required to support additional system functions.

3.12.2 Rotary Encoder Interfaces

Rotary encoders provide input through rotational motion and generate digital pulses corresponding to angular displacement [46]. These devices are commonly used in applications requiring parameter adjustment or menu navigation.

Rotary encoders can integrate both rotational input and pushbutton selection functionality, allowing multiple parameters to be controlled with a single device. However, they require more complex signal processing, including interrupt handling or polling-based decoding.

For the IRIS system, which primarily requires simple and discrete control actions, the additional complexity associated with rotary encoders is not justified. Their use would increase both hardware and software design complexity without providing meaningful benefits.

3.12.3 Toggle Switch Interface

Toggle switches provide a latching input mechanism that maintains a fixed ON or OFF state. These devices are commonly used for power control or mode selection in industrial systems.

While toggle switches offer high mechanical durability and clear state indication, they are not suitable for momentary control actions such as scan triggering or system reset. Additionally, their larger physical size and limited flexibility reduce their effectiveness in compact embedded designs.

As a result, toggle switches do not fully meet the functional requirements of the IRIS system.

3.12.4 Capacitive Touch Interfaces

Capacitive touch interfaces detect user input through changes in capacitance and are commonly used in consumer electronics due to their flexibility and lack of mechanical components.

These interfaces allow multiple virtual inputs to be implemented without increasing hardware complexity. However, capacitive touch systems are sensitive to environmental conditions such as electromagnetic interference, moisture, and user interaction through gloves.

In industrial environments, particularly those involving high-voltage equipment, capacitive touch interfaces may experience unreliable operation due to electrical noise. Additionally, the inability to reliably operate with insulated gloves makes them unsuitable for the IRIS system.

3.12.5 Physical UI Technology Comparison

A comparison of the evaluated physical user interface technologies is summarized in Table 3.18.

Table 3.19 – Physical UI Technology Comparison Table

Feature	**Pushbutton**	**Rotary Encoder**	**Toggle Switch**	**Touch Interface**
Input Type	Momentary digital	Incremental rotation + push	Latching	Capacitive
Complexity	Low	Moderate	Low	High
Environmental Robustness	High	High	Very High	Low
Power Consumption	Very Low	Low	Very Low	Moderate
Cost	Low	Medium	Low	Higher
Suitability	High	High	Moderate	Low

While each of these technologies provides viable solutions for user interaction in embedded systems, pushbuttons offer the best combination of simplicity, reliability, and compatibility with the IRIS system's operational constraints.

3.12.6 UI Approach Selection

Based on the comparison of available technologies, pushbuttons were selected as the physical user interface for the IRIS system.

Pushbuttons provide a simple and reliable method for implementing discrete control actions, such as system startup, scan initiation, and system reset. Their robustness in electrically noisy environments and compatibility make them well suited for industrial applications.

Additionally, pushbuttons require minimal hardware and software complexity, reducing overall system design effort while maintaining reliable operation.

3.12.7 Component-Level Comparison

Following the selection of pushbuttons as the preferred UI technology, several commercially available tactile switches were evaluated based on electrical compatibility, mechanical reliability, and ease of integration with the IRIS system.

QTETAK 6 mm x 6 mm Tactile Pushbutton

One candidate for the physical user interface is the QTETAK tactile pushbutton assortment kit, which includes 6 mm × 6 mm momentary tactile switches with multiple actuator heights [49]. These switches are widely used in embedded systems and prototyping applications due to their compact size and low cost.

The switches operate as normally open (NO) devices, closing the circuit only when pressed, making them suitable for discrete control actions such as scan triggering and system reset. They are compatible with low-voltage digital systems such as the ESP32-S3 and can be easily interfaced using standard pull-up resistor configurations.

The switches are designed for through-hole mounting, allowing straightforward integration into both breadboard prototypes and printed circuit boards. Additionally, the availability of multiple actuator heights within the kit provides flexibility in mechanical design, particularly when aligning the buttons with an enclosure or front panel.

However, as low-cost commercial components, these switches have some limitations. They are not sealed and therefore offer limited protection against dust and moisture. Additionally, their long-term durability may be lower than that of industrial-grade pushbuttons, particularly in harsh operating environments.

Despite these limitations, the QTETAK tactile switches provide a simple, cost-effective, and widely available solution, making them a strong candidate for the IRIS system.

E-Switch PV6 Series (PV6F24011) Panel-Mount Pushbutton Switch

Another candidate is the E-Switch PV6 series (PV6F24011) panel-mount pushbutton switch, which is commonly used in industrial control systems [50]. This switch is designed for mounting through an enclosure panel and offers significantly higher mechanical durability and environmental protection compared to small tactile switches.

Panel-mount pushbuttons often include features such as larger actuator surfaces, improved tactile feedback, and optional sealing for protection against dust and moisture. These characteristics make them well suited for long-term deployment in industrial environments.

However, the PV6 series introduces several drawbacks for the IRIS system. Its larger physical size, requiring a 16 mm panel cutout, makes it less suitable for compact embedded designs. It also requires additional mechanical integration into the enclosure, increasing design complexity. Furthermore, the cost of the switch is significantly higher than that of small tactile pushbuttons.

While panel-mount switches provide superior durability and environmental protection, their increased size, cost, and integration requirements make them less practical for the IRIS system's prototype-level design.

Omron B3U Series (B3U-1000P) SMD Tactile Switch

A third candidate is the Omron B3U series (B3U-1000P) surface-mount tactile switch, which is commonly used in compact electronic devices requiring high-density PCB layouts [51].

SMD tactile switches provide similar electrical functionality to through-hole pushbuttons and can be integrated into automated manufacturing processes. Their compact size makes them attractive for space-constrained designs.

However, SMD switches introduce additional complexity during prototyping and assembly. They require precise soldering techniques and are less convenient for iterative design and testing compared to through-hole components. Additionally, their smaller actuator size may reduce usability.

Due to these limitations, SMD tactile switches are less suitable for the IRIS system during the prototyping and development phase.

3.12.8 Pushbutton Comparison

Table 3.20 – Pushbutton Comparison Table

Feature	**QTETAK Tactile Switch**	**E-Switch PV6F24011**	**Omron B3U-1000P**
Mounting Type	Through-hole	Through-hole	Surface-mount
Voltage Rating	12 V DC	36 V DC	12 V DC
Current Rating	50 mA	2 A	50 mA
Actuation Force	~160 – 260 gf	~3 – 5 N	~1.6 N
Size	6mm x 6 mm	16 mm panel	~3 x 2 mm
Cost	Very Low	High	Low
Ease of Prototyping	High	Low	Moderate
Mechanical Robustness	Moderate	Very High	Moderate

Suitability	High	Moderate	Moderate

While each of these options provides a viable solution for implementing a physical user interface, the QTETAK tactile switches offer the best balance of cost, simplicity, and ease of integration for the IRIS system.

3.12.9 Pushbutton Selection

Based on the comparison presented in Table 3.16, the QTETAK 6 mm × 6 mm tactile pushbuttons were selected as the physical user interface components for the IRIS system.

These switches provide all necessary functionality for implementing discrete user input actions, including system initialization, scan triggering, and system reset. Their through-hole design simplifies prototyping and PCB assembly, while their compact size allows flexible placement within the system enclosure.

Although panel-mount switches offer improved durability and environmental protection, these features exceed the requirements of the IRIS system, which is intended for prototype development and demonstration rather than long-term industrial deployment. Similarly, while SMD switches offer a smaller footprint, their increased assembly complexity and reduced usability make them less suitable for this application.

The QTETAK tactile switches provide a cost-effective and practical solution while maintaining acceptable performance and reliability for the intended use of the IRIS system.

3.13 Storage Selection

Local data storage is an important component of the IRIS system, enabling the temporary and persistent storage of thermal scan data, system logs, and configuration parameters. While the primary method of data transmission is through wireless communication, local storage provides redundancy in situations where network connectivity is unavailable or unstable. This ensures that collected thermal data is not lost and can be retrieved or transmitted later.

In addition to data logging, local storage supports buffering of thermal image data prior to transmission, allowing the system to manage variations in wireless throughput and maintain consistent operation. It also enables storage of system configuration settings, such as calibration parameters and operational modes, which must persist across power cycles.

The selected storage solution must be compatible with the ESP32-S3 microcontroller and integrate seamlessly with its available communication interfaces. Key selection criteria include storage capacity, read and write speed, interface compatibility (e.g., SPI or

SDIO), physical size, power consumption, and cost. The storage medium must also be sufficiently robust to handle frequent write operations associated with continuous thermal data acquisition.

To determine the most appropriate solution, several storage technologies were evaluated and compared based on these criteria.

3.13.1 Internal Flash Memory

The ESP32-S3-WROOM-1 microcontroller includes integrated flash memory, typically ranging from 4 MB to 16 MB [39], which is primarily used for storing firmware, program data, and system resources. This internal flash is directly accessible by the microcontroller and does not require additional hardware or external interfaces, making it a convenient and low-complexity storage option for embedded applications.

In the IRIS system, internal flash memory can be utilized for storing small amounts of non-volatile data, such as configuration parameters, calibration constants, and system settings that must persist across power cycles. Its tight integration with the microcontroller allows for fast access times and simplified software implementation.

However, internal flash memory presents several limitations when considered for thermal data logging. First, the available storage capacity is limited and must be shared with the system firmware, reducing the amount of space available for user data. Second, flash memory has a finite number of write and erase cycles, making it less suitable for applications involving frequent data logging, such as continuous thermal scanning. Third, the memory is not removable, which prevents easy data extraction or transfer without additional communication steps.

Due to these constraints, internal flash memory is not sufficient as the sole storage solution for the IRIS system. While it remains useful for storing configuration and low-frequency data, an external storage solution is required to support reliable and scalable logging of thermal scan data.

3.13.2 SD Card (MicroSD) Storage

MicroSD card storage is a widely used solution in embedded systems for high-capacity, removable data storage. MicroSD cards provide storage capacities ranging from a few gigabytes to hundreds of gigabytes, making them well-suited for applications involving continuous data logging, such as thermal imaging systems.

In the IRIS system, a MicroSD card can be interfaced with the ESP32-S3 microcontroller using the SPI or SDIO communication protocols. This allows for efficient read and write operations while maintaining compatibility with existing hardware interfaces. The relatively high data transfer rates of MicroSD cards enable the storage of thermal scan data in real time, supporting continuous operation without data loss.

One of the primary advantages of MicroSD storage is its removability, which allows data to be easily extracted and analyzed on external devices without requiring wireless transmission. This is particularly beneficial in scenarios where network connectivity is unavailable or when large datasets must be reviewed offline. Additionally, MicroSD cards are low-cost, compact, and widely available, making them a practical choice for embedded system design.

However, MicroSD storage introduces additional hardware complexity compared to internal flash memory, requiring a card socket and interface circuitry. File system management, such as FAT32 implementation, also increases software complexity. Despite these considerations, the significant advantages in storage capacity, flexibility, and data accessibility make MicroSD storage a strong candidate for the IRIS system.

3.13.3 External EEPROM / FRAM Storage

External EEPROM and FRAM devices provide non-volatile storage solutions that are commonly used in embedded systems for storing small amounts of persistent data. These devices typically interface with microcontrollers using I²C or SPI communication protocols and offer reliable data retention with low power consumption.

In the IRIS system, EEPROM or FRAM could be used to store configuration data, calibration parameters, or system logs that require high reliability and frequent updates. FRAM devices, in particular, offer significantly higher write endurance compared to traditional EEPROM, making them suitable for applications involving frequent write cycles.

However, these storage technologies are limited in capacity, typically ranging from a few kilobytes to a few megabytes, which makes them unsuitable for storing large datasets such as thermal scan images. Additionally, while FRAM provides faster write speeds and higher endurance, it comes at a higher cost per bit compared to other storage options.

Table 3.21 – Comparison of Non-Volatile Storage Options

Feature	**Internal Flash Memory**	**MicroSD Card Storage**	**EEPROM / FRAM Storage**
Typical Capacity	4–16 MB	GB to hundreds of GB	KB to a few MB
Removability	No	Yes	No
Interface	Internal	SPI / SDIO	I²C / SPI
Read/Write Speed	Fast	Moderate to High	Moderate (FRAM faster)
Write Endurance	Limited	Moderate	Very High (FRAM)

Data Logging Capability	Limited	Excellent	Poor
Hardware Complexity	Very Low	Moderate	Low
Software Complexity	Low	Moderate (file system)	Low
Cost	Very Low	Low	Moderate (per bit)
Suitability for IRIS	Limited	Highly Suitable	Limited

Due to their limited storage capacity, external EEPROM and FRAM devices are not appropriate as primary storage solutions for the IRIS system. Instead, they are better suited for supplementary roles, such as storing configuration data that requires high write endurance and reliability. Given the storage requirements of the IRIS prototype and the emphasis on system simplicity and integration, these technologies are not selected as the primary storage method.

Based on this evaluation, the internal flash memory of the ESP32-S3-WROOM-1 provides the most suitable balance of simplicity, reliability, and seamless integration for the IRIS system. While it offers lower storage capacity compared to MicroSD solutions, it is sufficient for storing buffered thermal scan data, system logs, and configuration parameters within the expected operational scope of the prototype. The elimination of external storage hardware reduces overall system complexity, minimizes PCB design challenges, and improves robustness by avoiding removable components. Additionally, direct access to internal flash enables faster data handling and simplified firmware implementation without the need for file system management. Therefore, internal flash memory is selected as the primary storage solution for the IRIS prototype.

3.14 Charger Selection

The IRIS system is designed to operate as a battery-powered embedded device to enable flexible deployment in industrial environments. However, due to safety regulations imposed on senior design projects, the implementation of onboard lithium battery charging circuits is not permitted.

Specifically, lithium-based batteries may not be charged within the system, and all charging must be performed using commercially available external chargers. This restriction is based on safety considerations, as the highest risk of lithium battery failure occurs during the charging process.

Battery charging circuits regulate both current and voltage during the charging process and incorporate protection mechanisms for safe operation [34].

As a result, the IRIS system power architecture must be designed to operate from a pre-charged battery while also supporting operation from an external wall adapter when available. Instead of implementing an onboard charging circuit, the design focuses on safe battery integration, power delivery, and seamless transition between battery and external power sources.

3.14.1 Linear Charger ICs

Linear charger integrated circuits are commonly used for charging single-cell lithium-ion batteries due to their simplicity and low component count. These devices regulate charging current and voltage using a linear control element and are widely used in portable electronics. Unlike simple power converters, battery charging systems require multiple control loops to regulate both current and voltage while managing dynamic interactions between the input source, battery, and system load [34].

However, the use of linear charging circuits is explicitly prohibited in the IRIS system due to project safety constraints. Implementing such circuits would introduce risks associated with improper charging, thermal runaway, and potential battery failure.

3.14.2 Switching (Buck) Charger ICs

Switching charger integrated circuits provide higher efficiency compared to linear chargers by using high-frequency switching regulators to control the charging process. These devices are typically used in systems requiring higher charging currents or improved thermal performance.

Despite their advantages, switching charger circuits are also prohibited for use in the IRIS system. The increased design complexity and associated safety risks during battery charging make them unsuitable under the project constraints.

3.14.3 Power Management ICs (PMICs)

Power management integrated circuits (PMICs) can integrate battery charging, voltage regulation, and system power management into a single device. These components are commonly used in advanced embedded systems to manage multiple power domains.

However, PMICs that include battery charging functionality are not permitted within the IRIS system design. The inclusion of charging capability, even as part of an integrated solution, violates project safety requirements and would prevent design approval.

3.14.4 Charger Technology Comparison

A comparison of common battery charging technologies is summarized in Table 3.22.

Table 3.22 – Charger Technology Comparison Table

Feature	**Linear Charger IC**	**Switching Charger IC**	**PMIC**

Efficiency	Low–Moderate	High	High
Design Complexity	Low	Moderate–High	High
External Components	Minimal	Inductor + passives	Moderate
Charging Capability	Yes	Yes	Yes
Allowed in IRIS	No	No	No

While each of these technologies provides viable solutions for battery charging in general embedded systems, none are permitted for use in the IRIS project due to safety restrictions. As a result, an alternative approach that eliminates onboard charging must be adopted.

3.14.5 Selected Charging Approach

Based on the project constraints, no onboard battery charging technology is implemented in the IRIS system. Instead, the system is powered by a commercially manufactured portable lithium-ion battery bank that is charged externally using its manufacturer-supplied AC/DC wall charger. This approach eliminates all onboard charging circuitry from the IRIS PCB while ensuring that all charging operations are performed by a certified, purpose-built charger designed specifically for the selected battery pack.

The selected battery pack is the Talentcell PB006B3 portable 12 V / 5 V lithium-ion battery bank (see Section 3.13.5) [52]. Because this product ships as a complete consumer power bank, the manufacturer includes a matched 12.6 V / 1 A AC/DC wall charger in the package. Charging the pack therefore requires no additional third-party charger and no custom circuitry. The IRIS system operates exclusively from the pre-charged battery bank during field deployment and from a DC barrel jack wall adapter during stationary bench use.

3.14.6 External Charging Solution

Because onboard charging circuits are not permitted, all charging of the IRIS battery pack is performed by the external AC/DC wall charger that is bundled with the Talentcell battery bank. Commercial chargers that are packaged with their target battery pack are factory-matched to the pack's cell configuration, chemistry, and protection circuitry, and are tested and certified as a complete system by the manufacturer. This provides proper current and voltage regulation, thermal protection, and fault detection without any design effort on the part of the IRIS team.

Using the manufacturer-supplied charger eliminates the risks associated with custom charging circuit design, including improper charge termination, thermal runaway, and overcurrent conditions. It also eliminates the selection risk and reliability variability associated with third-party universal chargers, since no mismatch between charger and pack is possible. This approach ensures compliance with project safety requirements while leveraging a reliable, industry-proven charging solution.

Additionally, the included charger simplifies the system architecture by removing the need for any charging circuitry or charger procurement, allowing the design to focus on power delivery and system operation rather than battery charging management.

Talentcell 12.6 V / 1 A AC/DC Wall Charger (Included)

The charger supplied with the Talentcell PB006B3 battery pack is a 12.6 V / 1 A constant-voltage AC/DC wall adapter specifically matched to the pack's three-series (3S) lithium-ion cell configuration [52]. A 12.6 V charge voltage corresponds to the fully charged state of a 3S lithium-ion stack (4.2 V × 3 = 12.6 V), ensuring that the pack is charged to its full rated capacity without exceeding the safe per-cell upper voltage limit. The 1 A charge rate is a slow-charge profile that completes a full charge in approximately 6--7 hours for the 6000 mAh pack, which improves long-term cycle life compared with aggressive fast-charging profiles.

The charger interfaces with the battery pack through the same DC5521 barrel connector used by the pack's 12 V output port, and charging is initiated simply by plugging in the charger with the pack's power switch in the appropriate position. An LED indicator on the charger transitions from red to green when the pack reaches full charge, providing simple end-of-charge feedback without requiring user intervention to terminate charging. The pack itself incorporates internal over-charge protection, over-discharge protection, and short-circuit protection circuitry, ensuring safe operation even in the event of charger or user error.

Because the charger is factory-matched to the battery pack, no comparison of third-party chargers is required, and no selection trade-off between charging accuracy, protection thresholds, or connector compatibility must be evaluated. All such considerations are handled internally by the manufacturer.

3.14.7 Selected Charger

The charger selected for the IRIS system is the 12.6 V / 1 A AC/DC wall charger supplied as part of the Talentcell PB006B3 battery bank package. This selection follows directly from the selection of the battery bank itself: because the Talentcell product ships as a complete consumer power bank with a factory-matched charger, no separate charger selection or procurement is required.

This approach offers several advantages over selecting a third-party universal charger. First, it eliminates the risk of mismatch between the charger's output voltage or termination behavior and the battery pack's internal cell configuration, which is a known failure mode for generic chargers used with multi-cell packs. Second, it reduces project cost by avoiding the purchase of a separate charger. Third, it simplifies the bill of materials and user documentation, since the battery and charger are a single integrated product. Finally, it guarantees compliance with project safety constraints, because all charging is performed by a certified commercial charger operating on its intended battery pack rather than by any onboard or custom-selected circuitry.

Therefore, the included Talentcell 12.6 V / 1 A AC/DC charger is adopted as the charging solution for the IRIS system, balancing safety, simplicity, and cost requirements without the need for additional charger evaluation.

3.15 Power Supply Design and Selection

The power subsystem is responsible for providing stable and reliable power to all components within the IRIS system, including the microcontroller, sensors, display, and motor system. Because the system includes sensitive measurement components, careful consideration must be given to both power source selection and voltage regulation. The design must ensure consistent operation, low electrical noise, and sufficient power capacity while maintaining simplicity and cost-effectiveness.

3.15.1 Power Distribution Requirements

To determine the overall power requirements of the system, each major component and its operating voltage must be considered. The system includes both low-power digital components and higher power components such as motors.

Table 3.23 – Power Distribution Table

Component	**Supply Voltage**	**Typical Current**	**Power Consumption**	**Description**
ESP32 MCU	3.3 V	200 mA	0.66 W	Main processing and communication unit
LCD Display	5 V	25 mA	0.125 W	User feedback and status display
Temperature Sensor	3.3 V	0.4 mA	0.00132 W	Environmental temperature monitoring
Accelerometer	3.3 V	1 mA	0.0033 W	Vibration detection
Stepper Motor (2×)	5 V	200 mA each	2.0 W total	Scanning mechanism
Motor Driver (2×)	5 V	10 mA	0.05 W	Motor control circuitry

3.15.2 Power Budget Analysis

Before selecting a battery, an estimated system power budget was developed to determine the minimum energy capacity required for the four-hour runtime specification.

Component-level current consumption values were drawn from manufacturer datasheets where available.

The two 28BYJ-48 stepper motors represent the dominant power consumers in the IRIS system. Each motor operates at 5 V with a coil resistance of 50 Ω per phase [29]. In the half-step drive sequence used by the ULN2003 driver, two phases are energized simultaneously at each step, drawing approximately 100 mA per active phase. With two phases energized per motor, each motor draws approximately 200 mA at 5 V, or 1.0 W per motor. With two motors operating simultaneously during a raster scan with one driving the horizontal axis and one driving the vertical axis, combined motor power draw is approximately 2.0 W during active scanning. It should be noted that during each scan row, only the horizontal motor steps continuously while the vertical motor holds position, and between rows the roles reverse. This duty cycle behavior means average motor power draw is lower than the simultaneous worst-case figure.

The ESP32-S3 microcontroller draws a typical current of 240 mA at 3.3 V during 802.11b Wi-Fi transmission, and approximately 95–100 mA during Wi-Fi receive operations [39]. During normal monitoring operation, the ESP32 alternates between active scanning control, data processing, and periodic Wi-Fi transmission. Using a typical active current of 190 mA at 3.3 V as a conservative estimate for mixed-mode operation, the ESP32 contributes approximately 0.63 W to the system power budget.

The TD2X thermopile detector is a passive SMD sensor that generates a voltage output proportional to incident infrared radiation without requiring an active bias current [38]. Its power consumption is negligible and is not included as a significant contributor to the system power budget. The remaining components, the LCD1602 display, MCP9808 temperature sensor, accelerometer, and ULN2003 driver boards contribute an estimated combined draw of approximately 0.5 W or less based on typical values from their respective datasheets.

Table 3.24 – Power Budget Table

Component	**Voltage**	**Typical Current**	**Power**
28BYJ-48 stepper motor ×2 (2 phases active each)	5 V	200 mA × 2	2.0 W
ESP32-S3 (mixed Wi-Fi active mode)	3.3 V	~190 mA	0.63 W
LCD1602 display	5 V	~25 mA	0.125 W
MCP9808 temperature sensor	3.3 V	~0.4 mA	negligible
Accelerometer	3.3 V	~1 mA	negligible
TD2X thermopile detector	— (passive)	negligible	negligible
ULN2003 driver boards ×2	5 V	~10 mA	0.05 W
Estimated Total	—	—	**~2.8 W**

At 2.8 W over a four-hour operating period, the minimum energy requirement is approximately 11.2 Wh. This figure establishes the minimum battery capacity the IRIS

system requires and is used as the basis for battery chemistry selection and cell sizing in the sections that follow.

3.15.3 Energy Source Technology Comparison

Several power source options were considered for the IRIS system, including battery power, Power over Ethernet (PoE), and external wall adapters supplied through a DC barrel jack.

Battery power provides portability and the ability to operate the IRIS system in locations where mains power is unavailable. A rechargeable battery pack allows the system to be deployed independently, supporting the monitoring use cases described in the system requirements. The primary limitation of battery power is finite operating time, which must be managed through careful capacity sizing and efficient power architecture. Power over Ethernet allows both power and data to be delivered over a single Ethernet cable. While useful in fixed industrial installations, PoE requires additional hardware including a PoE splitter or controller, increases system cost, and constrains deployment to locations with Ethernet infrastructure. This flexibility limitation makes PoE unsuitable as the primary power source for a portable thermal scanning system.

A DC barrel jack wall adapter converts AC mains power to a regulated DC voltage and provides continuous, uninterrupted power without capacity constraints. These adapters are widely available, cost-effective, and simple to integrate into embedded systems. While a wall adapter cannot support mobile or infrastructure-independent deployment on its own, it provides a valuable secondary power input for bench use, and extended stationary monitoring.

Table 3.25 – Energy Source Comparison Table

Power Source	Complexity	Cost	Portability	Suitability
Battery	Moderate	Moderate	High	High
PoE	High	High	Low	Low
Wall Adapter (DC Barrel Jack)	Low	Low	None	Secondary

Based on this comparison, a rechargeable lithium-ion battery pack is selected as the primary power source for the IRIS system, with a DC barrel jack input retained as a secondary power input for stationary operation. This dual-input approach ensures that the system can operate portably in the field while also supporting continuous mains-powered operation when mobility is not required.

3.15.4 Battery Chemistry Comparison

With battery power selected as the primary energy source, the appropriate battery chemistry must be identified. The most commonly used rechargeable battery chemistries in embedded and portable systems are Nickel-Cadmium (Ni-Cd), Nickel-Metal Hydride (Ni-MH), and Lithium-Ion (Li-Ion). Each chemistry presents distinct trade-offs in energy density, cell voltage, self-discharge rate, cycle life, and cost [53].

Ni-Cd batteries are among the oldest rechargeable chemistries and are well understood. They offer excellent cycle durability of over 1,000 charge-discharge cycles and perform reliably at low temperatures. However, Ni-Cd cells exhibit a nominal cell voltage of only 1.25 V, requiring multiple cells in series to reach useful system voltages. More significantly, they are subject to the memory effect and a reduction in effective capacity if the battery is not periodically fully discharged. They also contain cadmium, a toxic heavy metal that is subject to increasing disposal and import restrictions in many jurisdictions [54]. These environmental and maintenance concerns make Ni-Cd unsuitable for the IRIS system.

Ni-MH batteries improve on Ni-Cd in several respects, offering approximately 30–40% higher capacity for the same physical size and eliminating the cadmium content. Their nominal cell voltage of 1.25 V is identical to Ni-Cd, meaning that the same number of series cells is required to reach a given system voltage. Ni-MH cells have a relatively high self-discharge rate of 20–30% per month at 20°C, which is a significant drawback for a device that may be stored between deployments [53]. Their gravimetric energy density of approximately 90 Wh/kg is substantially lower than that of Li-Ion, resulting in a heavier battery pack for an equivalent energy capacity. While environmentally preferable to Ni-Cd, Ni-MH does not offer the performance or energy density required to meet the IRIS system's four-hour runtime specification within a compact and lightweight form factor.

Li-Ion batteries offer the highest gravimetric energy density of the three chemistries at approximately 210 Wh/kg, nearly double that of Ni-MH, allowing a given energy requirement to be met with a significantly lighter and smaller cell [53]. Li-Ion cells operate at a nominal voltage of 3.6 V per cell, reducing the number of series cells needed to supply system-level voltages compared to Ni-based chemistries. Their self-discharge rate is the lowest of the three chemistries, typically 5–10% per month at 20°C, making them well suited for devices that may remain idle between uses. Li-Ion cells require a constant-voltage charging protocol and must include protection circuitry to prevent overcharge and over-discharge, as discharging below approximately 2.5 V can permanently damage the cell through internal electrode corrosion [53]. Despite these requirements, Li-Ion is now the dominant chemistry for portable embedded systems due to its superior energy density, low self-discharge, and charge-discharge efficiency.

Table 3.26 – Battery Chemistry Comparison Table

Characteristic	**Ni-Cd**	**Ni-MH**	**Li-Ion**
Nominal Cell Voltage	1.25 V	1.25 V	3.6 V
Gravimetric Energy Density	~50 Wh/kg	~90 Wh/kg	~210 Wh/kg
Volumetric Energy Density	~140 Wh/L	~180 Wh/L	~210 Wh/L
Self-Discharge (per month)	15–20%	20–30%	5–10%
Typical Fast Charge Time	~1 hour	~1 hour	~1–2 hours
Cycle Life	>1,000	~500	~500–1,000
Memory Effect	Yes	Minor	No
Environmental Concern	High (cadmium)	Low	Low
Relative Cost	Low	Moderate	High

Suitability for IRIS	Low	Low	High

Based on this comparison, Li-Ion is selected as the battery chemistry for the IRIS system. Its superior energy density minimizes the physical size and weight of the battery pack required to meet the four-hour runtime specification, its low self-discharge rate supports intermittent deployment scenarios, and its wide adoption in portable electronics ensures that compatible external charging solutions are widely available.

3.15.5 Battery Pack Selection

Following the selection of Li-Ion as the battery chemistry, specific battery products were evaluated to identify the most suitable option for the IRIS system. Early in the design process, the use of individual 18650 cells assembled into a custom two-cell series pack was considered. However, this approach would have required the team to source, assemble, and spot-weld the pack, integrate a separate battery management system (BMS) for over-charge and over-discharge protection, and procure and validate a separate external charger. Under the project's senior design safety constraints, any self-assembled multi-cell lithium pack also raises concerns regarding cell matching, solder joint reliability, and the absence of a manufacturer-certified enclosure.

For these reasons, the design was revised to use a commercially manufactured portable lithium-ion battery bank as a single integrated power source. A portable battery bank is a consumer product in which multiple lithium-ion cells, a protection circuit, output regulation, a status display, and an enclosure are all assembled and certified by the manufacturer. The pack is charged externally using a manufacturer-matched wall charger and connects to the IRIS PCB through a standard DC barrel jack, requiring no charging circuitry or BMS design on the IRIS board. This approach preserves all of the advantages of lithium-ion chemistry while fully satisfying the project's prohibition on onboard charging and reducing the risk and scope of the battery subsystem design.

The primary evaluation criteria for the battery pack were usable energy capacity, output voltage and current rating, output connector compatibility, included charger, physical form factor, and cost. The system power budget of approximately 2.8 W over four hours yields a minimum energy requirement of 11.2 Wh, which any candidate pack must exceed with sufficient margin to account for regulation losses, real-world variation in component power draw, and capacity degradation over the pack's cycle life.

Three commercially available portable lithium-ion battery banks were evaluated as candidates.

Anker PowerCore Slim 10000 (PowerCore 10K)

The Anker PowerCore Slim 10000 is a consumer-grade portable power bank rated at 10,000 mAh at a 3.7 V nominal cell voltage [55], corresponding to a total stored energy of approximately 37 Wh. It is built around a lithium-polymer cell stack and is engineered primarily for charging mobile devices such as smartphones and tablets. The unit provides three ports: a USB-C port that supports both 5 V / 3 A input and 5 V / 3 A output, a USB-A output port also rated at 5 V / 3 A, and a Micro-USB input port for legacy charging. Anker's proprietary PowerIQ and VoltageBoost technologies dynamically adjust output current to match the connected device's charging profile, with total output power ranging from approximately 7.5 W to 15 W. The pack also includes a trickle-charging mode intended for low-power devices such as earphones or Bluetooth speakers, activated by a double-press of the power button. Physically, the unit is one of the slimmer 10,000 mAh packs on the market, measuring 5.99 × 2.81 × 0.61 inches and weighing 8.6 oz, with a scratch-resistant housing certified to a 3.2 ft drop test. The pack retails for approximately $25.99 and is supplied with a USB-C to USB-C cable, though no AC wall charger is included in the package.

From a power-delivery standpoint, however, the Anker PowerCore 10K is not directly suitable for the IRIS system as currently architected. The fundamental limitation is that all output ports are 5 V only -- the pack provides no 12 V DC output. The IRIS power architecture specifies a 12 V DC barrel-jack input (DC5521) that is regulated down to the 5 V and 3.3 V system rails through the onboard buck converters, and both the two 28BYJ-48 stepper motors and the ULN2003 driver boards are specified to operate from a 5 V rail supplied by that regulator chain. Powering the IRIS system directly from the Anker pack would require either rearchitecting the PCB to accept a 5 V input (eliminating the 12 V-to-5 V buck stage and the barrel-jack input entirely) or inserting a 5 V-to-12 V boost converter between the pack and the existing input, which would introduce efficiency losses and defeat the purpose of using a pre-regulated pack. In addition, the combined worst-case system load of approximately 2.8 W nominal (with transient motor current spikes that can exceed the pack's 3 A per-port limit when both motors energize simultaneously at start-up) is close enough to the Anker's 15 W port ceiling that margin is limited. The pack also lacks a DC barrel-jack output, meaning no direct mechanical compatibility with the DC5521 input on the IRIS board, and Anker does not publish a specified discharge cutoff or protection behavior under sustained non-device loads (as opposed to intermittent phone charging), which introduces uncertainty in a continuous-draw application. Finally, because no AC wall charger is included, recharging the pack requires the user to supply their own USB-C charger rated at 5 V / 3 A or higher, partially offsetting the low unit cost.

The Anker PowerCore 10K is a well-regarded product for its intended application -- charging 5 V USB mobile devices -- and its 37 Wh capacity would comfortably exceed the IRIS four-hour runtime requirement if the electrical interface matched. However, its 5 V-only output, absence of a DC barrel-jack connector, and lack of an included wall charger make it incompatible with the current IRIS power architecture without significant redesign. For these reasons, the Anker PowerCore 10K is not selected for the IRIS system, and a 12 V DC output battery bank such as the Talentcell PB006B3 is retained as the preferred solution.

KU XIU S3 Qi2.2 Magnetic Power Bank (10,000 mAh)

The KU XIU S3 is a consumer-grade portable power bank rated at 10,000 mAh at a 3.7 V nominal cell voltage [56], corresponding to a total stored energy of approximately 37 Wh. Unlike conventional DC power banks, this product is designed primarily around the Qi2.2 wireless charging standard for MagSafe-compatible iPhones. Its dominant feature is a 25 W wireless charging surface on the top of the enclosure, secured to the target device by an array of MagSafe-compatible magnets, along with a built-in foldable kickstand that allows the pack to function as a charging-capable display stand in either portrait or landscape orientation. A built-in LED digital display shows battery percentage and charging status in real time. The pack is constructed around a solid-state lithium-ion cell chemistry, which the manufacturer states has passed needle-penetration safety testing and eliminates liquid electrolyte leakage at the material level. The unit measures 4.00 × 2.78 × 0.87 inches, weighs approximately 80 g (2.8 oz), and retails for approximately $62.99 with occasional promotional pricing near $56.69.

For wired connections, the KU XIU S3 provides a single integrated USB-C port operating at a nominal 5 V. This port serves as both the recharge input for the pack and the only available wired output. No DC barrel jack, no secondary USB-A port, and no selectable voltage rail (9 V, 12 V, or otherwise) are provided. No AC wall charger is included in the package; the user must supply their own USB-C charger and cable to recharge the unit. Manufacturer-published specifications focus almost exclusively on the wireless charging profile for iPhone models 12 through 17 and do not provide detailed wired output current curves or discharge cutoff behavior under continuous non-device loads.

These characteristics make the KU XIU S3 fundamentally incompatible with the IRIS power architecture. The IRIS system requires a 12 V DC input delivered through a DC5521 barrel jack, which is subsequently regulated to the 5 V and 3.3 V rails used by the motors, microcontroller, and sensors. The KU XIU S3 provides no 12 V output of any kind: its wireless output is usable only by devices with a MagSafe-compatible Qi2.2 receiver coil, which the IRIS enclosure and PCB do not possess, and its wired USB-C output is 5 V-only with no barrel-jack connector. Using this pack as the IRIS power source would therefore require both a mechanical adapter (USB-C to DC5521) and an electrical redesign of the IRIS input stage to accept 5 V directly or to boost 5 V up to 12 V, neither of which is within the scope of the current design. In addition, the primary feature set of the product - wireless charging, magnetic alignment, a kickstand, and a digital display - provides no value to a permanently enclosed embedded system that draws power through a fixed cable, meaning the user pays a price premium for capabilities that the IRIS system cannot use. At approximately $63, the pack is also nearly twice the price of the 6000 mAh Talentcell PB006B3 while providing roughly half the stored energy in a form factor optimized for an unrelated use case.

Although the solid-state cell chemistry is a genuinely interesting safety feature and the overall product quality appears acceptable for its intended market, the KU XIU S3 is designed as a MagSafe accessory for modern iPhones rather than as a general-purpose DC power source. For these reasons, the KU XIU S3 is not selected for the IRIS system, and the Talentcell PB006B3 is retained as the preferred battery pack.

Talentcell PB006B3 12 V / 5 V Lithium-Ion Battery Pack (6000 mAh)

The Talentcell PB006B3 is a purpose-built portable DC power bank rated at 6000 mAh at an 11.1 V nominal pack voltage, corresponding to a total stored energy of 66.6 Wh (equivalent to 18,000 mAh referenced to a 3.7 V single-cell basis) [52]. Unlike consumer power banks that are designed around USB charging profiles for mobile devices, the PB006B3 is specifically marketed toward the DIY and low-power equipment market -- LED strips, CCTV and IP cameras, 12 V amplifiers, modems, robotic telescopes, and similar 12 V DC loads -- which makes it directly suited to the electrical interface requirements of the IRIS system. The pack is constructed around a three-series (3S) lithium-ion cell stack assembled and certified by the manufacturer, and ships in a rectangular black enclosure measuring 5.1 × 3.0 × 1.0 inches and weighing approximately 300 g.

The pack provides two outputs: a primary 12 V DC output delivered through a DC5521 barrel jack (inner positive, outer negative), with an actual output voltage range of 12.6--9.0 V tracking the cell stack from full charge to cutoff, and a secondary 5 V USB-A output rated at up to 2 A [52]. The 12 V output is not strictly regulated; it follows the natural discharge curve of the 3S stack, which is fully acceptable for the IRIS system because the downstream buck converters on the IRIS PCB are specified to accept an input across this full voltage range and produce clean 5 V and 3.3 V rails regardless of pack state of charge. The DC5521 connector is a direct mechanical match for the barrel jack specified on the IRIS PCB as the secondary wall-adapter input, allowing the same physical interface to be used for either battery or mains operation. A five-LED fuel gauge on the enclosure displays pack state of charge in 20% increments, and a physical power switch isolates the output when the pack is not in use, which both prevents parasitic discharge during storage and eliminates the auto-off behavior common to USB-only power banks that can cause low-draw loads to be shed unexpectedly.

Protection circuitry integrated within the pack includes over-charge protection, over-discharge protection, and short-circuit protection, which fully satisfies the project's safety constraint prohibiting any onboard battery management or charging circuitry on the IRIS PCB. The pack ships with a matched 12.6 V / 1 A AC/DC wall charger -- sized correctly for the 3S cell configuration -- and a DC 1-female-to-2-male splitter cable, eliminating the need for separate charger selection, procurement, or evaluation [52]. The manufacturer provides an 18-month warranty. Talentcell has specialized in 12 V lithium-ion battery packs since 2001, and the PB006B3 is an Amazon's Choice product with a 4.7-star rating across more than 4,500 customer reviews, with reported multi-year service life (one reviewer reported eight years of continuous weekend use with only modest capacity fade) and consistent customer service support for warranty claims.

At the IRIS system power budget of approximately 2.8 W, the pack's 66.6 Wh of stored energy yields a theoretical runtime of approximately 23.8 hours -- nearly six times the four-hour minimum runtime requirement. Even after accounting for buck converter efficiency (typically 85--90%), transient motor current spikes, and progressive capacity fade over the pack's cycle life, the runtime margin remains well in excess of project requirements. At a unit cost of $32.99, the pack is also substantially less expensive than competing MagSafe and USB-PD consumer power banks, despite providing nearly twice the stored energy and the specific 12 V DC output format the IRIS system requires. For these reasons -- direct electrical compatibility with the IRIS 12 V input, DC5521 mechanical compatibility, integrated protection circuitry, included matched charger, generous runtime margin, and favorable cost -- the Talentcell PB006B3 is selected as the battery pack for the IRIS system.

Table 3.27 – Portable Battery Bank Comparison Table

Feature	**Talentcell PB006B3**	**Anker PowerCore Slim 10000**	**KU XIU S3 Qi2.2**
Chemistry	Lithium-Ion (3S stack)	Lithium-Polymer	Solid-State Lithium-Ion
Nominal Pack Voltage	11.1 V	3.7 V	3.7 V
Rated Capacity	6000 mAh (at 12 V)	10,000 mAh (at 3.7 V)	10,000 mAh (at 3.7 V)
Total Stored Energy	66.6 Wh	~37 Wh	~37 Wh
12 V DC Output	Yes (12.6--9.0 V, DC5521)	No	No
5 V Output	Yes (USB-A, up to 2 A)	Yes (USB-A + USB-C, 5 V / 3 A)	Yes (USB-C, 5 V only)
Wireless Output	No	No	Yes (Qi2.2, 25 W MagSafe)
Output Connector for IRIS	DC5521 (direct match)	USB-C / USB-A (incompatible)	USB-C only (incompatible)
Protection Circuitry	OCP / ODP / SCP	OCP / OTP (device-focused)	OCP (solid-state needle-pen. tested)
State-of-Charge Display	5-LED bar (20% increments)	4-LED bar	Digital LED percentage display
Physical Power Switch	Yes	No (auto-off)	No (auto-off)
Included Charger	12.6 V / 1 A AC/DC wall charger	None (cable only)	None (cable only)
Dimensions	5.1 × 3.0 × 1.0 in	5.99 × 2.81 × 0.61 in	4.00 × 2.78 × 0.87 in
Weight	~300 g	~244 g (8.6 oz)	~80 g
Warranty	18 months	18 months	12 months
Est. Runtime at 2.8 W	~23.8 h	~13.2 h (if interface matched)	~13.2 h (if interface matched)
Unit Cost	~$32.99	~$25.99	~$62.99

Suitability for IRIS	**High (selected)**	Low (5 V only, no barrel jack)	Low (MagSafe accessory, no 12 V)

Based on the comparison in Table 3.24, the Talentcell PB006B3 is selected as the battery pack for the IRIS system. Although the Anker PowerCore Slim 10000 and KU XIU S3 both offer nominal capacities of 10,000 mAh at the single-cell reference level, their stored energy of approximately 37 Wh is substantially less than the Talentcell's 66.6 Wh because both are built around single-cell 3.7 V architectures rather than a 3S stack. More critically, neither competing pack provides a 12 V DC output in any form: the Anker's three ports are all 5 V, and the KU XIU S3 offers only a 5 V USB-C port alongside its 25 W Qi2.2 wireless surface. Neither pack includes a DC5521 barrel-jack connector, meaning that using either as the IRIS power source would require both mechanical adaptation and an electrical redesign of the IRIS input stage.

The Talentcell PB006B3 is the only candidate that directly matches the IRIS electrical interface: its 12.6--9.0 V DC output through a DC5521 barrel jack is mechanically and electrically compatible with the system's existing input stage, and its secondary 5 V USB-A output provides a redundant auxiliary path if needed. The pack is also the only candidate that ships with a matched AC/DC wall charger, eliminating the need for separate charger selection and fully satisfying the project's prohibition on onboard charging circuitry. A physical power switch prevents the auto-off behavior common to USB-focused consumer power banks, which is particularly important for a low-draw application like IRIS where the system's nominal current consumption might otherwise be interpreted by the pack's control logic as a disconnected load. Finally, despite being the second-most-expensive option by a small margin over the Anker and roughly half the cost of the KU XIU, the Talentcell provides nearly twice the stored energy of either competitor and a runtime of approximately 23.8 hours at the IRIS power budget -- nearly six times the four-hour minimum requirement. For these reasons, the Talentcell PB006B3 is adopted as the battery pack for the IRIS system.

3.15.6 Voltage Regulation Technology Comparison

Because different components within the IRIS system require different supply voltages, voltage regulation is necessary to convert the 7.2 V nominal battery pack input to the appropriate levels for each subsystem. The system requires two regulated rails: a 5 V rail supplying the stepper motors, motor drivers, and LCD display, and a 3.3 V rail supplying the ESP32-S3 microcontroller, temperature sensor, accelerometer, and other low-power digital peripherals.

Several regulator topologies were considered for generating these rails, including linear regulators, switching regulators, and a hybrid approach combining both technologies. Linear regulators provide voltage regulation by dissipating the difference between input and output voltage as heat through a series pass transistor. They are simple to implement, require minimal external components, and produce very low output noise, making them well suited for sensitive analog and sensor circuits where supply cleanliness is critical. However, linear regulators become increasingly inefficient as the input-to-output voltage differential grows. Regulating directly from the 7.2 V battery pack down to 3.3 V through a linear regulator alone would result in a voltage drop of approximately 3.9 V. At the ESP32-S3's typical operating current of 190 mA, this would dissipate approximately 0.74 W as heat in the regulator, representing a significant and unnecessary efficiency loss for a battery-powered system.

Switching regulators use high-frequency switching and passive energy storage components, typically an inductor and output capacitor, to convert voltage with substantially higher efficiency than linear regulators. Rather than dissipating excess energy as heat, switching regulators transfer energy in discrete pulses controlled by a feedback loop, achieving typical efficiencies in the range of 70–90% depending on the input-to-output differential and load current. This makes them well suited for higher current loads such as the stepper motors and motor driver circuitry. The primary disadvantage of switching regulators is that their switching action introduces output voltage ripple and high-frequency noise, which can degrade the performance of sensitive analog measurement circuits if not adequately filtered or isolated from downstream sensitive components.

A hybrid approach uses a switching regulator for the primary voltage conversion from the battery pack input, followed by a linear regulator downstream to generate a clean, low-noise rail for sensitive subsystems. This configuration captures the efficiency advantage of switching regulation at the high-power conversion stage while preserving the low-noise output characteristics of linear regulation for components where supply quality is critical. Because the linear regulator's input is the already-regulated switching output rather than the raw battery voltage, its input-to-output differential is small, minimizing heat dissipation while retaining the noise suppression benefit.

Table 3.28 – Voltage Regulator Technology Comparison

Regulator Type	**Efficiency**	**Output Noise**	**Complexity**	**Best Suited For**
Linear Regulator	Low	Very Low	Low	Sensor and analog circuits
Switching Regulator	High	Moderate	Moderate	Motors, high-current loads
Hybrid Approach	High	Low	Moderate	Overall system

Based on this comparison, a hybrid regulation architecture is selected for the IRIS system. The LM2596 switching buck converter generates the 5 V rail directly from the 7.2 V battery pack, and the AMS1117-3.3 low-dropout linear regulator generates the 3.3 V rail from the 5 V bus. This limits the linear regulator's input-to-output differential to 1.7 V, substantially reducing its thermal dissipation compared to regulating directly from the battery while still delivering a clean, low-noise 3.3 V supply to the ESP32-S3 and sensitive peripherals.

3.15.7 Voltage Regulator Model Evaluation

Following the selection of a hybrid regulation architecture, specific regulator components were evaluated for each voltage rail. The primary evaluation criteria were input voltage compatibility with the 7.2 V battery pack, output voltage accuracy, output current capacity sufficient to supply all connected loads, efficiency, thermal performance, and integration complexity.

LM2596 (onsemi) 5 V Switching Buck Regulator
The LM2596 is a fixed-frequency step-down switching regulator capable of driving a 3 A load with a minimum number of external components [42]. It operates from an input voltage range of 4.5 V to 40 V, which comfortably accommodates the IRIS battery pack voltage range of approximately 8.4 V fully charged to 5.0 V at the low-voltage cutoff of the two series cells. The LM2596 switches at a fixed frequency of 150 kHz, which sets the sizing requirements for the external inductor and output capacitor. In the standard 5 V fixed-output configuration, the recommended external components consist of a 33 µH inductor, a 1N5822 Schottky catch diode, a 100 µF input capacitor, and a 220 µF output capacitor, all of which are widely available and low cost. The device includes internal thermal shutdown, activating at a junction temperature of 150°C, frequency foldback current limiting that reduces switching frequency to approximately 30 kHz under output short or overload conditions to limit average power dissipation, and an ON/OFF control pin that allows the regulator to be disabled by a logic-level signal when not required.

The 5 V rail in the IRIS system must supply the two 28BYJ-48 stepper motors at up to 200 mA each, the two ULN2003 driver boards at approximately 10 mA each, the LCD1602 display at approximately 25 mA, and the AMS1117-3.3 input at approximately 200 mA, for a combined worst-case draw of approximately 645 mA. This is well within the LM2596's 3 A continuous output rating, providing a comfortable current margin. The LM2596 is available in TO-220 and D2PAK packages, both of which support through-hole or surface-mount integration on the IRIS PCB. It carries a unit cost of approximately $1–$2 and is stocked by all major distributors, ensuring reliable availability throughout the project lifecycle.

One consideration with the LM2596 at 150 kHz is that its switching noise must be adequately filtered before reaching the AMS1117-3.3 input. The 5 V output capacitor specified in the datasheet application circuit, a 220 µF low-ESR electrolytic, provides the primary ripple filtering, and the AMS1117-3.3's 60 dB minimum ripple rejection at 120 Hz provides additional attenuation of any residual noise before it reaches the 3.3 V rail and the ESP32-S3.

AMS1117-3.3 (Advanced Monolithic Systems) 3.3 V Linear Post-Regulator
The AMS1117-3.3 is a fixed-output low-dropout linear regulator providing a regulated 3.3 V output with a maximum output current of 1 A and a guaranteed dropout voltage of 1.3 V at 0.8 A load [41]. Fed from the LM2596's 5 V output, the AMS1117-3.3 operates with an input-to-output differential of 1.7 V, well above its 1.3 V maximum dropout voltage, ensuring full regulation is maintained across all expected load conditions. Line

regulation is specified at 0.5 mV maximum and load regulation at 15 mV maximum for the 3.3 V variant, providing stable supply voltage across the range of current demands presented by the ESP32-S3 and connected peripherals. Output noise is specified at 0.003% of output voltage RMS across 10 Hz to 10 kHz, and ripple rejection is 60 dB minimum at 120 Hz, both of which are well suited to the noise-sensitive analog measurement circuitry in the IRIS system. The device includes internal thermal shutdown activating at 165°C and current limiting under overload conditions.

The 3.3 V rail must supply the ESP32-S3 at approximately 190 mA during mixed-mode Wi-Fi operation, the MCP9808 temperature sensor at 0.4 mA, the accelerometer at 1 mA, and other low-power peripherals, for a combined worst-case draw of approximately 200 mA, well within the AMS1117's 1 A rating. At 1.7 V dropout and 200 mA load, the regulator dissipates approximately 0.34 W, which is thermally manageable in a SOT-223 surface-mount package with appropriate copper pour on the PCB as recommended in the AMS1117 datasheet thermal guidelines. The AMS1117-3.3 requires only a 22 µF tantalum output capacitor for stability under all operating conditions, and no protection diodes are required between the adjustment and output pins due to internal current-limiting resistors. It carries a unit cost of under $1 and is one of the most widely used 3.3 V regulators in ESP32-based embedded systems, with extensive application documentation and broad community validation.

Table 3.29 – Voltage Regulator Model Comparison

Specification	**LM2596**	**AMS1117-3.3**
Topology	Switching Buck	Linear LDO
Rail Generated	5 V	3.3 V
Input Voltage Range	4.5 V – 40 V	4.8 V – 15 V
Output Voltage	5 V (fixed)	3.3 V (fixed)
Maximum Output Current	3 A	1 A
Worst-Case IRIS Load	~645 mA	~200 mA
Switching Frequency	150 kHz	N/A
Dropout Voltage	N/A	1.3 V max at 0.8 A
Output Noise	Moderate (filtered)	0.003% VRMS
Ripple Rejection	N/A	60 dB min at 120 Hz
Efficiency	~73% (12 V in, 5 V out, 3 A)	~66% (1.7 V drop at 200 mA)
Thermal Shutdown	Yes (150°C)	Yes (165°C)
Key External Components	33 µH inductor, catch diode, 220 µF capacitor	22 µF tantalum output capacitor
Package	TO-220 / D2PAK	SOT-223 / TO-252 / SO-8
Approx. Unit Cost	~$1–$2	<$1
Suitability for IRIS	High	High

3.15.8 Selected Voltage Regulation

Based on the evaluation above, the IRIS system adopts a hybrid regulation architecture in which the LM2596 switching buck converter generates the 5 V rail directly from the 7.2 V nominal battery pack input, and the AMS1117-3.3 low-dropout linear regulator generates the 3.3 V rail downstream from the 5 V bus. This two-stage architecture distributes the total voltage conversion across two devices, each operating at a favorable point for its respective topology. The LM2596 handles the larger voltage drop from the battery pack with typical efficiency in the range of 70–75% at the IRIS operating point, minimizing energy loss and heat generation at the stage where it matters most for battery runtime. The AMS1117-3.3 then performs a small 1.7 V dropout conversion with a thermal dissipation of approximately 0.34 W, well within its continuous rating, while delivering a clean 3.3 V supply with 60 dB of ripple rejection that suppresses residual switching noise from the LM2596 before it reaches the ESP32-S3, the MCP9808 temperature sensor, and the TD2X thermopile detector. This arrangement ensures that the accuracy of analog measurements is not compromised by the switching activity of the primary regulation stage, while the overall power architecture remains efficient enough to meet the four-hour runtime specification from the two-cell Panasonic NCR18650GA battery pack.

3.15.10 Summary

The selected power supply design provides a balance between efficiency, reliability, and measurement accuracy. By using a wall adapter combined with a hybrid voltage regulation, the IRIS system can achieve a stable operation while minimizing noise and power loss. This design supports monitoring applications and aligns with the system's performance and cost requirements.

3.16 Wireless Communication Module Selection

Wireless communication is a core requirement of the IRIS system, enabling the transmission of reconstructed thermal image data and system status information to an external web-based monitoring interface. Because the system is intended for deployment in industrial environments where wired data connections may not be readily accessible, reliable wireless connectivity is essential for practical operation.

The selected wireless technology must support sufficient data throughput for transmitting thermal image frames, operate reliably within the range of a local area network, and integrate directly with the ESP32-S3-WROOM-1 microcontroller without requiring additional external hardware. To determine the most suitable solution, several wireless communication technologies were evaluated and compared based on data rate, operating range, power consumption, infrastructure requirements, and compatibility with the IRIS system architecture.

3.16.1 Wi-Fi (IEEE 802.11)

Wi-Fi is one of the most widely used wireless communication technologies and operates using the IEEE 802.11 standard [39]. It provides high data throughput, typically ranging from several megabits per second to hundreds of megabits per second depending on the standard and configuration. This makes Wi-Fi well suited for applications that require the transmission of moderate to large data payloads, such as image data or continuous monitoring streams.

Wi-Fi networks rely on existing local area network infrastructure, such as routers or access points, allowing devices to communicate directly with web servers or cloud-based interfaces. This capability aligns well with the IRIS system requirement to transmit thermal image data to a web-based monitoring platform.

However, Wi-Fi generally consumes more power than lower-data-rate wireless technologies and may be more susceptible to interference in congested network environments. Despite this, its high data rate and native support for internet-based communication make it a strong candidate for the IRIS system.

3.16.2 Bluetooth Low Energy (BLE)

Bluetooth Low Energy (BLE) is a short-range wireless communication technology designed for low power consumption and intermittent data transmission. BLE is commonly used in wearable devices, sensors, and low-power embedded systems where battery life is a primary concern.

BLE offers significantly lower data rates than Wi-Fi, typically on the order of hundreds of kilobits per second and operates over shorter communication distances. While BLE supports simple device-to-device communication, integration with web-based monitoring systems often requires an intermediary device such as a smartphone or gateway.

For the IRIS system, which must transmit thermal image data directly to a remote interface, BLE introduces limitations in both data throughput and system architecture, making it less suitable than higher-bandwidth alternatives.

3.16.3 Zigbee (IEEE 802.15.4)

Zigbee is a low-power wireless communication protocol based on the IEEE 802.15.4 standard and is commonly used in sensor networks and industrial monitoring systems. It is designed for low data rate applications, typically supporting data rates up to 250 kbps, and offers the advantage of mesh networking, which can extend communication range through intermediate nodes.

Zigbee is highly efficient in terms of power consumption and is well suited for distributed sensor networks where devices transmit small amounts of data periodically. However, Zigbee networks require dedicated coordinators or gateways to interface with standard IP-based networks.

Because the IRIS system requires direct transmission of thermal image data to a web-based interface and does not implement a mesh network architecture, Zigbee introduces unnecessary system complexity and insufficient data throughput for this application.

3.16.4 LoRa (Long Range)

LoRa is a long-range wireless communication technology designed for low-power, low-data-rate applications such as remote sensing and Internet of Things (IoT) deployments. It can achieve communication distances of several kilometers, making it suitable for geographically distributed systems.

However, LoRa operates at extremely low data rates, typically ranging from a few kilobits per second to tens of kilobits per second. This makes it unsuitable for applications requiring the transmission of image data or frequent updates.

While LoRa provides excellent range and power efficiency, the IRIS system operates within a local area environment and requires higher data throughput. As a result, LoRa does not meet the system's performance requirements.

3.16.5 Wireless Technology Comparison

A comparison of the evaluated wireless communication technologies is summarized in table below.

Table 3.30 – Wireless Technology Comparison Table

Feature	**Wi-Fi (802.11)**	**Bluetooth LE**	**Zigbee**	**LoRa**
Typical Data Rate	Up to 54+ Mbps	Up to 2 Mbps	Up to 250 kbps	0.3–50 kbps
Operating Range	~45 m (indoors)	~10–100 m	~10–100 m	Up to 15 km
Power Consumption	High	Very Low	Low	Very Low
Infrastructure Required	Router / Access Point	Gateway or Phone	Coordinator Node	LoRa Gateway
Native IP Network Support	Yes	No	No	No
ESP32-S3 Native Support	Yes	Yes	No	No

Wi-Fi provides the highest data rate of all evaluated technologies and natively supports IP-based network communication, allowing the IRIS system to transmit thermal image data directly to a web-based monitoring interface without requiring an intermediary device. While BLE is also natively supported by the ESP32-S3, its limited throughput and lack of direct IP connectivity make it unsuitable for image data transmission. Zigbee and LoRa both lack native ESP32-S3 support and do not meet the data rate requirements of the application. Therefore, Wi-Fi was selected as the wireless communication technology for the IRIS system.

3.16.6 Wireless Technology Selection

Based on the comparison of available wireless technologies, Wi-Fi was selected as the communication standard for the IRIS system. Wi-Fi provides sufficient data throughput for transmitting reconstructed thermal image frames to the external web interface, operates over existing local area network infrastructure, and supports direct IP-based communication without requiring an intermediary device or gateway.
No external wireless module is required for this implementation. The ESP32-S3-WROOM-1 selected in Section 3.6 includes an integrated Wi-Fi transceiver, allowing the IRIS system to establish wireless connectivity without additional hardware [39]. This simplifies the overall system design and reduces both component count and integration complexity.

3.17 Communication Protocol Selection

The communication subsystem of the project is responsible for enabling data transfer between the microcontroller, sensors, display, and external interfaces. Because the system integrates multiple hardware components with different data requirements, selecting appropriate communication protocols is critical to ensure reliable and efficient operation.

The IRIS project requires communication protocols for three main purposes:

- Sensor data acquisition (temperature and accelerometer)
- Peripheral control (display, motor control interfaces)
- Debugging and external interfacing (USB/UART communication)

To satisfy these requirements, several commonly used embedded communication protocols were evaluated, including UART, I²C, and SPI. Each protocol offers different advantages in terms of speed, complexity, and scalability.

3.17.1 UART Communication Protocol

Universal Asynchronous Receiver Transmitter (UART) is a simple serial communication protocol that allows data transfer between two devices using transmit and receive lines. UART does not require a shared clock signal, which simplifies implementation.

Advantages of UART include:

- Simple hardware implementation
- Minimal wiring (transmit, receive, and ground)
- Widely supported by microcontrollers

Disadvantages of UART include:

- Limited point-to-point communication
- Lower scalability for multiple devices
- Moderate data transfer speed

UART is commonly used for debugging, firmware programming, and communication with external devices such as PCs.

3.17.2 I²C Communication Protocol

Inter-Integrated Circuit (I²C) is a synchronous communication protocol that allows multiple devices to share a common two-wire bus consisting of a data line (SDA) and a clock line (SCL). Each device on the bus is assigned a unique address, allowing multiple peripherals to communicate with a single microcontroller.

Advantages of I²C include:

- Supports multiple devices on a single bus
- Requires only two communication lines
- Widely used for sensors and low-speed peripherals

Disadvantages of I²C include:

- Lower data transfer speed compared to SPI
- Susceptible to noise over longer distances
- Requires proper addressing and bus management

I²C is commonly used for connecting sensors, displays, and other low-speed devices in embedded systems.

3.17.3 SPI Communication Protocol

Serial Peripheral Interface (SPI) is a high-speed synchronous communication protocol that uses separate lines for data transmission and clock signals. Unlike I²C, SPI uses individual select lines for each connected device.

Some advantages of SPI are:

- High data transfer speed
- Full-duplex communication
- Reliable data transfer for high-speed applications

Some disadvantages of SPI are:

- Requires more wiring (multiple lines per device)
- Limited scalability without additional hardware
- More complex hardware implementation

SPI is typically used for high-speed communication with memory devices, displays, and high-performance sensors.

3.17.4 Wi-Fi Communication Protocol

WiFi (IEEE 802.11) is a wireless communication protocol that enables high-speed data transfer over a local area network or the internet [39]. In embedded systems, WiFi is commonly implemented using integrated modules or system-on-chip solutions such as the ESP32, which includes a built-in WiFi transceiver [39].

Advantages of WiFi include:

- High data transfer speeds over wireless connections
- Enables remote monitoring and IoT integration
- No additional wiring required between communicating devices
- Supports standard networking protocols (TCP/IP, HTTP, MQTT)

Disadvantages of WiFi include:

- Higher power consumption compared to wired protocols
- Susceptible to wireless interference and signal degradation
- Requires network configuration and security management
- Adds latency compared to direct wired communication

WiFi is commonly used for remote data logging, cloud integration, over-the-air (OTA) firmware updates, and IoT applications.

3.17.5 Communication Protocol Comparison

The key characteristics of each communication protocol are summarized in the table below.

Table 3.31 – Communication Protocol Comparison Table

Protocol	**Data Rate**	**Wiring Complexity**	**Multiple Device Support**	**Advantages**	**Disadvantages**
UART	Low-Moderate	Low	No	Simple, widely supported	Limited scalability
I²C	Moderate	Very Low	Yes	Multi-device support, minimal wiring	Slower than SPI
SPI	High	Higher	Limited	Fast and reliable	More complex wiring
WiFi	High	None (Wireless)	Yes	Remote access, IoT capable	Higher power consumption

Based on this comparison, each protocol serves a different role within the system. I²C is best for connecting multiple low-speed devices, UART is useful for debugging and external communication, and SPI is preferred for high-speed data transfer when required.

3.17.5 Selected Communication Protocols

The IRIS project utilizes a combination of communication protocols to meet the requirements of each subsystem.

I²C

I²C was selected as the primary communication protocol for the temperature sensor, accelerometer, and LCD display. These devices require relatively low data rates and benefit from the ability to share a communication bus.

The use of I²C reduces the number of required microcontroller pins and simplifies wiring, which is important for maintaining a compact and organized system design.

UART

UART is used for debugging, system monitoring, and firmware development. It allows direct communication between the microcontroller and a host computer, enabling real-time data observation and system diagnostics.

This protocol is particularly useful during development and testing, as it provides a simple and reliable interface for troubleshooting.

SPI

SPI was considered for applications requiring higher data transfer rates, such as external memory or advanced display modules. Although it is not heavily used in the current prototype, it remains available as an option for possible system expansion.

Wi-Fi

Wi-Fi was selected to enable wireless communication between the IRIS system and external networks or host devices. Since the ESP32 microcontroller includes an integrated Wi-Fi module, no additional hardware is required. Wi-Fi allows the system to transmit sensor data remotely, support over-the-air firmware updates, and integrate with IoT platforms or dashboards for real-time monitoring.

This is particularly valuable for deployment scenarios where physical access to the device is limited or where continuous remote monitoring is required.

3.17.6 Final Communication Architecture

The final communication architecture of the system is designed to balance simplicity, scalability, and performance. I²C serves as the primary protocol for sensor and peripheral communication, minimizing wiring complexity while supporting multiple devices. UART provides an interface for debugging and development, ensuring reliable system monitoring. SPI remains available for high-speed communication if required.

This combination of protocols ensures that the system can efficiently handle data acquisition, control, and communication tasks.

Table 3.32 – Final Communication Architecture Comparison Table

Subsystem / Component	**Communication Protocol**	**Interface Type**	**Purpose**
Temperature Sensor	I^2C	Digital	Environmental temperature measurement
Accelerometer	I^2C	Digital	Vibration and motion detection
LCD Display	I^2C	Digital	User feedback and system status display
ESP32 MCU (UART)	UART	Serial	Programming, debugging, and system monitoring
Motor Driver	GPIO	Digital	Stepper motor control signals
Thermopile	Analog to ADC (ESP32)	Analog Input	Infrared signal acquisition
ESP32 Wi-Fi Module	Wi-Fi (IEEE 802.11)	Wireless	Remote monitoring and IoT integration

3.18 Software System and Selection

The software subsystem of the project is responsible for controlling hardware components, processing sensor data, reconstructing thermal images, and communicating results to an external interface. Because the system integrates multiple hardware components and real-time operation, selecting appropriate software is critical.

The software must be capable of handling multiple tasks simultaneously, including motor control for scanning, data acquisition from sensors, signal processing, and wireless communication. To determine the most suitable software, several strategies and platforms were evaluated.

3.18.1 Software Coding Language

The most fundamental determination that must be made when designing the software is to find the appropriate coding language for the project. Coding languages differ in their libraries and specializations and leveraging one that will have the appropriate support and that will interface well with the chosen hardware will be key to constructing an effective software subsystem.

The specific kind of MCU and the choice between MCU and microcomputers greatly influences the determination of language. For example, in the case of a microcomputer, languages less traditionally associated with embedded systems (e.g. Java or Python) may have been investigated as strong candidates for building the software. This is due to their perceived ease of use along with the fact that a microcomputer would be better suited to their relatively more resource intensive executions. In the case of IRIS, the determination was made to go with an MCU; more specifically, the ESP32.

The choice of the ESP32 dramatically reduces the scope of research around viable languages to only a select few. It is worth noting that in the realm of embedded languages, C, and to a lesser extent C++, have primacy over other languages in the industry [9]. The two are greatly benefited by their own popularity, meaning library support will be much greater, even in the face of technically viable alternatives. Research concerning an appropriate fit for the ESP32 mainly focuses between the two of them although a third option, MicroPython, is investigated as well.

3.18.1.1 C Language

The C language is the favorite of the embedded world and has many qualities that make it a proper fit for IRIS. The ESP32 is limited in its size and processing capabilities and needs to operate swiftly and efficiently. Its memory is not large, meaning languages with a large overhead are greatly disadvantaged. The C language is incredibly performant and is relatively "low level" among high-level languages, meaning it does not have this issue. It is capable of providing access directly to GPIOs for interfacing with peripherals. It also provides manual memory management which, when done correctly, makes it incredibly efficient. Manual management means that C lacks an automatic memory management system or "garbage collector" that has its own overhead and can slow down the system. This absence keeps the system deterministic and makes it so that C works very well in real time operating considerations, maximizing responsiveness, effectively allocating the ESP32s memory and computing power, and working well with FreeRTOS and other libraries of the ESP-IDF development framework.

Not to mention the long and extensive history of C means that a plethora of libraries have been written for it. The MCU needs to interface with a variety of components, such as steppers and sensors, so the availability of public code means that compatibility and integration will be much smoother. There is also a human element in the determination of the best language. C is the coding language that the authors are most familiar with, creating a further incentive in favor of the language.

C is a strong contender, but it also comes with a host of disadvantages. Its lower-level nature that makes it lightweight and efficient also makes it difficult to code for, possibly harder to debug, and lack many of the conveniences of other languages. The absence of a garbage collector means that memory leaks are inevitable without proper coding, and C's pointers mean that segmentation faults are also an issue. With proper coding, C remains the best tradeoff of functionality and time investment.

3.18.1.2 C++

While not being a direct superset of C, C++ was developed independently as a fork and as such remains largely compatible with much of C and its libraries, and C code can frequently be made to run in C++. This means that many of the same points that apply to C can also be similarly applied to C++. It is also worthwhile to note that both the Arduino and ESP-IDF development frameworks for the ESP32 support C and C++ coding.

It can run both procedural and object-oriented code, but the advantages of C++ come in its object-oriented foundation. Object-oriented programming can also make maintaining and modifying a larger body of code easier by having different classes and objects. These can then inherit properties or give a more intuitive understanding of how the code works. This potential ease of use would pair nicely with the many subsystems of IRIS.

Where C++ falls short is that, while its use confers a number of benefits, object-oriented programming simply introduces complexity. It increases overhead to manage the features it offers, and it makes coding in it different and unfamiliar to traditional C. It is especially unappealing due to there being no C++ experience present in the group, meaning time would be spent on learning C++ that would be put to better use on C. The main determination with C++ then comes to whether the benefits of C++ outweigh the costs of learning and applying it.

3.18.1.3 MicroPython

One of the main advantages of Python is that it is a very high level, intuitive language to use. Python features like dynamic typing mean that the code more closely matches human logic rather than having to closely observe typing rules. Generally speaking, coding with Python is simpler than C and its onerous compiler. This comes at the cost of a larger amount of overhead. Python utilizes large amounts of memory to execute code, and some of the libraries can be very computationally intensive. MicroPython is an attempt to bring the advantages of traditional Python while slimming it down for specifically embedded work.

MicroPython's simplicity is appealing, yet it also offers unique libraries to enable low level functionality akin to C and C++. There also exists a decent amount of experience using Python among the authors, giving it further appeal.

One of the main drawbacks of MicroPython is that it is just not nearly used as much as the former two languages. While it does support most popular Python libraries [10], it has less support specifically in embedded. This means that libraries that do exist may not integrate well with MicroPython's optimizations, and libraries for specific hardware parts might vary in quality or availability. Another issue is that it does fully implement all new features from newer versions of Python, reducing compatibility with Python. Exploring MicroPython offers an interesting alternative in embedded programming but offers only marginal alternative benefits while possibly introducing more problems.

3.18.1.4 Language Comparison and Selection

Table 3.33 – Software Language Comparison Table

	C	**C++**	**MicroPython**
Use Case	Lower-level programming and low overhead	Object Oriented features and	Python Coding simplicity and familiarity
Library Availability	High	Highest	Moderate

Familiarity	High	Low	Moderate
Ease of Use	Low	Moderate	High

Overall, the choice of software development language was chosen to be C. C is familiar, reliable, and applicable. The added value of the other two languages did not compare to the potential challenges presented by each. C is more than capable of meeting IRIS' software requirements.

3.18.2 Software Development Framework

Now that a determination has been made on the language of the software, the code must now be written and supported in an integrated development environment (IDE). The IDE most fundamentally serves as a code editing and creation software. In that capacity, the IDE provides the toolchain and native support for the libraries that accompany it. The collection of libraries and code specifically supported by each IDE can be referred to as the environment's framework. It is the code in this framework that facilitates interfacing with the microcontroller through C. The choice of IDE is heavily dependent on the choice of framework, as generally the IDE will have the most ease of use with its corresponding framework.

The choice of ESP32 as a microcontroller further informs the choice of development framework. The two most popular frameworks are the ESP-IDF and Arduino frameworks. They both host robust libraries and have many drivers written for their respective ecosystems. The following sections will compare the two and ascertain how they meet the needs of IRIS.

3.18.2.1 Arduino Framework

The Arduino IDE and Framework are best understood as relatively intuitive and generalist in the realm of embedded systems. The Arduino Framework is not specific to the ESP32 but does offer support for ESP32 programming, and many ESP32 libraries utilize Arduino Framework code. Arduino offers a simplified API, meaning it is frequently used in hobbyist spaces due to it being more beginner friendly. This means that implementation and prototyping with Arduino is generally easier than its ESP-IDF counterpart. This straightforwardness comes at a cost, however, as it has limited lower-level coding capabilities due to the abstractions it uses. These in turn can make optimizations harder to implement. Arduino does run FreeRTOS, but it does not offer as robust real-time coding options as ESP-IDF. This can make coordinating the different sensors and transmitting data for IRIS potentially more difficult. The lack of granularity and emphasis on accessibility might not be worth the cost for a project on this scale.

3.18.2.2 ESP-IDF Framework

The ESP-IDF Framework is Espressif's official framework for the ESP32. The learning curve is steeper with the ESP-IDF but rewards the user with more control and flexibility. Being the official framework, the ESP-IDF can more fully support all of the microcontroller's capabilities and can better access low-level capabilities. It also features more robust real-time programming with its relatively more complex APIs. Another factor is that the ESP-IDF is generally more professional and used more widely in industry. This means that experience from this framework is more valuable even with similar qualifications. The last factor is that of experience. The authors are generally more experienced with the ESP-IDF framework from prior coursework and as such would spend less time grasping the fundamentals. The ESP-IDF framework offers a great level of control and provides many fitting features for IRIS, with the proper coding and support.

3.18.2.3 Framework Comparison and Selection

Table 3.34 – Software Language Comparison Table

	Arduino	**ESP-IDF**
Use Case	Easy to use and many very accessible libraries	Better compatibility with ESP32, better lower-level and RTOS programming
Library Availability	Many easy to use and popular libraries	Less libraries, Arduino ones must be ported
Familiarity	Moderate	High
Ease of Use	High	Moderate

The stronger real-time performance and the less restrictive programming design means that ESP-IDF is the natural choice as the selected development framework for the IRIS project. The authors have experience with prior FreeRTOS and ESP32 coding, making it an intuitive and powerful selection.

3.18.2.3 Arduino on the ESP-IDF Framework

While the selected framework for the bulk of the code and IDE are ESP-IDF, there remains a powerful integration with Arduino code in the form of library porting. Introducing Arduino as a library component seems simplistic and straightforward. It unlocks the expansive array of Arduino libraries and can aid the coding process by taking advantage of the simplified nature of Arduino code. Unfortunately, this approach introduces numerous problems. Most prominently, Arduino and ESP-IDF integration requires stability and compatibility between both versions and libraries in use. This means using an older compatible version of both, which introduces problems with the other dependencies of both frameworks. Finding compatible dated libraries for both introduces an entirely new layer of complexity. That is not to mention the tension inherent between the two coding ecosystems. Arduino's simplicity and relative lack of emphasis on RTOS principles means that it can block and interfere with other real time programs. Overall, Arduino integration was deemed to have more drawbacks and introduce more complexity than what it afforded to IRIS.

3.18.3 Web Development Technology and Selection

The data and processing that IRIS performs has so far been largely inaccessible to the end user. A physical UI does exist but does not meet the expectation of the IRIS project to reduce physical inspections. The accompanying web interface seeks to address this issue by offering a remote way to review thermal scan results, monitor system status, and receive hotspot alerts. The nature of the web application will be expanded upon in Chapter 7, but it is important to understand that the website will be hosted locally on a laptop accompanying the IRIS hardware. This laptop runs the HTTP server that the ESP32 communicates with over the local Wi-Fi network, receiving 16×16 thermal grids, system telemetry, and alert events, then serving these to a browser-based frontend for the end user.

Selecting the right web stack requires evaluating three distinct layers: the backend language and framework that handles incoming data from the ESP32 and serves the frontend, the frontend framework that renders the thermal heatmap and user interface in the browser, and the data storage mechanism that retains scan history and alerts. Each layer is evaluated separately in the following subsections.

3.18.3.1 Backend Language: Python

Python is a high-level, interpreted language with a long history in web development. Its primary appeal for IRIS lies in its simplicity, the team's existing familiarity with the language, and the maturity of its web frameworks. Frameworks such as Flask and FastAPI allow a functional HTTP server to be deployed in fewer than fifty lines of code, with built-in support for routing, JSON request handling, and template rendering. Python also has strong scientific computing libraries — NumPy, SciPy, and matplotlib — which are directly relevant to IRIS because they could be used to perform additional processing on the thermal grid (interpolation, filtering, statistical analysis) on the backend rather than the resource-constrained ESP32.

The main drawbacks of Python in a web context are runtime performance and concurrency. Python is slower than compiled languages, and its Global Interpreter Lock limits true parallelism in multithreaded applications. For IRIS, however, the data volume is small; each scan produces only 256 temperature values, and the request rate is low, so raw throughput is not a meaningful constraint. Python's familiarity to the team and its extensive ecosystem make it a strong candidate.

3.18.3.2 Backend Language: Go

Go is a compiled, statically typed language developed by Google specifically with networked services in mind. It offers excellent runtime performance, native concurrency through goroutines, and a built-in HTTP server in its standard library, meaning a Go web service can be deployed without external framework dependencies. Go binaries are also self-contained, simplifying deployment to the accompanying laptop.

Despite these technical advantages, Go presents practical drawbacks for the IRIS project. No team member has prior experience with Go, meaning a significant portion of the project timeline would be spent on language acquisition rather than feature development. Go's third-party web ecosystem, while growing, is also smaller than Python's or JavaScript's, particularly in areas such as templating, real-time WebSocket support, and authentication libraries. Given that IRIS has modest performance requirements that

Python or JavaScript can easily satisfy, Go's primary advantages are not meaningfully exploited by the project, while its primary cost — the learning curve — is fully incurred.

3.18.3.3 Backend Language: JavaScript (Node.js)

JavaScript is the native language of the web browser and, through the Node.js runtime, can also be used on the server. This single-language full-stack capability is its principal advantage: time invested in learning JavaScript pays off on both the frontend and backend, and data structures (most notably JSON) flow between layers without translation. Node.js is event-driven and non-blocking by design, which makes it particularly well suited to applications that maintain persistent connections or stream data in real time, exactly the pattern IRIS needs when the ESP32 pushes new thermal grids and the frontend updates the displayed heatmap without requiring a manual refresh.

Node.js also has the largest package ecosystem of any web platform through npm, providing well-maintained libraries for HTTP routing (Express), real-time bidirectional communication (Socket.IO), and database access (Sequelize, Prisma). The Express framework in particular is mature, well documented, and lightweight, making it a natural fit for a small project like IRIS.

The main drawback of Node.js for this team is unfamiliarity — none of the authors have significant prior experience with it. However, the cost of learning JavaScript is offset by the fact that the frontend will require JavaScript regardless of which backend language is chosen. Learning it once and using it on both ends is more efficient than learning Python (or Go) for the backend and JavaScript separately for the frontend.

3.18.3.4 Backend Language Comparison and Selection

Table 3.35 – Backend Language Comparison Table

Feature	**Python**	**Go**	**JavaScript (Node.js)**
Use Case	Simple and well supported, scientific libraries	Performant, concurrent backend services	Unified frontend/backend, real-time apps
Performance	Moderate	High	High
Real-Time Support	Moderate	High	High
Familiarity	High	Low	Low
Ease of Use	High	Low	Moderate
Suitability	High	Low	High

Node.js was selected as the backend technology for the IRIS system. The decisive factors were its native suitability for real-time data streaming, which directly serves the requirement to push new thermal grids from the ESP32 to the browser as they arrive; the unification of frontend and backend in a single language, which minimizes total learning overhead across the stack; and the maturity of the Express ecosystem, which provides production-ready libraries for every component the project requires.

3.18.3.5 Frontend Framework Selection

The frontend is the layer the end user actually interacts with, presenting the 16×16 thermal grid as a color-mapped heatmap, displaying alerts when hotspots are detected, and providing controls to initiate scans and review history. Three approaches were considered: a plain HTML/CSS/JavaScript implementation, the React framework, and the Vue framework.

A plain HTML/CSS/JavaScript implementation has the lowest learning curve and the smallest dependency footprint. For an application with as few distinct views as IRIS, this approach is technically sufficient. However, it scales poorly as interactivity grows; managing dynamic updates to the heatmap, alert list, and status indicators by hand written DOM manipulation quickly becomes error-prone.

React is the most widely used frontend framework in industry and has the largest ecosystem of supporting libraries, including charting and visualization libraries that can render the thermal heatmap directly. Its component-based architecture makes it easy to encapsulate the heatmap, alert panel, and control bar as independent reusable units. The drawback is a steeper learning curve and more boilerplate than the alternatives.

Vue offers a middle ground between the simplicity of plain JavaScript and the structure of React. Its templating syntax is closer to standard HTML, making it more approachable for developers new to frontend frameworks, while still providing reactive data binding and component composition.

Table 3.36 – Frontend Framework Comparison Table

Feature	**Plain HTML/JS**	**React**	**Vue**
Learning Curve	Lowest	High	Moderate
Component Reusability	Low	High	High
Real-Time Update Handling	Manual	Built-in (state)	Built-in (reactivity)
Charting/Visualization Libraries	Limited	Extensive	Moderate
Suitability for IRIS	Low	High	Moderate

React was selected as the frontend framework for IRIS. Its component model aligns well with the natural structure of the IRIS interface (heatmap, alert panel, scan controls, history view), its real-time state management integrates cleanly with the Socket.IO library on the Node.js backend, and the availability of mature visualization libraries simplifies rendering the 16×16 thermal grid as an interactive color-mapped display.

3.18.3.6 Data Storage Selection

The IRIS web interface must retain scan history and alert events so that users can review past inspections rather than only viewing the most recent scan. Two storage approaches were considered: a flat-file approach using JSON files on disk, and a lightweight relational database using SQLite.

The flat-file approach is the simpler of the two and requires no additional dependencies. Each scan can be serialized as a JSON file and written to a directory on the host laptop, with filenames encoding the timestamp. This is sufficient for very small datasets but does not scale well, lacks query capabilities, and provides no protection against concurrent access.

SQLite is a self-contained, file-based relational database that requires no separate server process and is supported natively by Node.js through libraries such as better-sqlite3. It provides full SQL query support, transactional integrity, and efficient retrieval of historical scans by timestamp, severity, or other criteria. Because the entire database lives in a single file on the host laptop, deployment complexity is no greater than the flat-file approach.

SQLite was selected for IRIS data storage. It supports the query patterns the frontend will need (retrieving recent scans, filtering by alert status, computing summary statistics over historical data) without imposing the deployment overhead of a server-based database such as PostgreSQL or MySQL.

3.18.3.7 Final Web Stack Summary

Table 3.37 – Final Web Stack Table

Layer	**Selected Technology**	**Role**
Backend Runtime	Node.js	HTTP server, real-time event handling
Backend Framework	Express	Routing, middleware, API endpoints
Real-Time Communication	Socket.IO	Streaming thermal grids and alerts to browser
Visualization	React + Canvas/SVG Library	Thermal heatmap rendering
Data Storage	SQLite	Scan history and alert persistence
ESP32 Backend Protocol	HTTP POST (JSON) over Wi-Fi	Periodic scan upload from ESP32

This stack provides a complete, end-to-end web platform that satisfies the IRIS system's requirements for remote monitoring, real-time visualization, historical review, and alert notification, while keeping the deployment footprint small enough to run on a single accompanying laptop without specialized infrastructure.

Chapter 4 – Standards and Design Constraints

4.1 The Standards and Design of IRIS

The IRIS project is intended to provide continuous or semi-automated thermal monitoring of electrical switchgear through an existing infrared inspection viewport while preserving closed-door inspection practices. Because the system is associated with energized electrical equipment, standards related to electrical safety, equipment maintenance, enclosure protection, electromagnetic compatibility, and circuit board design must be considered. In addition to formal standards, the design is also constrained by practical limitations such as safe installation geometry, optical access through an IR window, harsh electrical environments, cost targets, and project timeline.

These standards and constraints influence aspects of the system design. Electrical safety standards affect how the system interacts with equipment and ensure that the device does not introduce additional hazards. Maintenance-related standards guide the need for repeatable and reliable measurements, which directly impact sensor placement, optical alignment, and system calibration. Similarly, electromagnetic compatibility considerations influence circuit design, grounding, and signal filtering to ensure accurate data in electrical noise environments.

At this stage of design, not every implementation detail has been finalized. However, the broad standards and realistic design constraints that most directly affect the project can already be identified and analyzed. These considerations help guide component selection, system architecture, and overall design strategy, ensuring that the system remains both practical and aligned with expectations.

It is also important to note that this project represents a prototype system rather than a fully certified industrial product. As a result, while the design is informed by relevant standards, it may not fully comply with all certification requirements. However, the system is still developed with these standards in mind to make sure the design remains realistic, safe, and represents real-world engineering practices.

4.2 Standards Related to Project and Impact

4.2.1 NFPA 70B – Electrical Equipment Maintenance

One of the most relevant standards for this project is NFPA 70B [16], which addresses electrical equipment maintenance practices. NFPA describes 70B as applying to electrical, electronic, and communications systems and equipment, and committee materials for the current cycle explicitly reference infrared thermographic inspection as part of electrical equipment maintenance.

This standard is highly relevant because the IRIS project is fundamentally a condition-monitoring and maintenance-support system. The purpose of the design is not to control switchgear directly, but to help maintenance personnel identify abnormal thermal behavior at terminations, bus connections, and other energized internal features before faults escalate. That use case aligns closely with the maintenance philosophy behind

NFPA 70B, where periodic inspection and predictive maintenance are used to improve reliability and reduce unexpected failures.

The impact of NFPA 70B on design is significant. First, it supports the use of infrared thermography as a legitimate maintenance method for energized electrical equipment. Second, it reinforces the importance of trendable, repeatable measurements, which affects how the IRIS system should be mounted and aligned behind the viewport. If the viewing geometry changes from scan to scan, the temperature data becomes less useful for maintenance trending. Third, it pushes the project toward a design that emphasizes repeatability, documentation, and long-term monitoring value rather than one-time spot measurement. For this reason, the IRIS system should be designed to keep a stable field of view, consistent distance to the monitored scene, and repeatable scan positioning over time.

In practical terms, NFPA 70B encourages a system architecture that can support routine data collection, hotspot detection, and maintenance records. Even though the senior design prototype may not implement a full enterprise maintenance database, the design should still aim to produce data in a form that could support maintenance decision-making.

4.2.2 NFPA 70E – Electrical Safety in the Workplace

Another major standard affecting the project is NFPA 70E [17], which focuses on electrical safety in the workplace. NFPA states that 70E is intended to help employers and employees avoid workplace injuries and fatalities caused by shock, electrocution, arc flash, and arc blast. The current development materials also state that when energized conductors or circuit parts are not put into an electrically safe work condition, only qualified persons are permitted to perform that work.

NFPA 70E is especially important to the IRIS project because a major motivation for the design is to reduce the need to open energized switchgear doors for thermal inspection. Traditional handheld thermography may require operator interaction near energized equipment, which can increase exposure to arc flash hazards. By placing a sensor system behind an existing IR viewport, the project supports a safer closed-door inspection approach and better aligns with the spirit of minimizing unnecessary interaction with energized parts.

The impact of NFPA 70E on the design includes several requirements. The system must not encourage unsafe maintenance practices or imply that unqualified users can interact with energized switchgear. It also means the device should be designed so that normal operation occurs from outside the enclosure, with no requirement for door opening during routine data collection. Any internal mounting hardware should be installed only during an appropriate outage or qualified maintenance interval. Likewise, any user interface, wireless access, or indicator lights should be positioned such that the operator can interact with the system from a safer location outside the arc flash boundary whenever possible.

Overall, NFPA 70E shapes the project toward a risk-reduction design philosophy. The goal is not only to measure temperature, but to do so in a way that reduces human exposure to energized conductors and supports safer maintenance workflows.

4.2.3 OSHA 29 CFR 1910.333 – Selection and Use of Work Practices

A third highly relevant requirement comes from OSHA 29 CFR 1910.333 [18], which addresses safe work practices near electrical equipment. OSHA states that live parts to which an employee may be exposed must be de-energized before the employee works on or near them, unless de-energizing introduces additional hazards or is infeasible. OSHA also requires lockout/tagout and verification of de-energization when circuits are placed in a de-energized state for work.

This OSHA requirement is directly relevant because the IRIS project will be associated with switchgear enclosures containing hazardous energized conductors. Even if the final system is meant for closed-door monitoring, the prototype still has to be installed, aligned, tested, and possibly serviced. OSHA work-practice rules affect how those activities are performed. For example, internal mounting of a camera, bracket, or sensor assembly should be assumed to occur only during a controlled de-energized installation process or under qualified supervision using approved procedures.

The design impact is important. The system should be constructed so that routine use does not require energized interaction, and maintenance tasks should be minimized after installation. This pushes the design toward robust mounting, low-maintenance components, and remote-readable outputs. It also favors modular wiring and connector choices that reduce the need for repeated enclosure access. In other words, OSHA 1910.333 does not only affect installation procedure; it also affects product architecture by encouraging a design that minimizes future exposure to hazardous electrical work.

4.2.4 NEMA 250 and Enclosure Protection Requirements

A supporting enclosure-related standard is ANSI/NEMA 250 [19], which covers enclosures for electrical equipment rated 1000 V maximum and defines protection expectations for enclosure types used indoors, outdoors, and in hazardous locations. NEMA's current materials also note the relationship between NEMA enclosure types and IEC enclosure classifications.

For the IRIS project, enclosure standards matter because the system is intended to work with existing switchgear enclosures and existing IR windows rather than replacing enclosure functionality. The design must avoid compromising the enclosure's protective function. Any added components, fasteners, brackets, cable entries, or external indicators should be evaluated so that the enclosure's intended protection against dust, incidental contact, and environmental exposure is not unintentionally degraded.

4.2.5 FCC Part 15 – Electromagnetic Interference / EMC

If the project includes digital electronics, clocked logic, Wi-Fi, Bluetooth, or other intentional or unintentional radiators, FCC Part 15 [20] becomes relevant. The example report you shared already used this standard appropriately, and it remains applicable here because the IRIS system may include an ESP32-class controller, digital display circuitry, and switching electronics near electrically noisy switchgear.

The design impact of FCC Part 15 is that the system should be laid out and filtered to reduce unwanted emissions and improve immunity to electrical noise. This affects PCB layout, grounding, cable routing, shielding strategy, decoupling, and enclosure placement. In a switchgear environment, EMI is not just a regulatory issue; it is also a performance issue, since noise can corrupt sensor readings, communication links, or motor-control signals.

4.2.6 IPC Standards for PCB Design

Because the project includes a custom electronics assembly, IPC PCB design standards are also relevant. Standards such as IPC-2221 [21] are commonly referenced for general PCB design practice, including conductor spacing, manufacturability, and layout considerations.

The impact on the project is straightforward: the PCB should be laid out to improve reliability, reduce debug time, and maintain safe spacing between traces carrying different functions. This is especially important if the board includes mixed-signal circuitry, motor-drive interfaces, display connections, and communication hardware within a compact footprint.

4.2.7 IEEE 802.11 Wireless Communication Standard

The IRIS system uses wireless communication to transmit monitoring data to an external user interface. Because the system relies on Wi-Fi connectivity through the ESP32 microcontroller, the IEEE 802.11 [22] wireless communication standard is relevant to the design.

The IEEE 802.11 standard defines the protocols used for wireless local area networks (WLANs), including communication frequency ranges, data transmission methods, and network security mechanisms. The ESP32 microcontroller used in this project supports IEEE 802.11 b/g/n protocols operating in the 2.4 GHz band. These protocols allow the system to transmit collected thermal monitoring data to a remote dashboard interface. Compliance with the IEEE 802.11 standard ensures compatibility with widely available wireless networking equipment such as routers and access points. This enables the monitoring system to integrate easily into existing industrial or facility networks without requiring specialized communication hardware.

Another design consideration related to the IEEE 802.11 standard is signal reliability in electrically noisy environments. Industrial electrical equipment can produce electromagnetic interference that may affect wireless communication quality. For this reason, the IRIS system must be designed with appropriate antenna placement and communication error handling to maintain reliable data transmission.

Overall, adherence to IEEE 802.11 standards allows the IRIS system to provide scalable network connectivity while maintaining compatibility with existing infrastructure.

4.2.8 IEC 60529 – Ingress Protection (IP) Ratings

Ingress Protection standards defined in IEC 60529 [23] describe how electrical enclosures protect internal equipment from dust, solid objects, and moisture. These ratings are commonly expressed as IP codes, such as IP54 or IP65, which define the level of environmental protection provided by an enclosure.

This standard is relevant to the IRIS project because the monitoring system will be installed inside or near the enclosure. These environments can expose electronic equipment to dust, vibration, and temperature fluctuations. Although the IRIS prototype may not require a fully sealed enclosure, its design must still consider protection against contaminants that could affect sensor accuracy or electronic reliability.

Maintaining enclosure protection is particularly important when installing equipment inside switchgear cabinets. Any additional mounting brackets, cables, or connectors must be positioned in a way that does not compromise the enclosure's protective characteristics.

Considering Ingress Protection standards during the design process helps ensure that the monitoring system can operate reliably within industrial environments where environmental exposure may be unavoidable.

4.3 Design Constraints

4.3.1 Constraints Overview

In addition to formal engineering standards, the IRIS system is subject to several practical design constraints that directly influence system architecture, component selection, and overall feasibility. These constraints are not independent; rather, they interact and often compete with one another. For example, improving measurement accuracy may require more complex optics or processing, which can increase cost and development time. As a result, the design process involves balancing these competing factors to achieve a practical and effective system.

4.3.2 Safety Constraint: Closed-Door Operation Around Energized Switchgear

The most important design constraint in this project is electrical safety. The IRIS system is being developed specifically for use with switchgear, where energized conductors, bus bars, and terminations may present shock and arc flash hazards. Because of this, the system must be designed around a closed-door operating philosophy.

This means the normal use case should not require the operator to open the switchgear enclosure to collect data. The system should work through an existing IR viewport and provide its readings externally through a display, communication link, or logged data output. This constraint strongly affects mounting strategy, cable routing, sensor alignment, and user interface placement. A design that requires frequent enclosure opening would undermine one of the project's central safety benefits.

This constraint also affects maintenance philosophy. The system should avoid components that frequently need adjustment, re-focusing, or replacement inside the cabinet. Once installed, it should remain mechanically stable so that data can be collected repeatedly without intrusive access.

In addition, this constraint extends to how users interact with the system. The device must provide clear and accessible outputs that can be interpreted without requiring close proximity to equipment. This may include remote monitoring capabilities, visible status indicators, or wireless communication. In this way, safety is not only a physical constraint but also a system-level requirement that influences user interface design and overall system usability.

4.3.3 Optical Constraint

For a raster-scanned thermal imaging system, optical standards ensure reliable performance and safety. Key specifications typically include MTF, spatial resolution, and radiometric accuracy, which provide benchmarks for lens and detector selection. Following standards allows our system to be compared to alternatives that may exist on the market or in research.

Design constraints in this project come from both physical and performance limits. The 2 mm x 2 mm detector sets the maximum spatial frequency before aliasing, while the scanning mirror limits the beam sweep angle. Lens choices, focal length, and F/# must balance diffraction-limited resolution with light collection and minimal aberrations across the field.

System-level design decisions are related to maintaining good image quality over the object scene. Aperture placement controls aberration balance and light throughput, while lens types like germanium plano-convex or meniscus provide low aberrations for infrared imaging. The design must manage the trade-off between speed, depth of field, and manufacturability to achieve clear, consistent thermal images. This leads us to one major optical design constraint imposed by the intended use of the imaging system.

Unlike conventional free space imaging systems, the IRIS project is intended to be able to monitor internal switchgear components through preexisting IR transmissive windows. This creates a fixed aperture stop placement in the scene to design around, affecting our viewing angle, field of view, and transmission/reflection losses.

Figure 4.1 – Switchgear enclosure example (R&B switchgear group)

This also increases the specificity of our system's design. A design that works well with one viewport size or one switchgear geometry may need adjustment for another installation. As a result, the final design should be developed with some degree of alignment flexibility while keeping the optical path stable enough for acceptable imaging quality.

4.3.4 Environmental and EMI Constraint

Switchgear environments create a challenging operating environment for electronics. Internal temperatures can rise above room ambient, airflow may be limited, and electrical noise from nearby conductors, switching events, and electromagnetic fields can interfere with low-level sensor and communication signals. This produces a combined environmental and electromagnetic compatibility constraint.

The project must therefore be designed so that the sensor, controller, display, motor driver, and communication subsystem remain reliable despite heat and noise. This affects component selection, enclosure materials, grounding, filtering, local regulation, decoupling capacitors, and cable management. If this is not handled properly, the system may produce inaccurate temperature readings, unstable communication, or scanning errors.

This constraint also pushes the team toward conservative engineering choices. For example, short internal signal paths, secure connectors, and clear separation between noisy and sensitive circuits will likely be more important than maximizing feature count.

Another important consideration is the interaction between switching electronics and sensitive analog measurements. Components such as motor drivers and switching regulators can introduce electrical noise that couples into sensor readings if proper layout and filtering are not implemented. This requires careful PCB design practices, including separation of analog and digital grounds, proper decoupling, and shielding where necessary to maintain signal integrity.

4.4 Practical Constraints

4.4.1 Economic Constraint

The principal practical constraint is cost. The IRIS system is intended to explore a lower-cost alternative to high-end industrial thermal cameras. Commercial fixed thermal cameras for industrial monitoring can cost several thousand dollars, especially when they include Ethernet, autonomous alarming, and industrial-rated housings. That cost motivates the project, but it also creates pressure for the prototype to remain economical.

The team must therefore balance functionality against budget. Costs associated with the IR sensor, optics, stepper motor, driver electronics, PCB fabrication, structural hardware, enclosure integration, and display/interface components all affect whether the system remains a credible lower-cost option. If the prototype becomes too complex or too component-heavy, it may lose one of its core advantages.

This constraint also encourages the use of commercially available off-the-shelf components wherever possible. Using widely available components reduces sourcing risk, simplifies replacement, and improves the overall scalability of the system. It also ensures that the design can be replicated without relying on specialized or difficult-to-source parts.

4.4.2 Time Constraint

The project is also constrained by the Senior Design I and Senior Design II schedule. The team must complete requirements, development, subsystem selection, schematic capture, prototyping, testing, and documentation within the academic timeline. This means some ideal features may need to be deferred in favor of producing a robust proof-of-concept. The time constraint affects technical decisions. It favors widely available parts, proven communication methods, simple local displays, and subsystem choices that are easier to prototype and debug within the semester. It also means the team should prioritize the functions that best demonstrate project value: safe closed-door measurement, repeatable scanning, and usable temperature output.

The limited timeline influences testing and validation strategies. The system needs to be designed in a way that allows testing of individual subsystems before full integration. This reduces debugging complexity and increases the likelihood that the final system will function as intended within the available development period.

4.4.3 Manufacturability and Serviceability Constraint

A final important constraint is manufacturability and serviceability. Even though the current goal is a prototype, the system should still be designed so it can be assembled, wired, and serviced without excessive difficulty. Internal switchgear space is limited, and installation labor in real equipment is expensive and safety sensitive.

For that reason, the design should favor modular mounting hardware, straightforward wiring, and components that can be replaced or adjusted without major disassembly. Good serviceability also supports long-term adoption, since a monitoring system that is difficult to install or maintain may not be practical in actual industrial use.

The ease of assembly during the prototyping phase must be considered. Components should be arranged in a way that minimizes wiring complexity and reduces the likelihood of installation errors. This is particularly important in confined spaces where access is limited and modifications after installation can be difficult.

When designing the system in CAD for 3D printing, geometric constraints must be considered. The printer has limits on minimum feature sizes, line widths, and vertical resolution (Z-layer thickness). Features smaller than roughly 0.5 mm may not print reliably, so all holes, slots, and walls should meet or exceed this threshold to ensure structural integrity and dimensional accuracy. Without keeping these design constraints in mind, CAD design files may be created which would create impossible printing geometries that may be ignored in the slicing and printing process.

Overhangs, supports, and bed adhesion also influence the CAD design. Parts with steep overhangs may require temporary support structures during printing, which adds post-processing time and can affect surface finish. Flat bases and chamfered features can improve bed adhesion and reduce warping, while minimizing the need for supports. Careful orientation of parts in the CAD model can balance printability with functional requirements.

As with any other form of manufacturing, tolerances must be accounted for within the design as well. Calibration and testing of the machine is required to allow for tolerancing and dimension accuracy to be as high as reasonable. To this end, calibration techniques exist and must be used fairly often, especially as the same material may have different shrinkage between manufacturers and even between colors or batches from the same manufacturer.

Finally, modularity and assembly should guide part design. Since 3D printed components may be brittle or have limited tolerance, connections like snap-fits, tabs, or screw bosses should be designed to be robust and printable. Clearance between moving parts must account for printer tolerances, and complex internal features should be simplified or split into multiple pieces to ensure successful fabrication and ease of assembly.

4.5 Additional Constraints

4.5.1 Power Constraint

The IRIS system must operate within the limits of available power while maintaining stable performance across all subsystems. Because the system includes both low-power digital electronics and higher power components such as motors, efficient voltage regulation and power distribution are required. Additionally, the infrared sensing subsystem is sensitive to electrical noise, so clean and well-regulated power is necessary to maintain measurement accuracy. Having steady, reliable power is critical to support and maintenance teams. If a product that is being sold on reliability, we must ensure that we test our product thoroughly to validate that the power subsystem performs consistently under all expected operating conditions, including worst-case loading scenarios and extended continuous operation. Power interruptions, voltage sags, or noise introduced by switching components must be identified and mitigated during the design and testing phases before deployment, as any instability in the power delivery system could compromise thermal measurement accuracy, trigger false alarms, or cause system resets that undermine the continuous monitoring capability that IRIS is designed to provide.

4.5.2 Measurement Accuracy Constraint

Accurate temperature measurement is essential for the system’s effectiveness. However, several factors can influence measurement accuracy, including emissivity variation, reflections within the enclosure, and transmission losses through the IR inspection window. These effects introduce uncertainty into the measurements and must be accounted for through calibration and careful system design. Emissivity variation is particularly challenging in switchgear environments because different materials such as bare copper bus bars, painted steel enclosure surfaces, and insulated conductors all emit infrared radiation differently at the same temperature. If the system assumes a fixed emissivity value across the entire scene, temperature readings for materials that deviate from that assumption will contain systematic error. To address this, the system should either apply emissivity correction factors for known materials in the monitored scene or be calibrated against reference targets of known temperature and emissivity.

Reflections present a second source of error. Polished or metallic surfaces inside the enclosure can reflect infrared radiation from other heat sources in the scene, causing the sensor to read an apparent temperature that does not represent the true surface temperature of the target. This effect is most pronounced on highly reflective surfaces such as bus bars or terminal lugs and must be considered when interpreting thermal data. Careful selection of measurement regions of interest and awareness of enclosure geometry can help reduce the impact of reflective errors.

Transmission loss through the IR inspection window introduces a third source of uncertainty. All IR window materials attenuate infrared radiation to some degree, and this attenuation varies with wavelength and window condition. A scratched, contaminated, or degraded window will transmit less infrared energy than a clean one, causing the system to underestimate target temperatures. To maintain accuracy over time, the system design should account for window transmission characteristics during calibration, and maintenance procedures should include periodic inspection and cleaning of the viewport to ensure consistent optical performance [13].

Chapter 5 – Application of ChatGPT and Other Similar Platforms

5.1 Overview and Usage Philosophy

During the development of the project, several artificial intelligence tools were explored to assist with research, documentation, and preliminary design investigation. Large language models (LLMs) have become increasingly common tools in engineering workflows, providing the ability to summarize technical concepts, suggest design approaches, and assist with writing documentation. Because this project involves a combination of optics, electronics, embedded systems, and software, AI-based tools were occasionally used to help accelerate early research and clarify unfamiliar topics.

To fully examine the impact of LLM usage in the development of IRIS, it is important to understand the constraints that accompany these tools. Most critically, that LLMs are not artificial general intelligence and do not logically reason the way humans do [8]. They are also known to "hallucinate" false information. These facts entirely shape the way LLMs are applied in this project as they cannot be relied upon to "think for you" in technical applications. Then what purpose do they serve? LLMs are superior to humans at tasks such as aggregating information from large swaths of the internet, combing through dense texts, and troubleshooting. As such, their role in IRIS focuses mostly on labor intensive and easily validated tasks.

Another key consideration of LLMs is ethical usage. Not only is using LLMs to offload intellectual work impractical, but it is also intellectually and academically dishonest. LLM usage is not inherently academically wrong, but it must be used in such a fashion that it facilitates the existing and original work of the user. Simply copying output from an LLM is functionally identical to copying the intellectual property of another author, just obfuscated through transformers and tokens. Each of the conversations explored below, and other instances are used with standards of academic integrity in mind.

5.2 Conversation 1

Refer to Figure 5.1 in Appendix C, for the Conversation 1 prompt and response from ChatGPT.

In this example, ChatGPT is prompted to search for sources for a claim. This usage is academically ethical as it serves to enhance the research process without plagiarism or circumventing the purpose of the assignment. These results from the LLM gave the research an alternative set of sources to verify. Notably, the third link returned a report from a reputable engineering statistics company. This report included its sources and methodology and was generally found to be a credible source. This instance of LLM usage is an example of a positive benefit to the project, as regular and scholarly search engines gave low quality or irrelevant content.

The response also provides a structured breakdown of supporting evidence, referencing survey data and long-running industry studies. While the sources are not directly cited in a formal manner, the LLM identifies credible categories of evidence, such as industry surveys. This serves as a useful starting point for further research, as it provides possibly credible sources. It does not provide concrete citations or answers, only suggestions that require independent verification. In an academic setting, this verification step is essential to maintain academic rigor.

Another notable part of the response is its inclusion of alternative languages. By acknowledging the presence of other languages such as C++, Python, and Rust, the LLM expands upon the prompt and provides alternatives in research. This is especially valuable in engineering design work, where tradeoffs must be considered. The discussion of why C remains dominant, including factors such as hardware control and performance, provides deeper context, rather than simply reciting the statistic.

Overall, this interaction represents a constructive use of AI in an academic design context. The LLM assists in finding directions for supporting evidence and introducing relevant technical considerations. At the same time, it does not replace the design or research work inherent to the project. When used in this manner, ChatGPT functions as a supplementary research tool that remains in line with the overall usage philosophy of the project.

5.3 Conversation 2

Refer to Figure 5.2 in Appendix C, for the Conversation 2 prompt and response from ChatGPT.

This response generated by ChatGPT recommended the ESP32 microcontroller as the most practical choice for this system. It justified this by highlighting key features, including integrated Wi-Fi and Bluetooth capabilities, a wide range of communication interfaces, and processing power operating at a given frequency. The response also emphasized the low cost of the ESP32.

For the IRIS system, this information was directly relevant. The project requires wireless communication for data transmission, multiple sensor interfaces for temperature monitoring and system feedback, and sufficient processing capability to handle data acquisition and control tasks. The ESP32 aligns with these requirements, and ChatGPT's recommendation helped reinforce the direction that was being considered during the design phase.

One of the pros of this response is the comparison between two viable options. By presenting both the ESP32 and STM32 along with their respective advantages and limitations, ChatGPT provided a clear response for evaluating microcontroller selection based on the system's priorities. This was particularly helpful during the design phase for the group.

However, the response also demonstrates some limitations. While ChatGPT identified the ESP32 as a strong candidate, it did not specify a particular module or provide detailed specifications for implementation. The design required selection of a specific component, such as the ESP32-S3-WROOM module, including considerations for memory size, pin configuration, and other characteristics. These details are important for system integration.

Overall, this conversation demonstrates that ChatGPT is very effective for identifying appropriate technologies and comparing design approaches. It can quickly highlight features and trade-offs, which are imperative during the early stages of system design.

5.4 Conversation 3

Refer to Figure 5.3 in Appendix C, for the Conversation 3 prompt and response from ChatGPT.

In this conversation, ChatGPT was prompted to identify applicable standards for a device mounted on or inside electrical switchgear, specifically for a microcontroller-based infrared camera system. The response emphasized that multiple overlapping standards must be considered rather than relying on a single organization such as IEEE or NFPA. It highlighted safety as the most critical factor and introduced key standards including NFPA 70 (National Electrical Code) and NFPA 70E, with a focus on installation requirements, arc flash hazards, and electrical safety practices.

This information was directly relevant to the IRIS project, as the system is intended to operate in or near energized switchgear environments. The identification of NFPA 70E was particularly important, as it addresses arc flash risk and personnel safety, which are critical considerations for any device interacting with high-voltage equipment. Additionally, the clarification that multiple standards must be satisfied helped shape the team's understanding of compliance requirements early in the design process.
One of the strengths of this response is its practical framing of standards. Instead of listing organizations in isolation, ChatGPT explained how each standard applies to real engineering constraints such as enclosure design, wiring practices, and safe operation. This made the information actionable and easier to integrate into the system design considerations.

However, there are limitations to this response. While ChatGPT identified relevant standards, it did not provide detailed clauses, certification requirements, or specific testing procedures required for compliance. For example, it did not address UL certification processes, insulation coordination, or environmental ratings (such as IP or NEMA enclosure types), which are essential for a deployable product. These details must be obtained directly from official standards documentation and manufacturer guidelines.

Overall, this conversation demonstrates that ChatGPT is effective for identifying regulatory frameworks and providing high-level guidance on safety standards. It serves as a useful starting point for understanding compliance requirements but must be supplemented with detailed standards review and engineering validation. This aligns with the course guidelines, which stress that LLMs should support research while maintaining critical evaluation by the design team.

5.5 Conversation 4

Refer to Figure 5.4 in Appendix C, for the Conversation 4 prompt and response from ChatGPT.

This response from ChatGPT focused on the trade-offs associated with implementing raster scanning using a single thermopile detector. It explained how spatial resolution, scan time, and thermal accuracy are interconnected in such a system. In particular, the response highlighted that increasing spatial resolution requires a larger number of scan points, which directly increases total scan time since measurements cannot be taken in parallel with a single detector.

The explanation also addressed how thermal accuracy is influenced by signal-to-noise ratio and measurement time. Higher accuracy often requires longer integration time at each scan point, further increasing total scan duration. Conversely, faster scans reduce measurement time per point, which can negatively impact accuracy and increase noise in the reconstructed thermal image.

For the IRIS system, this discussion is directly applicable because the design relies on a raster-scanned thermopile sensor to generate a thermal map. The system must balance resolution, scan speed, and accuracy. The ChatGPT response helped clarify how these parameters interact and reinforced the importance of selecting an appropriate grid size and scan rate for reliable hotspot detection.

One advantage of this response is that it clearly outlines the fundamental trade-offs in a way that is easy to apply to system design decisions. It breaks down the relationship between resolution and scan time while also incorporating accuracy considerations, which are critical for thermal monitoring applications. This made it useful during the design phase when determining system specifications such as frame rate and spatial resolution.

However, the response also demonstrates some limitations. While ChatGPT provided a clear explanation of the trade-offs between spatial resolution, scan time, and thermal accuracy, it did not translate these relationships into specific design or implementation guidelines. For example, the response did not define an optimal scan resolution (such as a 16×16 grid), acceptable scan duration, or required integration time per measurement. These parameters are critical for ensuring that the system meets performance targets.

Additionally, the response did not account for practical system constraints such as motor speed limitations, sensor response time, or synchronization between scanning motion and data acquisition. These factors must be considered during implementation to ensure reliable operation and accurate thermal mapping.

Overall, this conversation demonstrates that ChatGPT is effective for explaining fundamental concepts and identifying key design trade-offs in optical systems. It provides a conceptual foundation that supports early-stage decision making. However, detailed engineering design still requires further analysis, calculations, and validation using real system constraints and component specifications.

5.6 Impacts and Conclusions

The use of ChatGPT and other LLMs throughout the IRIS project had a major impact on both the design process and the overall learning experience. These tools were most effective during the early stages of development, where broad exploration of technologies, system architectures, and design trade-offs was required. By providing structured explanations and comparisons, ChatGPT helped accelerate the initial research phase and allowed the team to quickly narrow down viable design options.

In addition to early-stage design support, ChatGPT proved valuable for understanding complex concepts, identifying relevant standards, and analyzing system trade-offs. It enabled faster iteration of ideas and provided a foundation for making informed engineering decisions. This was particularly useful in areas such as microcontroller selection, communication methods, and system-level design considerations.

However, the limitations of LLMs were also evident throughout the project. While ChatGPT is effective at providing high-level guidance and conceptual explanations, it does not consistently deliver the level of detail required for final engineering implementation. Critical aspects such as exact component specifications, compliance requirements, and system constraints must still be verified through datasheets, standards documentation, and experimental validation.

Furthermore, the accuracy of responses can vary, and some outputs may be incomplete or lack necessary context. This highlights the importance of treating LLM-generated information as a starting point rather than a definitive solution. Engineering judgment, critical thinking, and verification remain essential components of the design process.

Overall, ChatGPT served as a powerful supplementary tool that enhanced productivity, supported learning, and improved the efficiency of the design workflow. When used appropriately and in accordance with academic guidelines, it can significantly benefit engineering projects. However, its effectiveness depends on responsible usage, proper validation of information, and integration with traditional engineering practices.

Chapter 6 – Hardware Design

This chapter presents the hardware architecture of the Infrared Reliability Imaging System (IRIS). IRIS is designed to perform non-contact thermal inspection of electrical switchgear enclosures by raster-scanning a single infrared thermopile detector across a 15° × 15° field of view using a two-axis stepper motor and mirror assembly. The resulting 16×16 grid of thermal measurements is processed by the onboard microcontroller and transmitted wirelessly to an external monitoring interface. The following sections describe each major hardware subsystem in detail, including the power delivery system, microcontroller and communication circuitry, motor control and scanning mechanism, infrared optical sensing chain, and the auxiliary sensing subsystems.

6.1 Power Delivery Subsystem

The IRIS power delivery subsystem provides regulated voltage rails to all onboard electronics from a single battery input. Two voltage domains are required for system operation: a 5 V rail for the stepper motor drivers, the LCD backlight, and the analog signal conditioning chain, and a 3.3 V rail for the ESP32-S3 microcontroller, the MCP9808 temperature sensor, and other low-voltage digital logic. Figure 6.1.1 illustrates the overall power tree, showing the cascaded regulation scheme used to derive both rails from the battery input.

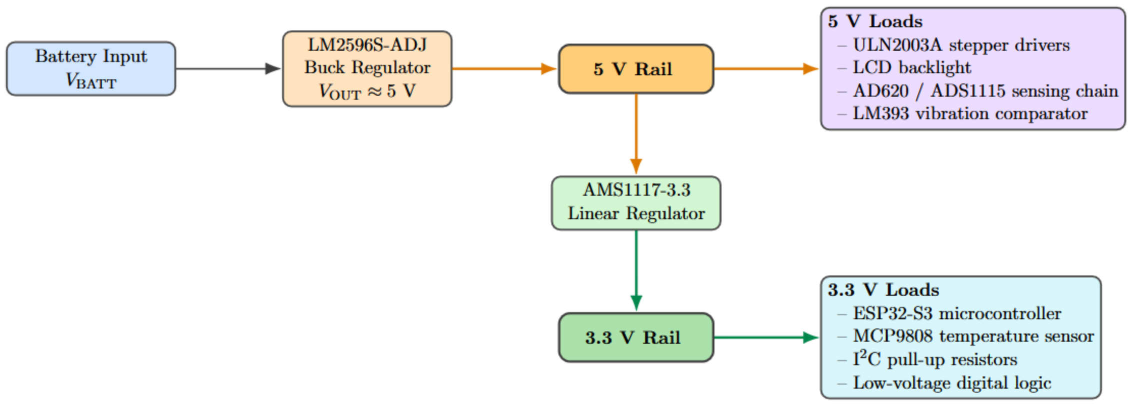

Figure 6.1.1 – IRIS Power Tree Block Diagram

A two-stage regulation topology was selected to balance efficiency and noise performance. The first stage employs an LM2596S-ADJ step-down switching regulator to convert the battery voltage (V_BATT) to a regulated 5 V rail. Switching regulation is used at this stage to maintain high conversion efficiency under the relatively large input-to-output voltage differential, minimizing power dissipation and extending battery runtime. The second stage employs an AMS1117-3.3 low-dropout linear regulator, which derives the 3.3 V rail from the 5 V output. A linear regulator was chosen for the second stage because the small voltage differential (1.7 V) limits dissipation to acceptable levels, while the absence of switching activity provides a low-noise supply suitable for the microcontroller and digital sensor interfaces.

6.1.1 5 V Switching Regulator (LM2596S-ADJ)

The LM2596S-ADJ operates in a standard buck topology, in which the regulator's switching output (pin 2) drives current through a 39 µH inductor (L1) to the output node. A Schottky diode (D1) provides a freewheeling path for the inductor current during the switch-off interval, ensuring continuous current flow and efficient energy transfer to the load. The schematic for this stage is shown in Figure 6.1.2.

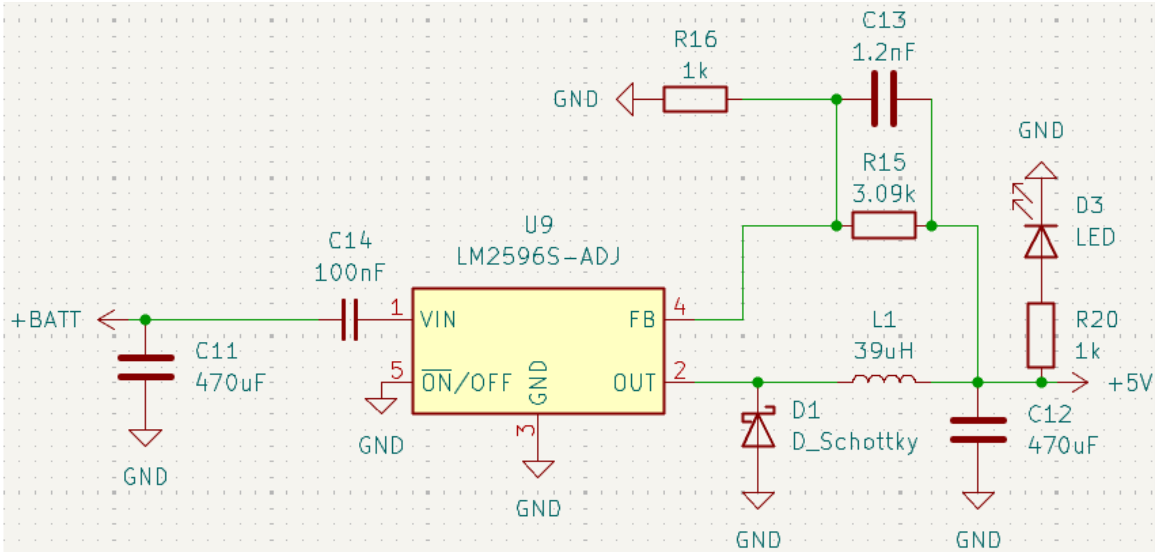

Figure 6.1.2 – LM2596S-ADJ 5 V Switching Regulator Schematic

Output voltage regulation is established through an external feedback network connected to the feedback pin (pin 4). A resistor divider consisting of R15 (3.09 kΩ) and R16 (1 kΩ) sets the nominal output voltage to approximately 5 V, based on the regulator's internal 1.23 V reference. A small feedforward capacitor (C13) is placed across the upper resistor to improve transient response and enhance loop stability under load steps.

A 470 µF electrolytic capacitor (C12) at the regulator output filters switching ripple and maintains a stable rail under varying load conditions. On the input side, a bulk capacitor (C11) is connected between V_BATT and ground to suppress input voltage transients and reduce conducted noise reflected back toward the battery. The ON/OFF pin (pin 5) is tied to ground, holding the regulator continuously enabled during normal operation.

6.1.2 3.3 V Linear Regulator (AMS1117-3.3)

The AMS1117-3.3 derives the 3.3 V logic rail from the 5 V switching output, supplying the ESP32-S3 microcontroller and associated low-voltage peripherals. The schematic for this stage is shown in Figure 6.1.3.

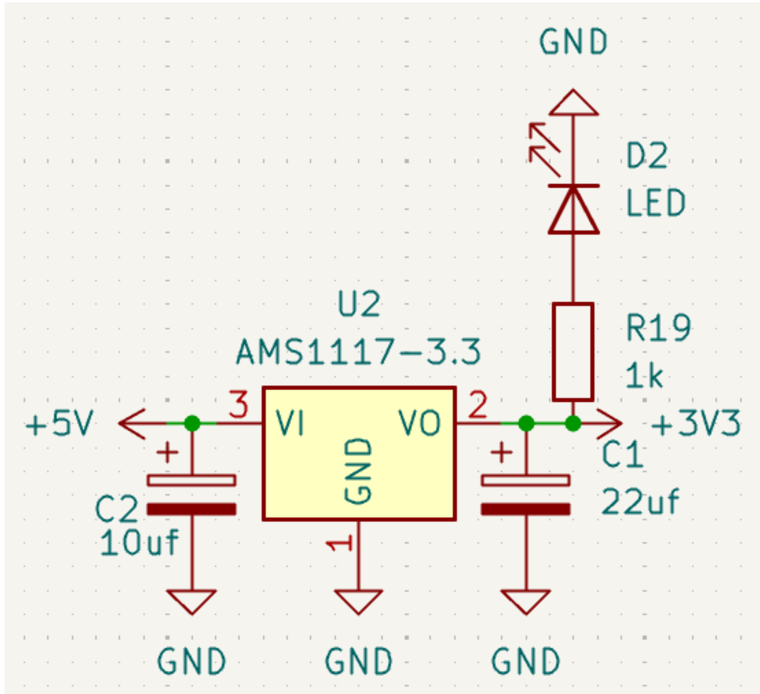

Figure 6.1.3 – AMS1117-3.3 Low-Dropout Voltage Regulator Schematic

Decoupling capacitors are placed at both the input and output of the regulator to ensure stable operation across the full load range. A larger bulk capacitor filters low-frequency variations resulting from load transients, while a smaller ceramic capacitor suppresses high-frequency noise that may couple from the upstream switching regulator or be generated internally by the load. Additional bypass capacitors are distributed near the power pins of each downstream digital device to provide local charge reservoirs and minimize loop inductance during fast transient events.

6.1.3 Power Distribution Summary

The 5 V rail supplies the ULN2003A stepper motor drivers (Section 6.3), the AD620 instrumentation amplifier and ADS1115 ADC in the thermopile sensing chain (Section 6.4), the LM393 comparator in the vibration detection circuit (Section 6.5), and the LCD module backlight (Section 6.6). The 3.3 V rail supplies the ESP32-S3 microcontroller (Section 6.2), the MCP9808 temperature sensor, and the I²C bus pull-ups. This separation ensures that high-current motor switching transients are confined to the 5 V domain and do not directly perturb the lower-noise 3.3 V logic supply.

6.2 Microcontroller Unit (MCU) Design

The central processing unit of the IRIS system is the ESP32-S3-WROOM-1 microcontroller module [39]. This device was selected for its integrated 2.4 GHz Wi-Fi capability, sufficient processing throughput for real-time data acquisition during raster scanning, and an extensive peripheral set including multi-channel ADC, UART, I²C, and native USB interfaces. Together, these features allow a single device to manage sensor acquisition, dual-axis motor control, and wireless telemetry without the need for an auxiliary coprocessor or external communication bridge. The ESP32-S3 connections are shown in Figure 6.2.1.

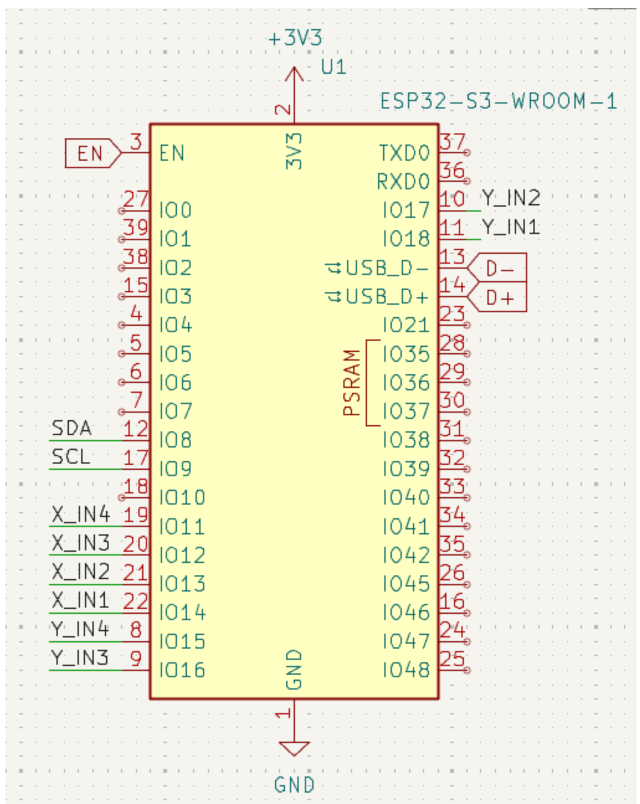

Figure 6.2.1 – ESP32-S3-WROOM Connections Schematic

6.2.1 Power and Reset Circuitry

The ESP32-S3 operates from a 3.3 V supply [39], provided by the AMS1117-3.3 regulator described in Section 6.1.2. Local decoupling capacitors are placed adjacent to each module power pin to suppress high-frequency noise and supply transients generated during Wi-Fi transmission, when current draw can momentarily exceed several hundred milliamps.

For correct operation, the Enable (EN) pin must be held high during normal use. This is achieved with a pull-up resistor connected to the 3.3 V rail, which keeps the device active at power-up. A momentary pushbutton is connected between EN and ground to allow manual reset by temporarily pulling the pin low, providing a recovery path during development and a means of clearing fault states in the field.

6.2.2 Peripheral Interfacing

The ESP32-S3 interfaces with the rest of the IRIS hardware through a combination of digital GPIO, ADC, I²C, and native USB connections. Stepper motor control signals are generated using four digital output pins per axis, routed to the ULN2003A driver inputs (Section 6.3); external driver circuitry is required to supply the inductive coil currents and to isolate the microcontroller from switching transients. The thermopile signal chain (Section 6.4) communicates with the MCU via the I²C bus through the ADS1115 ADC, while the integrated thermistor reference is sampled directly on GPIO2. The piezoelectric vibration detector output (Section 6.5) is routed to a GPIO pin configured for falling-edge interrupt detection, allowing asynchronous response to mechanical disturbance events without polling overhead. The MCP9808 temperature sensor and 1602 LCD module (Section 6.6) share a single I²C bus on the designated SDA and SCL pins, exploiting the addressability of the protocol to minimize GPIO usage. User input pushbuttons are connected to additional GPIO pins configured with pull-up resistors. The complete GPIO assignment is summarized in Table 6.2.1.

Table 6.2.1 – ESP32-S3 GPIO Pin Assignments

GPIO	Function	Subsystem
ADC1 (I2C)	Vibration sensor (interrupt)	Section 6.5
ADC2 (I2C)	Thermistor ADC input	Section 6.4
GPIO11–14	X-axis stepper (IN1–IN4)	Section 6.3
GPIO15–18	Y-axis stepper (IN1–IN4)	Section 6.3
SDA / SCL	Shared I²C bus	Sections 6.4, 6.6
GPIO3	User pushbutton(s)	—

6.2.3 USB and Programming Interface

The ESP32-S3 incorporates a native USB peripheral with built-in support for serial communication and firmware programming, eliminating the need for an external USB-to-UART bridge such as the CP2102 or CH340. This reduces component count, simplifies the PCB layout, and removes a common failure point during development. The USB lines are routed directly to a USB-C connector for communication with the MCU and the programmer.

6.3 Stepper Motor Driver Circuits

The IRIS scanning mechanism employs two unipolar stepper motors to provide independent control of the azimuth and elevation axes of the mirror assembly [15], [16].

Each motor is driven by a ULN2003A Darlington transistor array, which provides the current amplification required to energize the motor coils and electrically isolates the ESP32-S3 microcontroller from inductive load transients. The driver schematic is shown in Figure 6.3.1.

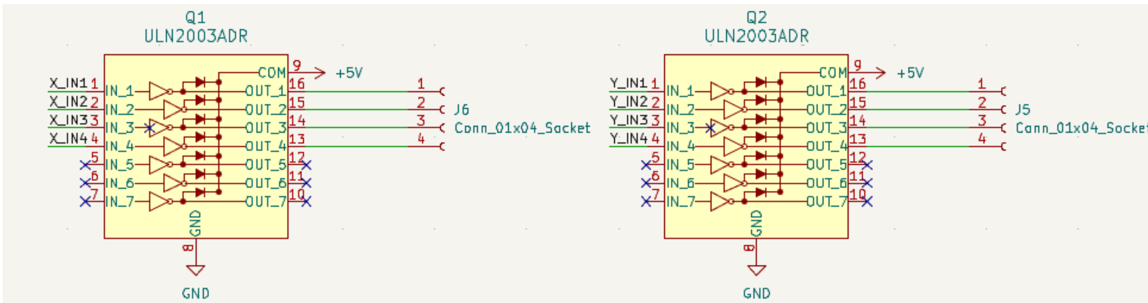

Figure 6.3.1 – ULN2003A Stepper Motor Driver Circuit Schematic

Control signals from the microcontroller are provided through four GPIO pins per motor (X_IN1–X_IN4 and Y_IN1–Y_IN4), as listed in Table 6.2.1. These signals connect directly to the ULN2003A inputs, while the corresponding outputs drive the four motor coils (blue, pink, yellow, and orange). The common (center-tap) wire of each motor is tied to the 5 V rail described in Section 6.1.1. In this configuration, the ULN2003A operates as a low-side driver, sinking current through each coil sequentially according to the stepping sequence generated by the microcontroller.

The COM pin of each ULN2003A is connected to the 5 V supply to enable the device's internal flyback diodes. These diodes provide a clamping path for the inductive voltage spikes generated when each coil is de-energized, protecting both the driver outputs and any other circuitry sharing the 5 V rail from transient overvoltage. The driver ground pin is connected directly to the system ground plane to ensure a low-impedance return path for the coil currents.

This configuration enables reliable, independent control of both stepper motors while shielding the microcontroller from the high currents and switching transients characteristic of inductive loads. The use of a dedicated driver per axis also simplifies firmware control, as each motor can be stepped in either direction independently without arbitration logic.

6.4 Infrared Thermopile Sensing Circuit

The infrared sensing subsystem forms the core measurement chain of the IRIS system. It is implemented around the HEIMANN HMS J21-F8.14 thermopile detector, which measures infrared radiation from the scanned scene. The thermopile operates as a passive transducer, generating a small differential voltage proportional to the temperature difference between the target object and the sensor's reference junction. The integrated

F8.14 optical filter provides spectral selectivity centered near 8–14 µm, improving sensitivity to thermal emissions from electrical equipment while rejecting out-of-band radiation such as visible light and reflected solar energy. The complete signal conditioning chain is shown in Figure 6.4.1.

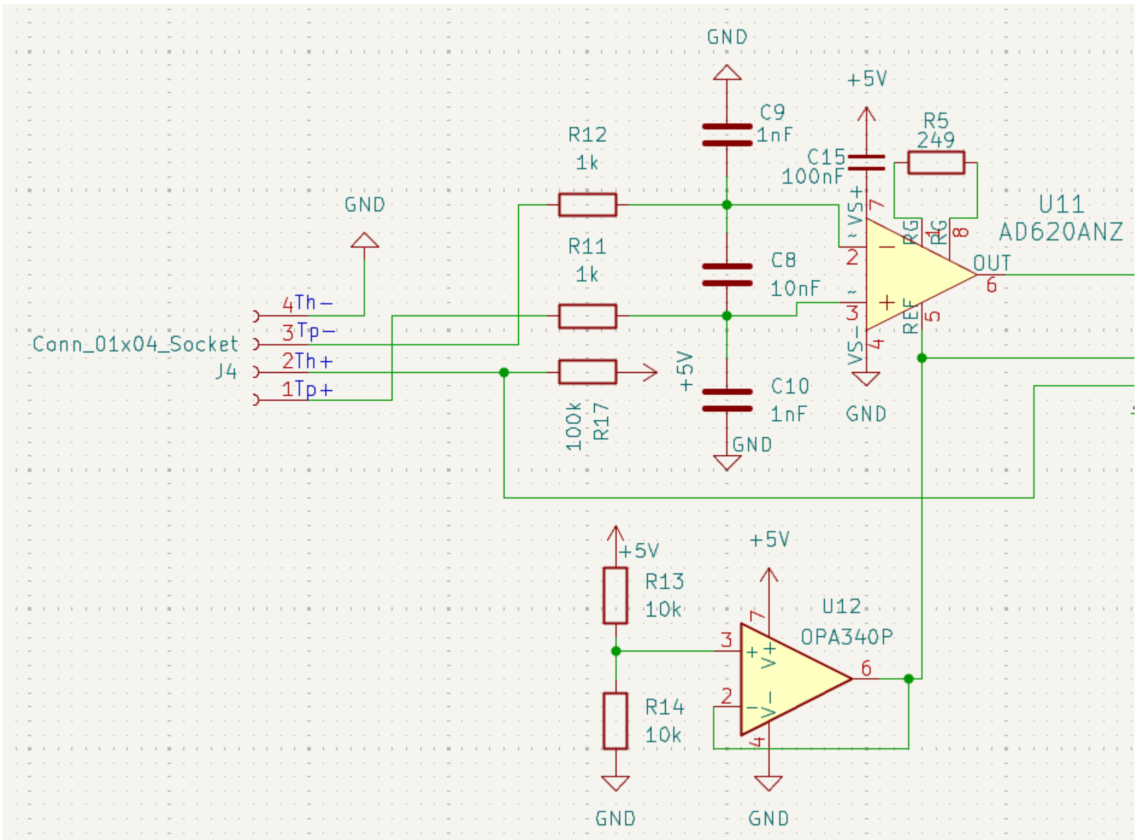

Figure 6.4.1 – J21 Thermopile Detector and AD620 Signal Conditioning Circuit Schematic

6.4.1 Instrumentation Amplifier Stage

The thermopile output signal is on the order of microvolts to millivolts, requiring precision amplification prior to digitization. The AD620 instrumentation amplifier was selected as the primary signal conditioning stage due to its high common-mode rejection ratio, low input offset voltage, and low input-referred noise — all critical parameters when amplifying low-level differential signals from a high-impedance source.

The amplifier gain is set by a single external resistor (R_G) according to the relationship:

$$G = 1 + (49.4\ k\Omega / R\_G)$$

In this design, R_G is selected to scale the expected thermopile output range into a voltage range well-matched to the downstream ADC, maximizing dynamic range while preventing saturation at the highest expected target temperatures.

To enable single-supply operation, the reference (REF) pin of the AD620 is biased at mid-supply (2.5 V) using a buffered voltage divider implemented with a rail-to-rail operational amplifier. This establishes a virtual ground that allows the amplified thermopile signal to swing both above and below the midpoint while remaining within the linear input range of the ADC.

6.4.2 Input Filtering

An input filtering network is implemented at the AD620 inputs to mitigate electromagnetic interference (EMI) and high-frequency noise pickup. The network consists of matched series resistors and shunt capacitors, configured to provide both differential-mode and common-mode low-pass filtering. This filtering stage is critical given the high source impedance and low signal amplitude of the thermopile output, which together make the front end particularly susceptible to noise coupling from the nearby stepper motors and Wi-Fi radio.

6.4.3 Analog-to-Digital Conversion

The amplified signal is digitized using the ADS1115, a 16-bit delta-sigma analog-to-digital converter with an integrated programmable gain amplifier and I^2C interface. The ADS1115 was selected for its high resolution and support for differential input measurements, which allow accurate capture of small signal variations across the scanned field. The ADC operates from the 5 V rail (Section 6.1.1), allowing full utilization of the amplified signal range centered around the 2.5 V virtual ground. The digital output is transmitted to the ESP32-S3 over the shared I^2C bus described in Section 6.6. The ADS1115 is configured in differential mode, allowing the measurement of the thermopile signal relative to the mid-supply reference, improving noise rejection and measurement accuracy.

6.4.4 Ambient Temperature Reference

In addition to the thermopile element, the HMS J21 sensor package integrates a 100 kΩ NTC thermistor for measurement of the sensor's ambient (cold-junction) temperature. Accurate radiometric calculation of absolute target temperature requires knowledge of this reference, since the thermopile output is proportional to the *difference* between target and reference temperatures rather than an absolute value. The thermistor is configured as the lower leg of a voltage divider against a fixed pull-up resistor, and the divider output is sampled by AIN2 of the ADS1115 (see Table 6.2.1).

This architecture provides a robust, high-resolution measurement chain for infrared sensing, combining precision amplification, careful noise rejection, and high-resolution digitization to accurately capture thermal variations across the scanned environment.

6.4.5 Actual PCB Implementation and Amplifier Circuit Redesign

During prototype development, the original signal conditioning circuit based on the AD620 instrumentation amplifier did not provide the performance required for reliable thermopile measurements. Although the initial design was intended to amplify the detector's microvolt-level output while rejecting common-mode noise, experimental testing revealed that the circuit was insufficiently stable for the desired measurement accuracy. This prompted a redesign of the analog front end, with greater emphasis placed on low offset, low drift, and improved DC performance. Rather than continuing to optimize the original circuit, the amplification stage was redesigned around the AD8629 precision operational amplifier using a reference circuit recommended for low-level sensor applications.

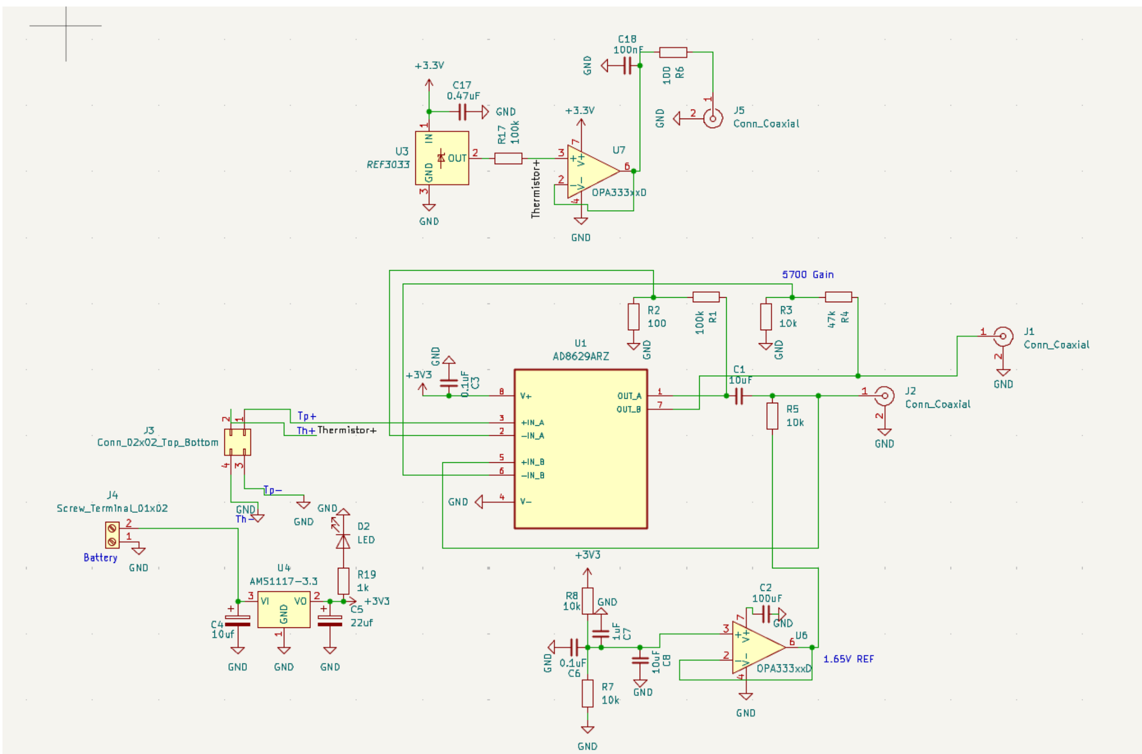

Figure 6.5.2 – J21 Thermopile Detector and AD8629 Signal Conditioning Circuit Schematic Revised

The revised signal conditioning circuit utilized both amplifiers contained within a single AD8629 package in non-inverting configurations. The first amplification stage provided a gain of approximately 1000 to raise the thermopile output above the noise floor of the downstream electronics while preserving the low-frequency thermal signal. A second non-inverting stage with a gain of approximately 200 provided additional amplification and output conditioning prior to analog-to-digital conversion. This two-stage architecture distributed the required gain across multiple stages, improving overall stability and allowing each stage to operate within a practical gain range. Combined with careful PCB layout, shielding, and subsequent calibration, the redesigned amplifier circuit provided the signal quality necessary for accurate temperature measurements throughout the completed system.

6.5 Vibration Detection Circuit

The vibration sensing subsystem provides detection of mechanical disturbances during operation, allowing the system to flag scans that may have been corrupted by motion or external impact. The subsystem is implemented as a discrete piezoelectric sensing circuit with an analog comparator stage, rather than a pre-packaged sensor module. This approach provides direct control over sensitivity and threshold behavior, allows tuning to the specific vibration profile of the scanning mechanism, and satisfies the custom-PCB requirements of the project. The schematic is shown in Figure 6.5.1.

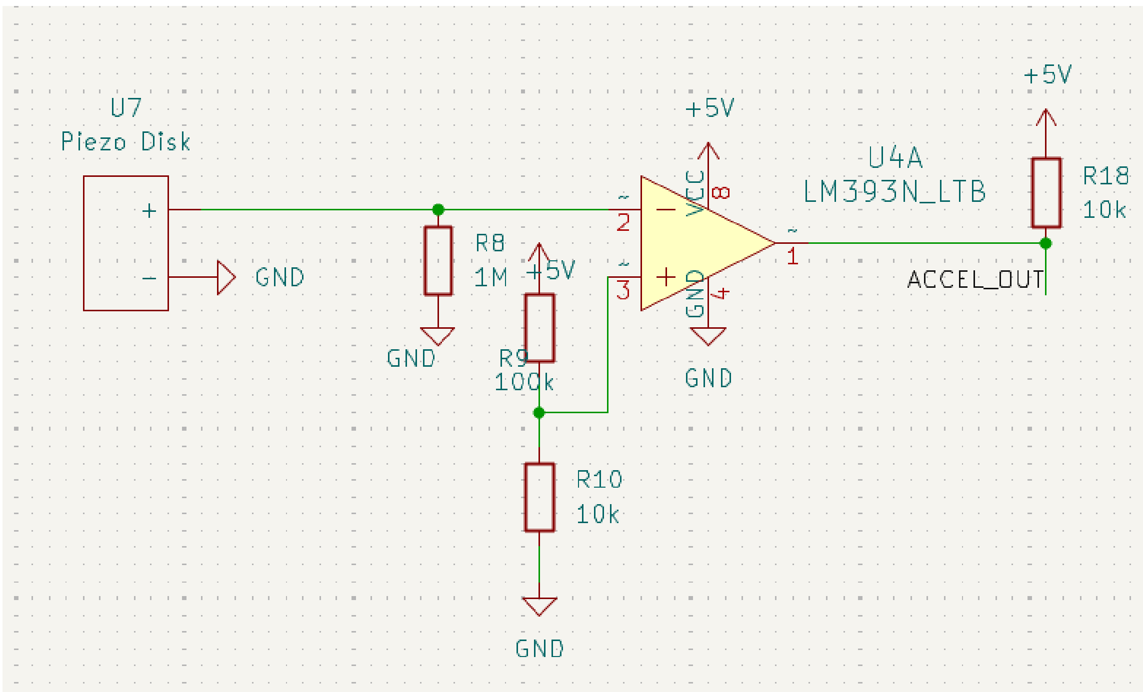

Figure 6.5.1 – Piezoelectric Vibration Sensor Interface Circuit Schematic

6.5.1 Piezoelectric Sensing Element

The sensing element is a piezoelectric film sensor, which operates on the piezoelectric effect: mechanical stress applied to the film generates a corresponding electrical voltage across its electrodes [37]. The output is an AC signal whose amplitude is proportional to the intensity of the applied disturbance. Small vibrations produce millivolt-level signals, while sharp impacts can generate volt-level transients.

A 1 MΩ load resistor is connected across the piezoelectric element to establish a stable bias point and define the low-frequency cutoff of the sensor response. This high impedance ensures that only dynamic mechanical events are detected, while slow drift from thermal expansion or static deflection of the mounting surface is rejected as out-of-band.

6.5.2 Comparator Stage and Threshold

The conditioned analog signal is fed into the inverting input of an LM393 comparator, which converts the continuous-amplitude piezoelectric signal into a clean digital pulse suitable for microcontroller interfacing. The comparator's non-inverting input is held at a fixed reference voltage generated by a resistor divider (100 kΩ and 10 kΩ) connected to the 5 V rail, producing a threshold of approximately 0.45 V.

When the instantaneous piezoelectric voltage exceeds this threshold, the comparator output transitions low, signaling a vibration event. When the signal remains below the threshold, the output remains high. This thresholding action effectively suppresses low-amplitude noise and produces a clean digital pulse on each significant disturbance.

The LM393 features an open-collector output, requiring an external pull-up resistor to define the logic-high level. A 10 kΩ pull-up resistor is connected to the 3.3 V rail (Section 6.1.2), ensuring direct logic-level compatibility with the ESP32-S3 GPIO. The output is routed to GPIO1, configured for falling-edge interrupt detection (see Table 6.2.1), so that vibration events trigger an asynchronous interrupt service routine without requiring continuous polling.

6.5.3 Sensitivity Adjustment

To allow flexible system tuning, the lower resistor of the threshold divider may be replaced with a trimmer potentiometer. This permits adjustment of the detection sensitivity during testing and calibration, allowing the threshold to be set above the baseline mechanical noise of the stepper motors while remaining sensitive enough to detect abnormal vibration events. This discrete implementation reduces component cost, improves design transparency, and provides robust, configurable vibration detection while satisfying the custom-PCB requirements of the project.

6.6 I²C Sensor and Display Interface

The IRIS system uses an Inter-Integrated Circuit (I²C) bus to interface with multiple digital peripherals, including the ADS1115 ADC of the thermopile chain (Section 6.4), the MCP9808 ambient temperature sensor, and the 1602 LCD display module. The I²C protocol was selected for its low pin count, native support for multiple devices on a shared bus, and built-in addressing scheme [40]. This consolidation allows all three devices to communicate with the ESP32-S3 over only two GPIO pins, freeing the remaining pins for the motor drivers and analog inputs.

The bus consists of a serial data line (SDA) and a serial clock line (SCL), both connected to designated GPIO pins on the ESP32-S3 (see Table 6.2.1). All three devices are connected in parallel to these lines and addressed individually using their unique 7-bit I²C addresses. Pull-up resistors are placed on both lines, referenced to the 3.3 V rail (Section 6.1.2), to establish proper logic levels and ensure reliable rising-edge transitions across the bus.

6.6.1 MCP9808 Temperature Sensor

The MCP9808 is a high-accuracy digital temperature sensor that interfaces directly over I²C [40]. Its primary purpose in the IRIS system is to provide an ambient reference for the enclosure interior, supplementing the thermopile's integrated thermistor with a board-level temperature measurement. The schematic is shown in Figure 6.6.1.

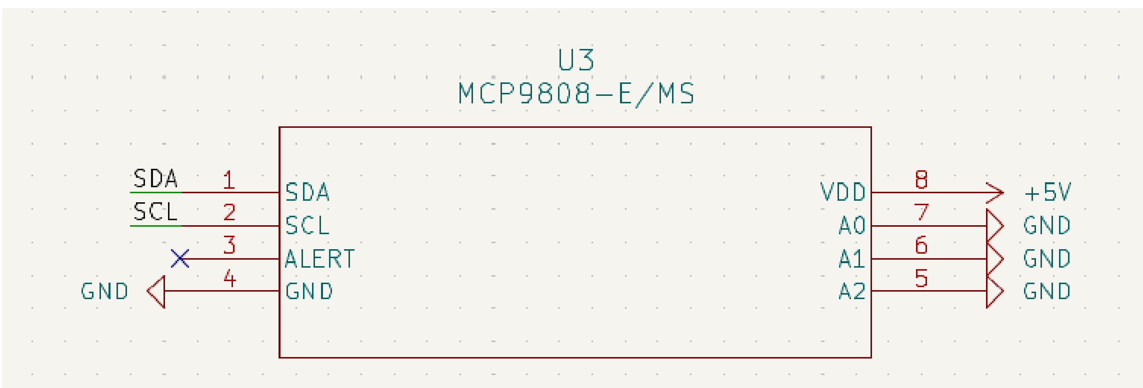

Figure 6.6.1 – MCP9808 I²C Temperature Sensor Connection

The sensor is powered from the 3.3 V rail and contains an internal sigma-delta ADC, eliminating the need for any external signal conditioning. The address selection pins (A0, A1, A2) are tied to ground, configuring the device to its default I²C address of 0x18. A 0.1 µF bypass capacitor is placed between the supply and ground pins, located as close as practical to the device to minimize loop inductance and provide local noise suppression.

6.6.2 1602 LCD Display Module

The display subsystem consists of a 1602 character LCD module fitted with an I²C backpack adapter [34]. The adapter integrates a PCF8574 I/O expander, which translates byte-wise I²C commands into the parallel signals required by the LCD's HD44780 controller. This approach reduces the GPIO requirement from seven parallel lines to the two shared I²C lines and simplifies routing on the main PCB. The schematic is shown in Figure 6.6.2.

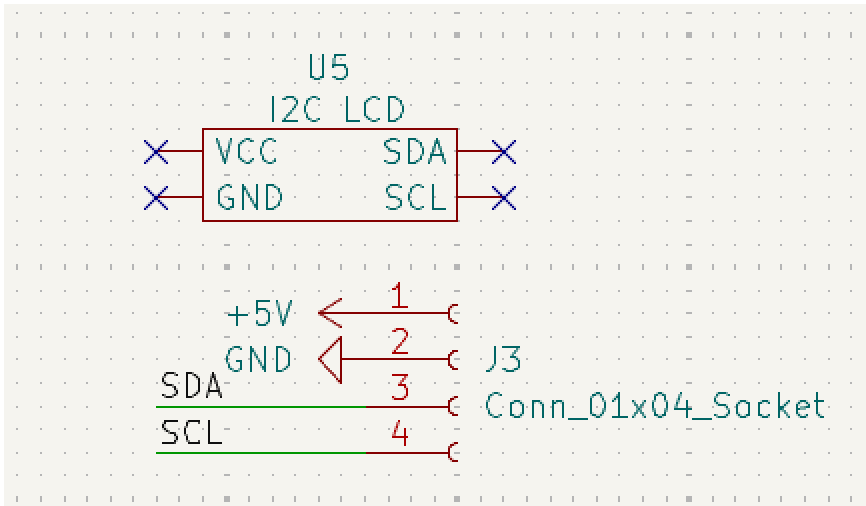

Figure 6.6.2 – 1602 LCD Display I²C Connection

The LCD module is powered from the 5 V rail to drive the display panel and backlight, while its I²C logic remains compatible with the 3.3 V bus through the open-drain nature of the protocol. The display provides real-time visual feedback during operation and testing, including system status, scan progress, and sensor readings, without requiring an external host interface. A 1x4 connector is included for easy detachment from the PCB.

6.6.3 AS5600 Magnetic Rotary Encoder

The AS5600 is a 12-bit contactless magnetic rotary position sensor used in the IRIS system to provide closed-loop angular feedback for the scanning mechanism. The sensor measures the orientation of a diametrically magnetized magnet placed above its sensing surface, producing an absolute angular reading over a full 360° range with a resolution of 0.087°. This feedback allows the firmware to verify commanded stepper positions, detect missed steps, and correct for accumulated mechanical backlash that would otherwise degrade the spatial accuracy of the raster scan. The schematic is shown in Figure 6.6.3.

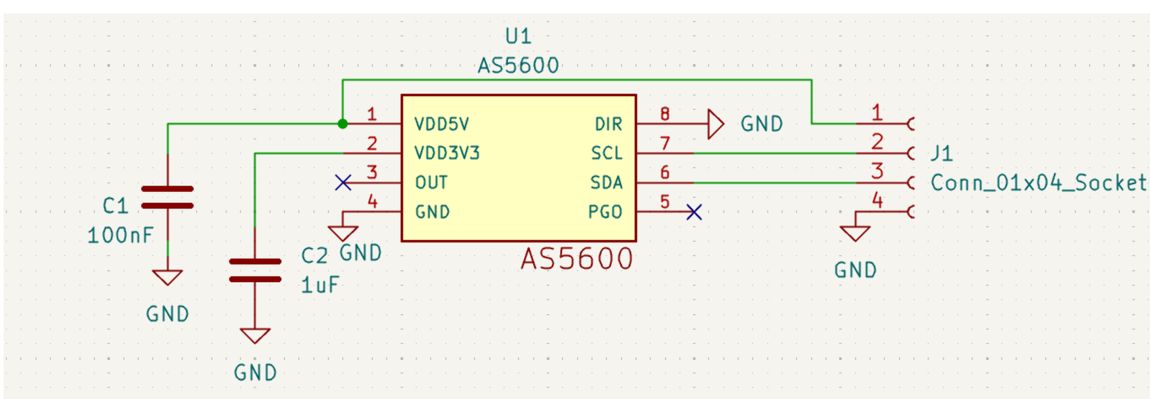

Figure 6.6.3 – AS5600 Magnetic Rotary Encoder Schematic

The AS5600 supports both 5 V and 3.3 V supply rails through its dedicated VDD5V and VDD3V3 pins. In this design, VDD5V is connected to the 5 V rail (Section 6.1.1) with a 100 nF bulk decoupling capacitor (C1), while VDD3V3 is decoupled with a 1 µF capacitor (C2) on the internally regulated 3.3 V output. This configuration uses the device's internal LDO to generate the analog supply for the Hall sensor array, providing improved noise immunity compared to direct 3.3 V operation.

The DIR pin is tied to ground, configuring the device for the default rotation polarity (clockwise rotation produces increasing angle values). The PGO (programming output) and OUT (analog output) pins are left unconnected, as the system uses the I²C interface exclusively for angle readout and does not require one-time programming of the device's non-volatile configuration registers in normal operation.

Because the sensor must be physically located at the axis of rotation to remain centered beneath the diametric magnet, the AS5600 is implemented on a small dedicated breakout board rather than on the main PCB. The breakout connects to the main board through a four-pin header (J1) carrying VDD, SCL, SDA, and GND. This separation also keeps the I²C bus traces on the main PCB short and allows the sensor to be repositioned during mechanical assembly without redesigning the main board.

The AS5600 communicates over the shared I²C bus at the fixed address 0x36, which does not conflict with the other devices on the bus.

6.6.4 Bus Address Management

Because all four I²C devices share the same physical bus, address management is essential to prevent communication conflicts. The ADS1115 (configurable, default 0x48), the MCP9808 (0x18), the AS5600 rotary encoder (0x36), and the LCD backpack (typically 0x27) operate at distinct addresses, allowing all four to coexist without arbitration. This shared-bus architecture also leaves the I²C interface open to future expansion, as additional sensors or peripherals can be added with minimal hardware modification provided their addresses do not conflict with the existing devices.

Chapter 7 – Software Design

To understand how IRIS specifically executes its core tasks, the following diagrams were generated. These illustrate the usages, functions, and relationships between the different subsystems. They also serve to demonstrate the integration of the disparate hardware components to produce a desirable result.

There are two major components of the software design for IRIS. There is the local code executed on the ESP32 and the web interface. The goals of the software design of each part are varied and serve to complement one another. The ESP32, for example, must manage the sensor data, interface with the LED/LCD/storage device, manage the stepper motors and raster motion, and wirelessly communicate with the web design all under real-time constraints. The web UI must be able to receive and display hardware information and present an alert based on the hotspot detection algorithm.

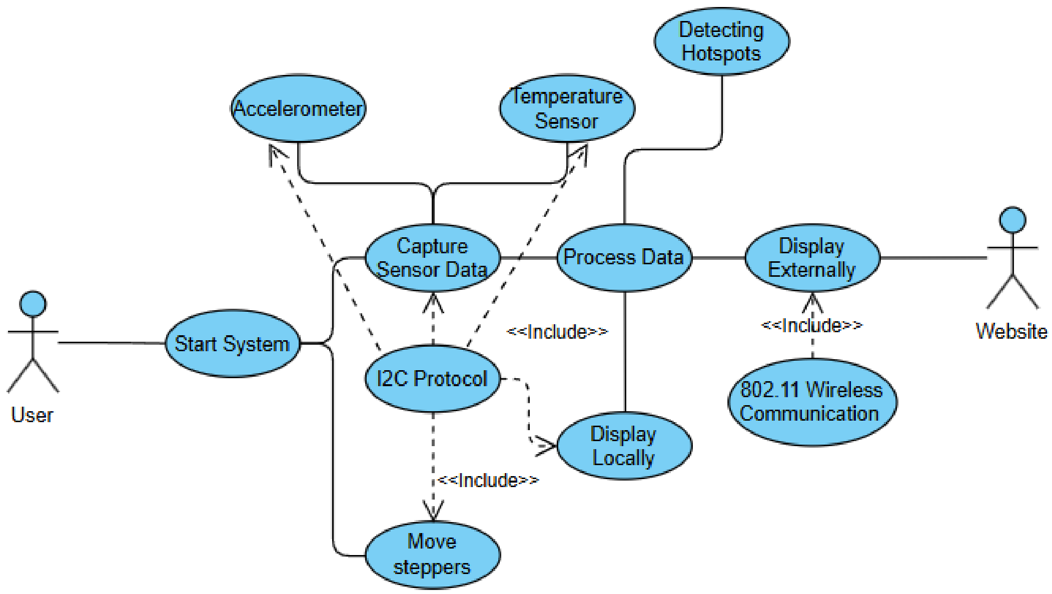

Figure 7.1 – Software Use Case Diagram

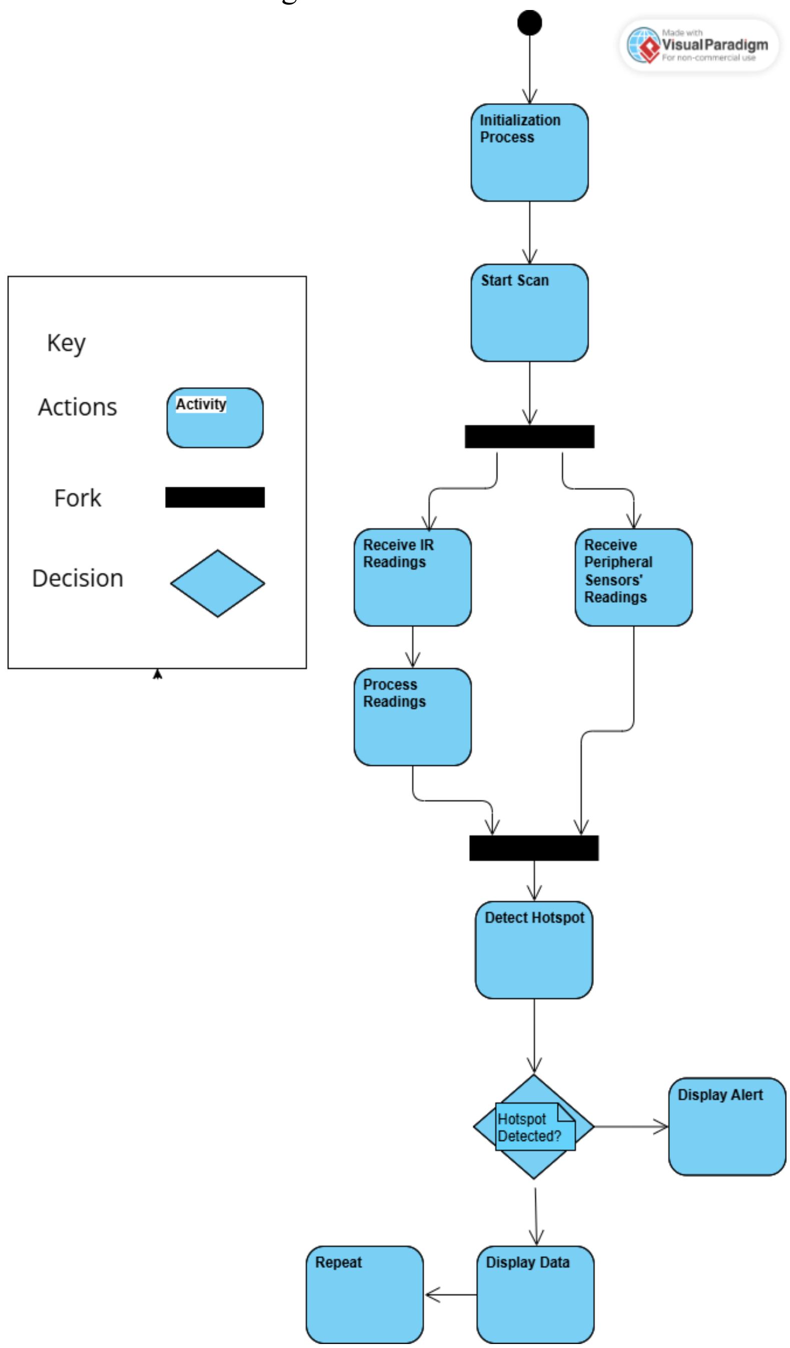

Figure 7.2 – Software Activity Diagram

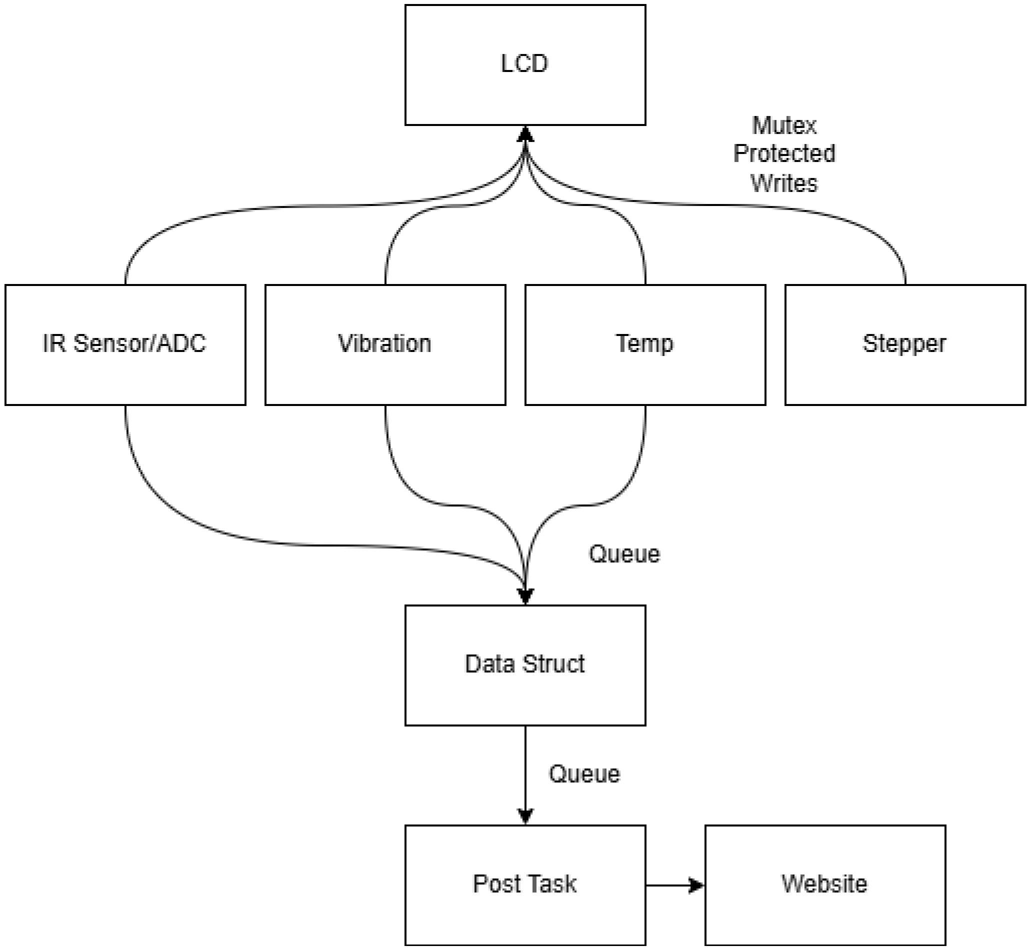

Figure 7.3 – Data Transfer Flowchart

7.1 Task Implementations

7.1.1 Elements of Real Time Development

The program is structured around the core principles of a real time operating system, specifically the task based scheduling model of FreeRTOS. Each major function of the system is encapsulated within its own task. Differing priorities means that more timing sensitive tasks can operate more smoothly by taking precedence over the CPU's other operations. The stepper motor control task is given the highest priority, ensuring that stepping remains consistent, which is critical for data acquisition. Other tasks are assigned different values, with network communication handled last. This prioritization means the code uses real time principles where deterministic behavior is preserved for time sensitive operations while less critical processes yield processor time when needed.

Task scheduling is cooperative and timing is managed in part through timing delays. By relying on non-blocking delays instead of busy waiting, the system maintains responsiveness and allows multiple tasks to execute in an interleaved manner.

Inter-task communication and synchronization are handled through synchronization primitives like queues and semaphores. For example, the POST task utilizes a queue to receive and aggregate data. This ensures safe and ordered data transfer between producer and consumer without requiring shared memory access. The vibration detection system uses a binary semaphore that is released inside an interrupt service routine. This allows the interrupt to signal an event to a task without performing extensive processing at interrupt level. Mutual exclusion of shared resources is enforced through a mutex which protects access and prevents garbage or interleaving.

Each task produces data that must be transmitted to the website. A unified data struct was implemented to integrate the different data values into one data type that can then be used with synchronization primitives. It also allows the tasks to update independently of one another. The temperature task generates periodic sensor readings, the vibration task represents discrete event detections, and the stepper task implicitly defines positional or scan state information based on its progression through lines and steps. These outputs can be consolidated into a shared data structure, potentially protected by a mutex or updated through a dedicated queue, where each task contributes its latest state. A separate POST task consumes this structured dataset and handles network transmission. This design decouples data acquisition from communication, allowing the timing of sensor sampling and motor control to remain deterministic and independent of one another, while network operations are handled in a unified manner. Table 7.1 lists out a collection of all of the FreeRTOS tasks initialized in the software.

Table 7.1 – List of Tasks

Tasks	Purpose
stepper_task	Manage raster scanning
ADC_task	Convert IR data to digital data and send
POST_task	Receive all data and post to backend server
temperature_task	Sending ambient temp data
vibration_task	Sending piezoelectric data
LCD_task	Manage the printing of LCD data

7.1.2 Hotspot Detection Algorithm

Simply collecting IR data from a sensor is not sufficient to achieve the maintenance goals of IRIS as the temperature data must be processed and understood. The benchmark used to quantify what a “hotspot” is critical to creating an algorithm. Certain connections have a maximum junction temperature that must be observed. These can vary based on the type of connections, and specific parts can have different acceptable heat limits. These are what can be referred to as “absolute” measurement thresholds.

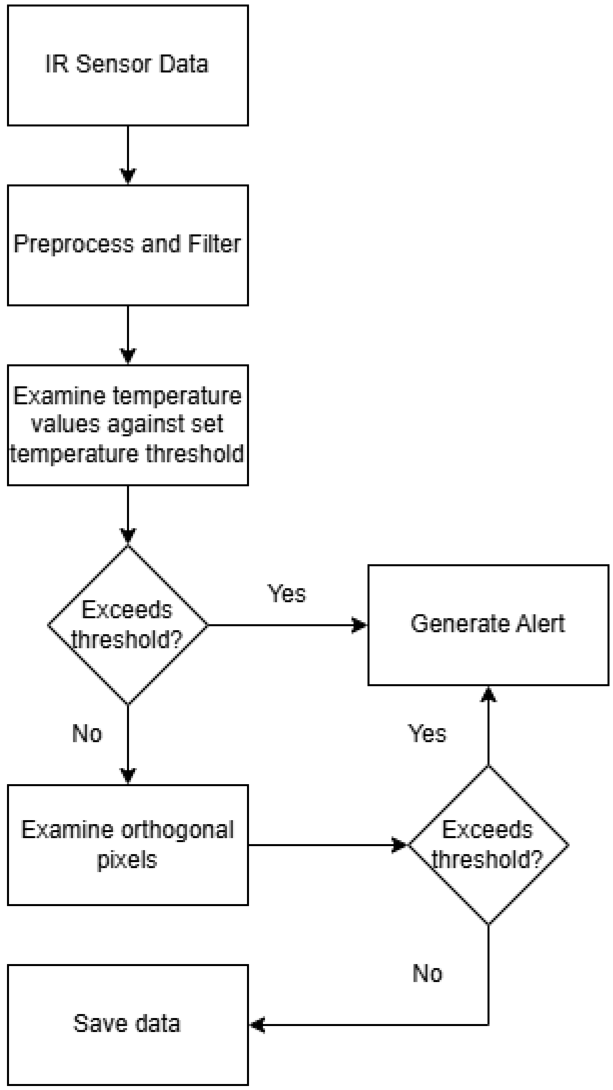

Figure 7.4 – Hotspot Algorithm Flowchart

7.1.3 Raster Scanning Algorithm

The stepper task implements a continuous raster scanning routine using two stepper motors, one controlling horizontal motion and the other controlling vertical motion. The task runs indefinitely inside a while loop, producing repeated scan frames. For each frame, the system iterates over a fixed number of lines defined by the number of lines per frame, in this instance being 16. Within each line, the horizontal motor first performs a forward scan by stepping a fixed number of increments leftwards, with a controlled delay between each step. This is to allow for IR sensor integration time. After completing the forward motion, the system pauses, and then executes a flyback phase where the horizontal motor reverses direction and returns to its starting position. This return motion includes an additional cushion to ensure consistent positioning and to mitigate mechanical slack.

Once the horizontal position is reset for the next line, the vertical motor advances downward by a small increment. This process repeats for each line, producing a raster scan pattern. After all lines in the frame are completed, the system performs a vertical reset by stepping the motor upward across the full vertical distance of the frame, plus a reset cushion to account for error. To address mechanical backlash, a small compensation sequence is then applied in the forward direction, restoring positional accuracy in the gears before the next frame begins.

7.2 UI Implementation

There are two UI elements that mirror the general structure of the software for IRIS. There is the local UI element, that being the LCD that must be maintained. Additionally, there is a Web interface to present the hardware information and process the data into a visual format.

7.2.1 Local UI

There are a few different key features that must be displayed on the local IRIS UI through the Sunfounder 1602 LCD. Below is a table that identifies these key metrics.

Table 7.2 – Key LCD Display Items

Data	Task	Purpose
Scanning	stepper_task	Ensure proper operation of the stepper.
Temperature	temperature_task	Measure the ambient temperature
Vibration	vibration_Task	Notify user of any detected vibration
Measurement	ADC_Task	Ensure that IR data is being received and transformed using the ADC.

7.2.2 Web UI

IRIS's intended goal is to facilitate autonomous remote hotspot thermal monitoring for electrical equipment. While prior chapters have expanded on the sensor and hardware implements of this task, the voltages, bytes, and signals of the board must be taken and made interpretable for the user. The website UI intends to achieve some of these tasks to facilitate the use of IRIS. The website UI should achieve the following as detailed below:

- Store data and display for records
- Visualize hotspots and the thermal visual scene
- Process incoming data and relay an alert on the page

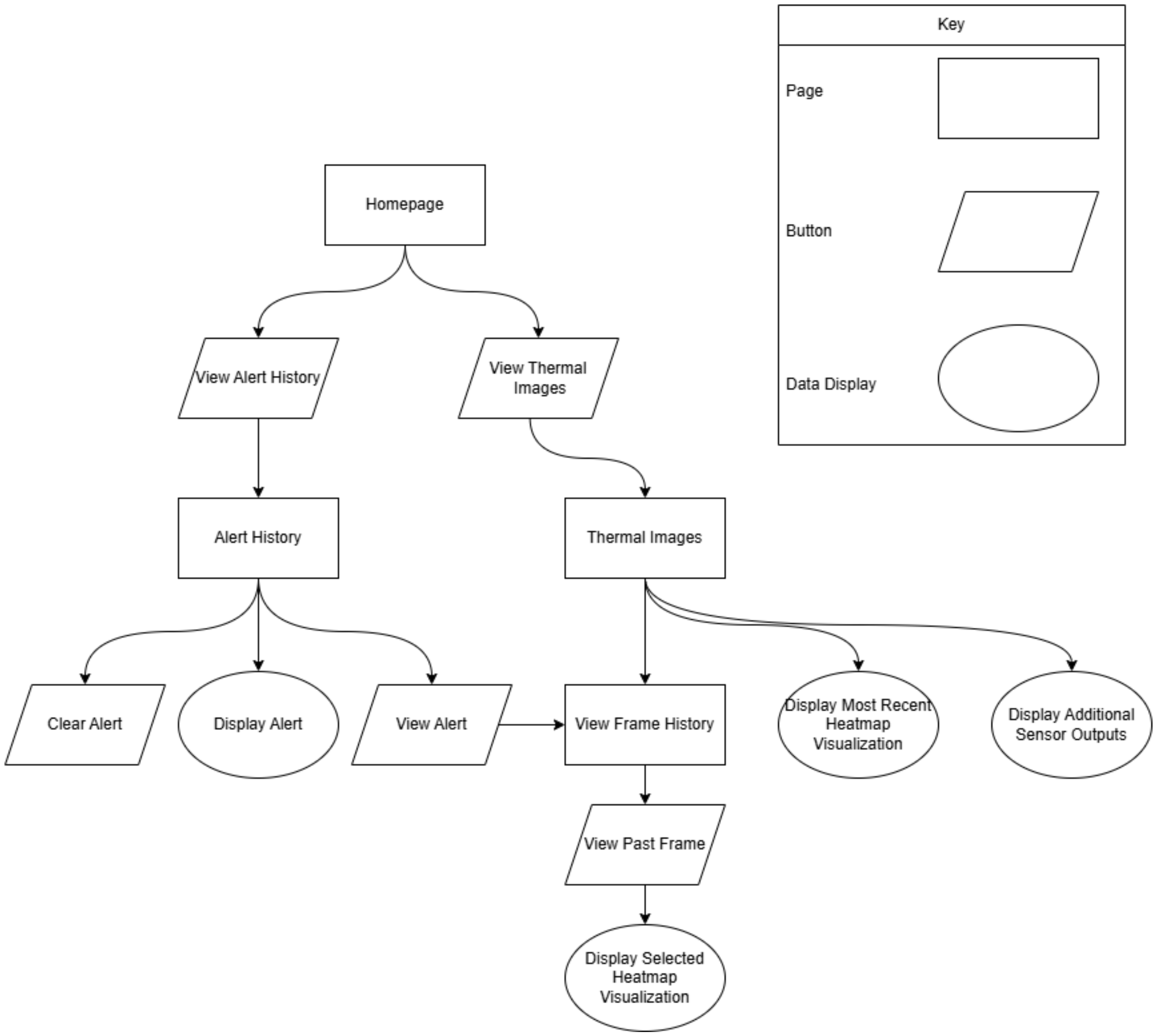

Figure 7.5 – Website UI Flowchart

Figure 7.5 represents a simplified layout of the website's framework. In the key provided, each shape indicates the page, data, and buttons to transition between pages. The buttons and data display represent the information on the screen, while the square pages represent the current webpage that the data is being displayed on.

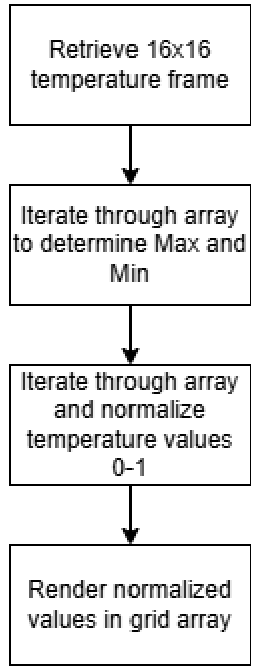

Figure 7.6 – Color Rendering Diagram

Figure 7.6 represents the conceptual process behind creating our heatmap on the website. The raster scanning process means that there are 256 neatly arranged temperature values that need to be mapped to a float value between 0-1. Once the data set's extrema have been determined, the preprocessing can take place using the following formula:

$$norm = (val - min) \div (max - min)$$

With this data, the values can be mapped to a color gradient from blue, the coldest value, to red, the hottest. The color codes of the gradient values in between would then multiply with the R and B values to generate the intermediate color codes.

7.3 Web Server Implementation

The IRIS backend architecture is utilizes a Node.js runtime environment hosted on a dedicated laptop to serve as the system's data preprocessing center. This setup creates a hardware-to-software wireless connection where the ESP32 transmits data from the sensors, sending 16×16 temperature data grids and system information via HTTP POST requests over a local Wi-Fi network. Using the Express framework, the backend receives these JSON, ensuring structured data handling locally.

For immediate visual feedback, Socket.IO is integrated to provide a bidirectional, low-latency communication channel, streaming incoming thermal data directly to the React frontend as it is received from the POST. Simultaneously, the backend utilizes SQLite to manage received data. The website's database allows the system to log prior frames and alert events with minimal overhead, ensuring timely display.

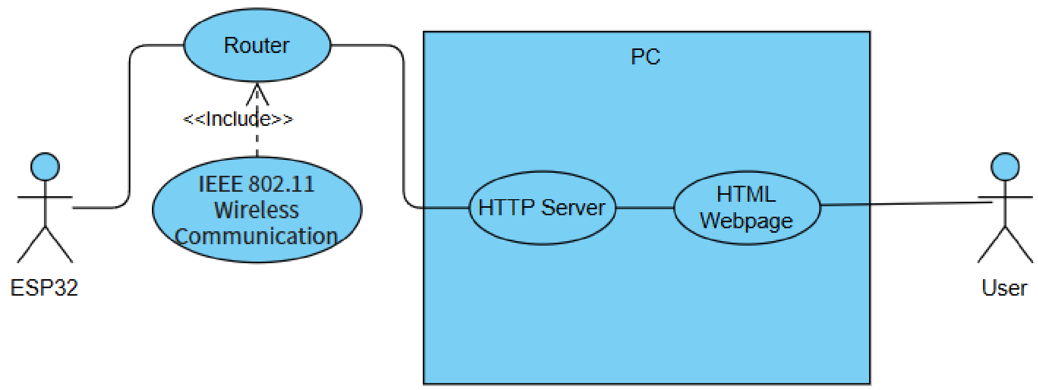

Figure 7.7 – Backend Communication Diagram

Chapter 8 – System Fabrication/Prototype Construction

8.1 Main PCB Layout

The PCB layout for the IRIS system was developed in KiCad, which provided an integrated environment for schematic capture, footprint management, and board layout. The board consolidates all electronic subsystems described in Chapter 6 onto a single rectangular two-layer board, including the power regulation stages, the ESP32-S3 microcontroller, the stepper motor drivers, the thermopile signal chain, the vibration detection circuit, and the I²C peripheral interface. To ensure reliable operation across both analog and digital domains, the layout was developed to meet four primary design goals:

Signal Integrity: The PCB must preserve the low-amplitude analog signals from the thermopile sensor without contamination from digital switching noise. This was achieved by physically separating the analog front-end from digital and power-switching regions. The thermopile sensor and its AD620 amplification chain are located in a dedicated analog section toward the middle-right of the board, isolated from both the stepper motor drivers in the lower-left and the digital activity surrounding the ESP32-S3 in the top-center. A continuous ground plane was implemented using polygon pours on both layers, providing a low-impedance return path for both analog and digital signals and reducing electromagnetic interference (EMI) coupling between subsystems.

Power Distribution: The PCB must deliver stable 5 V and 3.3 V rails to all subsystems with minimal voltage drop, even during high-current motor switching events. To meet this goal, the two regulators were placed at opposite corners of the board to thermally and electrically separate them: the 3.3 V AMS1117 regulator is located in the top-left near the ESP32-S3 and its low-voltage peripherals, while the 5 V LM2596 switching regulator is placed in the bottom-left to handle the higher-current paths feeding the motor drivers.

Trace widths were scaled to current requirements, with 0.50 mm traces for 3.3 V distribution and 0.80 mm traces for the 5 V supply and stepper motor connections. Standard signal routing used 0.30 mm traces, with 0.20 mm reserved for fine-pitch IC connections. Decoupling capacitors were placed as close as possible to each IC's power pins to minimize current loop area and suppress high-frequency supply noise.

Subsystem Organization: The PCB must arrange components in a logical, traceable manner that supports both initial bring-up and future debugging. Components were grouped by subsystem and arranged to minimize signal path lengths between functionally related parts. The ESP32-S3 occupies the top-center of the board as the central processing hub, with its USB programming interface positioned to its right for convenient access. The ADS1115 analog-to-digital converter is placed directly below the ESP32-S3 to keep its I²C lines short while remaining adjacent to the analog front-end it samples. The stepper motor driver section sits beneath the 3.3 V regulator, isolating its switching transients from the analog region. The piezoelectric vibration sensor occupies the bottom-right, with the MCP9808 temperature sensor placed just to its left to provide localized environmental monitoring. The full component placement is shown in Figure 8.1.1.

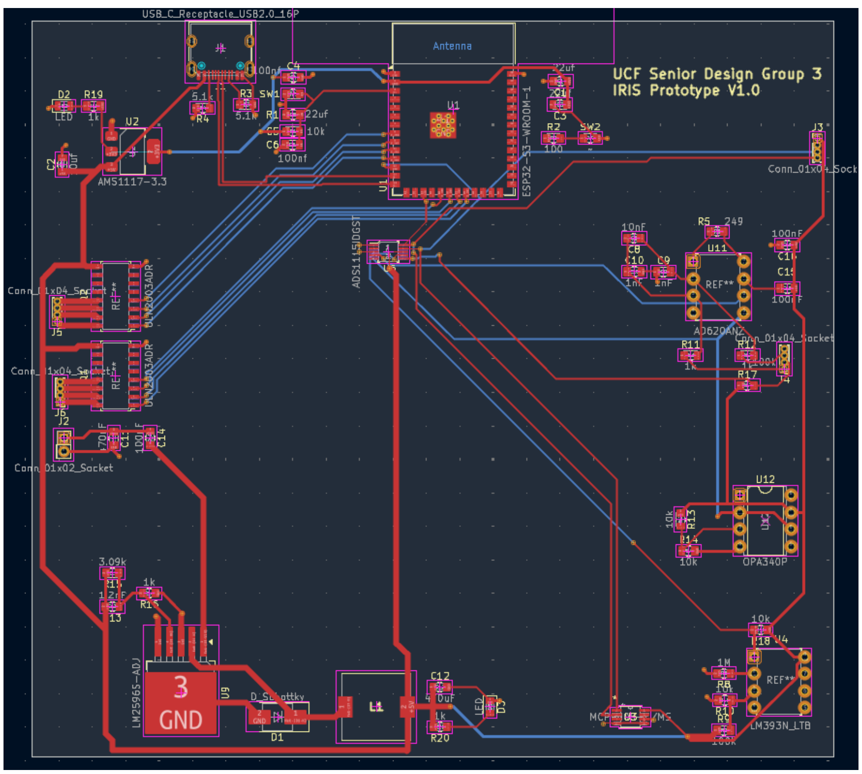

Figure 8.1.1 – IRIS PCB Layout (Top View)

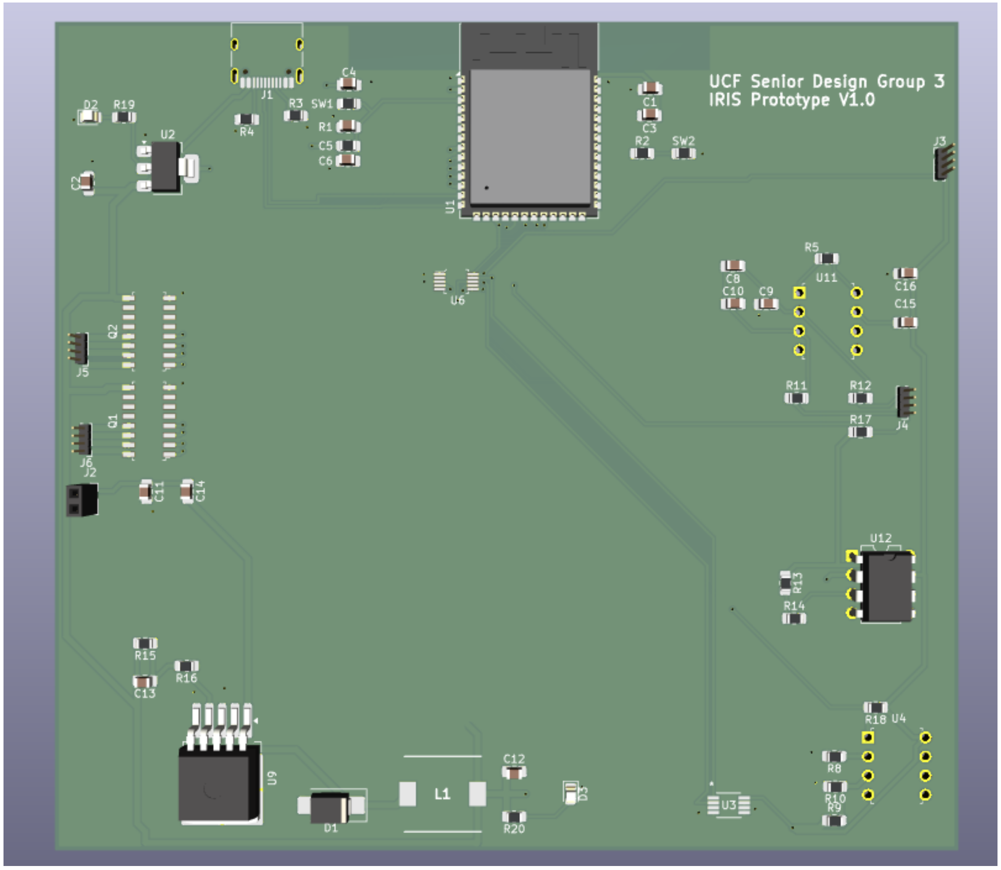

Figure 8.1.2 – IRIS PCB Layout (3D View)

Testability and Maintainability: The PCB must support iterative testing and modular integration with external subsystems. To meet this goal, header pins were provided for all off-board connections, including the stepper motors, the thermopile sensor, the LCD display, the user interface buttons, and the battery input. This modular approach allows individual subsystems to be disconnected for isolation testing without removing components from the board. All components, headers, and signal nets were labeled with silkscreen reference designators and signal identifiers, improving assembly accuracy and reducing wiring errors during bring-up.

Overall, the IRIS PCB layout reflects a structured design approach that balances electrical performance, mechanical organization, and system maintainability. The combination of subsystem separation, scaled trace widths, robust grounding, and modular external connections supports reliable operation while preserving the flexibility needed for testing and future revisions.

8.1.1 AS5600 Encoder Breakout Board

In addition to the main PCB, a small dedicated breakout board was designed to host the AS5600 magnetic rotary encoder. A separate board is required because the AS5600 must be mounted concentrically with the axis of rotation to remain centered beneath the diametric sensing magnet, a position that cannot be accommodated on the main PCB without compromising the layout of the rest of the system. The encoder breakout is shown in Figure 8.1.2.

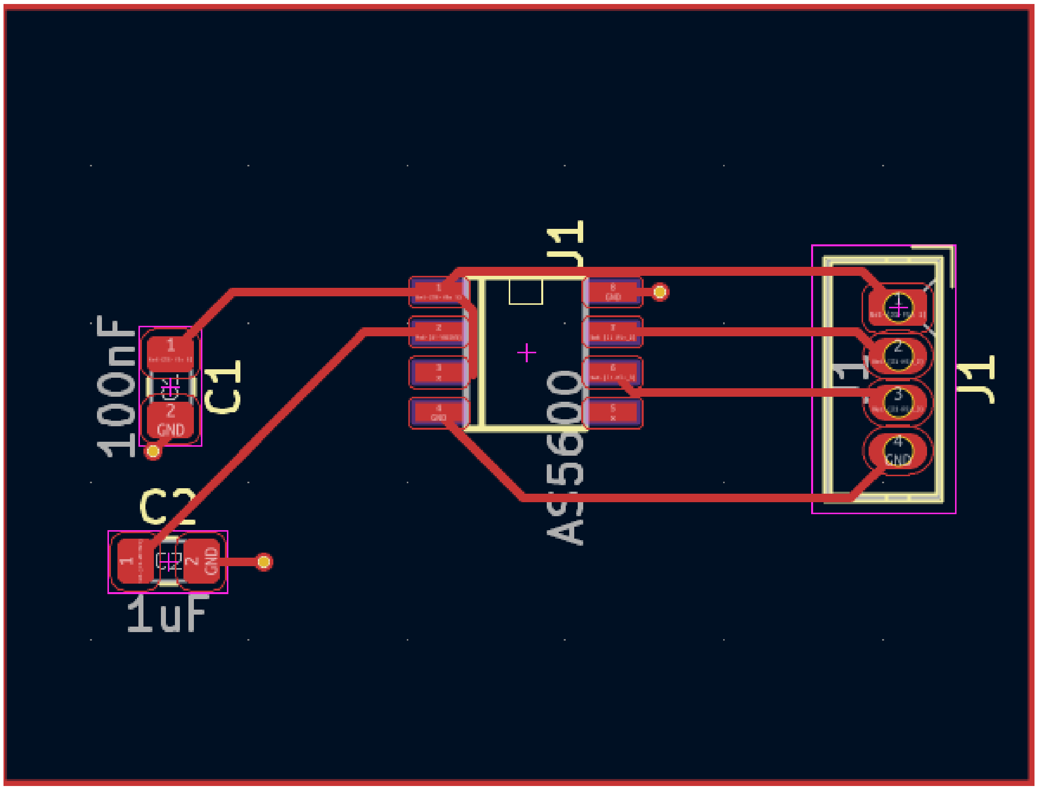

Figure 8.1.2 – AS5600 Encoder Breakout PCB Layout

The board is rectangular and minimally sized to keep its mechanical footprint compatible with the gimbal assembly described in Section 8.2. The AS5600 is placed at the geometric center of the board to align with the rotation axis when mounted, with the two decoupling capacitors (C1: 100 nF, C2: 1 µF) located immediately adjacent to their respective supply pins to minimize loop inductance. A four-pin header (J1) provides the off-board interface, carrying VDD, SCL, SDA, and GND to the main PCB through a short flexible cable. Mounting holes at each corner of the board allow it to be rigidly fixed to the rotating assembly so that the sensor remains in a known orientation relative to the magnet throughout the full range of motion.

Trace widths follow the same convention used on the main PCB: 0.30 mm for I²C signals and 0.50 mm for power distribution. A ground pour covers the unused board area to provide a low-impedance return path and reduce noise pickup on the I²C lines, which run alongside the stepper motor wiring during transit between the encoder and the main board.

8.1.2 PCB Revisions

The layout described above corresponds to an early revision of the IRIS main board. Following initial bring-up and mechanical fit checks against the gimbal assembly, the design was consolidated into a substantially smaller board, reducing the overall footprint by over 50%. The most significant change was the removal of the thermopile amplification chain from the main PCB. In the revised architecture, the AD620 was changed to an AD8629. The front-end was relocated to a dedicated external amplifier board mounted immediately adjacent to the sensor, so that the low-amplitude thermopile output is amplified at the point of measurement rather than being routed across the main board to reach the gain stage. This change improves signal integrity by minimizing the length over which the unamplified microvolt-level signal is exposed to conducted and radiated noise, and it simultaneously eliminates the need for a dedicated analog region on the main PCB — the constraint that had driven much of the original placement strategy. With the analog section removed, the remaining digital, power-regulation, and motor-driver subsystems could be packed more densely without the isolation clearances previously required between them. The final main board retains the ESP32-S3 and its USB programming interface, the 3.3 V and 5 V regulation stages, the stepper motor drivers, the ADS1115, and the I²C peripheral interface, and connects to the amplifier board through an SMA header carrying the amplified analog output along with its supply and ground references. The trace width conventions, ground pour strategy, and header-based modular interfacing described above were carried forward unchanged. The final board used in the assembled prototype is shown below.

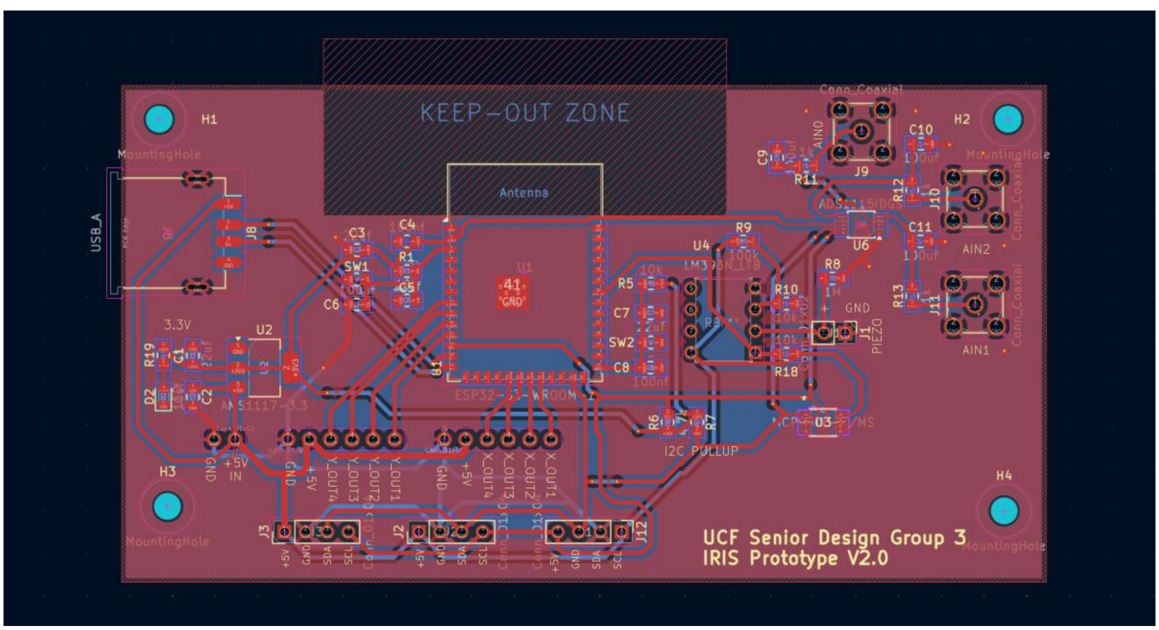

Figure 8.1.3 – Revised MCU PCB Layout

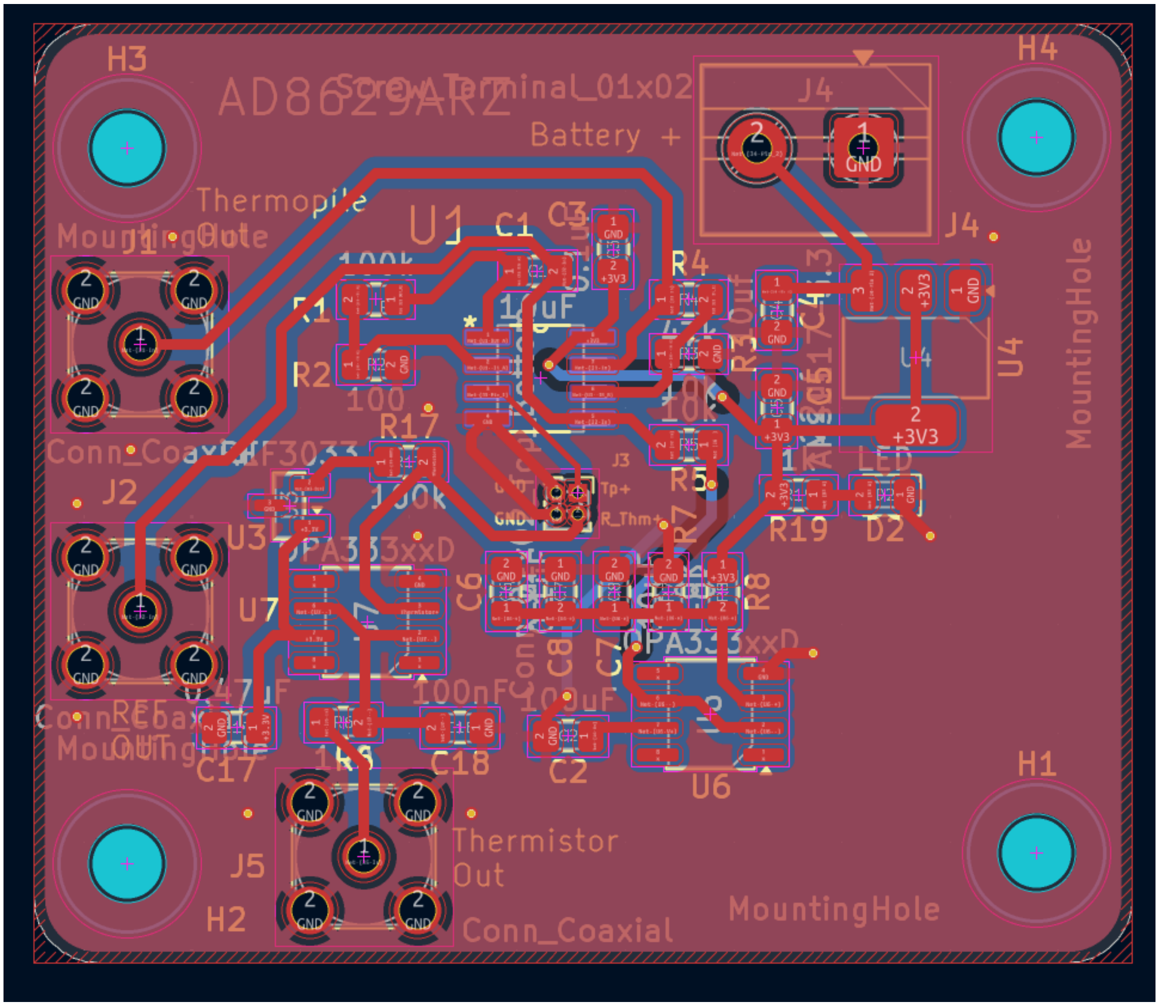

Figure 8.1.4 – Amplifier PCB Layout

8.2 Mechanical Design

To reconstruct an image, our system requires a mechanical design and implementation that is able to achieve accurate and precise mechanical beamsteering…

8.2.1 Pan-tilt gimbal architecture mechanics

A pan tilt architecture is a two degree of freedom positioning system that steers an object in a structured pattern over the scene. The horizontal “pan” axis typically forms the base of the system, providing rotation about a vertical axis while the vertical “tilt” axis is mounted on top and controls rotation about the horizontal axis. In our implementation, the horizontal stepper motor and its mount becomes the base of the system, meaning the entire upper assembly rotates with its motor shaft. This stacked architecture is common because it simplifies control by decoupling azimuthal and elevation control in the software while maintaining a relatively compact footprint. Additionally, freely available CAD designs online provide our team context on how they’re typically modeled and design considerations to be aware of. This provided our team with an appropriate starting point for our mechanical design.

In an ideal pan-tilt gimbal for optomechanical scanning, both axes of rotation would intersect precisely at the center of the mirror's front reflective surface, because this ensures that beam steering is purely angular with no unintended spatial displacement. When the axis of rotation passes through the reflective surface, the reflected ray pivots about a fixed point in space, producing a clean and predictable scan geometry that maps directly to angular commands. However, in practical implementations, this alignment is not achievable due to mechanical constraints such as the need for mounting hardware, bearings, and shaft support behind the mirror. As a result, the rotation axis is offset from the reflective surface, causing the mirror to sweep through a small arc as it rotates. This introduces a coupled effect where the reflected beam undergoes both angular deflection and slight translation, leading to distortions in the raster scan such as non-uniform spacing or pointing error that increases with angle. For this reason, our design aims to minimize the distance between the axis of rotation and the mirror surface. From there, we plan to account for the offset through calibration, in order to preserve scan accuracy and maintain a well-behaved imaging geometry.

8.2.2 CAD Design decisions and iterations

The CAD design for our project was accomplished in Autodesk fusion, with a strong design focus on structural integrity and manufacturability through 3D printing. Wall thickness was a key parameter here, as insufficient thickness led to unwanted flexibility whereas excessive thickness did not carry much limitation. This was one of the core benefits of the 3d printing technology, as thick walls are supported by infill rather than being solidly filled throughout. Overhang limitations inherent to the 3D printing process and filament material were also carefully considered. Instead of relying on unsupported features, produced by bridging or long overhang walls, 45° overhangs were incorporated into areas such as holes and bridging regions to improve print strength, reliability, and reduce the need for support structures. This ensured that the design remained both functional and practical to fabricate.

The initial CAD models were created with zero tolerances to establish clean geometry, and later tolerancing was introduced using the offset faces tool to ensure proper fit between components. To improve accuracy and reduce iterative approaches to component compatibility, reference models of key hardware components were inserted in the design. This included models of the KM100 mirror mount from Thorlabs, and the 28BYJ-48 stepper motor. With these designs in the workspace, we are able to project key geometric features onto our sketches as well as visually verify fit. The overall architecture of the design was also influenced by a publicly available pan-tilt gimbal design from Printables, but ultimately the entire system was designed from scratch to meet our project's needs.

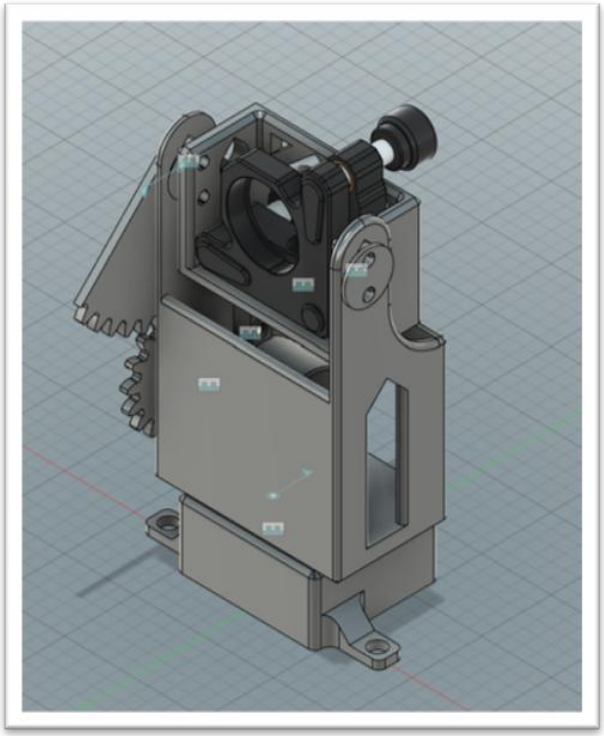

Figure 8.2 – First iteration design gimbal design

The first iteration relied heavily on hard-defined dimensions, which made the design process rigid and difficult to modify as issues arose. Although a functional system was eventually achieved, problems with clearance of moving parts and gear performance revealed weaknesses in this approach. In response, we began developing the second revision which adopted a more parametric design methodology, where key variables such as wall thickness and tolerances were defined as adjustable parameters. This enabled faster and more efficient iteration while reducing redesign time.

8.2.3 Gear System Design

In our mechanical design, the gearing system is the solution to the need for customizing the rotation of the mirror. The first problem to solve was to introduce rotation about the horizontal axis while keeping the weight distribution of the assembly roughly even. This constraint was put in place so as to not introduce too much inertia on any motor shaft. To that end our design, like other reference designs, does not have the output of the tilting motor and the rotation of the mirror collinear. Instead, they are separated along the vertical axis by some distance. In order for rotation at the tilting motor to cause rotation at the mirror axis, a meshing gear system must be used to translate the rotational movement over some distance. Gear design forces the mapping between motor shaft movement and mirror rotation to change, however its limitations can be overcome with calibration and their implementation comes with great benefit. More complex gearing systems can be implemented to achieve finer angular resolution, as well as greatly reduce or even eliminate mechanical backlash. For this reason, we determined that gear design is a power tool to ensure reliable operation of our imaging system.

8.2.3.1 Current gearing system implementation and limitations

Spur gears are one of the simplest and most direct ways to transmit rotational motion between parallel shafts, which made them a practical starting choice for our system. In our implementation, we press-fit a spur gear with 44 teeth onto the tilt motor shaft as the input gear, while a 17-tooth spur gear is directly attached to the mirror mount as the output. As the motor rotates, the teeth of the larger input gear engage with the smaller output gear, transferring motion to rotate the mirror about its horizontal axis. This creates a gear reduction, which we found to be successful in improving the system's performance by allowing larger motor steps to correspond to finer angular motion at the mirror. After implementing the gearing, we calibrated the vertical step size to account for this reduction so that the raster scan spacing matched our desired angular resolution.

However, in testing this approach revealed several limitations. Since the center distance between the gears is not rigidly fixed, the quality of gear engagement varies throughout the range of motion. This leads to noticeable backlash, where there is a delay before motion is transmitted when changing direction. We also observed regions where the system seems to struggle to move and then suddenly break free, which is likely caused by slight misalignment or inconsistent tooth contact. We attribute this as partially inherent to the Initially, we used gears that were 3 mm thick, but they proved too flexible and did not maintain reliable engagement. As a quick improvement, we increased the gear thickness to 10 mm, which made the gears more rigid and improved contact between the teeth. While this helped the system perform better for our raster scanning demonstration, it does not fully address the underlying issues with alignment and constraint, which we plan to improve in future iterations.

8.2.3.2 Design Revisions

Initial testing of the scanning mechanism identified sources of positioning error associated with mechanical compliance, friction, and inconsistent shaft support. To improve system performance, the transmission was redesigned using commercially available ball bearings to support the rotating shafts, reducing friction and minimizing radial play during operation. The printed structural components were also redesigned with increased wall thickness to improve stiffness and reduce deflection under load. In addition, the gearbox geometry was revised to rigidly define the center distances between mating gears through the housing itself. Dedicated input and output shafts, along with a rigidly supported idler shaft, were incorporated to improve alignment and maintain consistent gear meshing throughout operation. These modifications significantly improved the mechanical stability of the scanning mechanism while preserving the overall architecture of the pan-tilt system.

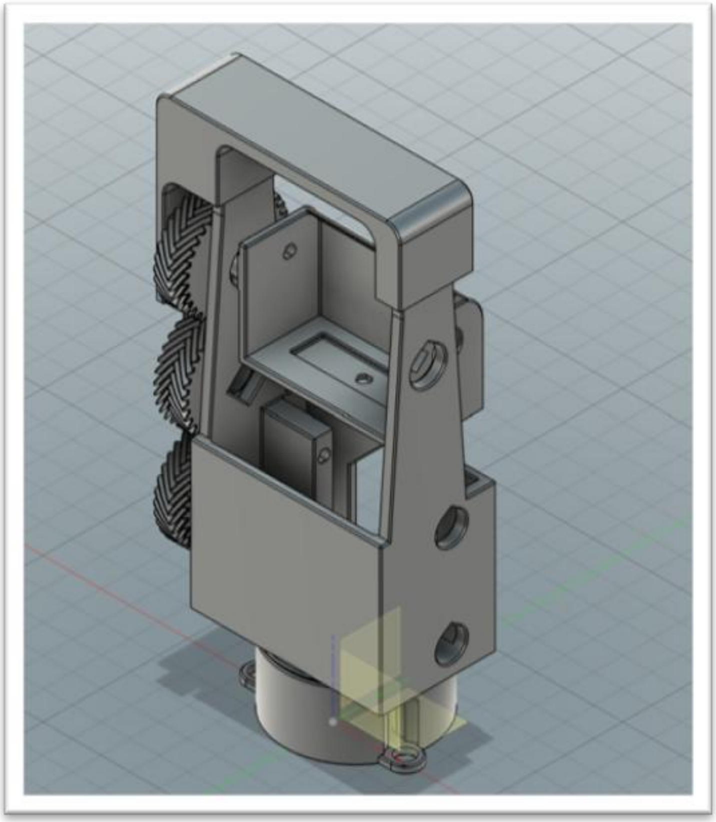

Figure 8.2.1 – Final Gimbal Design

8.2.4 Lens Tube & Translation Stage Design

A modular lens tube assembly was developed to support the optical components while providing precise adjustment of the detector position. The assembly was mounted to a custom translation stage that establishes the optical axis height and allows controlled motion along the optical axis for focusing. The translation stage uses a lead screw to provide fine linear adjustment, while three parallel guide rails constrain the motion and maintain alignment during translation. This configuration minimizes unwanted rotation and tilt of the detector assembly, allowing the focal position to be adjusted without significantly disturbing the optical alignment.

The lens tube was designed to securely integrate the objective lens, LWIR bandpass filter, and thermopile detector into a single assembly. Heat-set threaded inserts were incorporated into the printed components to provide durable mounting points for both the objective lens and the detector amplifier PCB. Rather than translating the detector independently, fine focus was achieved by rotating the amplifier board within the threaded lens tube, allowing the detector position to be adjusted relative to the fixed optical components. This approach simplified assembly while providing repeatable focus adjustment and facilitating iterative optical alignment during prototype development.

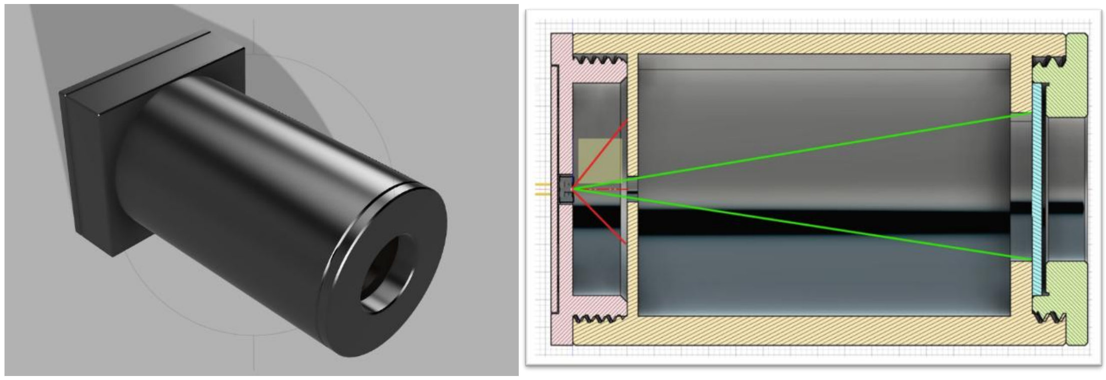

Figure 8.2.2 – Lens Tube Design and Cross-Sectional View

Additional design features were incorporated to improve measurement quality by reducing unwanted optical and electrical interference. An internal baffle lined with aluminum foil was positioned within the lens tube to restrict the detector field of view and reduce the amount of background infrared radiation reaching the thermopile from the enclosure. Surrounding the detector electronics, a custom Faraday cage was integrated into the assembly to shield the amplifier circuit from electromagnetic interference. Together, the optical baffling and electromagnetic shielding improved the stability of the detector output and helped preserve the integrity of the microvolt-level thermal signal during operation.

8.2.5 Additional Mechanical Designs

To support optical alignment and component mounting without the cost of commercial optical hardware, a custom optical breadboard and post mounting system was designed and fabricated using FDM 3D printing. The breadboard CAD design was free available online at printables.com, and was printed with a pause inserted at the appropriate layer height, allowing M6 hex nuts to be placed into recessed pockets before the print resumed and encapsulated them fully within the part. This created threaded inserts that accept M6 screws without requiring tapping or heat-set installation. Post holders and mounting posts were then redesigned in CAD to follow the same fabrication philosophy, with each component either printed over embedded nuts or designed with snap-fit channels that allow nuts to be slid in after printing. The M6 screw interfaces serve two distinct functions depending on location: screws through the base of the post holder thread into the breadboard nuts to fix the assembly's horizontal position, while a second screw through the post holder clamps the post itself in place through frictional clamping force, allowing vertical height adjustment before locking. Mounts for the laser module were designed using the same approach, and the method is easily extendable to the other optical components needed for our project.

The resulting mounting system replicates the core alignment functionality of commercially available optical post and breadboard hardware at a fraction of the cost. Like machined optical posts, the printed posts allow vertical translation of the mounted component by sliding within the holder before clamping, and the post holder's interface with the breadboard permits horizontal rotational adjustment for angular alignment within the optical plane. This provides the two degrees of freedom most commonly needed for single-detector scanning system alignment. However, deformation has been observed in the printed post material under clamping load, which reduces the rigidity and repeatability of the height lock over repeated adjustments. As a result, a design revision is under consideration to make the post holders compatible with existing machined metal posts available in the undergraduate laboratory, which would retain the low-cost printed breadboard and holder architecture while substituting the structurally critical post element with a more dimensionally stable metal alternative.

Chapter 9 – System Testing and Evaluation

9.1 Optoelectronic Feasibility Study

9.1.1 Radiometry Approach

Our radiometric analysis began with the Stefan-Boltzmann law, which provides the total radiant exitance from a grey body source as $M = \in \sigma T^4$. While this equation is simple, it's integrated over all possible wavelengths meaning it gives the total radiance over the entire spectral band. This is a problem as we are only interested in the 8-14 µm spectral band as a large portion of the energy from our target temperatures lie here, and noisy background will be filtered out. To address this, we applied an engineering shortcut using the fraction of energy function, F(λ,T), which quantifies the portion of total blackbody radiation emitted within a given wavelength range. By evaluating F(8-14 µm*T) for our target temperatures, we could directly estimate the percentage of emitted power captured by the detector's spectral response, allowing a more accurate calculation of the radiative power available without performing complex spectral integration over the entire blackbody curve. From our calculations, about 40% of the radiant exitance is in our wavelength band of interest, and that exitance is further reduced by an emissivity constant of about 0.8-0.9 for our electronic painted surfaces. In our approach, we notice that the surfaces have roughly the same emissivity, so a mean or average emissivity value can be used to great effect.

With the radiant exitance established, the next step was to account for the geometric coupling between the target, optics, and detector through appropriate solid angle definitions. Rather than using only the aperture-limited solid angle, we separated the analysis into two relevant terms: the detector acceptance solid angle and the instantaneous field-of-view (IFOV) solid angle. The detector solid angle was determined by assuming a field stop with a 1:1 conjugate at the detector plane, using a detector width of 1.2 mm, which yielded a value of approximately 0.040 sr. This represents the total angular extent of radiation the detector can accept through the optical system. In contrast, the IFOV solid angle, corresponding to the angular extent of a single resolution element on the target, was approximated using the small-angle relation $\Omega \approx \theta^2$, giving a value of 2.56×10^{-4} sr. This term governs how much of the target's radiance is resolved within a pixel. Together, these solid angles replace the simpler aperture-based estimate and more accurately describe the system's radiometric throughput: the detector solid angle defines the total collected radiation, while the IFOV solid angle determines how that radiation maps to a specific portion of the scene.

Finally, we derived the power at the detector using a modified radiometric relation. Adapted from a paper on thermal imaging of unresolved targets, the equation represents the differential or signal power at the detector when the target area's angular extent is smaller than the IFOV of the imaging system. It's also worth noting as well that the paper was utilizing a thermal sensor array, rather than a single detector.

$$\Delta P_{sensor} = A_{lens}(\tau_{sys}(L_{tgt} - L_{bg})\Omega_{lens} + L_{stray}\Omega_{stray})$$

Adaptations must be made to the formula for resolved imaging, which involves removing terms such as background radiance. In this case, the background radiance represents background energy at the object scene, which we do not have as our target area fills our IFOV. Instead, we must consider stray radiance, which appears in all our measurements as it represents radiance from the enclosure or the lens tube fitted to our sensor. In our analysis, we realized that the stray contribution is large, and so we are looking for a small power fluctuation corresponding to the scene on top of a decently large DC power contribution from the background.

$$P_{det} = A_{lens}\left(\tau_{sys}L_{tgt}\Omega_{lens}\right) + A_{detector}(L_{stray}\Omega_{detector})$$

Together, these design choices simplify the power equation, allowing us to model power at the detector depending on what temperature the target area is, allowing us to do contrast analysis and SNR analysis.

9.1.2 SNR Analysis

To estimate the detectability of thermal contrast in the scene, the power incident at the detector was calculated separately for a hot target at 90°C and a cold target at 40°C, both containing the energy from stray radiance at 30°C. Since the background radiance is present in both measurements, the differential signal power was extracted for each case by subtracting the background contribution, yielding a positive differential for the hot target and a negative differential for the cold target.

Afterwards, we needed to estimate the system noise from contributions from both thermal noise and electronic noise. The measurement bandwidth was determined by the per-pixel integration time, which we estimated to fall between 10 ms and 25 ms to allow sufficient collection at each pixel while remaining compatible with the thermopile's intrinsic time constant of 10 ms specified in the datasheet. Taking the integration time limits as the bounds, the corresponding bandwidth range is given by the inverse relationship f = 1/t, yielding an operating bandwidth of between 40 Hz and 100 Hz, and the noise calculations were performed at the 100 Hz end of this range as a conservative worst-case estimate of the system noise floor.

The total system noise was estimated by combining the dominant noise sources in quadrature. The first is the intrinsic Johnson noise of the thermopile resistance, given by$S_{n,TP} = \sqrt{4 * k_b T * R_{TP}}$ which is 37.3 nV/√Hz using the thermopile resistance of 84k ohm at 30°C. The second is the electronic noise of the AD620 instrumentation amplifier used as the first stage, which has two contributions: an input-referred voltage noise that rises significantly below the 1/f corner frequency of approximately 1 kHz, reaching an estimated 28 nV/√Hz at the 100 Hz operating point, and a current noise of 0.1 pA/√Hz which, flowing through the 84k ohm thermopile source impedance, contributes an additional 8.4 nV/√Hz. These two AD620 contributions combine to a total electronic noise of 29.2 nV/√Hz. The PGA second stage noise is negligible when since it's decreased by the AD620 gain according to Friis' formula for noise figures. The total input-referred noise spectral density was therefore computed as

$$S_{n,total} = \sqrt{S_{n,TP}^2 + S_{n,AD620}^2}$$

Which calculates to a total noise contribution of 47.4 nV/√Hz.

Metric	Magnitude	Note
Differential Voltage (mV)	135.5	
Total NEP (uW)	10.77	
Total NEP (mV)	62.6	Comparable to signal
Contrast SNR (Linear)	2.166	
Contrast SNR (dB)	6.713	Acceptable for detection
NETD (°C)	30	Not acceptable

9.1.3 Feasibility Conclusion

The feasibility analysis indicates that the system operates near the threshold of reliable detection but remains viable for identifying thermal contrasts. The measured differential signal of 135.5 mV is on the same order as the noise-equivalent signal of 62.6 mV (derived from a total NEP of 10.77 μW), yielding a contrast SNR of approximately 2.17 (6.7 dB). This places the system above the theoretical detection limit (SNR ≈ 1), indicating that hotspot signals are distinguishable from noise, though not with high confidence. While this SNR is slightly below the typical target range for robust detection (≈3–5), it is sufficient for basic hotspot identification under controlled conditions. Overall, the results suggest that the system is feasible for detection tasks, but performance would benefit from improvements in signal strength or noise reduction to enhance reliability and detection confidence.

It's worth noting that the noise figure we obtained represents around a 26% increase in total noise spectral density compared to a chopper-stabilized first stage since it introduces an unmitigated 1/f noise contribution that grows further at lower operating frequencies, making the AD620 a suboptimal first stage choice for this application. As we continue the project, the chopper amplifier presents itself as a solution to this problem by modulating and demodulating the signal to achieve the lower white noise in its noise bandwidth range as well as its typically low current noise. By combining chopper stabilization with low current noise input stages, the dominant noise contributors are reduced, lowering the effective NEP and enhancing NETD performance in the imaging system.

9.2 System Component Testing

9.2.1 Environmental Temperature Sensor Testing

Environmental temperature testing was conducted to verify that the MCP9808 temperature sensor accurately measures ambient room temperature and responds to heat sources. The test setup consisted of the temperature sensor interfaced with the ESP32 microcontroller, with real-time readings displayed on the LCD screen.

The initial test condition involved measuring the ambient room temperature. The sensor provided stable and consistent readings that reflected the surrounding environment, confirming proper operation and reliable communication between the sensor, ESP32 and LCD display.

To evaluate responsiveness, a finger was placed directly over the temperature sensor to introduce a heat source. The sensor detected an increase in temperature, which was immediately shown on the LCD display. This confirmed that the sensor is capable of detecting small temperature changes. After removing the finger, the temperature readings gradually returned to the base room temperature, demonstrating expected recovery behavior.

This test verified that the temperature sensor can accurately measure ambient conditions while also responding to nearby heat sources. These results confirm that the sensor is functioning as intended and is suitable for supporting environmental monitoring within the IRIS system.

9.2.2 Piezoelectric Accelerometer Testing

Piezoelectric accelerometer testing was conducted to verify that the vibration sensing subsystem of the IRIS system is capable of detecting mechanical disturbances. The sensor used operates based on the piezoelectric effect, where mechanical stress or vibration generates an electrical signal.

The test setup consisted of the piezoelectric vibration sensor connected to the ESP32, with the sensor output monitored and processed by the microcontroller. The system was also interfaced with the LCD display to provide real-time feedback when vibrations were detected.

Under static conditions, where no external vibrations were present, the sensor output remained near a steady baseline, indicating stable operation and minimal noise. To evaluate sensor responsiveness, vibrations were introduced by tapping near and on the sensor, lightly disturbing the surrounding surface. These disturbances caused the piezoelectric sensor to generate a voltage signal, which was detected by the ESP32.

When a vibration was detected, the system triggered a response that was displayed on the LCD screen, indicating the presence of a vibration. This provided immediate visual confirmation that the sensor input was successfully processed by the microcontroller. It was observed that stronger taps resulted in more noticeable responses, while lighter taps still produced detectable signals.

Understanding the stimuli that generates a response from the sensor is critical to informing how it will be implemented in the final product. The piezoelectric accelerometer’s wide sensor base means that flush connections with a surface of interest will generate the best and most consistent outputs.

Overall, this testing confirmed that the piezoelectric accelerometer is functioning correctly and that the system is capable of detecting and displaying vibration events. This validates the integration of the sensor with the ESP32 and LCD interface, supporting its use in monitoring mechanical disturbances within the IRIS system.

9.2.3 Stepper Motor Testing

Stepper motor testing was conducted to verify that the motors and driver circuitry produce accurate and repeatable motion for the mechanical scanning system. The motors were physically connected to the scanning mechanism and controlled through step and direction signals generated by the ESP32.

The system responded consistently to command step inputs, producing controlled motion of the scanning mechanism. Repeated tests showed stable operation, though minor positional deviations were observed due to mechanical backlash.

Overall, the motors successfully drove the scanning system and demonstrated sufficient performance for prototype operation.

9.2.4 ESP32-S3 Testing

ESP32 testing was done using a development board in conjunction with a breadboard-based prototype to verify communication with all subsystems. The ESP32 interfaced with sensors, the LCD display, and motor drivers through I^2C and GPIO connections.

The functionality of the ESP32-S3 was verified by a few of the following metrics:

- Power
- Flash
- Pins

The ESP32-S3's power system was found to be operational, using both the USB-C and 5 V input power pins and lighting up the development board's LED.
The ESP32-S3 was programmable, ensuring proper firmware operation on both the board and the IDE.
The output voltages of the pins were read and the pullup resistor functionality was utilized, ensuring normal GPIO operation.

9.3 Mechanical Evaluation

9.3.1 Scan Geometry and Step Accuracy

Our mechanical system's performance requires evaluation to determine its capabilities for scanning since angular movement resolution is directly related to spatial sampling resolution. Our approach was to evaluate the performance using a laser beam as a tool. The laser beam provides coherent light which can be visually tracked to provide us insight into our system's mechanical scanning characteristics. To achieve high spatial quality in our imaging, calibration is necessary to ensure that the part of the scene the system is imaging is accurate and repeatable.

Our calibration process involves optical alignment of the system and then between the system and the object to ensure a proper starting position for repeatability. The object scene at this stage consists of a flat surface with symmetrical and evenly spaced markings, similarly seen on grid paper. The intended object scene spatial extent is marked, as we begin to manually home the mechanical system to place the beam path where the intended start for the raster pattern is. This process can be automated later using mechanical switches or the rotary encoder IC to allow for accurate homing. After the system is homed, we power on the system and allow it to run. The firmware flashed controls the system to following a raster scanning pattern, where the number of steps that motor takes is directly proportional to the distance the beam travels on the object scene. After making an appropriate guess for how many steps the motor should take to complete one line of scanning, we measure the distance traveled by the beam and compare it to the intended distance traveled. This allows us to calculate the error of the programmed path and adjust the program parameters to hone in on the optimal script parameters for the ideal calibrated movement.

After we are satisfied with the parameters corresponding to the most reliable movement, we can characterize the final movement error by comparing the intended distance traveled to the actual distance traveled, resulting in the following table.

Horizontal movement error

Vertical movement error

9.3.2 Repeatability and Backlash

As the scanning system completes a frame, it will often need to reset to its original position to start a new frame. In that case, simply reversing all of the motor steps taken should result in the system at its original position. In practice, this is not the case. The motor system suffers from hysteresis, especially in its vertical movement

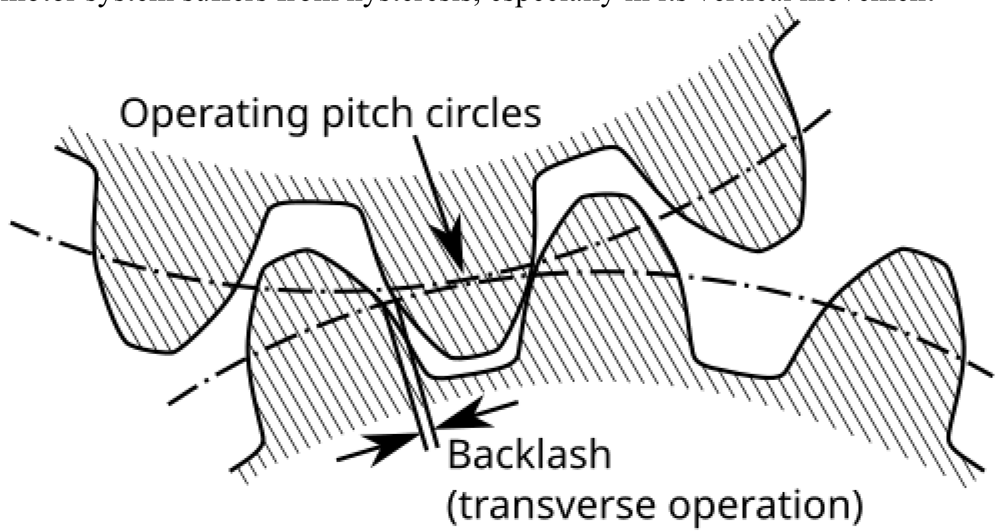

Figure 9.1 – Backlash Visualization

This hysteresis can be attributed predominantly to the backlash from the spur gear design. Spaces between the teeth of the gears mean that when changing the direction of motion, these small distances must be traveled before stepping can occur. These distances differ from the normal operation of the device and are only incurred when changing direction, meaning there is drift between frames of operation. The vertical stepping, which relies on these gears, acquires a fair portion of error over repeated trials which violates the raster scanning principle and critically endangers valuable measurements.

In order to maintain stability and reliability, the raster must traverse the same path every time and eliminate backlash. Many possible solutions have been considered in this regard, like changing the gear system as mentioned in Chapter 8. However, for the purposes of testing the viability of the stepper system, a software implementation was utilized to ensure proper operation of the mechanical system.

The error introduced from this method is fairly consistent and regular, and only needs correction when changing direction. Two related solutions were implemented to accommodate both vertical flyback and the reinitialization of the raster scan. For vertical flyback, an overcorrecting compensation was added to ensure that the sensor traverses the entire distance it traveled in addition to the error that was introduced. This means that drift accumulates far more slowly, increasing accuracy. A backlash compensation was also introduced in the form of a pre-loading of the downward direction on the gears immediately following flyback, but prior to regular raster behavior. These steps are critical in ensuring that the gear is receiving full torque when the raster begins.

With these methods in place, the raster scan could be completed and repeated over the course of many frames with a negligible drift introduction, thus verifying the mechanical system.

9.4 Overall Integration

The overall integration of the IRIS system was conducted to verify that all hardware and software subsystems operate cohesively as a unified embedded system. This phase evaluates system-level functionality, where the ESP32-S3 microcontroller coordinates sensor input, motor control, data processing, and user interface output in real time.

The integrated system consists of the ESP32-S3, the environmental temperature sensor, the piezoelectric vibration sensor, the stepper motor and driver circuitry, and the LCD display. All components were interconnected through their respective communication interfaces, including I^2C for the temperature sensor and GPIO/analog input for the vibration sensor and motor control signals. The LCD display serves as the primary user interface for real-time feedback.

During operation, the ESP32 continuously acquires temperature data from the environmental sensor while simultaneously monitoring the output of the vibration sensor. In parallel, the microcontroller generates step and direction signals to control the stepper motor, enabling controlled mechanical movement within the system. These tasks are executed concurrently, demonstrating the ESP32’s ability to manage multiple subsystems in real time.

The system processes all inputs and updates the LCD display accordingly. Ambient temperature readings are displayed continuously, providing a stable reference of environmental conditions. When a vibration event is detected, the system generates an immediate response that is shown on the LCD, indicating the presence of mechanical disturbance. Motor operation was observed to be consistent and responsive to control signals, with repeatable motion during testing.

Integration testing confirmed that sensing and actuation subsystems operate simultaneously without interference. The temperature sensor maintained stable readings while the vibration sensor responded to mechanical inputs such as tapping or surface disturbances. At the same time, the stepper motor operated reliably under ESP32 control, demonstrating consistent movement and proper driver functionality.

The LCD interface provided clear and immediate feedback, allowing users to observe system behavior in real time. The responsiveness of the display, combined with stable motor operation and reliable sensor readings, confirms that the system is capable of coordinated sensing, actuation, and user interaction.

9.5 Actual Implementation

During the second phase of development, the optical design was transitioned from individual subsystem testing to full system implementation. To simplify alignment before installing the infrared optics, a laser alignment module was designed with the same external profile as the final lens tube assembly. This allowed the laser module to be mounted directly into the translation stage, establishing the optical axis height and verifying that the two-axis scanning mirrors directed the beam across the intended field of view. Once the scanning geometry was validated, the laser module was removed and replaced with the completed lens tube containing the objective lens, filter, and thermopile detector.

As development progressed, the optical breadboard configuration was replaced by a modular enclosure designed specifically for system integration. The enclosure was constructed with removable side panels to provide easy access to the optical, mechanical, and electronic subsystems during assembly and troubleshooting. The base plate served as the primary structural component, containing the mounting features for the scanning mechanism, translation stage, electronics, and supporting hardware. This modular approach allowed individual components to be adjusted or replaced without requiring significant changes to the overall assembly.

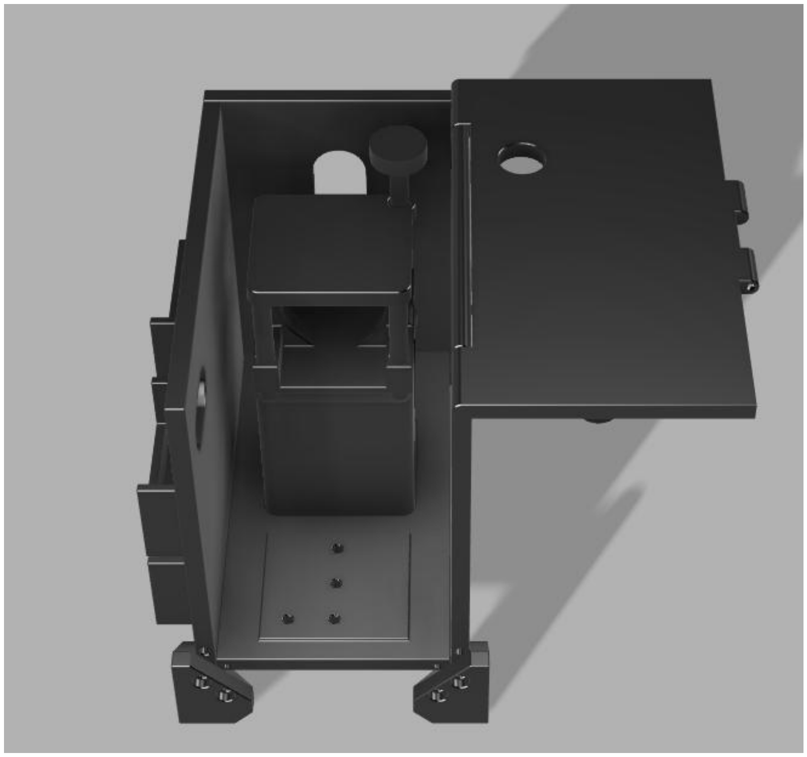

Figure 9.2 – Render of final system enclosure

Final optical alignment and calibration were performed iteratively using the translation stage and the system test target. The lead screw was used to adjust the detector position along the optical axis until the strongest and most consistent detector response was obtained, while the test object was used to refine the focal position and temperature calibration. This iterative process of alignment, measurement, and adjustment ultimately produced successful thermal image reconstruction while enabling the system to achieve its temperature accuracy requirements and maximize image quality at the intended working distance.

The enclosure also performed the necessary functions of keeping the electronics assembly together, while providing access for purposes of debugging or otherwise altering the system. In our actual fabrication some panels did not print well, and this caused only cosmetic defects. The actual function was acceptable, and so many of the printed pieces moved on to the final design.

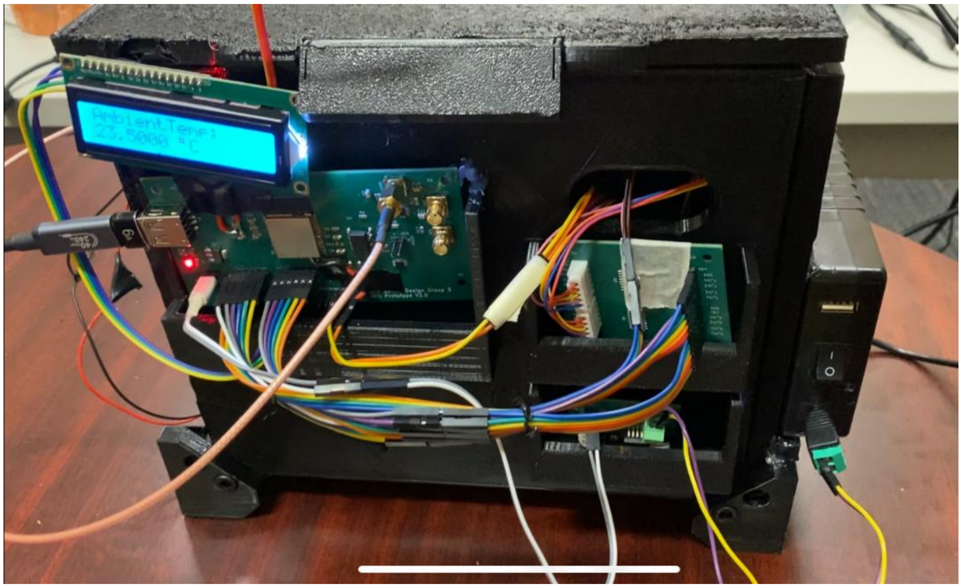

Figure 9.3 – Project IRIS Assembled

Chapter 10 – Administrative Content

10.1 Budget

The project budget is targeted at less than $1,000. While this figure is not a strict limit, the expenditures are personally funded, as the project is not externally sponsored. The objective is to minimize individual contributions while ensuring that established quality standards and performance expectations are maintained.

10.2 Bill of Materials

Table 10.1 – BOM

Qty	Part #	Part Name	Source	Unit Cost	Final Cost
1	24952	Lens PCX ZnSe 38.1 x 76.2mm Uncoated	Edmund Optics	$312.67	$312.67
1	PF10-03-M02	Ø 1” Mid-Infrared Enhanced Gold Mirror	Thorlabs	$98.45	$98.45
2	HMS J21	Thermopile Sensor	Boston Electronics	$38.20	$76.39
1	N/A	SMA Connectors	Amazon	$7.44	$7.44
1	MR128-2RS	Ball Bearings	Amazon	$7.49	$7.49
1	N/A	SMA Connectors (2nd Set)	Amazon	$9.57	$9.57
1	N/A	K-Type Thermocouple	Amazon	$8.19	$8.19
1	N/A	Aluminum Stock	Amazon	$6.38	$6.38

Qty	Part #	Part Name	Source	Unit Cost	Final Cost
1	N/A	Polyimide Heating Strips	Amazon	$9.49	$9.49
1	N/A	MOSFET Driver Module	Amazon	$8.99	$8.99
1	N/A	9V Batteries	Amazon	$0.00	$0.00
1	N/A	9V Battery Holders	Amazon	$0.00	$0.00
1	N/A	Copper/Aluminum Tape	Amazon	$0.00	$0.00
1	N/A	Black PETG Filament	Sunlu	$29.98	$29.98
1	N/A	Solder Paste	Amazon	$9.99	$9.99
1	INA333	INA333 Development Board	Amazon	$12.77	$12.77
1	AS5600	AS5600 Encoder Development Board w/ Magnets	Amazon	$8.99	$8.99
1	ESP32	ESP32 Development Board	Amazon	$19.82	$19.82
1	N/A	Battery Connectors	Amazon	$3.57	$3.57
1	ADS1115	ADS1115 ADC Development Board	Amazon	$11.89	$11.89
1	AD620	AD620 Amplifier Development Board	Amazon	$12.99	$12.99
1	LM2596	LM2596 Buck Converter Module	Amazon	$7.99	$7.99
1	N/A	Piezo Disk with Development Board	Amazon	$7.89	$7.89
1	MCP9808	MCP9808 Temperature Sensor Development Board	Amazon	$13.09	$13.09
1	AMS1117	AMS1117 3.3 V Regulator Board	Amazon	$6.49	$6.49
1	N/A	TalentCell Battery Pack	Amazon	$0.00	$0.00
1	N/A	Jumper Wire Kit	Amazon	$7.07	$7.07
1	N/A	I²C LCD Display	Amazon	$10.00	$10.00
1	28BYJ-48 + ULN2003	Stepper Motors & Driver Boards	Amazon	$8.51	$8.51
1	N/A	DigiKey Components and Shipping	Digikey	$151.19	$151.19
1	N/A	PCBs and Stencils	PCBWay	$104.85	$104.85

10.3 Distribution of Worktable

The following table outlines the distribution of work and tasks that were assigned to each member of the group.

Table 10.2 – Distribution of Worktable

Name	Major	Role	Task
Shea Meyer	Computer Engineering	Primary	PCB Design
		Primary	Microcontroller Integration
		Primary	Sensor Data Processing
		Primary	IOT and Web functionality
		Secondary	Servo and Mirror Coordination
Jason Ha	Photonic Science & Engineering	Primary	Optical System Design
		Secondary	Image processing and Display
		Secondary	Optical/Imaging system calibration
Sean Willie	Electrical Engineering	Primary	Enclosure Design
		Secondary	Power Supply Design
		Secondary	PCB Design
Andrew VanAuken	Electrical Engineering	Primary	BMS/Protection
		Secondary	Display & UI
		Secondary	Auxiliary Temperature and Vibration Sensors

10.4 Milestones

The following tables outline the key milestones achieved during Senior Design 1 and the projected timeline for Senior Design 2.

Table 10.3 – Project Milestones for SD1

Start Date	End Date	Task	Description
01/20/26	1/20/26	Group Recruiting	Recruited: Sean Willie (EE), Andrew VanAuken (EE), Jason Ha (PSE), and Shea Meyer (CpE).
01/21/26	1/21/26	Start Brainstorming Project	We brainstormed ideas for our project.
01/23/26	01/28/26	Form Committee	We contacted and got Dr. Yang, Dr. Kulik and Dr. Grimming as our reviewers.
01/24/26	01/30/26	Divide & Conquer Document	Completed the 10 pages for the Divide & Conquer document.
02/04/26	02/04/26	Divide & Conquer Meeting	Meet with our advisors over Zoom to discuss our project proposal.
02/04/26	02/06/26	Divide & Conquer Document Revision	After we complete the meeting, we make the necessary revisions.
02/07/26	02/21/26	Background Research & Standards	Conduct research to support Midterm Report by evaluating proposed single-detector raster scanning thermal imaging approach along with infrared sensing. Research included subsystem-level investigation of infrared detectors, optics, scanning mechanisms, embedded processing, and power based on datasheets, applications, industry standards, etc. References and citations were used for comparison of performance, cost, and feasibility to justify the design decisions and specifications.
02/14/26	03/01/26	Hardware Feasibility Evaluation	Perform evaluation of potential infrared sensors, optics, MCU, motors, and power solution based on system-level

			requirements from the goals and specifications. Components were evaluated based on datasheets, prior use cases, etc. to assess parameters such as sensitivity, FOV, timing and processing, power consumption, etc. The evaluation is mainly for identifying viable hardware options rather than finalizing component selection.
02/21/26	03/08/26	Defining Preliminary System	Define the preliminary architecture: sensing approach, scanning method, power distribution, communications, etc.
03/01/26	03/15/26	Preliminary Testing and Concept Validation	Perform simulations and early testing to verify raster scanning approach and hardware to meet specification requirements.
03/11/26	03/11/26	Advisor Feedback Meeting	Met with advisors Dr. Chan and Dr. Leisher to review research findings, proposed system architecture, and preliminary design. This feedback helps refine the Midterm Report before it is submitted.
03/18/26	03/18/26	Reviewer Feedback Meeting	Met with project reviewers to present project approach, research, and preliminary design. We will incorporate their feedback to improve the Midterm Report before it is submitted.
01/24/26	03/27/26	Midterm Report	Complete the Midterm Milestone Report.
01/24/26	04/03/26	Midterm Report Revision	Make any revisions to the Midterm Milestone Report.
04/10/26	04/10/26	Ordering Components	Order infrared detectors, optics, MCU, motors, power components, and sensors before starting Senior Design 2.
01/24/26	04/28/26	Final Senior Design Document	Complete the final document for Senior Design 1.
04/28/26	04/28/26	Mini Demo Video	Mini demo of our project.

Table 10.4 – Project Milestones for SD2

Start Date	End Date	Task	Description
05/13/26	05/20/26	PCB Validation Testing	Perform functional testing of fabricated PCB including power regulation verification, MCU programming, peripheral communication, and basic sensor validation.
05/18/26	05/30/26	Mechanical Assembly & System Integration	Integrate PCB with optics assembly, scanning motors, power subsystem, and enclosure. Also verify electrical, mechanical, and optical alignment required for raster scanning thermal data acquisition.
05/25/26	06/05/26	Firmware Integration & Data Acquisition	Integrate motor control, sensor sampling, and communication firmware. Verify timing between scanning hardware and detectors for accurate thermal mapping.
06/01/26	06/10/26	Calibration and Performance	Calibrate scanning, temperature response, and system. Also, performance metrics such as FOV coverage, noise behavior, and system response time.
06/11/26	06/24/26	System-Level Testing & Scenario Evaluation	Conduct testing of the monitoring system, including simulated thermal events, threshold verification
07/06/26	07/14/26	Demo Preparation & Verification	Verify system stability, usability, and reliability in preparation for final evaluation and demonstration.
07/10/26	07/20/26	Finalize the Document	Compile all testing data and results into the final report.
07/21/26	07/23/26	Final Presentation Rehearsal	Prepare presentation materials and conduct practice runs for the final presentation and system demonstration.
07/24/26	07/24/26	Final Presentation	Present and demonstrate final project to advisors, reviewers, etc.

Chapter 11 – Conclusion

The IRIS project successfully demonstrated the design, implementation, and characterization of a low-cost raster-scanned thermal imaging system for hotspot detection using a single LWIR thermopile detector. Throughout the project, the team applied engineering principles across optical design, optomechanical systems, embedded control, analog electronics, and system integration to develop a functional prototype from initial concept through final testing. The iterative design process required continuous refinement of the optical architecture, scanning mechanism, and signal acquisition electronics to achieve reliable system performance.

The completed prototype successfully integrated the optical, mechanical, and electronic subsystems into a working thermal imaging platform. Through iterative testing and calibration, the team achieved successful thermal image reconstruction and met the project's primary engineering specifications, including frame rate, hotspot detection capability, and temperature accuracy across the intended operating range. Design improvements such as the refined scanning mechanism, adjustable optical alignment system, low-noise amplifier circuitry, optical baffling, and electromagnetic shielding contributed significantly to the final system performance and reliability.

The project demonstrates that a mechanically scanned, single-detector architecture can provide a practical and economical alternative to focal plane array-based thermal imaging for applications where high frame rates are not required. By combining commercially available components with custom optomechanical and optoelectronic design, the team produced a proof-of-concept system capable of accurately detecting and localizing thermal hotspots. The knowledge gained throughout the design, implementation, and characterization process provides a strong foundation for future improvements in imaging speed, spatial resolution, and system packaging while demonstrating the feasibility of low-cost infrared imaging for industrial monitoring applications.

Appendices

Appendix A - *References*

Here’s your updated reference list in plain text format, cleaned and consolidated according to the style you provided:

[1] Colbert IR Services, Inc., "Colbert IR," https://www.colbertIR.com, accessed Jan. 29, 2026.

[2] LayerZero Power Systems, "INSIGHT IR Cameras," https://www.layerzero.com/Innovations/Industry-Firsts/INSIGHT-IR-Cameras.html, accessed Jan. 28, 2026.

[3] FLIR Systems, "FLIR AX8 Thermal Imaging Camera," Datasheet. [Online]. Available: https://www.mouser.com/datasheet/2/227/71201_0101_en_US_A4-2580050.pdf

[4] Optris GmbH, "Xi 410 Infrared Camera," Datasheet, 2023. [Online]. Available: https://optris.com/wp-content/uploads/2024/10/Xi-410-DS-EN2023-05-B_web.pdf

[5] A. Daniels, Field Guide to IR Systems, Detectors, and FPAs, 3rd ed. Bellingham, WA, USA: SPIE Press, 2018, doi: 10.1117/3.2315935.

[6] G. M. Gibson et al., "Single-pixel imaging 12 years on: a review," Optics Express, vol. 28, no. 19, pp. 28190–28225, 2020.

[7] Teledyne Vision Solutions, "Line Scan Camera Primer," https://www.teledynevisionsolutions.com/learn/learning-center/machine-vision/line-scan-primer/, accessed Mar. 26, 2026.

[8] Voltrium, "Line Scan Cameras vs Area Scan Cameras," https://www.voltrium.com.sg/en/line-scan-cameras-vs-area-scan-cameras/?srsltid=AfmBOopQi0JPdAduvEaobplmWNfCm1SUVTbY1azByonPoncZ-E2FSfn_, accessed Mar. 26, 2026.

[9] ResearchGate, "Functional overview of the polygon scanner," https://www.researchgate.net/figure/Functional-overview-of-the-polygon-scanner-Fig-2-Picture-of-the-polygon-scanner_fig6_287208310, accessed Mar. 26, 2026.

[10] PCMag, "Raster Scan," https://www.pcmag.com/encyclopedia/term/raster-scan, accessed Mar. 26, 2026.

[11] A. Abubakar et al., "Rechargeable Batteries for Energy Storage: A Review," ResearchGate, 2024. [Online]. Available: https://www.researchgate.net/publication/378947399_Rechargeable_Batteries_for_Energy_Storage_A_review

[12] G. Long et al., "Experimental Study on Vibration Mechanism and Prevention Technology of Heavy Load Switchgear," in Proc. IEEE Int. Conf. High Voltage

Engineering and Applications (ICHVE), 2022, doi: 10.1109/ICHVE53725.2022.9961537.

[13] P. Pirozelli et al., "Assessing Logical Reasoning Capabilities of Encoder-Only Transformer Models," arXiv:2312.11720, accessed Mar. 24, 2026. [Online]. Available: https://arxiv.org/pdf/2312.11720

[14] Barr Group, "2018 Safety and Security Survey," https://barrgroup.com/embedded-systems/market-surveys/2018-safety-security, accessed Mar. 24, 2026.

[15] R. Condit and D. W. Jones, "Stepping Motors Fundamentals," Microchip Technology Inc., Chandler, AZ, USA, Appl. Note AN907, 2004.

[16] C. Fiore, "Stepper Motors Basics: Types, Uses, and Working Principles," Monolithic Power Systems, Article A-0040, Rev. 1.0, Jun. 2023.

[17] M. Alsabbagh, MicroPython Cookbook. Birmingham, UK: Packt Publishing, 2019.

[18] IRISS, Inc., "10 Things You Need To Know About IR Windows," IRISS Technical Guide, 2009.

[19] Colbert IR Services, Inc., "View Ports & IR Window - Safe Viewing of High Voltage Switchgear," Colbert IR Services, Inc.

[20] Eaton Corporation, "IR Windows Applied in Switchgear Assemblies," White Paper, https://www.eaton.com/content/dam/eaton/markets/mining-metals-minerals/knowledge-center/white-paper/IR-windows-applied-in-switchgear-assemblies.pdf, accessed Jan. 29, 2026.

[21] National Fire Protection Association, "NFPA 70B: Recommended Practice for Electrical Equipment Maintenance," NFPA, Quincy, MA, USA, 2023. [Online]. Available: https://www.nfpa.org/codes-and-standards/nfpa-70b-standard-for-electrical-equipment-maintenance/70b

[22] National Fire Protection Association, "NFPA 70E: Standard for Electrical Safety in the Workplace," NFPA, Quincy, MA, USA, 2024. [Online]. Available:

https://www.nfpa.org/codes-and-standards/nfpa-70e-standard-for-electrical-safety-in-the-workplace/70e

[23] U.S. Occupational Safety and Health Administration, "29 CFR 1910.333: Selection and Use of Work Practices," U.S. Department of Labor, Washington, DC, USA. [Online]. Available: https://www.osha.gov/laws-regs/regulations/standardnumber/1910/1910.333

[24] National Electrical Manufacturers Association, "ANSI/NEMA 250-2020: Enclosures for Electrical Equipment (1000 Volts Maximum)," NEMA, Rosslyn, VA, USA, 2020. [Online]. Available: https://www.nema.org/docs/default-source/standards-document-library/ansi_nema_250-2020-contents-and-scope76f809d7-afad-4aa1-80cd-e1d09b60f2e5.pdf

[25] U.S. Federal Communications Commission, "Title 47 CFR Part 15: Radio Frequency Devices," FCC, Washington, DC, USA. [Online]. Available: https://www.ecfr.gov/current/title-47/chapter-I/subchapter-A/part-15

[26] IPC, "IPC-2221B: Generic Standard on Printed Board Design," IPC, Bannockburn, IL, USA, 2012. [Online]. Available: https://www.ipc.org/TOC/IPC-2221B.pdf

[27] IEEE, "IEEE Std 802.11-2020: IEEE Standard for Information Technology — Telecommunications and Information Exchange Between Systems — Local and Metropolitan Area Networks — Specific Requirements Part 11: Wireless LAN Medium Access Control (MAC) and Physical Layer (PHY) Specifications," IEEE, New York, NY, USA, 2020. [Online]. Available: https://ieeexplore.ieee.org/document/9363693

[28] International Electrotechnical Commission, "IEC 60529: Degrees of Protection Provided by Enclosures (IP Code)," IEC, Geneva, Switzerland, 2013. [Online]. Available: https://www.wewontech.com/IEC60529-%20IP-Standard.pdf

[29] Rajguru Electronics (I) Pvt. Ltd., "Stepper Motor 5V 28BYJ-48 Datasheet," Rajguru Electronics, n.d.

[30] STEPPERONLINE, "17HE08-1004S NEMA 17 Stepper Motor Datasheet," STEPPERONLINE, n.d.

[31] PBC Linear, "NEMA 17 Stepper Motor Datasheet," PBC Linear Engineering, n.d.

[32] Sanyo Denki Co., Ltd., "SANMOTION F2 2-Phase Stepping Systems Catalog," Cat. No. S0832B027, Sanyo Denki, 2025.

[33] B. Earl, "All About Stepper Motors," Adafruit Industries, last updated June 3, 2024. [Online]. Available: https://learn.adafruit.com/all-about-stepper-motors

[34] HandsOnTec, "I2C LCD1602 Module Datasheet," HandsOnTec, n.d. [Online]. Available: https://www.handsontec.com/dataspecs/module/I2C_1602_LCD.pdf

[35] UCTRONICS, "0.96-Inch OLED Display Module U602602 Datasheet," UCTRONICS, n.d. [Online]. Available: https://www.uctronics.com/download/Amazon/U602602.pdf

[36] Waveshare Electronics, "2.13inch e-Paper HAT Manual," Waveshare, n.d. [Online]. Available: https://www.waveshare.com/wiki/2.13inch_e-Paper_HAT_Manual

[37] TE Connectivity, "540A Series Piezoelectric Accelerometer Datasheet," TE Connectivity, n.d. [Online]. Available: https://mm.digikey.com/Volume0/opasdata/d220001/medias/docus/2614/540A.pdf

[38] Thorlabs, "TD2X Unmounted Thermopile Detector Drawing and Specifications," MTN010549-D02, Thorlabs, Jan. 2016. [Online]. Available: https://media.thorlabs.com/globalassets/items/t/td/td10x/mtn010549-d02.pdf

[39] Espressif Systems, "ESP32 Series Datasheet," v5.2, Espressif Systems, 2023. [Online]. Available: https://www.espressif.com/sites/default/files/documentation/esp32_datasheet_en.pdf

[40] Adafruit Industries, "MCP9808 High Accuracy I²C Temperature Sensor Breakout Board," Adafruit Industries, n.d. [Online]. Available: https://www.adafruit.com/product/1782

[41] Advanced Monolithic Systems, "AMS1117 Low Dropout Voltage Regulator Datasheet," Advanced Monolithic Systems, n.d. [Online]. Available: https://media.digikey.com/pdf/Data%20Sheets/UTD%20Semi%20PDFs/AMS1117.pdf

[42] Texas Instruments, "LM2596 SIMPLE SWITCHER Step-Down Voltage Regulator Datasheet," Texas Instruments, n.d. [Online]. Available: https://www.ti.com/lit/ds/symlink/lm2596.pdf

[43] Manuals+, "UMLIFE AS5600 Magnetic Encoder Module User Manual," Manuals+, n.d. [Online]. Available: https://manuals.plus/asin/B094F8H591

[44] MCSensors, "Thermopile Sensor HMS-J21-F4.26 Datasheet," MCSensors, n.d. [Online]. Available: http://www.mcsensors.com/PDF/Spec_ThermopileSensor_HMS-J21-F4.26.pdf

[45] Texas Instruments, "ADS1115 16-Bit Analog-to-Digital Converter Datasheet," Texas Instruments, n.d. [Online]. Available: https://www.ti.com/lit/ds/symlink/ads1115.pdf

[46] DigiKey, "Understanding Rotary Encoders: Key Types, Technologies, and Use Cases," DigiKey, n.d. [Online]. Available: https://forum.digikey.com/t/understanding-rotary-encoders-key-types-technologies-and-use-cases/44606

[47] MagnTek, "MT6701 Magnetic Encoder Datasheet," MagnTek, n.d. [Online]. Available: https://uploadcdn.oneyac.com/attachments/files/brand_pdf/magntek/F3/CA/MT6701QT-STD.pdf

[48] Analog Devices Inc., "ADA4522-1/ADA4522-2/ADA4522-4 Zero-Drift Operational Amplifiers," Analog Devices Inc., 2025. [Online]. Available: https://www.analog.com/media/en/technical-documentation/data-sheets/ada4522-1_4522-2_4522-4.pdf

[49] Amazon, "Momentary Tactile Push Button Switch Assortment Kit," Amazon, n.d. [Online]. Available: https://www.amazon.com/Momentary-Tactile-Button-Switch-Assortment/dp/B07LCBLB8N

[50] E-Switch, "PV6 Series Anti-Vandal Pushbutton Switch Datasheet," E-Switch, n.d. [Online]. Available: https://configured-product-images.s3.amazonaws.com/Datasheets/PV6.pdf

[51] Omron Electronics, "B3U Series Ultra-Miniature Tactile Switch Datasheet," Omron Electronics, n.d. [Online]. Available: https://www.mouser.com/ProductDetail/Omron-Electronics/B3U-1000P

[52] TalentCell, "Rechargeable 12V 6000mAh / 5V 12000mAh DC Output Lithium-Ion Battery Pack," TalentCell, n.d. [Online]. Available:

https://www.amazon.com/TalentCell-Rechargeable-12000mAh-Multi-led-indicator/dp/B00ME3ZH7C

[53] C. Simpson, "Characteristics of Rechargeable Batteries," Texas Instruments, Application Report SNVA533, 2011. [Online]. Available: https://www.ti.com/lit/an/snva533/snva533.pdf

[54] D. MacBeth, "Rechargeable Battery Applications," Michigan State University College of Engineering, East Lansing, MI, Nov. 2013.

[55] Anker, "PowerCore Slim 10000 Portable Charger," Anker, n.d. [Online]. Available: https://www.amazon.com/Anker-Travel-Ready-Technology-High-Speed-Output/dp/B0D5CLSMFB

[56] KU XIU, "S3 Qi2.2 Magnetic Power Bank (10,000 mAh)," KU XIU, n.d. [Online]. Available: https://www.amazon.com/KU-XIU-Solid-State-Magnetic-Portable/dp/B0FCS6PZQH

[57] EPCOS AG (TDK Electronics), "NTC Thermistors – General Technical Information," Munich, Germany, 2018. [Online]. Available: https://www.tdk-electronics.tdk.com/

[58] Microchip Technology Inc., "Temperature Sensor Design Guide: Precision Temperature Measurement with Silicon IC Temperature Sensors, Thermocouples, RTDs and Thermistors," Chandler, AZ, USA, 2004. [Online]. Available: https://www.microchip.com/

[59] FTVOGUE, "Ceramic Piezoelectric Vibration Sensor Module with Adjustable Threshold Output," FTVOGUE, n.d. [Online]. Available: https://www.amazon.com/dp/B0DCG7XH1W

[60] Analog Devices, "AD620 Low Cost Low Power Instrumentation Amplifier," AD620 Datasheet, Rev. H, Norwood, MA, USA, 2011. [Online]. Available: https://www.analog.com/media/en/technical-documentation/data-sheets/ad620.pdf

[61] Analog Devices, "AD8420 Wide Supply Range, Micropower, Rail-to-Rail Instrumentation Amplifier," AD8420 Datasheet, Rev. A, Norwood, MA, USA, 2015. [Online]. Available: https://www.analog.com/media/en/technical-documentation/data-sheets/AD8420.pdf

[62] Analog Devices, "AD8421 3 nV/√Hz, Low Power Instrumentation Amplifier," AD8421 Datasheet, Rev. A, Norwood, MA, USA, 2020. [Online]. Available: https://www.analog.com/media/en/technical-documentation/data-sheets/AD8421.pdf

[63] Heimann Sensor GmbH, "Specification: Thermopile Sensor HMS-J21-F4.26," HMS-J21-F4.26 Product Specification, Rev. 0.1, Dresden, Germany, Jul. 2004.

[64] Texas Instruments, "ADS111x Ultra-Small, Low-Power, I²C-Compatible, 860SPS, 16-Bit ADCs with Internal Reference, Oscillator, and Programmable Comparator," ADS1113/ADS1114/ADS1115 Datasheet, SBAS444E, Dallas, TX, USA, Dec. 2024. [Online]. Available: https://www.ti.com/lit/ds/symlink/ads1115.pdf

[65] Texas Instruments, "ADS101x Ultra-Small, Low-Power, I²C-Compatible, 3.3kSPS, 12-Bit ADCs With Internal Reference, Oscillator, and Programmable Comparator," ADS1013/ADS1014/ADS1015 Datasheet, SBAS473F, Dallas, TX, USA, Jan. 2025. [Online]. Available: https://www.ti.com/lit/ds/symlink/ads1015.pdf

[66] Microchip Technology, "MCP3004/3008 2.7V 4-Channel/8-Channel 10-Bit A/D Converters with SPI Serial Interface," MCP3004/3008 Datasheet, DS21295D, Chandler, AZ, USA, 2008. [Online]. Available: https://ww1.microchip.com/downloads/en/DeviceDoc/21295d.pdf

Appendix B - Copyright Permission

Appendix C - ChatGPT Responses

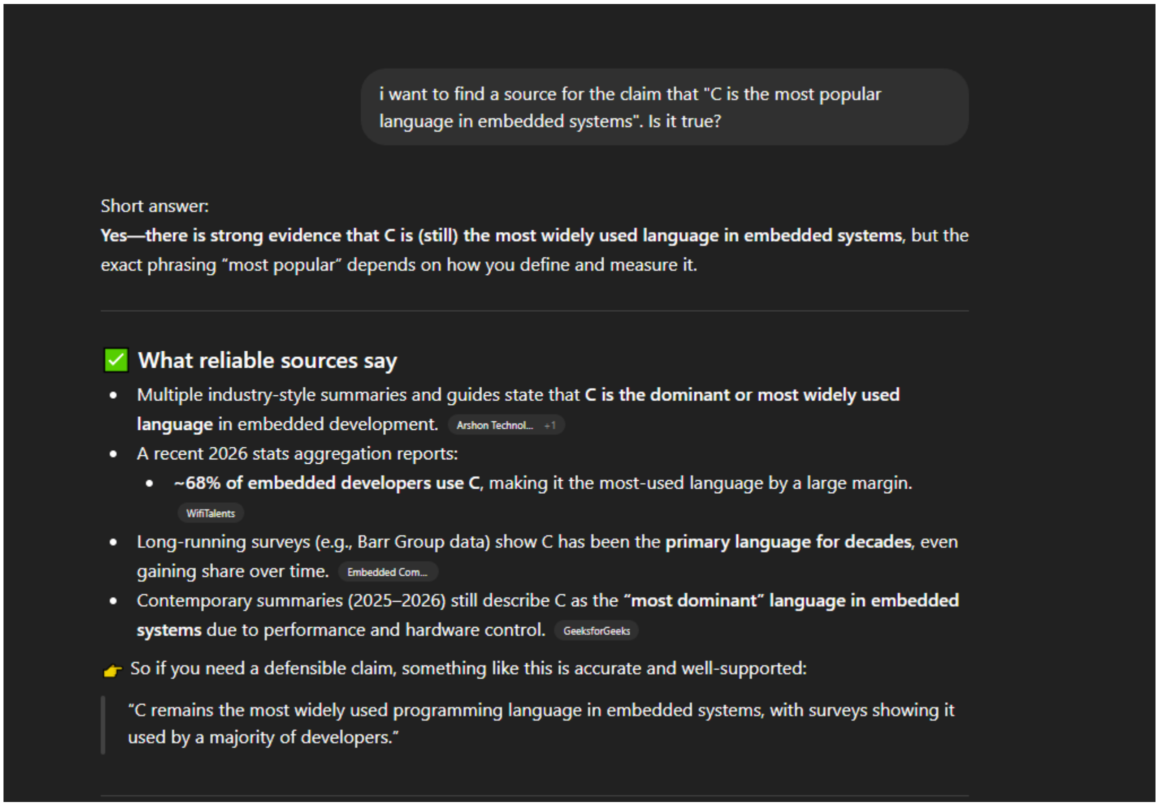

Figure 5.1 – Conversation 1

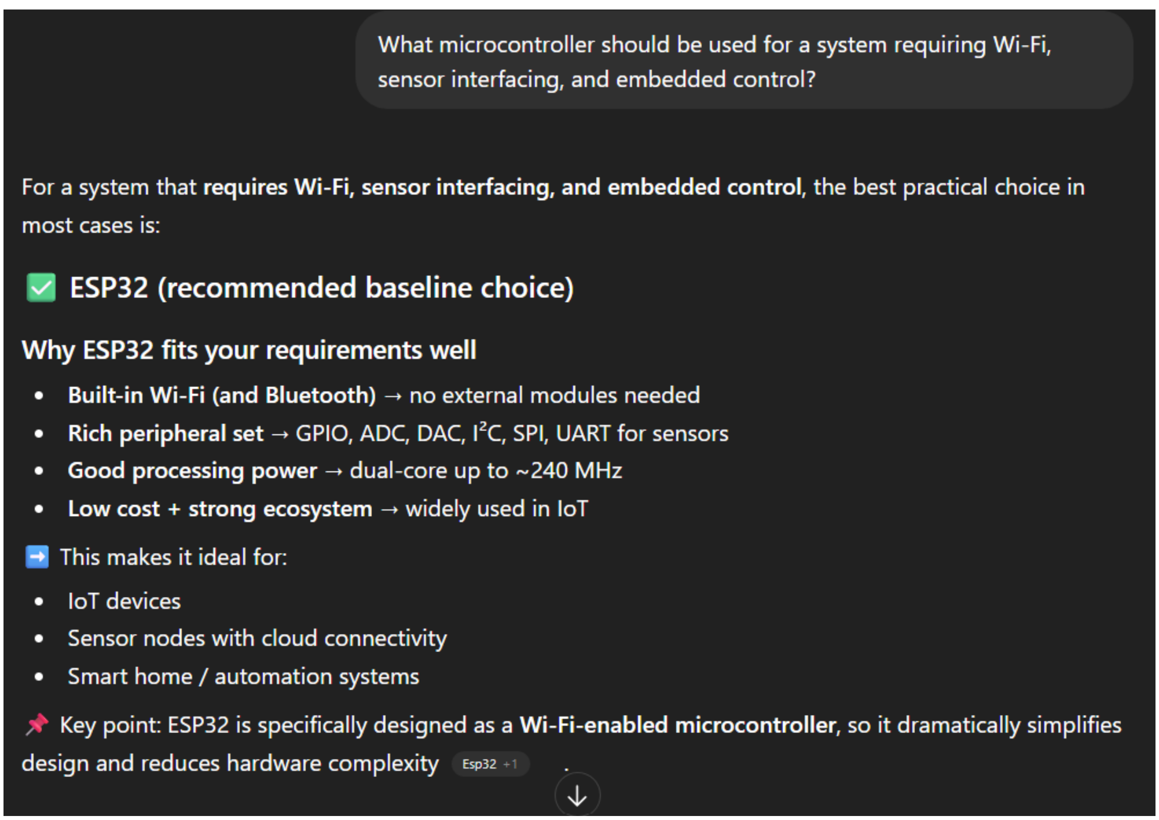

Figure 5.2 – Conversation 2

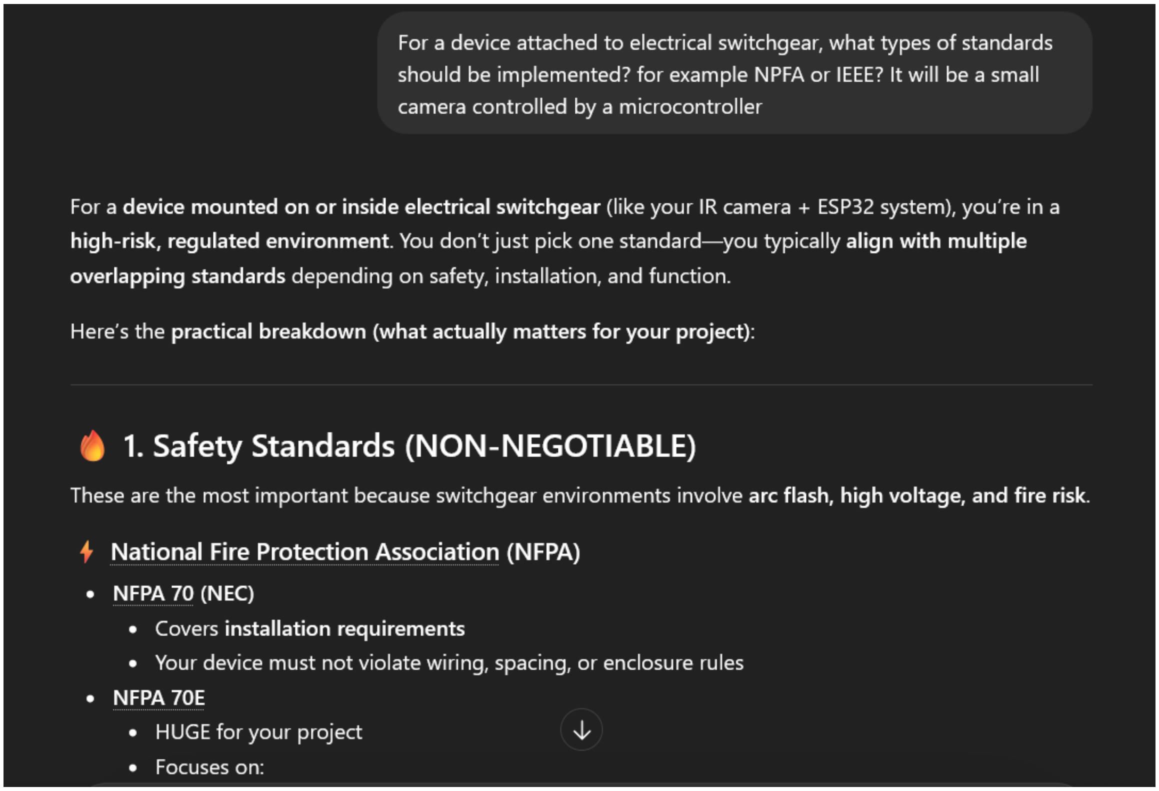

Figure 5.3 – Conversation 3

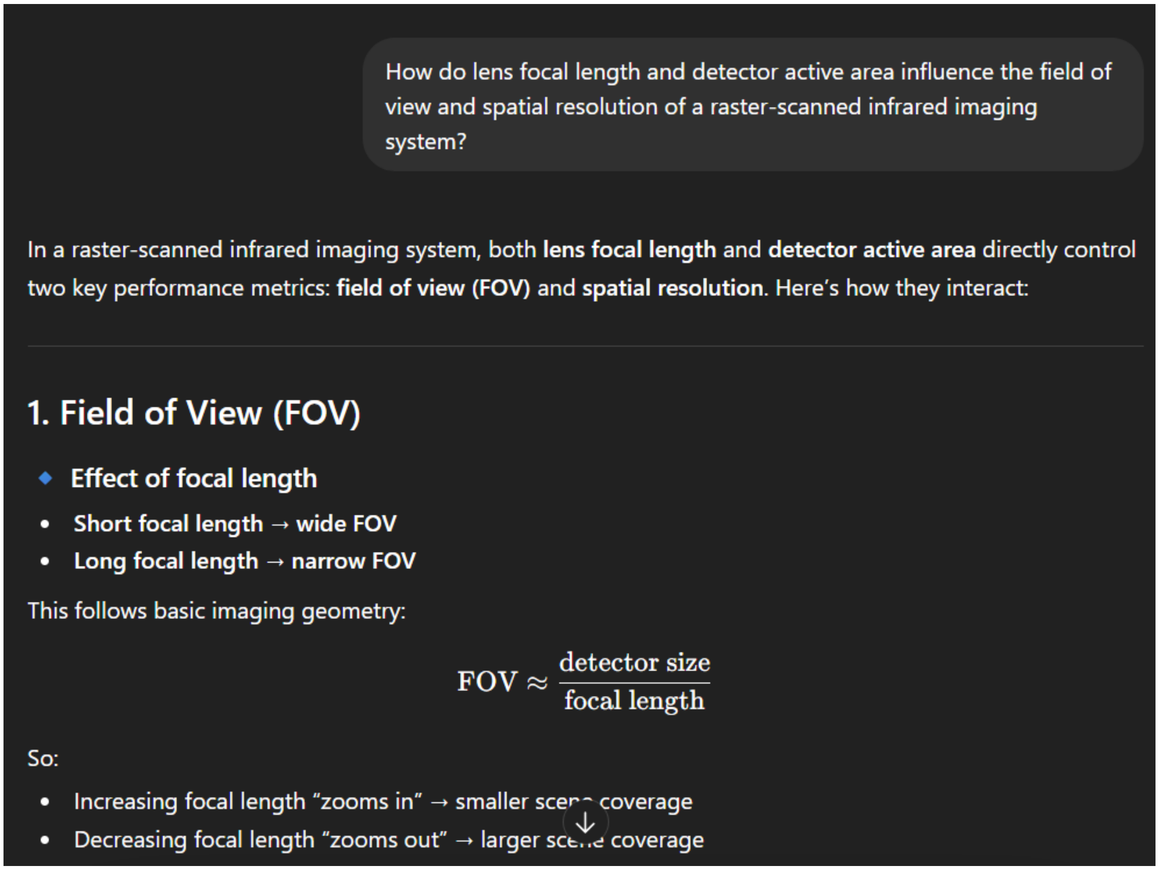

How do lens focal length and detector active area influence the field of view and spatial resolution of a raster-scanned infrared imaging system?

In a raster-scanned infrared imaging system, both **lens focal length** and **detector active area** directly control two key performance metrics: **field of view (FOV)** and **spatial resolution**. Here's how they interact:

1. Field of View (FOV)

◆ **Effect of focal length**

- **Short focal length → wide FOV**
- **Long focal length → narrow FOV**

This follows basic imaging geometry:

$$\text{FOV} \approx \frac{\text{detector size}}{\text{focal length}}$$

So:

- Increasing focal length "zooms in" → smaller scene coverage
- Decreasing focal length "zooms out" → larger scene coverage

Figure 5.4 – Conversation 4